THESIS TITLE

CONTINUOUS AND BATCH HIGH GRADIENT MAGNETIC FILTRATION (HGMF) OF GASES

By

Okeke Olisa Onukwugha

MSc. (UMIST)

This Thesis is submitted to The University of Sheffield in partial fulfilment of the requirements for the degree of Doctor of Philosophy.

Department of Mechanical Engineering

January 1988

TO MY PARENTS

BENNETT

AND

KEZIAH

ACKNOWLEDGEMENT

I wish to express my gratitude to Professor R F Boucher the head of Department of Mechanical Engineering for his continual help and guidance throughout the duration of this study.

I also wish to thank the technical staff especially Messrs. B Carlisle, P Kennett and J Goodliffe for providing their expertise throughout the duration of this investigation.

Lastly, I extend special gratitude to my family especially my father whose immense financial contribution saw to the successful completion of this endeavour.

SUMMARY

Conventional magnetic separation is a long established technique in mineral processing for tramp iron, and for concentrating magnetic ores. Its use was generally restricted to the separation of strongly magnetic materials. Recently, the application of this method has been slightly modified to include the filtration of micron sized paramagnetic particles. This method is called the High Gradient Magnetic Separation (HGMS) and maximizes the magnetic forces by using electromagnets to separate small and weakly paramagnetic particles. The main advantage is that separation is highly efficient and can be carried out at high flow rates with a minimum head loss across the filter.

In this study, tests were carried out with two types of filters - randomly packed cylindrical wire filter matrix and well ordered woven wires. Cupric Oxide (CuO) dust with particle distribution of less than two microns was used for the investigation. The CuO was chosen as a representative paramagnetic dust. Specific tests were carried out to determine the effects of individual operating parameters such as matrix packing fraction, magnetic field strength, and gas velocity on filter loadability and efficiency.

The results showed that for both randomly packed and woven wire filters, increasing packing fraction produced better loadability and sustained capture efficiency, although not in proportion to the mass of wire used. Increasing entrainment velocity produced slightly improved result for randomly packed filter unlike that obtained from woven wires.

A novel idea of applying a fluidic diverter to HGMF was introduced. The main objective was to increase the flow residence time in the filter matrix , thereby increasing the chances of more particles being captured. The results obtained from the application of fluidic flow diverter showed poor collection for very small particles but good filtration for larger particles.

Prediction of theoretical collection efficiencies were made using the single wire single particle model. The collection efficiencies of the smallest particle range agreed with those obtained from experiments but large deviations were present for the biggest particles in the case of random wires.

Pressure drop measurements were also carried out for the filters used over the range of operating parameters applied. The results were plotted in two basic forms that incorporated flexibility in their interpretation and usage.

CONTENTS

LIST OF FIGURES

LIST OF PLATES

LIST OF TABLES

NOMENCLATURE

A	Relative magnitude of induced magnetization due to applied field H_o
A_e	Effective capturing surface
A_f	Cross-sectional area of an arm of the diverter
A_n	Cross sectional area of nozzle
B	Magnetic flux vector
C_d	Drag coefficient
D_f	Diameter of the diverter output pipe
D_n	Nozzle diameter
E	Filtration efficinecy
E_f	Effectiveness factor
E_s	Field strength
F	Packing fraction
F_{bf}	Buoyant force of the fluid acting on a particle
F_d	Drag force on particle
F_e	Force due to charge e
F_f	Friction factor
F_g	Net gravitational force acting on the particle
F_{gp}	Gravitational force acting on a single particle
F_m	Force on a dipole
F_m	Magnetic force on particle
Fr	Froude number
G	Dimensionless gravitational force parameter
H	External magnetic field strength
H_i	Induced field
H_o	Applied field

I	Total uniform fractions in a polydisperse system
K	Dimensionless viscous force parameter
K_1	Coefficient of pressure drop in the reducer
L	filter length
L_r	Length of reducer
M	Magnetization of a paramagnetic sphere
M_o	Line dipole of moment
M_s	Saturation magnetization of fiber
N	Number of particles per unit volume
N_c	Number of particles of a given size that are collected per unit length per unit time
N_e	Total particle per unit length extracted from a filter matrix
N_i	Nuber of particles per unit volume of a given size at upstream section
N_n	Number of nozzle widths
P_r	Pressure drop across reducer
P	Particle penetration
Pe	Peclet number
Q_c	Minimun flow rate required to fluidize the largest nickel sphere
Q_f	Flow rate through one arm of the diverter
Q_n	Flow rate through the nozzle
R	Ratio of particle to wire radius
Re_{max}	Maximum Reynolds number
Re_{min}	Minimum Reynolds number
Re	Reynolds number
S	Transient (Switching) Strouhal number

S_s	Screen solidity
T_s , T_t	Switching and Nozzle transport time resp.
U_t	Terminal velocity
V	Bulk fluid velocity
V_a	Flow velocity in the filter matrix
V_e	Supply voltage
V_f	Velocity of fluid through an arm of the diverter
V_m	Matrix volume
V_{mf}	Minimum fluidizing velocity
V_n	Nozzle velocity
V_o	Volume of particles
V_p, V_θ	Velocity of particle with respect to container and to fluid respectively
$V_{fr}, V_f\theta$	Average velocity of displaced fluid in radial and azumuthal directions respectively
V_t	Particle terminal velocity in fluidized bed
W	Dimensionless magnetic force parameter
W_n	Nozzle width
X	Collision radius of particles
X_c	Theoretical critical collision radius
X_e	Experimental critical collision radius
X_o	Original X-coordinate
X_t	Particle instanteneous X-coordinate
a	Wire cross-sectional area
b	Particle diameter
e	Elementary charges
g	Force due to gravitational acceleration
l_c	Length of wire cylinder in a grid

l_s	Side length of cubic lattice
l_t	Length of wire in a given size of matrix
m	Mass of single particle
n	Number of cubes in an idealized matrix (Number of grids in series)
q	Number of charges
r	Position vector
s	Wire radius
t	Time
α	Constant
β	Approach angle of a particle
ζ	Total fractional volume occupied by the mixture
ζ_f	Fractional volume occupied by the fluid
η_d	Direct interception efficiency
η_{dd}	Diffusion deposition efficiency
η_i	Inertial deposition efficiency
$\eta_{d,dd,i}$	Combined collection efficiency
θ	Angle of particle with respect to wire
μ	Viscosity of Air
μ_o	Magnetic permeability of a vacuum
ν	Dynamic viscosity of air
ρ_f	Density of the fluid
ρ_p	Particle density
$\overline{\rho}_p$	Mean particle density for polydisperse systems
Θ_s	Fluid stream width infront of a sampling nozzle
τ	Dimensionless time it takes a particle to travel one wire radius
ϕ	Scalar potential field

X	Susceptibility of particles
$\bar{X}$	Mean susceptibility distribution in polydisperse flow
$\psi(\rho)$	Distribution functions related to particle density
$\psi(X)$	Distribution functions related to particle susceptibility
Γ	Rate of change of R
∇	Volume enclosed by the surface of flux
θ	Rate of change of theta

CHAPTER ONE

INTRODUCTION

1.1 Introduction

This thesis is concerned with Continuous and Batchwise High Gradient Magnetic Filtration (HGMF) of air borne paramagnetic dust. Continuous HGMF deals with the traditional technique where dust is instantaneously extracted as it passes through the filter medium. This is slightly different from the batchwise type where the filtrate is momentarily brought to rest before leaving the filter volume. HGMF generally involves the removal of particles from gaseous flow, based on their magnetic susceptibility. This makes HGMF technique most appropriate for filtering ferromagnetic and paramagnetic dusts. Several widely used industrial processes in the iron, steel and ferro-alloy industries emit large quantities of waste gas containing magnetic particles. These processes can be controlled by other methods such as Electrostatic Precipitation and Fabric Bags, but the application of HGMF offers the opportunity of combining their high magnetic properties with conventional filtration phenomena. Other advantages of applying HGMF include the use of high flow velocity resulting in a high throughput, ultimately leading to massive reduction of the filter size and hence cost of space and manufacture of filters. Again, no inherent health or safety hazard is associated with the application of HGMF.

In this work attention is focused on less susceptible particles dumped into the atmosphere from power generation

plants, mining and automotive exhaust. These small particles are responsible for many disabilitating illnesses and in certain cases acid rain. They have very low magnetic susceptibilities; as low as 2.4×10^{-4} SI units compared to 1.5 SI units for magnetic materials. For the efficient removal of these types of dust by HGMF, either a relatively high field strength will be required or the filtering medium must be well adapted. It is therefore towards the suitability of applying HGMF, and finding ways of making the process perform more efficiently that this investigation is directed.

1.2 Composition of Atmospheric Air

Air is a mixture of many gases. Normal air will consist of approximately 21% oxygen, 78% nitrogen, 1% argon, , 0.3% carbon dioxide and small traces of other gases. It will also contain varying amounts of foreign material, commonly referred to as permanent atmospheric impurities. These materials can arise from such natural processes as wind, erosion, sea spray evaporation, volcanic eruption; and man made activities such as electrical power generation plants, transportation, industrial processes, mining, and smelting, construction and agriculture. Hence, air contaminants can be particulate or gaseous, organic or inorganic, visible or invisible, submicroscopic, microscopic or macroscopic; toxic or harmless. A loose classification based on the origin or method of formation of these materials are:

(i) Dust, Fumes, and Smokes

(ii) Mist and Fog

(iii) Vapours and Gases

1.2.1 Dust

This is solid particles projected into the air by natural forces such as wind, volcanic eruption, or earthquakes, or by mechanical processes including crushing, grinding, blasting and drilling. Some of these processes produce dust by the reduction of larger masses, while others simply disperse materials that are already pulverized. Generally, particles are not dust unless they are smaller than about 100 micrometers. Dusts may be mineral, such as rock, metal, or clay; vegetable, such as grain, wood, cotton, or pollen; or animal, including wool, hair and silk.

1.2.2 Fumes

These are solid particles commonly formed by condensation of vapours of normally solid materials. Metallic fumes are generated from molten metals and usually occur as oxides because of the highly reactive nature of the finely divided matter. Fumes may also be formed by sublimation, distillation, or chemical reaction, whenever these processes create airborne particles predominantly smaller than 1 micron. Fumes which are permitted to age tend to agglomerate into larger clusters.

1.2.3 Smokes

These are extremely small solid and/or liquid particles, produced by incomplete combustion of organic substances such as tobacco, wood, coal, oil, and other carbonaceous materials. The term smoke is commonly applied to a

mixture of solid, liquid, and gaseous products, although technical literature distinguishes between such components as soot or carbon particles, fly ash, cinders, tarry matter, unburnt gases, and gaseous combustion products. Smoke particles vary considerably in size, the smallest being much less than 1 micron. The average size is often in the range of 0.1 to 0.3 microns.

1.3 Sources and Types of Atmospheric Contaminants

1.3.1 Industrial Air Contaminant

Many industrial processes produce air contaminants in the form of dusts, fumes, smoke, mist and fog, vapour, and gases. These are in most cases controlled at source by conventional methods of dust control but HGMS is becoming increasingly applied especially to dusts with magnetic properties. Zero concentration of all contaminants is economically unfeasible. Absolute control of all contaminants cannot be maintained, and therefore workers in such industries usually assimilate small quantities of the various toxic materials without injury. The basis of the science of industrial hygiene is that most air contaminants become toxic only if their concentration exceeds a minimum allowable limit for a specified period of time. These limits for industrial exposure to air contaminants are normally set in advisory standards prepared by professional societies or government agencies.

1.3.2 Radioactive Air Contaminants

Radioactive contaminants may be particulate or gaseous, and are physically similar to ordinary industrial contaminants.

Many radioactive materials would be chemically toxic if present in high concentrations, but in practically all cases, the factor which necessitates limiting their concentration in air is radioactivity. The hazard from most radioactive air contaminants is due to their effects on being taken into and retained in the body. This is known as the internal radiation hazard. Inert gases such as Argon-41, Krypton-85, and Zenon-135, are unlikely to be retained, but are hazardous because the whole body comes in contact with radiation from the gas in the air which surrounds it. These gases are, therefore, external radiation hazards. In cases of serious nuclear accident like the Chenobyl, where a complete melt down of the plant is possible, HGMS can be used to arrest most of the particulates liberated since they would have the magnetic properties of their parent materials. In most cases they are stainless steel. Deposited materials on the ground increases the external radiation hazard.

1.3.3 Nuclear Fallout

As a result of the explosion of a nuclear device, large quantities of highly radioactive elements known as fission products are formed. Some of these are paramagnetic (eg. Oxides of Uranium) and therefore can be controlled by HGMF system. These rise rapidly with heated air and then descend to the earth, while moving horizontally with air currents that prevail at various altitudes. Particle sizes are extremely small when the fission products are formed, and remain so, in the absence of significant quantities of dust. However, if detonation is near the ground, large quantities of dirt are sucked up into the fireball. The

fusion products then attach themselves to these comparatively large dirt particles and descend rapidly to the earth. Thus, the sizes of particles that would need to be captured are relatively larger and therefore enhancing the posibilities of their capture when HGMF is applied.

1.3.4 Atmospheric Dusts

Atmospheric dust is a complex mixture of smokes, mist, fumes, and dry granular particles. These are called aerosols when they are suspended in a gas stream. A sample of atmospheric dust gathered at any given point will generally contain materials common to that locality, together with other components which originated at a distance but were transported by air current or diffusion. These components vary with the geography of the locality, the season of the year, the direction and strength of the wind, and proximity of dust sources.

HGMS can be used to arrest some of these atmospheric dusts especially if they originated from regions where ferro-alloy industries are located. Also , the results obtained from this investigation would form a basis for the application of HGMS to other atmospheric dusts with very low magnetic susceptibilities.

1.4 Particulate Contamination Hazards

1.4.1 Health Hazards

Irritation of the nasal passages by dust and its soiling effects are matters of common concern. The unpleasant

manifestations, such as hayfever and asthma, are known to layman. Unfortunately, the case against dust and air pollution is not confined to their unpleasantness. Silicosis caused by the inhalation of minute particles of silica [1], and pneumoconiosis are serious pulmonary diseases that can cause disability or death. Various industrial processes discharge hazardous particles and gases into the atmosphere. This as well as constituting a problem for the populace is a danger to green vegetation in the form of acid rain [2]. Most prominent among these are power plants that use coal as their fuel, since the imbedded sulphur is liberated after combustion. This then reacts with the atmospheric moisture to form sulphuric acid [3]. Some proportion of the sulphur in coal exists in pyritic form. Pyrites are paramagnetic and therefore readily removable by HGMS process.

1.4.2 Air Pollution

Continued pollution of the atmosphere by emissions from combustion equipment and unclean gases from commercial and industrial establishments places a severe burden not only on the engineer who must select air ventilation supply equipment but also on the entire population. Several disasters and dramatic air pollution incidents have increased concern. The Meuse valley disaster of 1930 in Belgium [4], the London smog of 1952 and 1962 [5], and more recent incidents in Los Angeles and other cities [6], are classic examples in the history of air pollution. In some of these instances, pollution may arise from metallurgical industries. A typical example is the Basic Oxygen Dust (BOF), which are highly magnetic and therefore can be controlled by

magnetic method.

1.4.3 Explosion and Fire Hazard

Another danger of air borne micron sized particles and gaseous fumes is fire and explosion [7,8,9]. Fine dust of combustible material dispersed in air at appropriate concentration can burn with great rapidity, releasing sufficient heat to produce a self propagating reaction which may build up to explosive violence. The dust cloud need not be pre-existent, for the rush of gases at the combustion front of an initially local explosion may raise into the air dust previously deposited on exposed surfaces, the process thus becomes self propagating. Deposits of only a fraction of a millimetre thick may suffice. HGMS is not readily applicable to combustible materials, but the results obtained from the separation of the very low susceptible dust can form a basis for a future investigation of the use of HGMS in this field.

1.4.4 Hazard In Microelectronics Manufacture

The manufacture of integrated circuits for computers and various microprocessors is of increasing importance. Higher speed of operation and lower costs require higher circuit densities, thus further miniaturization. Circuit elements have features in the submicron size domain and are quite sensitive to contamination by particles of comparable size [10]. People, equipments, and piping generate particles which are transported to the vicinity of the product and some of which are deposited. The deposition rate depends upon the air borne particle

distribution and concentration, and the deposition velocities caused by various deposition mechanisms. Particulate contamination can lead to failure of chips, reducing yield (the fraction of chips that are usable) and raising costs; sometimes to the point of making the process a commercial failure. Clean environment can be achieved by channelling all air through an HGMF filter. This can be particularly advantageous because suitable compact HGMS systems can be designed to suit any given case.

1.4.5 Miscellaneous Hazards

The necessity for filtration is not only found in air cleaning but in other various industrial processes, such as, excluding bacteria during food processing [11]; in air conditioning [12]; and the preparation of pharmaceuticals [13]. Another crucial environment where filtration is vital is in hydraulic circuits. Filtration in hydraulic circuits play one or two roles; either to protect a certain component from large scale contamination which may cause immediate damage, or to remove contamination from the system as a whole [14]. HGMS would particularly be useful in removing hydraulic contaminants. This is because most of the particulates found in hydraulic circuits are ferritic and therefore are highly magnetic.

1.5 Particulate Contamination Control

All the above objectives can be achieved by various modes of filtration [15]. These include: the following physical

principles which are either employed alone or in combination:

(i) Gravity

(ii) Centrifuging

(iii) Inertia

(iv) Interception

(v) Diffusion

(vi) Electric Forces

All dust filtration equipment encompass one or more of these natural phenomena. For example, electrostatic precipitators make use of charges possessed or imparted to the dust to effect removal. Most fibrous filters and scrubbers make use of inertia, interception, and diffusion to clean air. An example of gravitational settling can be found in various sedimentation processes [16], while cyclones represent centrifuging.

1.6 Research Objectives

For the purposes of this research, emphasis is solely placed on removal of paramagnetic dust from gaseous flow by the High Gradient Magnetic Filtration (HGMF) method. Here, the term "dust" denotes solid particles which are smaller than 2 microns and are usually formed by mechanical processes such as grinding, crushing and blasting used in the ferrous and ferro-alloy industries. These constitute the greatest health risk, as they can penetrate and stick permanently on the soft tissues of the lungs.

The main objectives of the research project are

centered on the following points:

(i) Providing collection efficiency data for paramagnetic material using randomly packed cylindrical stainless steel wire (AISI 430). (Continuous HGMF).

(ii) Application of an ordered filter medium like woven wire as an HGMF filter. (Continuous HGMF).

(iii) Using the existing total filter models for randomly packed and ordered matrices to predict their initial collection efficiencies.

(iv) Determination of the filter medium resistances to enable initial estimation of the power requirement of the system.

(v) Design of a suitable fluidic diverter and its application to high gradient magnetic filtration of paramagnetic dusts. (Batchwise HGMF).

The dust selected for the study was Cupric Oxide (CuO) of less than two microns in size (APPENDIX E). CuO is merely an example of a paramagnetic dust with a very low magnetic susceptibility. This choice was based on the fact that some particulates discharged into the atmosphere especially from non-ferrous industries are paramagnetic. This is also true for fumes from the chimneys of power stations. So the results obtained in the filtration of CuO dust can be applied to most other dusts of comparable susceptibility, hence saving time and money for individual investigations.

1.7 Concept of HGMF/HGMS

The term HGM "Separation" as has been used, is usually reserved for processes where two or more materials are being sorted; as is obvious in the discussion above. HGM "Filtration", however is used mostly in the context of solid/liquid separation. The solids involved are in the micron to sub-micron region. The subtle difference existing between the two processes is found in the forces existing in the system. While gravitational forces will be considered as most prominent force in a typical separator, it is usually neglected in particulate filtration analysis. Again the method of entrainment of dusts in HGMF processes promotes the effects of hydrodynamic forces; but this is usually negligible in HGMS processes. Therefore as the main objective of this project was the removal of micron-sized CuO dust from air, the term High Gradient Magnetic Filtration will be henceforth adopted in all discussions.

The process of HGMF is primarily based on the interaction between magnetic particles and ferromagnetic filter medium placed in an external magnetic field. The filter materials can be of various forms including grooves, plates, balls and wires [17]. The applied field magnetizes the wire and induces a magnetic dipole in the particle. The convergence of the applied field near the wire produces a region of highly non-uniform field intensity that attracts the dipolar particles towards the wire, much like a bar magnet attracting iron filings [18].

In its simplest and practical form, HGMF consists of a canister packed with fibres of a ferromagnetic material of very small diameter. The canister is placed in a magnetic field that

is generated by say a solenoid, and the resulting tractive magnetic forces provide high efficiency filtration of particles as the carrier fluid passes through the canister (Figure 1.1). Depending on the physical characteristics of the system, inertial, viscous and gravitational forces may also act on the particle in the vicinity of the wire as is shown in Figure 1.2. The high porosity of the filter provides a particle wire phenomenon instead of cake collection mechanism or mechanical capture that dominate in conventional filtration as in fabric bags. Filtration may be continued until the pressure drop across the canister becomes prohibitively high due to the decreased size of the interstitial flow paths or until heavy loading on the wires decreases the collection efficiency.

To regenerate the filters, the magnetic field is removed and the canister is backflushed with either compressed air or high pressure water. A continuous process could be achieved by using a system of several parallel modules, with each module providing filtration for a pre-determined time interval [19]. When the flow is diverted from a module, the magnetic field of the loaded module is de-energized, the filter is cleaned, re-energized and ready for reuse. An alternative scheme that results in zero downtime of the magnet is to construct the magnet and canister so that the loaded filter can be continuously or intermittently removed from the magnetic region and replaced by a clean filter without interrupting the filtration process. Both cyclic and continuous systems are commercially available.

A novel idea of applying a flow diverter to HGMF process (termed Batchwise HGMF) will be tested. As shown in

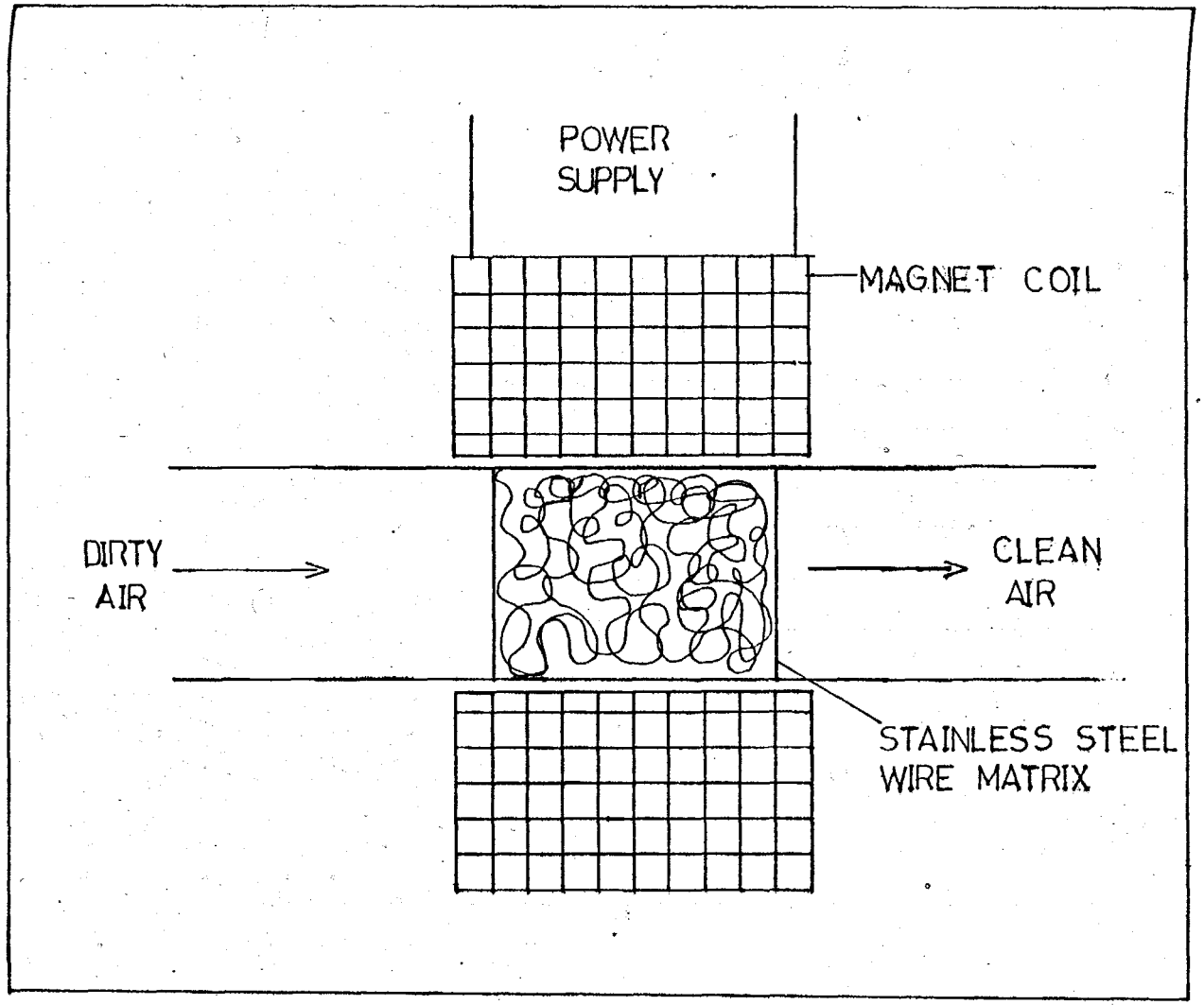

FIG. 1.1; SCHEMATIC REPRESENTATION OF A TYPICAL HIGH GRADIENT MAGNETIC FILTRATION (HGMF)

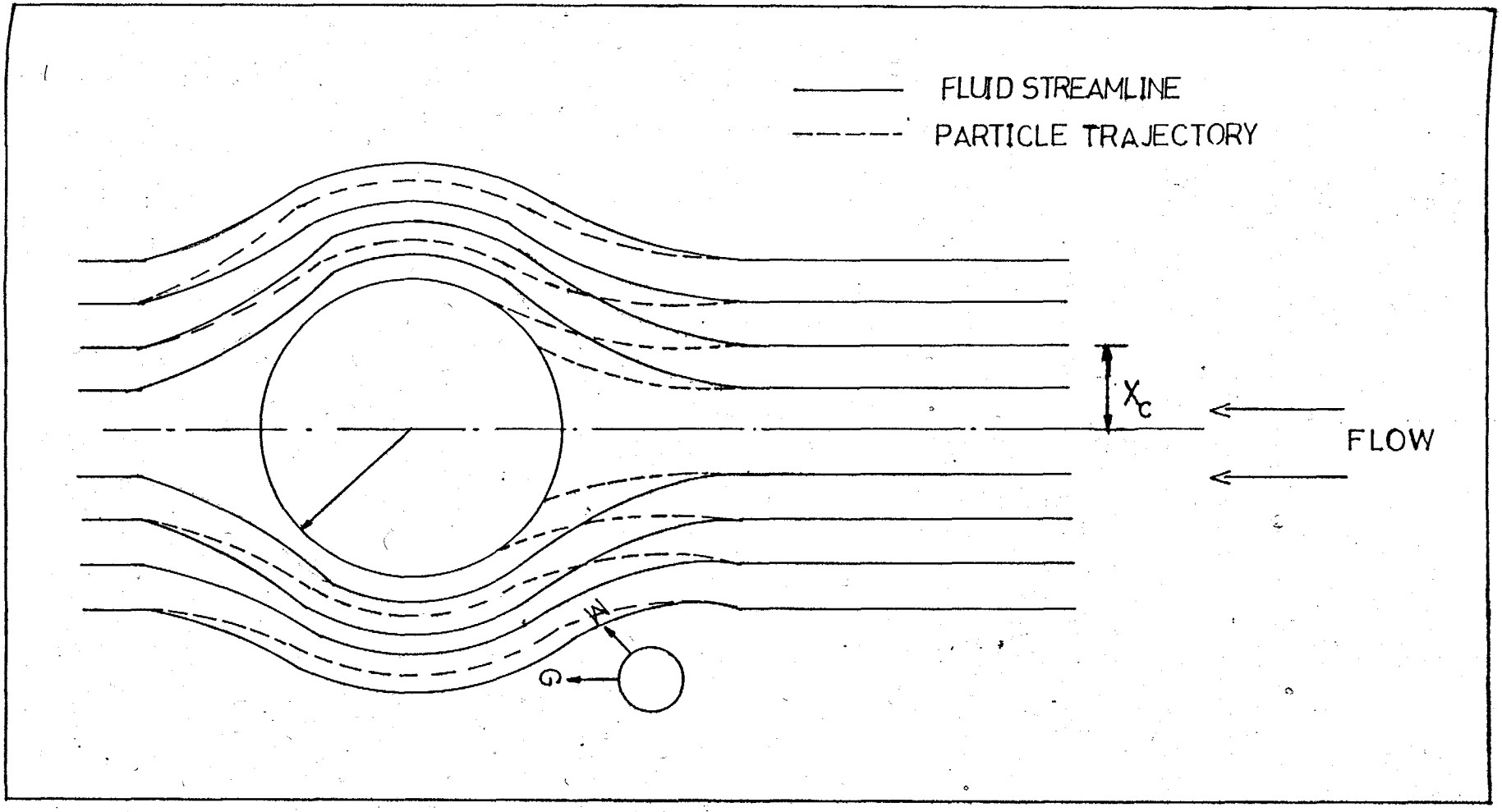

FIG. 1.2: CROSS SECTION OF SPHERICAL PARTICLE NEAR A UNIFORMLY MAGNETIZED WIRE

Figures 1.3, this involves directing the dirty fluid alternatively to the two output pipes that house the filters. The main advantage of applying such a device lies in increasing the flow residence time in the filtration matrix, while still maintaining a relatively high main flow velocity in the duct. This entails switching the flow from one output pipe to the other with a frequency that allows a volume of air that is equivalent to that of the filtering zone; thus achieving a residence time that is equal to the switching time. With this arrangement, it can also be possible to force the dirty air through one outlet until the filter on the opposite side is replaced.

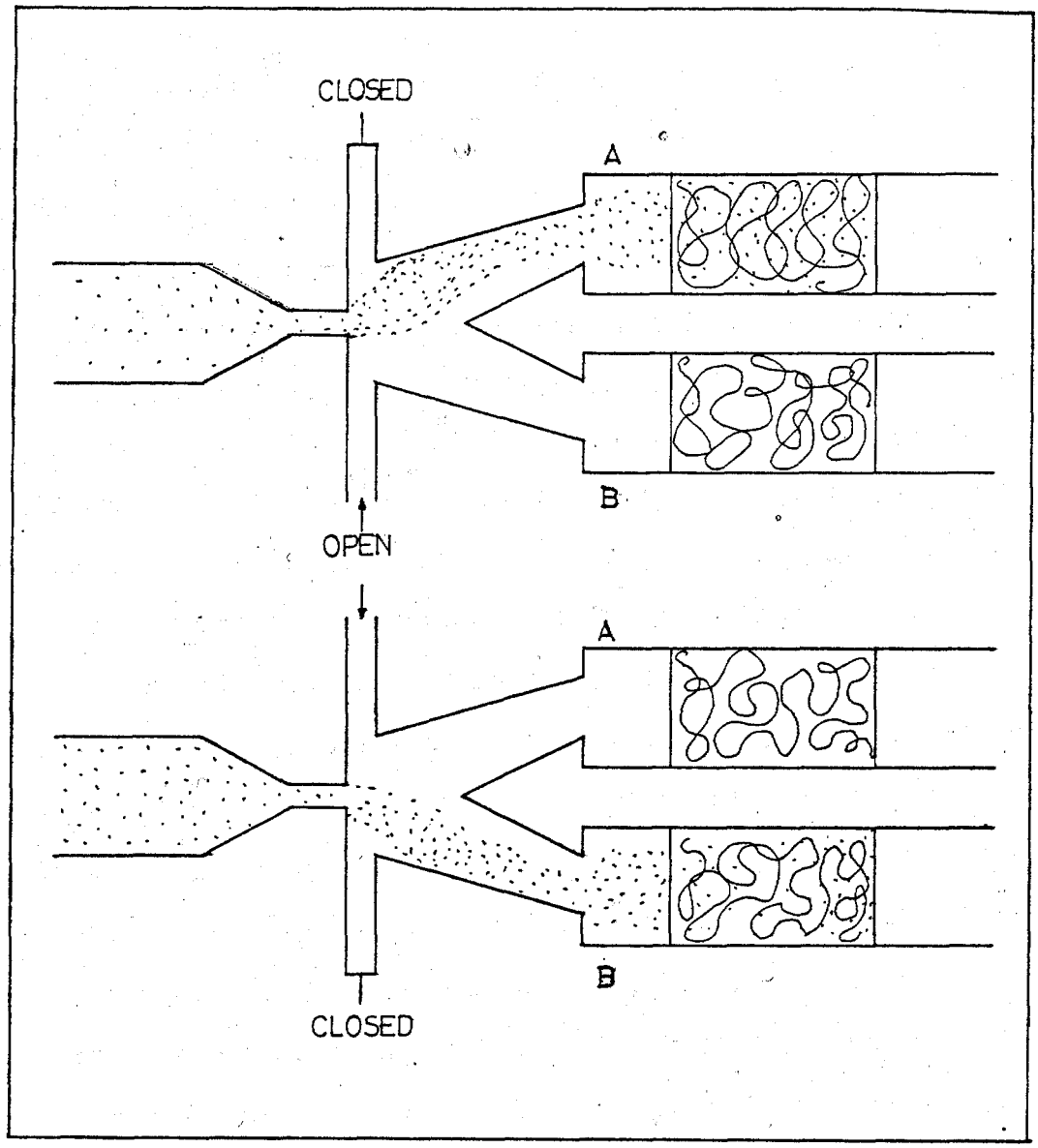

FIG. 1.3: APPLICATION OF FLOW DIVERTER TO HGMF PROCESS

CHAPTER TWO

METHODS OF ACHIEVING PARTICULATE CONTROL

2.1 Introduction

Industrial growth has had a cumulative effect on the problem of controlling contaminant. Not only has the atmosphere in many cities become more polluted, but the intensity of pollution at its source has increased. Accompanying this increase in pollution, is a public awareness of the need for more effective air cleaning; this awareness has resulted in the adoption of stringent regulations pertaining to the collection of dust and contaminant. Air cleaning devices that remove particulate matter are available over a large range of intended duties, from light loads such as , cleaning rooms and air conditioning, to heavy industrial air cleaners. Light-duty air cleaners typically used in air-conditioning systems handle dust concentration up to $4mg/m^3$; whereas, heavy duty devices for process exhaust cleaning, handle up to $70000mg/m^3$, with no well defined upper limit. Some process or pneumatic conveyors are designed to filter much higher dust concentration. Light-duty equipment is often selected for the control of noxious emissions that constitute a health hazard; for example, radiative particles, beryllium particles, or biological air borne wastes, in which the mass loading may be low.

2.2 Rating Air Cleaning Devices

The main operating characteristics that distinguishe the various types of these air cleaners are efficiency, air flow resistance, and life or the dust holding capacity [20]. Efficiency measures the ability of the air cleaner to remove particulate matter from air stream. Average efficiency over the life of the filter is the most meaningful for most types and applications. Air flow resistance (or just "resistance") is the static pressure drop across the filter at any given flow rate. (The term pressure drop is used inter-changeably with resistance). Dust holding capacity defines the amount of a particular type of dust that the air cleaner can hold when operated at a specified air flow rate to some maximum resistance value, before its arrestance is seriously reduced as a result of the dust collected. Described below is the most common particulate control equipment, termed dust collectors. They are usually applied as air pollution control measure to process emission having particulate concentration ranging from 20 to 40000mg/m^3 .

2.3 Bag Filters and Baghouses

Fabric bags are a widely used form of high efficiency collector for both dust and fumes. Each fabric filter element consists of a woven or felted textile material in the shape of a tube or flat supported envelope. Many individual filter elements are contained in a single housing having gas inlet and outlet connections, a dust storage hopper, and cleaning mechanisms. Fabric filters may be used for control of dust concentration in

the range of $1mg/m^3$ to $100g/m^3$ with particles sizes down to submicron fumes. Special fabrics permit operation at a relatively high temperature of about 250°C and resist the corrosive chemical constituent of the filtered gas or collected materials [21]. The basic principle is to select a fabric membrane which is permeable to gas but which will retain the dust. Initially, dust is deposited both on the surface fiber and within the depth of the fabric, but as surface layer builds up, the dust layers themselves become the dominating filter medium. As the dust cake thickens, the resistance to gas flow increases. A typical bag filter is shown in Figure 2.1.

Periodic cleaning of the filter medium is necessary to control the gas pressure drop at the filter. The most common cleaning methods include reverse air flow, mechanical shaking or rapping, vibration and compressed air pulsing. Shaking or back flow of gas can be accomplished either manually or automatically. In some cases, both methods are used simultaneously. The cleaning mechanisms do not result in the fabric returning to its "as new" condition. It is actually undesirable to over clean the fabric because the particles deposited within the depth of the cloth help to reduce the pore size between the fibres; thus enabling a higher efficiency of cleaning to be achieved.

2.4 Wet Dedusters and Dedusters

The characteristic of wet dedusters which sets them apart from the other gas cleaning equipment is the use of a scrubbing liquid like water to achieve the collection of particulate matter. The scrubbing liquid is usually dispersed in

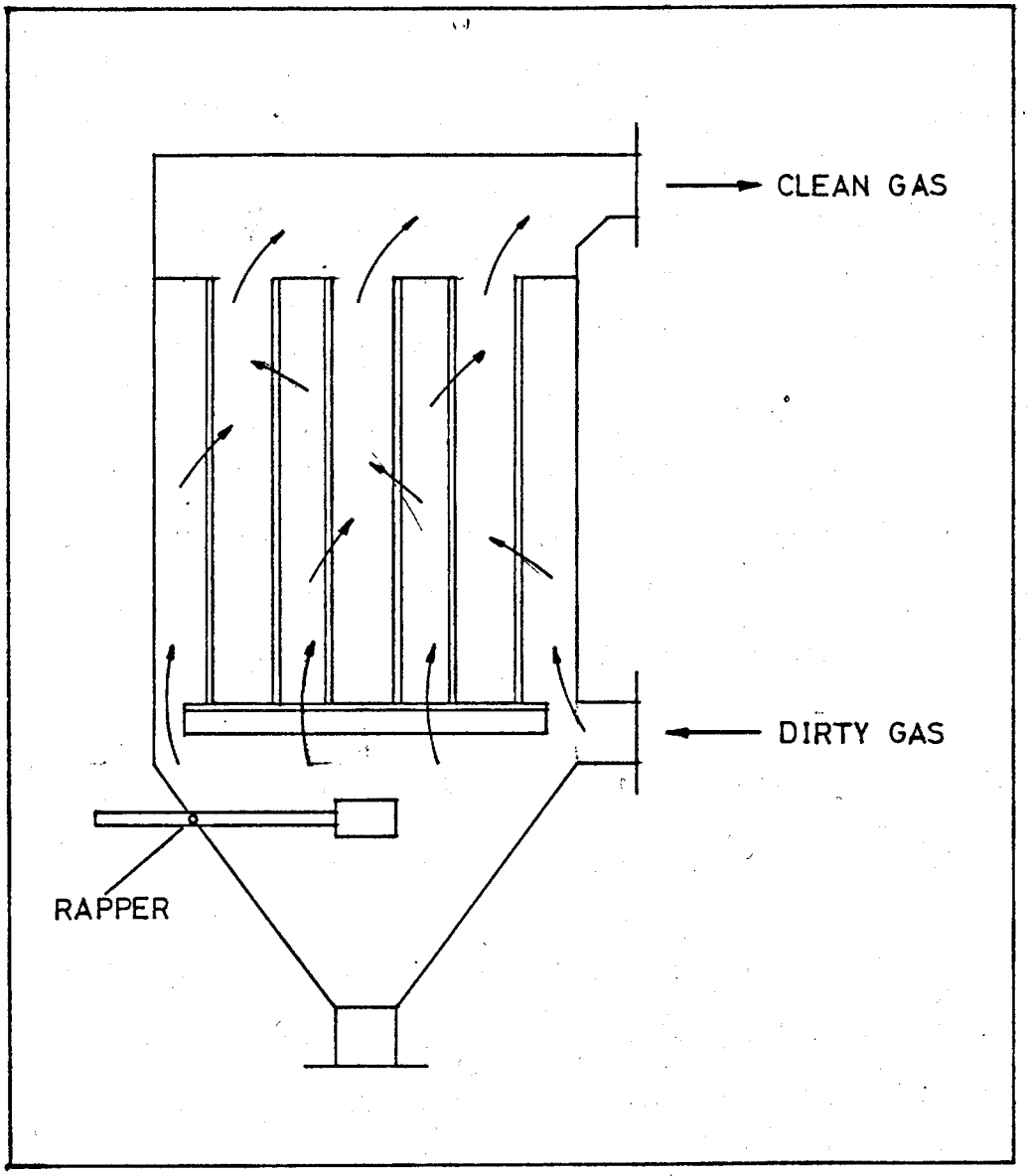

FIG. 2.1: SCHEMATIC DIAGRAM OF A SURFACE FILTER (BAG FILTER)

a spray, or spread in a film over the internal surfaces of the scrubber (Figure 2.2). Downstream of the collection zone, some form of spray eliminator is usually required. The equipment and mode of operation used in demisters, which collect fine liquid particulate, are essentially similar to those of dedusters.

The major mechanism by which fine particles are captured in a deduster is by impaction onto wet surfaces, in the form of droplets as the gas flow round the droplets. The chance of a particle becoming captured depends on the balance between its inertial force, which causes it to move towards the droplet and the aerodynamic drag force exerted upon it by the gas, that tends to cause it to move around the droplet and escape. Thus large fast moving particles are collected more readily than small particles moving at lower velocities. Other mechanisms are sometimes significant in wet washers. The most notable of these is condensation, which can increase the effective diameter of the particles, thus making them easier to be collected.

2.5 Cyclone Dust Separators

High operational efficiency, simple construction, and low maintenance costs make the cyclone the most extensively used type of collector for relatively coarse dusts. Materials that can be collected include, boiler fly ash, saw dust, cement, and oil refinery catalysts. Indeed, cyclones find application in most processes where dry powders are produced or handled. The basic limitation is in its application to binary mixtures. The most common form of cyclone with major constituent features is shown in Figure 2.3. The dust laden air enters the upper cylindrical

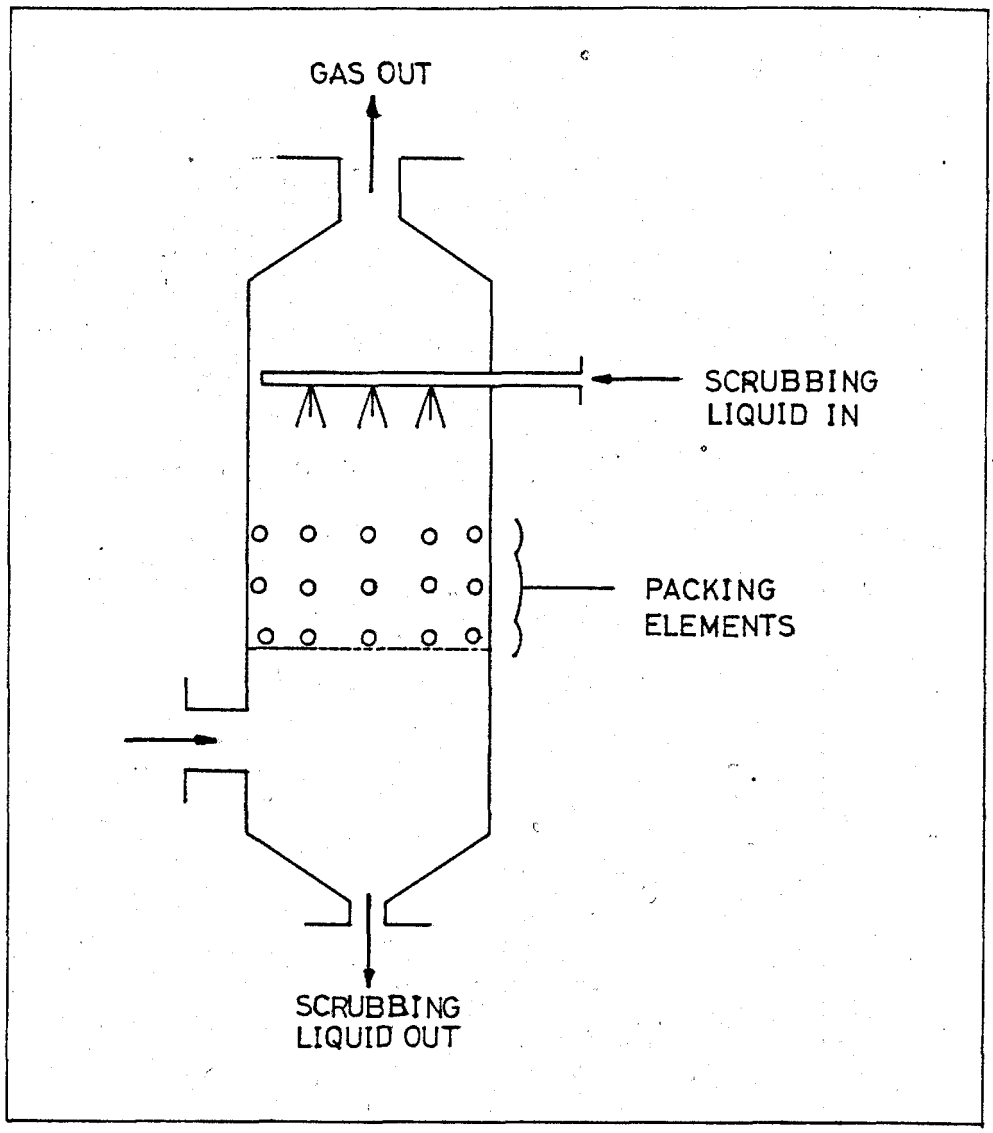

FIG. 2.2: PACKED BED DEMISTER/DEDUSTER

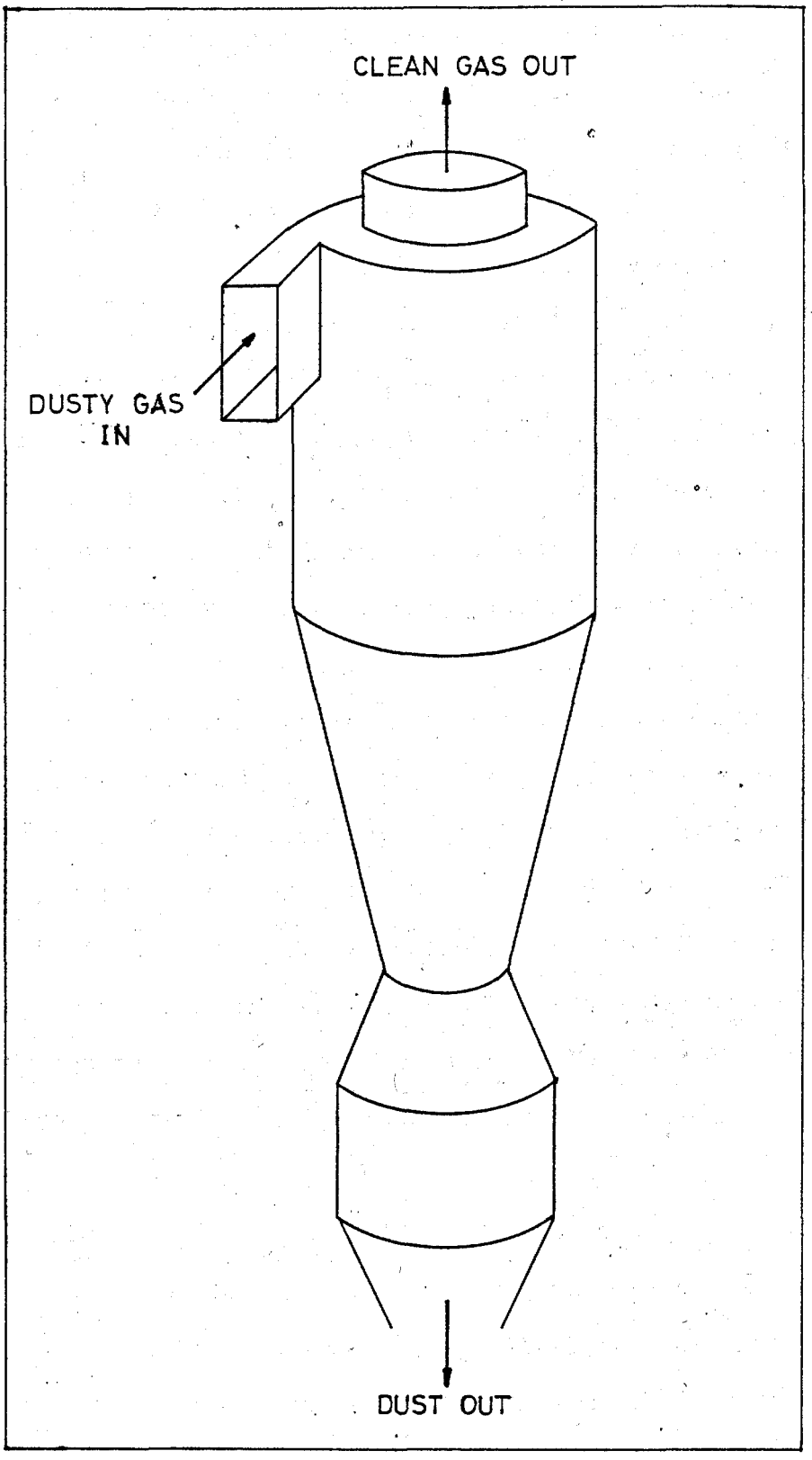

FIG. 2.3: TYPICAL CYCLONE DUST SEPARATOR

portion of the cyclone chamber through a tangential inlet duct. The flow spirals downwards into a lower conical section and inwards, towards the axis with increasing spin velocity and is discharged through the top of the casing. Suspended dust particles thrown outwards by centrifugal force arising from the rotation find their way down into the air tight dust hopper at the lower end of the cone. Different basic variations of the above design has successfully been applied. For example, the dust may be discharged into the dust hopper at the lower end of the cone through a plain opening or through a small annular opening. The gas outlet duct is sometime tappered so that the diameter increases towards the discharge end. Other variations include imparting spin to the air entering axially by deflector vanes in the annulus between the outlet duct and outer cylinder instead of a tangential entry. The outlet may be brought out of the cyclone at the opposite end from the entry, passing through the dust collection chamber (uniflow cyclone). Such a cyclone may be double ended with tangential entry at the centre. Efficiency may be increased by drawing off a portion of the gas flow along with the separated dust and passing this through a second collection. A higher pressure drop may be acceptable in this secondary collection since a smaller volume of gas is involved.

2.6 Electrical Dust Collector (Electro-Precipitator)

In the dust collectors discussed so far, the dust particles are either displaced by gravitational, centrifugal or a form of hydrodynamic force. If an electrical charge q is introduced into an electrical field, then a force F_c is exerted

on it in the direction of the potential gradient [22]. This force is directly proportional to the field strength E_s multiplied by the number of charges (q); that is

$$F_c \propto q\, E_s \qquad (2.1)$$

Equation (2.1) indicates the conditions to be set up in the displacement zone. A similar electric charge must be imparted to all the dust particles, and an electrical field of suitable direction and strength must be present.

As the dust particles, depending on their origin will either be already charged or of mixed charge this is inadequate for electrical displacement. The first requirement is therefore parallel electrical charging of the particles to expose them to the effects of the electrical field. These two processes can take place in separate zones or be superimposed to each other in a single zone. A conventional form of typical electrical dust collector is shown in Figure 2.4. The dust collection zone, that is, displacement zone and removal zone, consists of an earthed tube with a thin wire insulated from the casing and suspended in the centre of it. To this is applied a negative voltage of up to -40000 Volts, which sets up a potential gradient between the wire and the tube wall. The generation of the charges, whether positive or negative, also take place in this zone. In the immediate vicinity of the thin wire, there is a sharp potential gradient which, at an adequate voltage of given polarity, produces a negative corona discharge. The negative charges thus produced move towards the earthed tube. The dust particles now entering the dust collection zone first become negatively charged

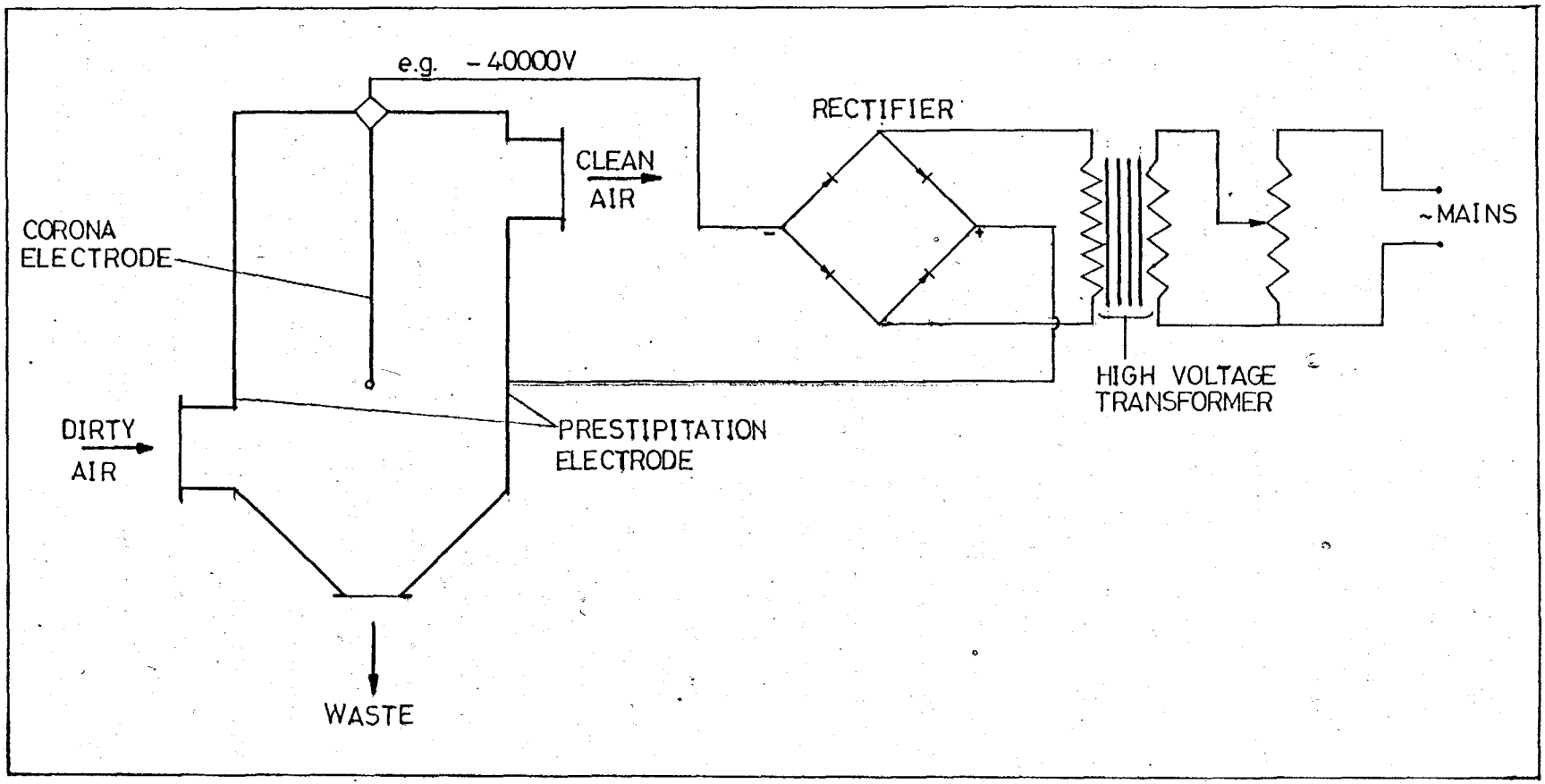

FIG. 2.4: DIAGRAM OF A BASIC ELECTRICAL DUST COLLECTOR

and then experience a force, according to equation (2.1), which displaces the particles towards the tube wall where they adhere. The tube wall, also called the receiving or precipitating electrode, is the removal interface. The particles removed are those whose adhesion forces exceed the transport forces of the passing gas. The particles adhere as a result of van der Waals, capillary and electrical forces [22]. The captured dust is loosened at set time intervals by rapping the precipitation electrode, to make it fall under gravity into the dust bunker.

The central electrode is called the discharge or corona electrode, and current flowing between the electrodes is called the corona or ionic current. The high DC voltage required for the corona discharge can be produced by a transformer and rectifiers as also shown in Figure 2.4. For continuous operation the precipitation electrodes must be cleaned at regular intervals or continuously. The requirements being the minimization of ingress of dust into the directly adjacent gas stream. One of the best methods of meeting this requirement is irrigation of the precipitation electrodes, to give a descending liquid film which removes the dust particles from the dust collection zone. This also eliminates the problem of back discharge. Two drawbacks are that the gas temperature must be correspondingly reduced, and corrosion resistant materials must be used. Costs are also increased because of the additional water and sludge circulation. Another way of meeting the above requirement is to discount the gas feed during cleaning. This involves parallel systems and consequently increased costs.

The dry method of cleaning, generally consists of

periodic vibration or rapping of the electrodes. To avoid re-entrainment of dust by the gas stream, the precipitation electrodes can be designed to provide flow stagnation zone where the dust can drop into the bunker; however, not all the dust can be precipitated in the stagnation zones. The proportion of the dust precipitated called the "Absorptive Capacity" of the precipitation electrode is unity in the case of irrigated precipitation electrodes. Efforts are normally made in the usual dry cleaning technique to minimize loosening of or turbulence in the dust layer during and after cleaning.

The above discussion indicates that there are four underlying process to electrical dust collection, namely :

(i) Generation of charges

(ii) Charging of the particles

(iii) Displacement of the particles under electrical forces (electrical field)

(iv) Removal of the particles via the precipitation electrode and its cleaning.

2.7 Disadvantages of These Separators Compared to HGMF

With regards to the stated problem of research, all the above described methods may be applied, but with several limitations, these include:

For Fabric Bags

Baghouses suffer from temperature limitations if the filter

bags were made of cotton, the maximum operating temperature is about 80°C even though some glass fiber filter bags can withstand temperature of up to 260°C with increasing material costs. Gas temperatures close to the Curie temperature of the filter material are possible with the HGMS process. The Curie temperature of the ferritic stainless steel wool is 680°C .

Most filter bag materials are not ideal for handling abrasive dusts in corrosive, acidic and alkaline gases, whereas the stainless steel wool matrix in an HGMF process should cope with these extreme environments.

Maintenance costs for bag filters are appreciable because the filter medium must be replaced regularly.

For Wet Dedusters

The most important advantage HGMF has over this type of process is that wet dedusters need to have special facilities for slurry treatment. And this results in extra costs in setting up very large plants. The cost of water usage is also appreciable.

The state of the materials being removed is changed by the spray of water. Thus, increasing the possibility of adverse chemical reaction with the scrubbing liquid that might lead to corrosion or deposition problems. Also in cases where the

filtrate is required in dry state, extra cost of energy will be incurred in drying.

Another advantage of HGMF over wet deduster, although less important, is the loss of thermal buoyancy in the slack plume.

Cyclone Dust Collectors

The disadvantage of cyclone dust collector is the low collection efficiency of submicron particles. This problem tends to be amplified by the secondary flow present in the centre of most conventional cyclones. There are also difficulties in the removal of light or needle shaped materials.

In cases where abrasive dust is removed, irreparable damage can be inflicted on the separating surfaces of the cyclone. Thus, requiring either complete replacement of this surfaces or expensive repairs. An alternative arrangement which is best but expensive is to coat the surfaces with wear resistant material.

Electrical Dust Collector (Electro-Precipitator)

One limitation of this method of dust control is that it is restricted to applications where there are no explosive gases in the gas stream. This is because of the sparking

nature of the unit. Unlike the electrostatic precipitator, there is no corona discharge in an HGMF system. Therefore HGMF can be applied safely to clean gas streams which contain explosive gases.

The dust particles to be cleaned by electrostatic precipitator must not be electrically resistant, so that particle charging is possible. HGMF can be used to treat any electrical resistant particles as long as they possess magnetic properties. Even for those particles which are not magnetic, strong magnetic seeding particles can be made to bond to the non-magnetic ones, which can then be treated in the usual way by HGMF. Thus, a wide range of substances are amenable to HGMF.

For most electrostatic precipitators for industrial applications, the negative corona gives a higher corona current and consequently higher particle charges than that of a positive corona. Thus, a negative corona yields better particle collection than a positive corona for a given applied voltage at the discharge electrode. A successful negative corona operation requires electron absorbing gases. Thus, the increasing drive to eliminate sulphurous gas emissions lead to difficulties in the operation of electrostatic precipitators, and HGMF may offer an alternative process.

Compared with HGMF, the gas velocity through the

electrostatic precipitator is relatively low, typically in the range of 1 to 2 m/s when compared to that of HGMF. Superficial gas velocities above 10 m/s has been used for HGMF tests with reasonable collection efficiencies. Thus, an electrostatic precipitator will be much bigger in size than an envisaged HGMF unit when handling the same quantities of dust laden fumes.

The build up of dust on the discharge electrodes must be discharged continuously to ensure its efficient operation. The method usually employed to keep the discharge wire clean is to rap them mechanically. This consists of imparting sharp blows to the discharge wire assembly, and to the wire itself by means of spring loaded hammers, operated by cams mounted on a rotating shaft. This continuous rapping weakens the strength of the discharge wires and leads to structural failure. These expensive discharge electrodes have to be frequently replaced. Such replacement does not occur in HGMF system. Even the dust loaded matrix of an HGMF process does not need replacement it can be cleaned and re-used.

Estimate of the capital costs and the energy consumption of HGMF and two other conventional methods were given by Gooding et al [23]. The costs in 1977 were: HGMF - \$6653 per m^3 s and Electrostatic Precipitator - \$4042 per m^3 s. The capital cost of an HGMF system is somewhat higher than the precipitator but they projected that it is still well within economic competitiveness due to the accuracy of the estimates. The

estimates of the power requirements show that the scrubber requires several times more energy than either the precipitator in terms of energy utilization. The economic gain of an HGMF system occupying less space has to be taken into account as well.

CHAPTER THREE

DEVELOPMENT OF MAGNETIC SEPARATORS

3.1 Introduction

All elements in the periodic table are affected in some way when placed in a magnetic field, although with most substances the effect is too slight to be detected. The ease with which magnetic properties may be induced in a substance by the action of magnetic field is called magnetic susceptibility. All substances are permeable to some extent; and may be classified as paramagnetic when more or diamagnetic when less permeable than free space. Substances that show very strong paramagnetism can be be called ferromagnetics. The magnetic force exerted on a particle in a given magnetic field depends on the relative susceptibilities of the particle and the surrounding medium. When the susceptibility of a particle exceeds that of the medium, the force is attraction; and conversely, when it is less repulsion occurs. Since air is the usual test medium, substances attracted to the poles of a magnet are rated as paramagnetic, while those repealed are referred to as diamagnetic. It is important to point out that small amount of impurities or external influence can alter the magnetic properties of these materials; for example, when ferromagnetic materials are heated above their Curie temperature (temperature at which the relative permeability of the ferromagnetic material falls to unity) they become paramagnetic.

Mixtures susceptible to magnetic separation are those in which valuable materials and non-magnetics fall into different classes like strongly magnetic, weakly magnetic or nonmagnetic. Theoretically, it is possible to separate materials whose susceptibility is in the ratio of 5 or 10 : 1; but practically, success usually depends on other factors such as relative particle sizes. Impurities in natural minerals may so alter permeabilities as to render published indices of susceptibility unreliable. Hence, except for separation of strongly magnetic from clearly nonmagnetic substances, the safest procedure in determining whether a mixture is separable by magnet is by testing.

3.2 Principles of Magnetic Separators

Magnetic separation utilizes the force of a magnetic field, coacting with some other forces to produce differential movements of magnetic mineral grains through the field. Fundamentally, differences in the magnetic permeability of minerals constitute the basis for separation , but practically, separation is influenced by the specific gravity, size, and purity of the material being separated, and by mechanical and electrical attributes of the separator. A typical example of this is found in the separation of either valuable minerals from non-magnetic gangue (rocks in which ores are imbedded) tin-bearing mineral cassiterites often associated with traces of magnetite or wolframite.

3.3 Essentials of Magnetic Separators

Certain elements of design is commonly incorporated in all magnetic separators. The prime requirement as already mentioned is the provision of a high intensity field in which there is a steep field strength gradient. In a field of uniform flux, such as in Figure 3.1, magnetic particles may orient themselves, but will not move along the lines of flux. The most straight forward method for producing a converging field is by providing a V-shaped pole above a flat plate, as in Figure 3.2. The tapering of the upper pole concentrates the magnetic flux into a very small area giving high intensity. The lower flat pole has the same total magnetic flux distribution over a larger area. Thus, there is a steep field gradient across the gap by virtue of the different intensity levels. An alternative method of producing a high field gradient is by using a pole which is constructed of alternate magnetic and non-magnetic lamination Figure 3.3.

The introduction into a magnetic field of particles which are highly susceptible concentrates the lines of force so that they pass through them Figure 3.4. Since the lines of force converge on the particles, a high field gradient is produced which causes the particles themselves to behave as magnets, thus attracting each other. Flocculation, or agglomeration of the particles can occur if they are highly susceptible, and if the field is intense. This has great importance as these "flocs" can entrain gangue and can bridge the gaps between magnetic poles, reducing the efficiency of separation. Flocculation is especially serious with dry separating machines

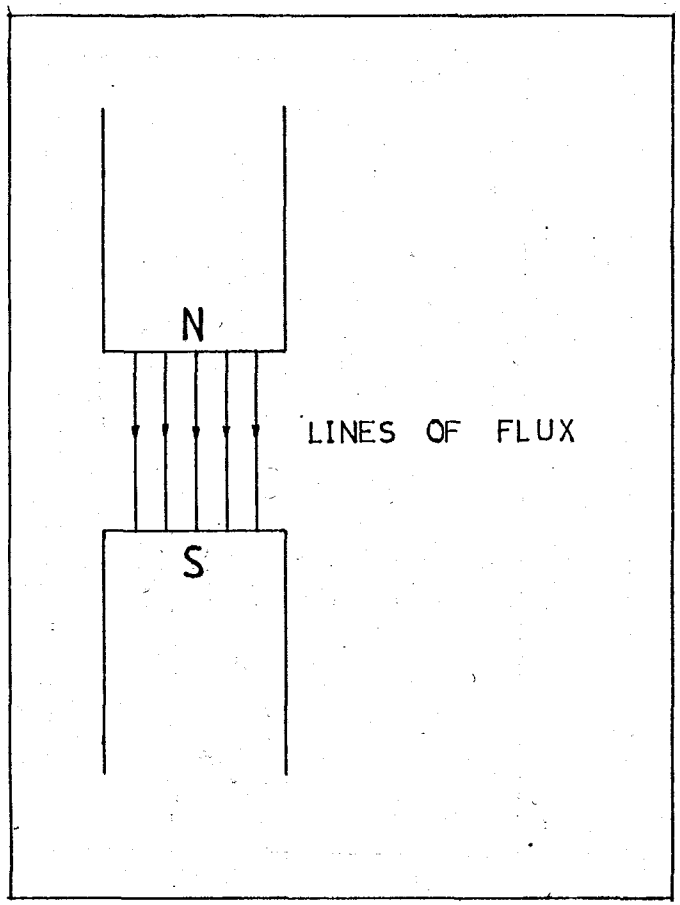

FIG. 3.1: FIELD OF UNIFORM FLUX

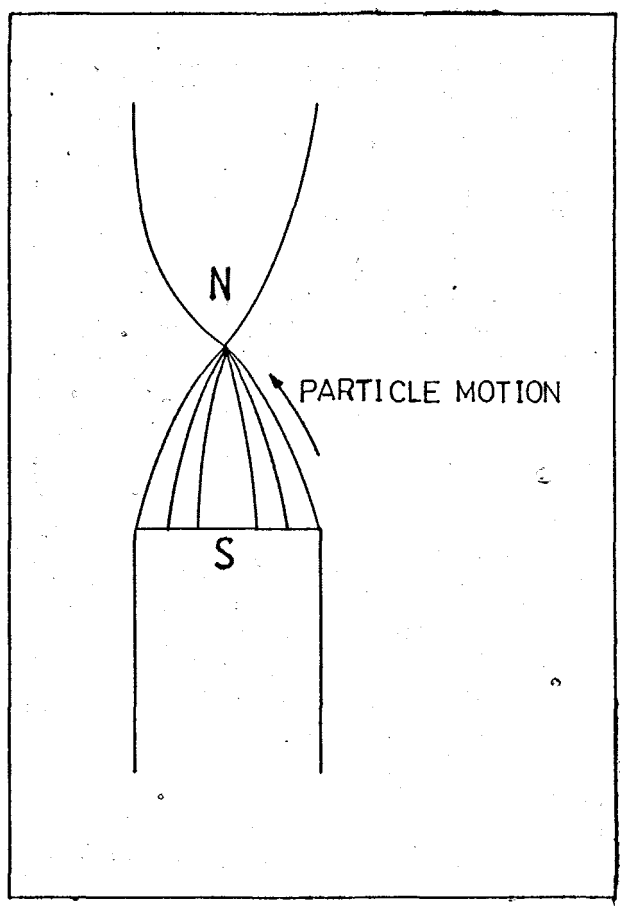

FIG. 3.2: CONVERGING MAGNETIC FIELD

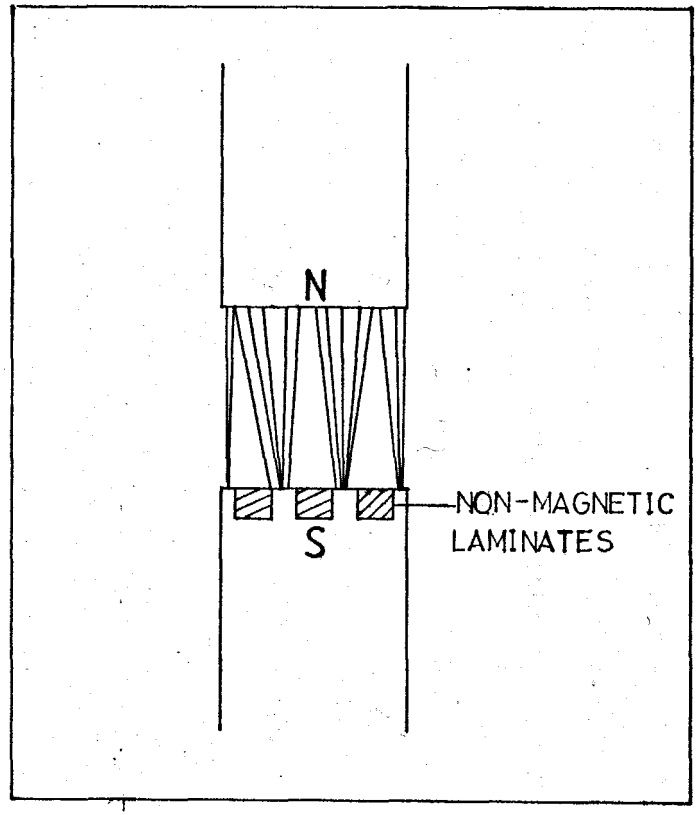

FIG. 3.3: PRODUCTION OF FIELD GRADIENT BY LAMINATED POLES

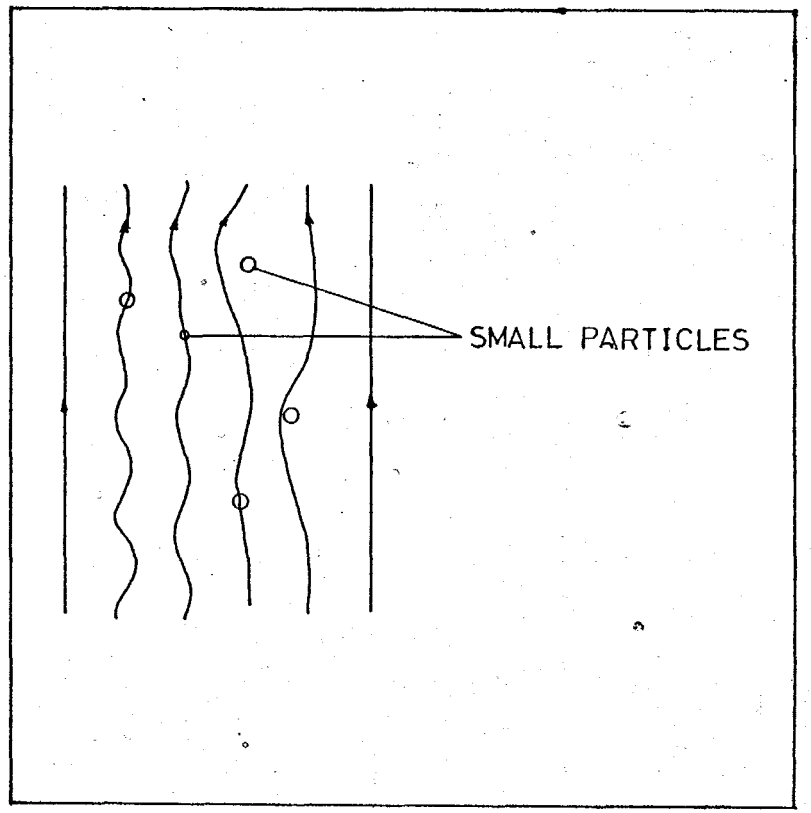

FIG. 3.4: CONCENTRATION OF FLUX ON SMALL PARTICLES

operating on fine materials. If the ore can be fed through the field in a nonlayer, this effect is less serious, but the capacity of the machine is drastically reduced. Flocculation is often minimized by passing the material through a consecutive magnetic field, which are usually arranged with successive reversal of the polarity. This causes the particle to turn through 180^{o} , each reversal tending to free the entrained gangue particles. The main disadvantage of this method is that flux tends to leak from pole to pole, reducing the effective field strength.

Provision for collection of the magnetic and non-magnetic fractions must be incorporated into the design of the separator. Rather than allow the non-magnetics to contact the pole pieces, which will cause problems of detachment, most separators are designed so that the magnetics are attracted to the pole pieces, but come into contact with some form of conveying device. Non-magnetic disposal presents no problems, free fall into a bin is often being used. Middlings are readily produced by using a more intense field after the removal of the highly magnetic fraction.

Early application of separators were confined to the separation of relatively large particles of strongly magnetic materials. Such single surface separators were mostly similar in the sense that they employ a single surface for separation or collection of magnetic particles. The magnetic forces on these surfaces are often produced by permanent magnets, but as in the case of belt and high gradient devices, an electromagnet may be used. The active separation volume for each of these separators

is roughly the area of the magnetized surface on the separator, multiplied by the range of the magnetic force. In order for these devices to have practical throughput, the range of magnetic force must be extended. However, such a range implies a relatively low magnetic field gradient and weak magnetic tractive forces. This limits the usefulness of some of these devices to large particles of strong magnetic susceptibilities.

The development of high gradient matrix type of magnetic separators has greatly extended the range of applications. They produce stronger short range magnetic forces over a much larger surface area by employing different types of ferromagnetic materials as separators.

Commercial magnetic separators are continuous process machines and separation is carried out on a moving stream of particles passing into and through the magnetic field. Close control of the speed of passage of the particles through the field is essential, which rules out free fall as a means of feeding. Belts and drums are very often used to transport the feed through the field.

3.4 Functions of the Magnetic Forces

Most magnetic separators employ two or more field forces when using magnetic attraction to divert susceptible particles from gravitational or inertial trajectories. Others are close to the sorter principle in operation, like when susceptible particles are magnetically lifted from a conveyor. Analysis of the action employed in most magnetic separators shows that the magnetic field force is used to perform three main functions.

These are:

(i) To divert susceptible particles from their previous direction of motion.

(ii) To provide a force sufficient to sustain mass transport. of these particles.

(iii) To retain the separated magnetics.

The tractive force used for providing these three functions is the product of magnetic field strength, the gradient of the magnetic field, and the susceptibility of the particle. Hence, capacity of a magnet to lift a particular material depends not only on the intensity of the field strength, but also on the field gradient; that is the rate at which the field intensity increases towards the magnetic surface.

The equation defining the relationship is given below as:

$$F \propto H.\frac{dH}{dL} \qquad (3.1)$$

where F is the force on the particle, H the field intensity, and $\frac{dH}{dL}$ the field gradient.

Therefore, in order to generate a given lifting force, there are several combinations of field and gradient which will give the same effect. Production of a high field gradient as well as high intensity is therefore an important aspect of separator design.

In most recent applications, the efficiency of HGMS medium depends largely on having very high field gradient, because the other two factors are limited by circumstances beyond operational choice. A high field gradient entails a rapid decline in field

strength with distance from the pole of convergence. Hence it is invariable that the useful tractive force extends only over short distance from each pole. The commonly adopted engineering solution in high gradient magnetic separation is a large multiplicity of poles by the introduction of ferromagnetic structure. The structures develop a strong magnetic force on their edges that is approximately inversely proportional to their diameter. And the ranges of the magnetic force is proportional to the diameter of the characteristic size of the structure. The force produced is intense and permits entrapment of very fine weakly magnetic particles. Highly susceptible particles are permanently retained by the nearest magnetic pole they encounter. The magnetic force holds the susceptible product and fluid drag (with or without assistance from gravity) in some circumstances try to remove them. The main disadvantages here are the risk of failure to retain very small magnetic particles passing too fast or at great distance from the locus of high tractive force, and the risk of blockage if the supply of magnetics exceed available capture spots. So, the problem of rate of transfer of susceptible particles, relative to transit rates and total residence times, become the limiting factors in the whole process.

3.5 Classification of Magnetic Separators

There are several types of magnetic separators, each varying in design, operation and application. Many differ according to whether the feed is coarse or fine, wet or dry, and low, medium or high permeability. Major types have been classified on several basis such as:

(i) Intensity of magnetic field; as low, medium, and high intensity.

(ii) Medium; in which separation take place as wet or dry.

(iii) Mechanical devices used in the presentation of material to the magnet, as on a belt, pulley, drum, shaking tray, or free fall through a fluid.

(iv) Mode of disposal of products, as by gravity, cross or longitudinal belts, sprays and scrapers.

(v) Current characteristics; whether alternating, or direct current separators.

(vi) Nature of magnetic phenomena utilized; as in induced attraction hysteretic repulsion, coercive force reaction.

(vii) Motion of magnets; for example, whether they are stationary or moving.

(viii) Method used to get the magnetic material unto the collecting surface. When the feed is introduced directly unto the collecting surfaces, the separator is classified as Holding Type. When the collecting surface attracts particles from a feed stream moving in close proximity, it is termed Pick-Up Type.

The classification adopted here is based on simply the potential intensity of the magnetic forces required to effect capture. These are conventional separators which utilize strong fields of permanent magnets and high gradient devices which functions efficiently with a lower field strength as it relies rather more

on the field gradients.

3.6 Conventional Separators

Drum separators are probably the most common type of magnetic separator. Drum separators of the holding type consists of rotating horizontal cylinders of nonmagnetic material, normally brass or bronze, surrounding magnet banks confined to the inner surfaces of the drums. The banks may either be stationary or rotating. They are built up of individual flat magnets, arranged radially around the drum axis and wound to produce opposite polarities in adjacent poles. Electrical connections are made through a hollow shaft supporting one end of the drum. The most common use of the dry and wet drum separators are the beneficiation of iron ores. Roll separators are used to treat less strongly magnetic iron bearing ores, while pulley separators are most often used in the removal of tramp iron from various feeds. These separators may use either permanent magnets or electromagnets and can operate in a continuous mode if required.

3.7 Dry Drum Separator

A schematic diagram of the operation of dry separator is shown in Figure 3.5. In this type of conventional separator, the feed material (dry in this case) is introduced at the top of a rotating drum. The particles are carried downward along the drum by the combined action of gravitational and frictional forces which transmit the rotation of the drum to the particles. Magnetic forces produced by the stationary magnet within the drum

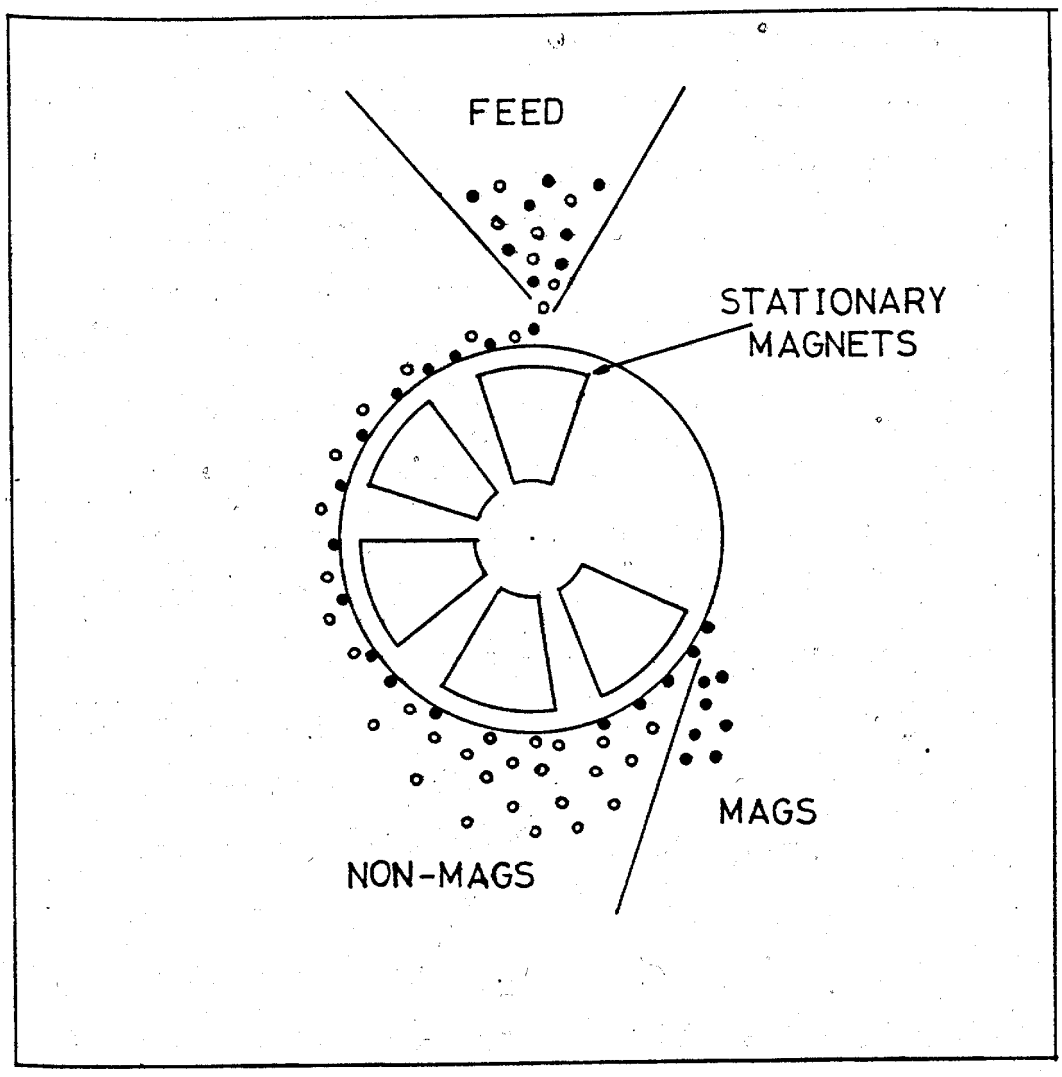

FIG. 3.5: ILLUSTRATION OF DRY DRUM SEPARATOR

hold the more magnetic particles against the rotating drum. These particles are deposited to the right as the drum moves past the end of the magnet. The non-magnetics fall freely off the drum to the left. Dry drum separators can be used to treat particles as small as 100 microns. The performance in producing concentrates is strongly affected by the humidity of the feed. If the humidity is high, small particles may stick to larger particles resulting in a less complete separation.

Since the nonmagnetic drum in Figure 3.5 turns past the stationary alternating poles of the magnets within the drum, it may be said that the magnetic particles experience a force of varying magnitude as it rides on the surface of the drum. This variation in the strength of the magnetic force introduces a tumbling motion of the magnetically trapped particles, and this aids in their separation from the unwanted nonmagnetic particles. The reversal of the magnet between poles also results in the rotation of particles with remnant moments; although specific motion of particles is dependent on its size [24].

3.8 Wet Drum Separator

This type of separator usually find application in slurries, clay industries and treatment of some process waste. The magnet is normally the same type as that found in the dry application. Three major types of these separators are discussed below.

3.8.1 Concurrent Separator

In the concurrent drum magnetic separator the feed

slurry is passed through the trough in the same direction as the rotation of the drum (Figure 3.6a). Magnetic Particles are attracted to the rotation surface of the nonmagnetic drum by the stationary magnets within the drum. The nonmagnetic particles sink to the lowest point in the trough and are drawn off as tailings. The magnetic concentrate is carried by the rotating drum up over the weir to the right. This type of separator produces a high grade concentrate for particles on the order of a few millimetres in diameter. The separation is relatively clean since the magnetic particles are affected by the competing magnetic and hydrodynamic drag forces all along the periphery of the drum. This cleaning occurs even though the variation in force due to the alternating poles within the drum does not produce the same degree of particle motion on the drum as is seen in the dry separator where the viscous forces of the slurry are not present. Since the concurrent tank separator often produces tailing in which a relatively large amount of magnetic material remains, the tailings are often treated again in a counter-rotating drum separator.

3.8.2 Counter-Rotating Separator

In the counter rotating separator shown in Figure 3.6b, the feed is passed through the trough opposite to the direction of drum rotation. The magnetic particles are picked up on the surface of the drum and carried off to the left. This device produces a high recovery but generally a low-grade concentrate since most of the magnetic particles are trapped in a short section of the drum and there is little opportunity for the mat

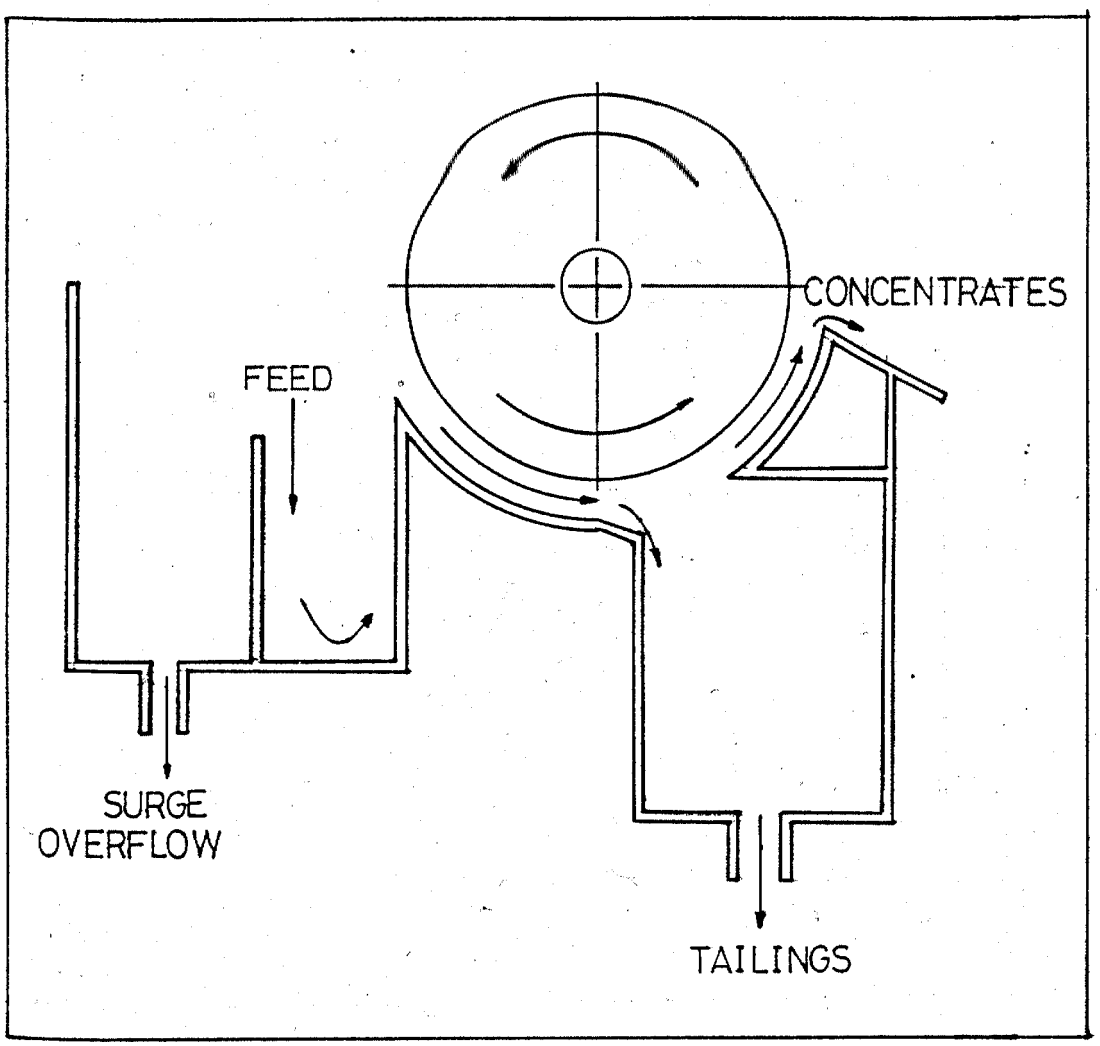

FIG. 3.6(A): CONCURRENT DRUM SEPARATOR

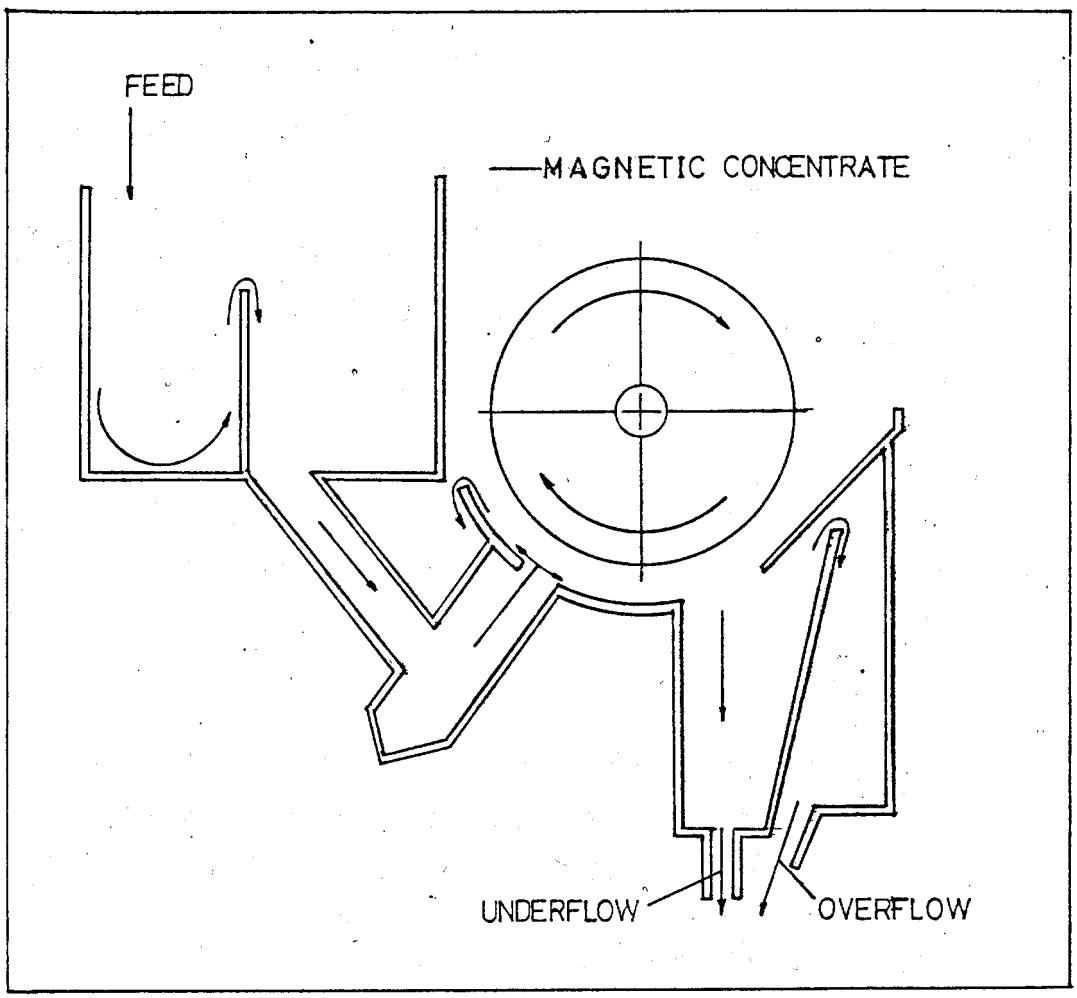

FIG. 3.6(B): COUNTER-CURRENT DRUM SEPARATOR

of trapped particles to release entrained nonmagnetic particles. High recovery also results from particles being picked up further downstream by the drum and be carried back as concentrate. Counter-rotating separator can be used to treat particles down to 100 microns. It has been considered to have a larger capacity than the concurrent separator because of its ability to pick up magnetic particles not immediately entrained.

3.8.3 Counter-Current Separator

This type of magnetic wet drum separator is often used as a finishing separator because it produces an extremely clean concentrate with good recovery for particles down to about 70 microns. This device retains some features of the concurrent and counter-rotating types (Figure 3.6c) but possesses instead three drum tandem separators. The feed is introduced at approximately the mid point in the magnetic section of the drum. The flow of the feed slurry is opposite to the direction of the drum rotation while the entrained particles travel in the same direction. The particles are then washed by water introduced on the left side of the tank. The cleaned concentrate is overflowed to the left.

A feature common to all wet drum separators is the overflow of the concentrate slurry at the end of the tank. This is desirable to prevent the magnetic particles from being drawn through the air water interface, which results in loss. In some devices in which a dewatered concentrate is desired, the magnetic particle are drawn up above the surface of the slurry and scraped off the drum. In these cases the slurry must be recirculated to recover the lost magnetic particles.

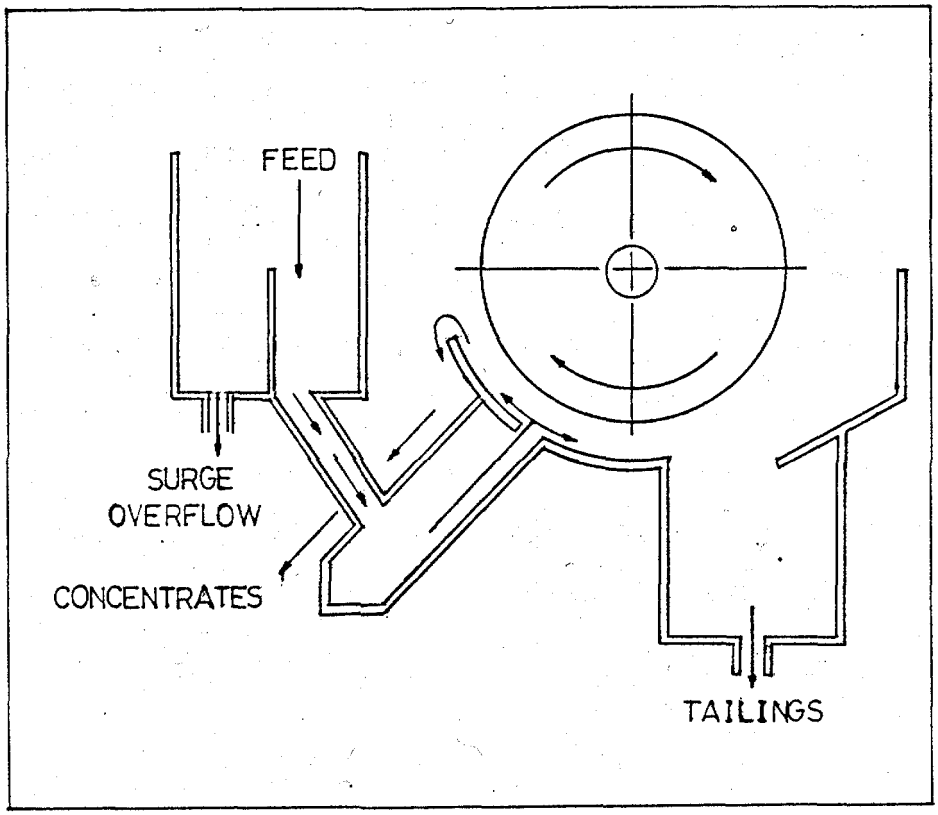

FIG. 3.6(c): COUNTER ROTATING DRUM SEPARATOR

3.9 Belt Separator

Belt type magnetic separators comprise a large class of devices. The belts are used to transport the feed material into the magnetic field region and transport the tails out. A belt may also be used to transport the magnetically captured material out of the field region. The magnetic particles attracted from the field belt may be thrown off to the side by the use of discs [25] suspended over the belt against which the magnetic material is attracted. Or, the magnetic material may simply be attracted to a suspended (guard) magnet and removed by hand. In wet belt magnetic separators, the feed in a slurry is introduced to the belt on whose surface magnetic forces exist, to hold and transport the trapped particle away. These forces are produced by magnets of alternating polarity behind the belt [26] and [27]. Belt separators are used to beneficiate minerals and remove tramp iron. For application to mineral separation, the Wetherill high intensity separator [28] represents a sophisticated type of cross belt device.

3.10 Grate Separator

A simple and very common type of magnetic separator is the grate separator shown [28]. The separator consists of series of tubes placed in the pipe through which the feed is passed. The tubes often stainless steel, are packed with discs or short rods alternately magnetized to produce essentially radial magnetic fields. Ceramic magnets are used to produce strong permanent fields in this highly demagnetizing geometry. Devices like this type are commonly used to separate bits of tramp iron from a

variety of feeds, including grains, foodstuffs, and other normally dry, low density materials. The amount of tramp iron that is normally caught is relatively low so that this type of separator can be cleaned periodically by hand. The grates may be rotated to reduce build-up and bridging of trapped material on the upper bars. Separators of this type are commonly inserted into ducts through which a gravitationally transported feed stream is flowing.

3.11 High Gradient Devices

Many high gradient type magnetic separators have been devised because of the larger magnetic forces that can be obtained with them. These devices (which include Frantz-Ferrofilter and Jones Separator) have been called "induced pole" devices since the field gradients are produced by applying a relatively small uniform background magnetic field to a ferromagnetic medium like grids, screens, grooved plates or steel wool and inducing magnetic poles along their edges. Since large magnetic gradients can generally exist only in small volumes, these separators are designed for the separation of micron sized magnetic particles. To produce high gradients and large magnetic forces over a large surface area to trap practical number of particles presents some problems. Needles, with their axis parallel to the applied field produce high gradients with relatively low field but the available trapping surface is very limited. By contrast filaments magnetized perpendicular to their long axis have large demagnetizing factor, but much greater surface area. It is on this principle that the present high

SHEFFIELD
UNIVERSITY

gradient magnetic filters for the filtration of sub-micron paramagnetic dusts are based. Described below are two early examples of these separators.

3.12 Frantz-Ferrofilter

The Frantz-ferrofilter is a magnetic separator consisting of a series of screens or grids placed in the bore of a solenoid magnet. Small particles of iron and other fairly strong magnetic minerals are trapped from slurries or dry feeds. The feed flows in from the bottom of the device passing through the screens and out at the top. The screens are made from ribbons of magnetic stainless steel. The induced poles are along the edges of the ribbons which make up the screens. The magnetic field produced by the coils surrounding the screens need not be large since the demagnetizing factor of the ribbon is low. However, the use of ribbons tends to reduce the number of screens per unit of magnetized volume and hence the capacity of such a device. Some of these devices operate noncontinuously as it has to be interrupted intermittently with the magnet switched off in order for the magnetic particles to be backwashed. The usual application of these devices is for the removal of fine iron impurities in various fluids. A special application of this type of device has been in waste water treatment [29]. The filter is used to remove very fine suspended solids after a magnetic seeding (addition of magnetic iron oxide and coagulant) has been applied [30].

3.13 Jones Separator

Jones magnetic separators utilize a series of grooved plates, placed between the poles of an electromagnet [29]. The slurry with particles to be separated is passed through the chamber containing the plates. The magnetic particles are trapped along the edges of the groves where the field gradient and the magnetic forces are large. The nonmagnetic particles and slurry liquid pass through the chamber and out below. As in the Frantz-ferrofilter the magnetic particles can be washed out when the magnetic field is reduced to zero. Although relatively large field gradients are produced, the capacity of this device is limited by the surface area available in the grooved plates. This has been discussed by Stone [31] and Jones [32].

3.14 Beneficiation by HGMF Process

The magnetic separation technology was given new impetus with the introduction of separators using steel filaments in relatively high field with an efficient magnetic circuit for the electromagnet. This has been found to be economical in several applications. The magnetic susceptibility and the size distribution of the particles to be removed are the key parameters that determine the practicality of application. Some of the areas where HGMF has been applied are discussed below.

3.14.1 Particulate Emission Control

Large quantities of non-ferrous materials can be found in the atmosphere. The commonest and the most damaging sources

arising from the combustion of fuel, especially solid fuel, are power generating plants. The discharged grit, ash, smoke, and sulphur dioxide can be controlled by HGMF.

3.14.2 Beneficiation Of Weakly Magnetic Iron Ores

With ever decreasing deposits of iron ores large enough to make magnetic drum beneficiation effective, the need arises for a better and more effective methods of retrieving these ores. There are vast deposits of oxidized taconites which can be used if an economic method were available. These ores consist mainly of small grains of hematite, geothite and iron silicates mixed with chert. To liberate the iron containing minerals from the chert, the ore is ground to a size of less than 30 microns. This can be beneficiated, to iron level acceptable for steel making by HGMF process. Previous conventional magnetic separators like drum and belts was ineffective because of low susceptibility and reduced size of the particles.

3.14.3 Coal Desulphurization

There is a growing effort to create cost effective, economically sound methods of utilizing coal as a clean fuel. Sulphur occurs in coal in two forms; mineral sulphur is chemically bound to discrete mineral impurities which can be removed by physical cleaning and organic sulphur which is associated with the coal structure and requires more elaborate processing for its removal. The mineral sulphur in coal occur down to micron sizes. Effective pyrite removal by deep cleaning processing of coal requires grinding to liberate the sulphur

before the application of physical separation methods. The useful constituent of coal are diamagnetic while a good proportion of the undesirable sulphur is in the form of paramagnetic iron compounds called pyrites, which can be removed by HGMF. Other components in the coal, normally ending up as ash, are also paramagnetic in nature and can be removed by this technique [33].

Indeed, emission level of sulphur oxides and ash from coal burning facilities are set to stringent standards (for example, 5 grams of SO_2 per million joules of coal burnt). The particulate emission standard can generally be met with the use of electrostatic precipitators, but HGMF method has successfully been applied to the removal of sulphur oxide emissions from the flue gases.

3.14.4 Cleaning Of Liquid Streams

There are two types of applications of HGMF in cleaning fluids. The simplest is the direct removal of suspended magnetic solids like iron oxides from steel mill waste water. The other involves precipitating dissolved contaminant onto magnetic "seed" particles. The basic advantage of HGMF over conventional waste water treatment is the high throughput that can be handled, even for the removal of very fine particles.

3.14.5 Application to Iron and Steel Industries

Iron and steel are one of the largest industrial users of process water, with most of the water used for cooling and quenching of gases evolved during scarfing. A large volume is also used in making and forming of steel, descaling and hot

forming, and the control of unwanted particulates that result. Currently, the principal method for removal of fine particulates from these waste is sedimentation in large clarifiers with the addition of chemical flocculents. The problem of water clean-up is particularly difficult especially in the rolling mills where the separation of fine particulates, emulsified oil and water is required. The sizes of most of these dusts signifies that the clarifier must be operated at very low overflow rates which are generally of the order of 0.1cm/sec. The application of HGMF in removing these suspended solids reduces the large investment in capital and space.

3.14.6 Clean-Up Of Fuel Lines In Power Plant

HGMF filters have been found to be effective in the control of magnetic debris in fuel oil and steam lines. This is usually necessary to prevent clogging in mechanical atomizers or burner nozzles. Conventional filters were found to be ineffective in this application.

3.14.7 Biological Application

HGMS Technology has been applied to the separation of red cells from whole blood [34] and can lead to a potential small scale application of the technique to producing plasma from low red blood cell levels or to preparing extremely pure red cell population. When red blood cells are in their deoxygenated state their susceptibility relative to water is 0.3×10^{-6} emu/cm^3 (about two orders of magnitude lower than CuO). These red blood cells have been filtered out using HGMF process without any observable

biological damage, although at a very low velocity.

3.14.8 Cleaning of Kaolin Clay

The HGMF beneficiation of kaolin clay represents the first application of magnetic separation technology in commercial processing of micron sized weakly magnetic materials. Kaolin is a white alumino-silicate mineral which occurs in nature as a finely divided particulate dispersion. Quality clays are principally employed as filling and coating agents in the manufacture of paper products and sold largely on the basis of white colour and rheological properties. The application of HGMS has grown in competition with other well established wet physical beneficiation methods like floatation and selective sedimentation, both of which are complex process, sensitive to reagent costs. The magnetic technology not only competes favourably because of its simplicity, low cost and high clay yield, but is expected to increase the economic incentive of re-opening abandoned reserves of quality kaolin clays.

Summary of Magnetic Separators Reviewed

Drum Separator : Use of drums with either permanent magnet or electromagnet; Remove particles from 100 microns diameter; Forces present are gravity and hydrodynamic drag.

Belt Separator : Use of belt to transport and remove tails; Beneficiate minerals and tramp iron from 150 microns; Major force is gravity.

Grate Separator : Consists of series of tubes; High demagnetization; Remove particles from 200 microns diameter; Major force present is gravity.

Frantz-Ferrofilter : Utilize series of screens/grids; High demagnetization factor; Remove micron sized particles; Hydrodynamic force present.

Jones Separator: Utilize grooved plates; capacity limited by surface area; Hydrodynamic force present.

CHAPTER FOUR

PRESSURE DROP IN FILTER MEDIA

4.1 Introduction

Maintenance of a given flow of air through a filter causes pressure drop across its faces. Pressure drop is the second most basic quantity describing the properties of a given filtration material after collection efficiency for the design of filters. In certain cases it is even more important since it is not difficult to prepare a filter having efficiency of 99.99%, but the high pressure drop of such a filter will make any practical use nearly impossible.

Pressure drop affects the main power consumption of the filter system as its requirements are directly proportional to flow rate and pressure loss. In some practical applications, the pressure drop across a filter is used to monitor efficiency of operation. Deposition or capture of particles by a filter also causes a resistance rise, although this may be accompanied by an initial rise of collection efficiency. The mass of dust deposited for a given resistance rise depends on several factors like, particle size and shape, hydrodynamic, gravitational forces and in this particular case magnetic force.

The two types of filters used in this investigation are randomly packed filamentous wires and woven wires. The results of the tests are presented in various forms that can be of help to a filter designer.

4.2 Theory of Medium Resistance

The chief difficulty encountered when dealing with randomly packed matrix is the highly complex geometry of the wire orientation. This causes the flow to follow tortuous channels making it nearly impossible for a complete hydrodynamic analysis. This led to the simplification of the problem to orderly arranged metallic screens. Metallic screens in the form of woven wire is a practical filter medium that is very close to the assumptions made for the theoretical model.

There are three main methods of predicting the pressure loss of a filter. These are the orifice analogy, the randomly packed bed analogy, and the use of drag coefficient. In the use of these methods, the material of the filter is assumed impermeable; thus the wire is considered to be a flow barrier with the screen pores forming the flow channels. In randomly packed bed analogy, approximate expressions are used for the division of flow, both in and around the wires. In the drag coefficient approach, the pore walls are treated as obstacles to the flow of viscous fluid. The drag of the fluid on each portion of the wall is estimated using simplified forms of the Navier-Stokes equations; the sum of all the drags being taken to equal the flow resistance of the medium. In view of the fact that the filter wires are fairly smooth and cylindrical, the orifice and drag theory methods have been most successful in predicting the resistance of these materials to fluid flow. A simplified version of this model for "smooth" cylindrical wire is developed below.

The fan model filter was adopted for the woven wire. This consists of parallel equidistant rows of circular cylinders

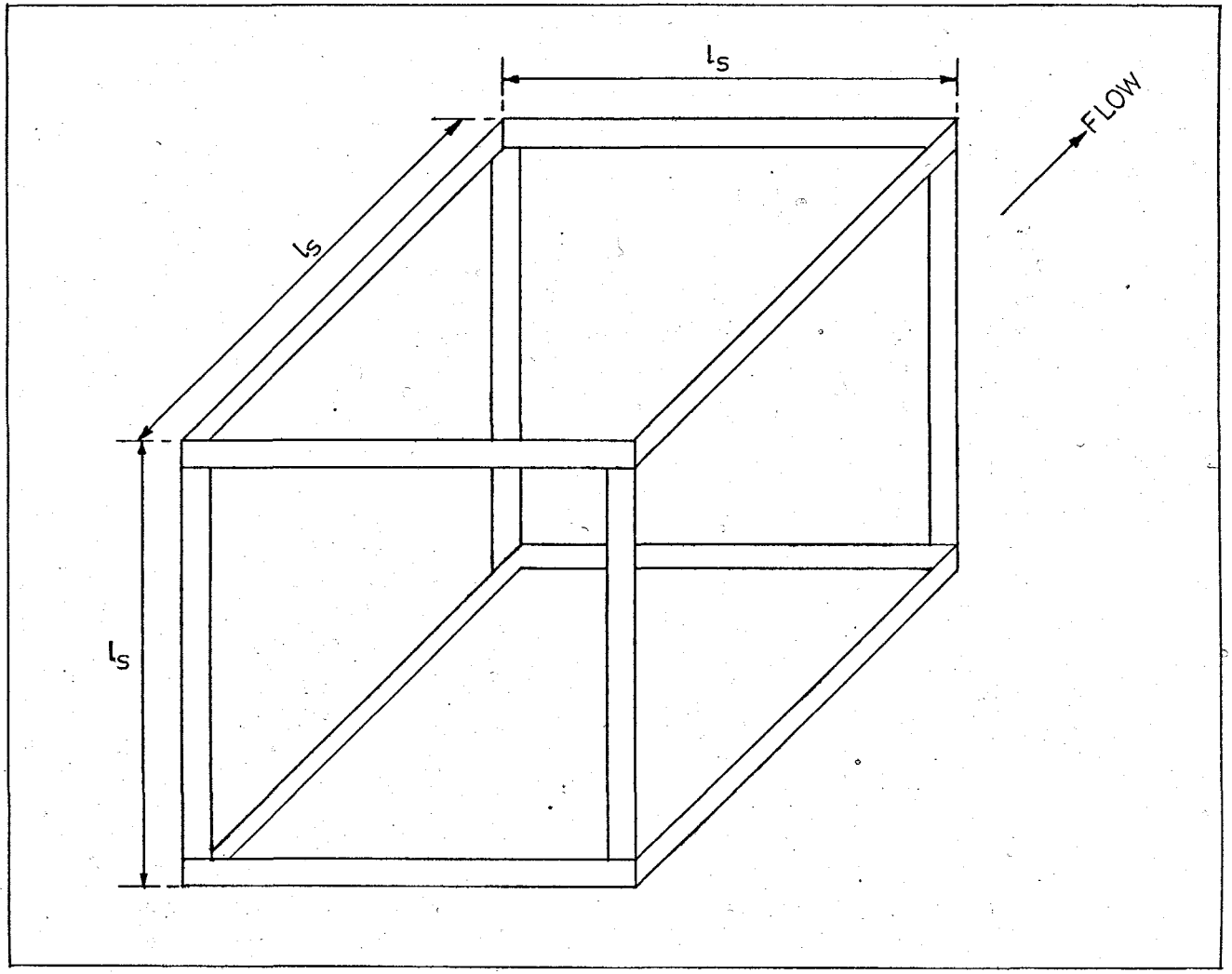

FIG. 4.1: REGULAR CUBIC LATTICE MODEL

in a plane perpendicular to the flow direction. In the same plane, the cylinders are parallel and equidistant, but the axis of the cylinders at different planes are oriented at random. The wire screens used here consisted of rows of parallel, equidistant cylinders that are interwoven with other rows at 90^{o} angles; a stack of these closely resembles the fan model.

4.3 The Simple Cubic Lattice Model

A number of equations of theoretical, empirical and semi-empirical nature has been suggested for predicting the resistance of filters. Those dealing with fibrous filter models with regular geometry and arrangement for which the flow is known have been described by Davies [35] and Lee [36]. In this analysis, the simple cubic lattice model [37] used for the experimental data over a range of Reynolds numbers for cylindrical wires is developed.

The model assumes the random matrix to be modelled as a regular lattice of cubes, size l_s , having a face normal to the flow (Figure 4.1). Given the wire volume V_w and matrix volume V_m , the packing fraction F which is a ratio of two parameters are given by :

$$F = \frac{V_m}{V_w} \tag{4.1}$$

The number of cubes (n) in the matrix is given by :

$$n = \frac{V_m}{3\, l_s\, a} = \frac{V_w}{l_s^3} \tag{4.2}$$

Where a is the fiber cross-sectional area.

Solving equation (4.2) for l_s gives

$$l_s = \sqrt{\frac{3\,a}{F}} \tag{4.3}$$

Assuming that the drag on cylinders parallel to the flow is negligible compared to those normal to it, the matrix can be modelled as a series of parallel square meshes distance l_s apart (Figure 4.1). In this model, two-thirds of the fibres are therefore effective [38]. In a matrix of face area A, the length of fiber l_c in such a single mesh is given by:

$$l_c = \frac{A}{l_s^2}\, 2\, l_s \tag{4.4}$$

This represents the length of a fiber for a single mesh of area A.

Drag defined as the force component parallel to the relative approach velocity, exerted on a body by a moving fluid is given by:

$$F_d = \frac{C_d A_e \rho_f V_a^2}{2} \tag{4.5}$$

where A_e is the projected area of the body on a plane normal to the flow, V_a the flow velocity in the filter matrix, and F_d is the drag force.

The momentum equation gives the drag force for a single mesh (Figure 4.2) as:

$$F_d = \nabla P A \tag{4.6}$$

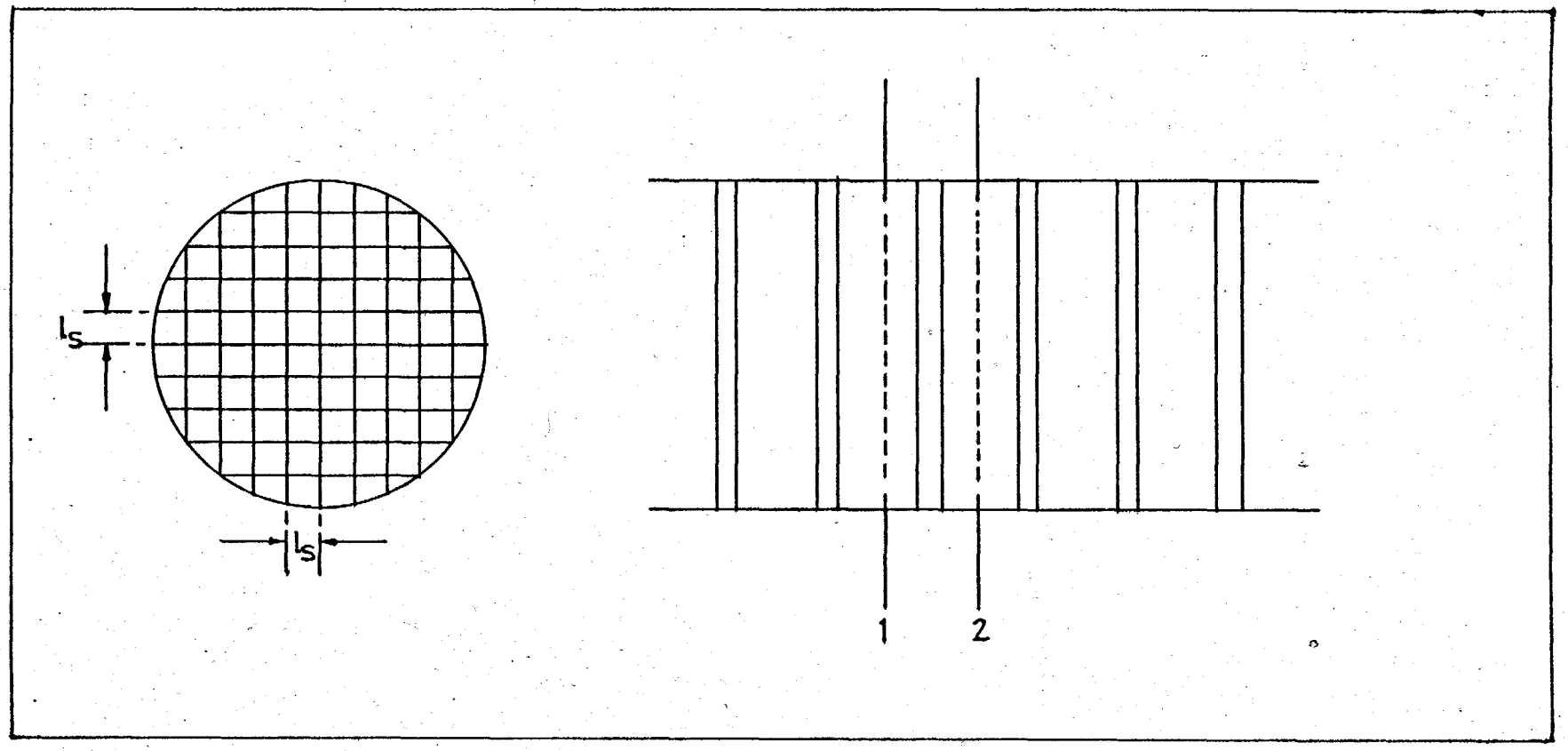

FIG. 4.2: SERIES OF SQUARE MESHES IN IDEAL MODEL

assuming that the momentum flux is the same upstream and downstream; for example at stations 1 and 2 on Figure 4.2. Therefore the loss in pressure across is obtained by combining equations (4.4), (4.5), (4.6) to give

$$\nabla P = \frac{F_d}{A} = \frac{C_d \rho_f V_a^2 A_e \; 1/2}{(\frac{3a}{F})^{1/2} \cdot l_c} \tag{4.7}$$

A_e is given by the area of the cylinder facing the flow which for a single mesh is the length of the wire l_c multiplied by the diameter of the wire, d.

Substituting for A_e equation (4.1) becomes:

$$\nabla P = \frac{C_d \rho_f V_a^2 l_c d}{(\frac{3a}{F})^{0.5} l_c} \tag{4.8}$$

But the total number of meshes is given by $\frac{L}{l_c}$; therefore the total pressure drop across the filter can be estimated by

$$\nabla P = \frac{C_d \rho_f V_a^2 L d}{(\frac{3a}{F})^{0.5} l_s} = \frac{C_d \rho_f V_a^2 L d}{(\frac{3a}{F})} \tag{4.9}$$

The model so far does not take into account the blockage effects (or interference) but only estimates the pressure drop in a loosely packed matrix from a knowledge of only C_d as a function of Reynolds number. From equation (4.9), the coefficient of drag of the entire filter can be calculated using:

$$C_d = \frac{\nabla P \left(\frac{3a}{F}\right)}{\rho_f V_a^2 L d} \tag{4.10}$$

If the above formulation is correct, C_d values should approach that of an isolated cylindrical fiber, and this would be elucidated in the discussion of the experimental results. Assuming that all the flow in the passages of the filter were entirely parallel to the direction of the main flow upstream, the mean velocity of the flow in the filter will be slightly higher than that of the main flow. This is because of the slightly restricted flow channels. The mean velocity of the flow in the filter can be estimated with

$$V_a = \frac{V}{1 - F} \tag{4.11}$$

where V is the bulk fluid velocity.

Substituting for V_a in equation (4.10) give

$$C_d = \frac{\nabla P \left(\frac{3a}{F}\right) (1-F)^2}{\rho_f V^2 d L} \tag{4.12}$$

Substituting for a above, which is $\frac{\pi d^2}{4}$ equation (4.12) becomes:

$$C_d = \nabla P \frac{3 \pi d}{4} \frac{(1-F)^2}{\rho_f V^2 L} \tag{4.13}$$

C_d is a function of Re defined by $Re = \frac{\rho_f V d}{\mu}$ which becomes

$$Re = \frac{\rho_f V d}{\mu (1-F)} \tag{4.14}$$

with blockage effect correction.

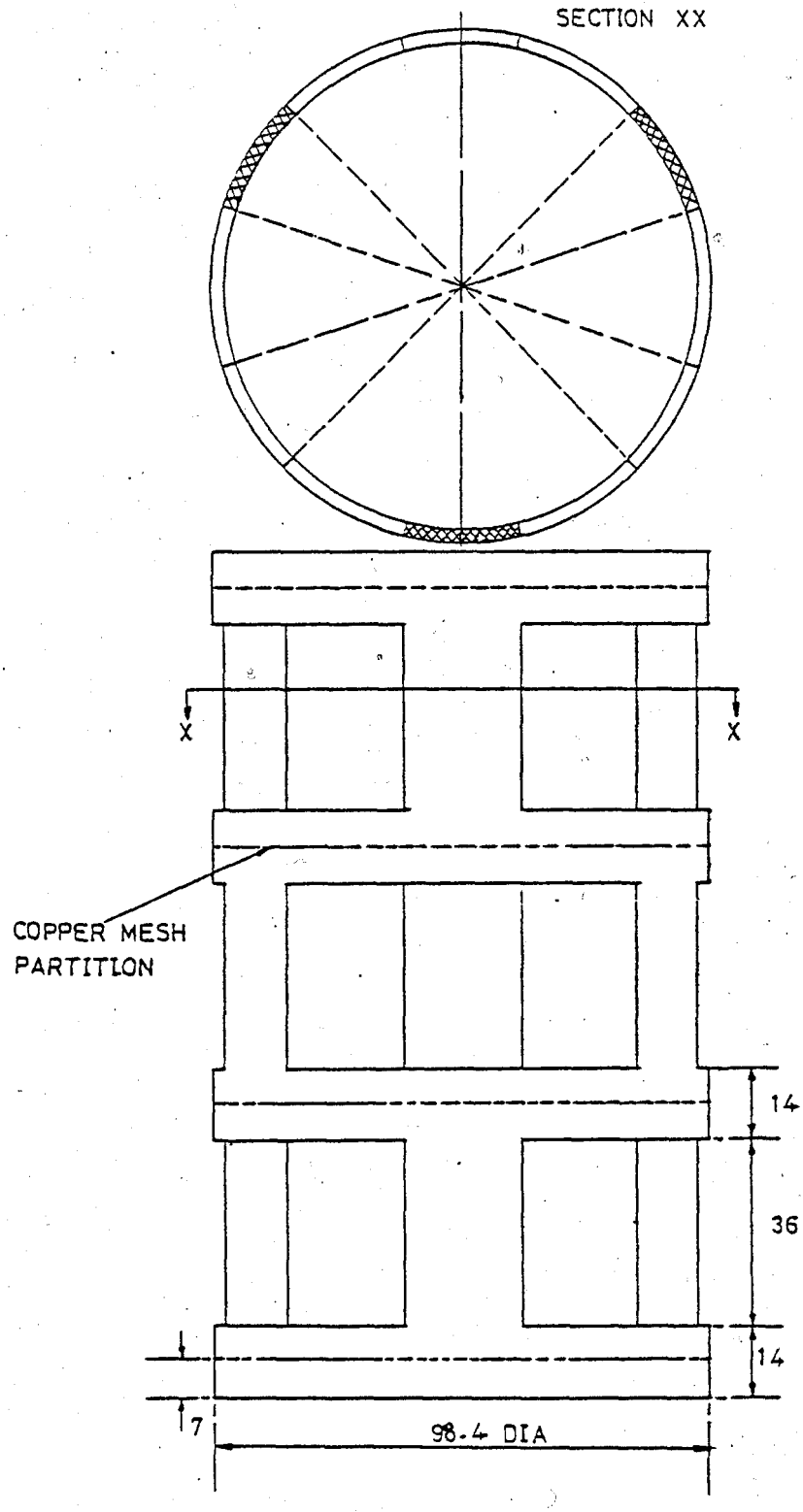

FIG. 4.3: TYPICAL FILTER MATRIX

4.4 Woven Wire Model

The development of this model follows the same procedure as above. Taking the size of the square of mesh as l_s Figure 4.1, the number of squares per unit area is given by :

$$\frac{1}{l_s^2} \tag{4.15}$$

The length of the wire per square of mesh is $2l_s$ so that the length of cylinder per mesh l_c is $\frac{2}{l_s}$.

The drag coefficient C_d is thus given by :

$$C_d = \frac{\nabla P}{1/2\rho_f V^2 d} \frac{l_s}{2n} (1 - B)^2 \tag{4.16}$$

Where n = number of grids in series

d = diameter of wire

and nd defines the thickness of the filter.

4.5 Pressure Loss of Clean Filter Matrix

Tests were performed on the two types of filters used in this study to determine their resistances. The first consists of 50μm stainless steel wires [PLATE 4.1], packed randomly into a filter matrix [PLATE 4.2]. The filter matrix is constructed from PVC tube of 98.4mm diameter with length varying from one filter to the other from 25-50mm. A typical sample of one of the filter matrices used is shown in Figure 4.3. Windows were cut from the body to allow for the packing of the wires. The whole matrix unit was also divided into compartments separated by copper screens of large pore sizes for easy packing. The length of each compartment as separated by the copper screens was 50mm. Investigations were

performed for various operating characteristics such as, packing density, flow rates, and filter length. PVC was chosen because of its non-magnetic properties as will be pointed out later. (As the matrices will be placed in an externally created magnetic field, a magnetic matrix will create external magnetic capture zones). The matrix was made as thin as possible to reduce its resistance when empty. The second type of filter consists of woven wires (PLATE 4.3) applicable to practical installations. They were packed such that they touched each other. Data on pressure losses were obtained with increasing numbers of wire screens. The effect of separating a battery of screens with rings were also investigated. The test was carried out within the range of velocity encountered in practical appliances (1 - 40 m/s).

4.6 Test Procedure

The above tests were performed with the use of the main experimental rig described in Chapter Seven (Figure 7.1), but with the magnet switched off. The operation involved switching on the main fan with the filter put into the duct. The pressure drop across the duct was monitored from two static pressure tappings located upstream and downstream of the filter zone. These were connected through flexible PVC tubes to a digital manometer (Furness Controls Ltd, Berhill England), from where the difference was read off. Also present are tappings located downstream of the filter to measure the velocity profile of the flow after it has passed through the filter matrix. There are flow controls located at the entrance of the duct and just before the fan, to control the air flow rate in the duct. Initially

tests were carried out with empty matrices to establish their resistances. These were then compensated for in the real tests.

4.7 Discussion of Pressure Drop Results

The results of this test can basically be classified into two groups:- Random and Woven wire results. The reason for this demarcation is entirely based on the formulation of the expression predicting the drag coefficients from experimental data. In the random wire arrangement, the experiment was performed over two different lengths of the matrix with varying packing densities but the same wire diameter of 50 μ . For woven wire, meshes with different pore sizes were tested, the major variation being the number of meshes stacked during each test.

Figure 4.4 shows a typical set of results obtained for a filter of length 5 cm, packing fractions of 0.50% to 1.50%, and flow velocity of up to 40 m/s. The curves plotted on a logarithmic scale show the variation of pressure drop as functions of flow velocity. A linear regression of the sets of data were performed with the points fitted into a first order expression of the form $\frac{\nabla P}{L} = F^x V K + C$. C is the intercept of the line passing through the points on $\frac{\nabla P}{L}$ axis, F is the packing fraction, x is a constant, V represents the the duct centre velocity, while K is the slope of the line. The adoption of such a mathematical expression indicates the pressure drop across the filter to be linear with the flow rate at these velocities for any chosen packing fraction. Table 4.1 below gives a comprehensive list of the variables defining each of the straight

line passing through the various groups of data points on Figure 4.4. Although for any given packing fraction a different expression for each set of the data will be preferred for higher accuracy, a detailed study of the table reveals very small differences in the variation of the slope (K) in each case. Attempt was therefore made to approximate the whole set of data with a single expression. This was achieved by the use of averaged values of the intercept (c), and the gradient (k). For Figure 4.4, the result was a linear expression of the form

$$\frac{\nabla P}{L} = F^{0.01}\ 1.5835V - 0.2234 \qquad (4.17)$$

that predicts the mean pressure per unit length of the matrix. The correlation coefficient, which is a measure of how well the straight line was fitted (confidence factor) was 99.7%. It must be emphasized that equation (4.17) should be used with caution as it tends to overshoot at high flow velocity. A better approximation was discovered for a range of 'x' values for the various packing fractions tested.

The scatter of the data point groups in Figure 4.4 was least expected. It can be attributed to experimental, equipment or human errors. The initial high drift of the experimental points may have been due to the big range of the digital manometer used, which tended to be less sensitive at low pressure. Another important source could have been from large scale eddies formed by high turbulence in the vicinity of the filter, which could have been encouraged by the randomness of the wire. This was seen to diminish with increased packing fraction as is obvious in Figure 4.5, where the highest packing fraction

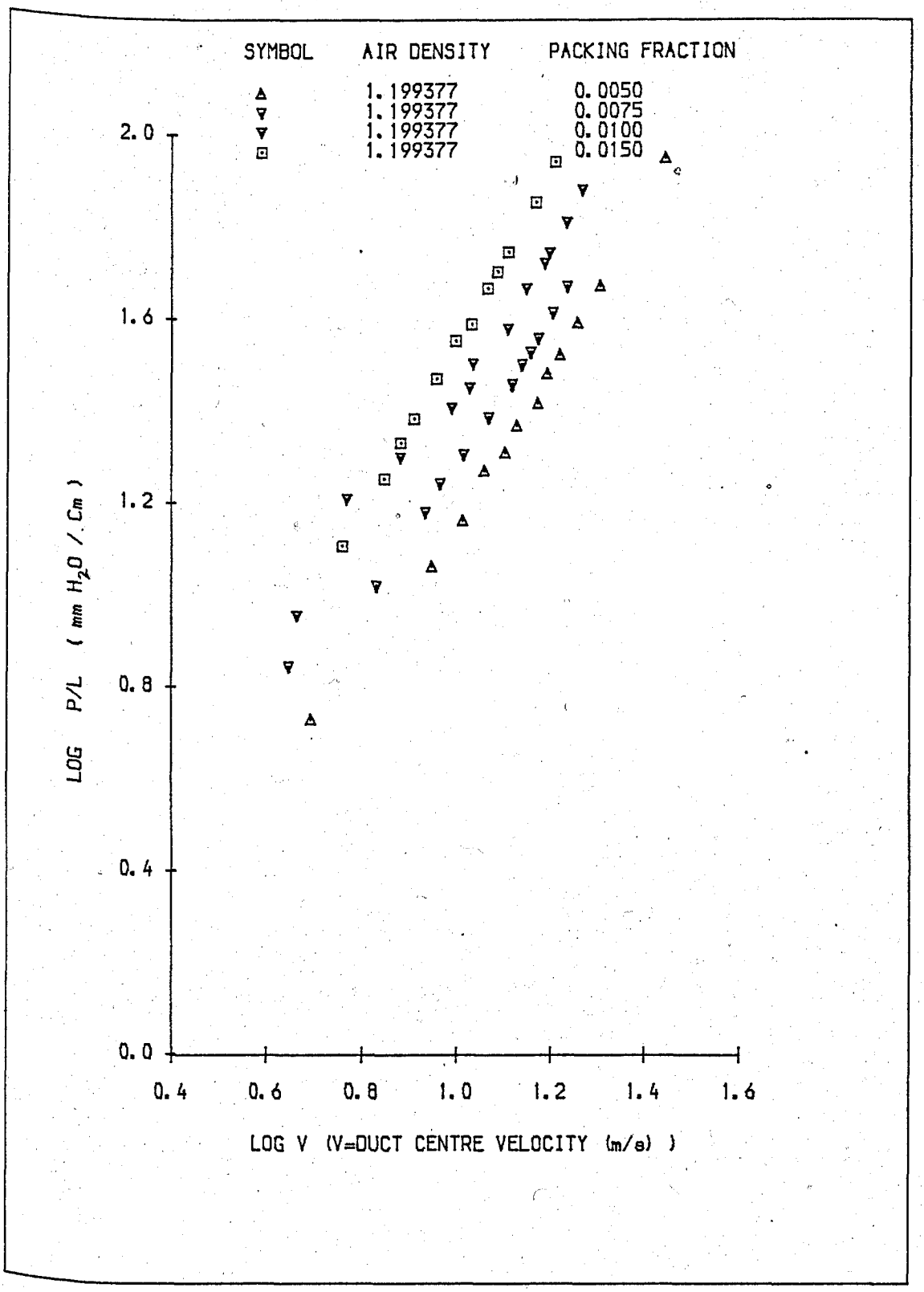

FIG. 4.4: PRESSURE DROP - 5 CM FILTER LENGTH

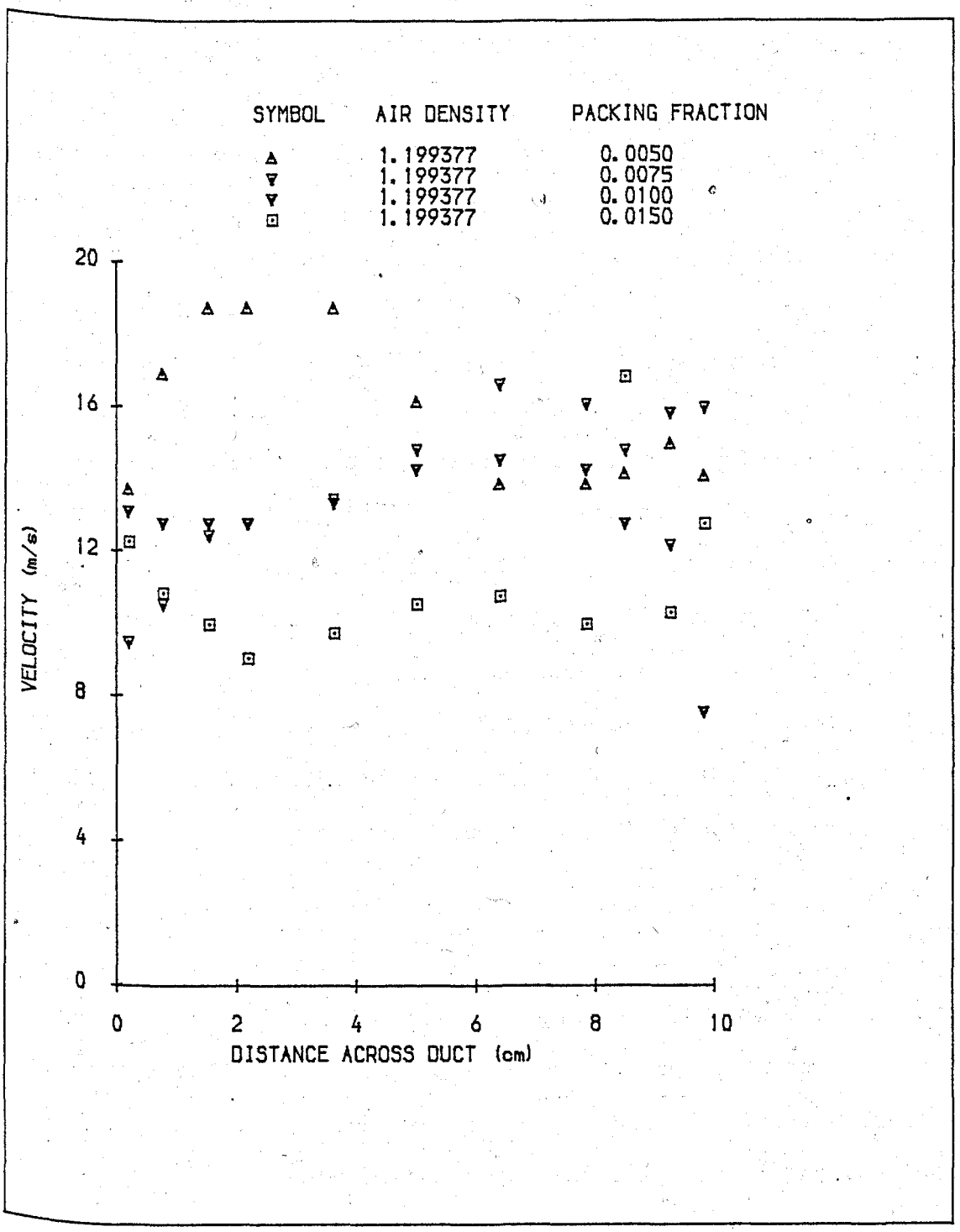

FIG. 4.5: CORRESPONDING VELOCITY PROFILES (FOR FIG. 4.4)

of 0.015 has the most even velocity profile. Another important point revealed by these downstream velocity profiles is the homogeneity of the wire packing in the matrix. For very badly packed matrices are easily identifiable by wide variation in the values of the velocity traverse.

Also, there seem to be a critical packing fraction below which the unevenness of the flow profiles become pronounced irrespective of the uniformity of the packing. For packing densities above these values, the flow sees the random wires as straigthners that tend to break up the large scale eddies rather than obstacles. To investigate this further, another filter of length 15 cm was tested with 0.005, 0.0075 and 0.010 packing fractions. The results obtained are shown in Figures 4.6 and 4.7, and Table 4.2. Here again, the smoother profiles with high packing is amplified by Figure 4.7. The average gradient from the table is 1.523 with 99% correlation factor. The expression that predicts the mean pressure drop per unit length is given by

$$\frac{\nabla P}{L} = F^{0.01}\ 1.523V - 0.308 \qquad (4.18)$$

Similar experiments were carried out using woven wire. Tests varied from the application of just one mesh to as many as 20. There are two reasons for including these tests. The first is that the woven wire would be used eventually for filtration tests and therefore a knowledge of the resistance was necessary; and secondly, the result is used to clarify the problems encountered with the explanation of the random behaviour of the previous filters. Figures 4.8 shows the logarithmic plot of P/n against flow velocity while Figure 4.9 shows their profiles. It is

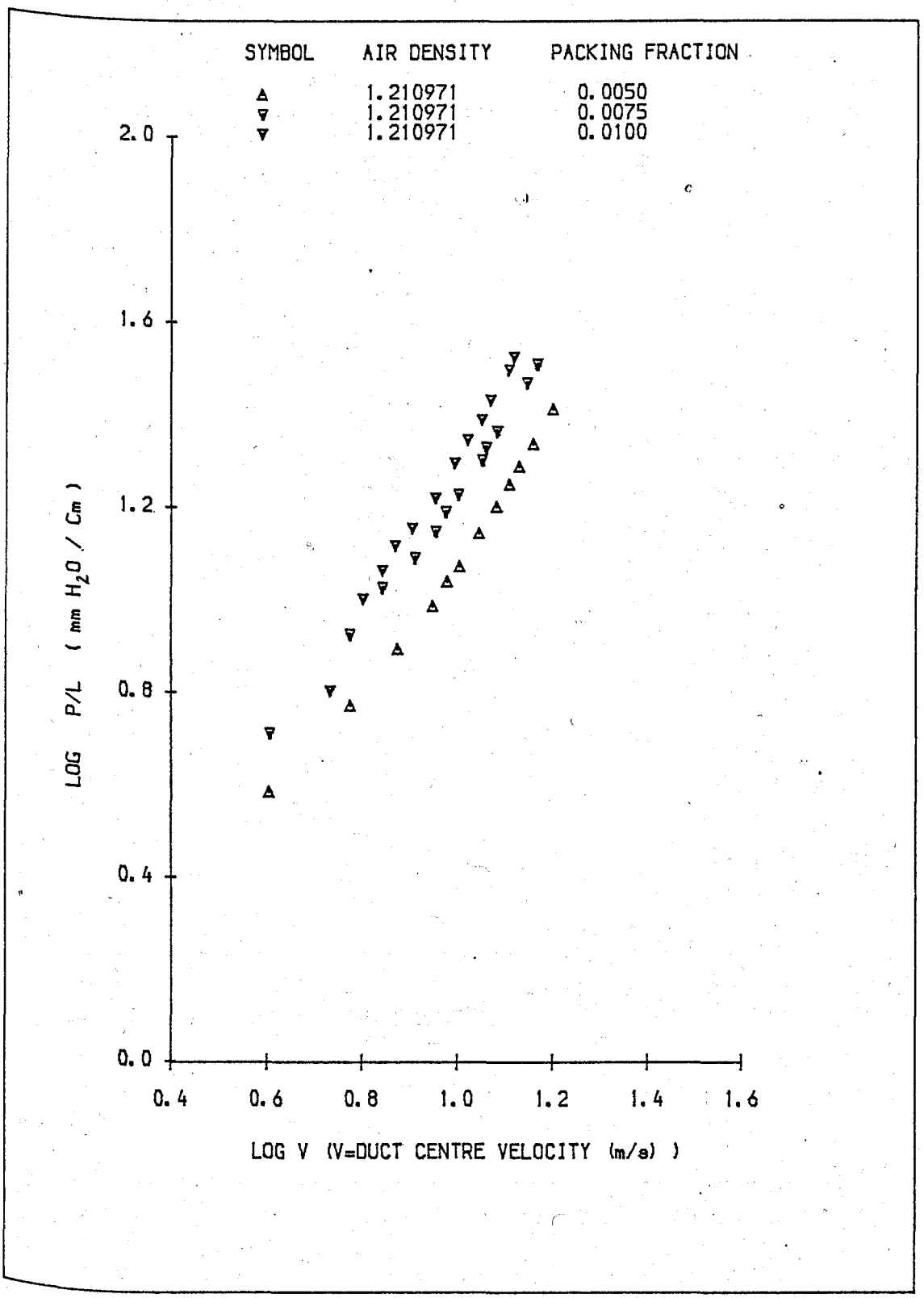

FIG. 4.6: PRESSURE DROP - 15 CM FILTER LENGTH

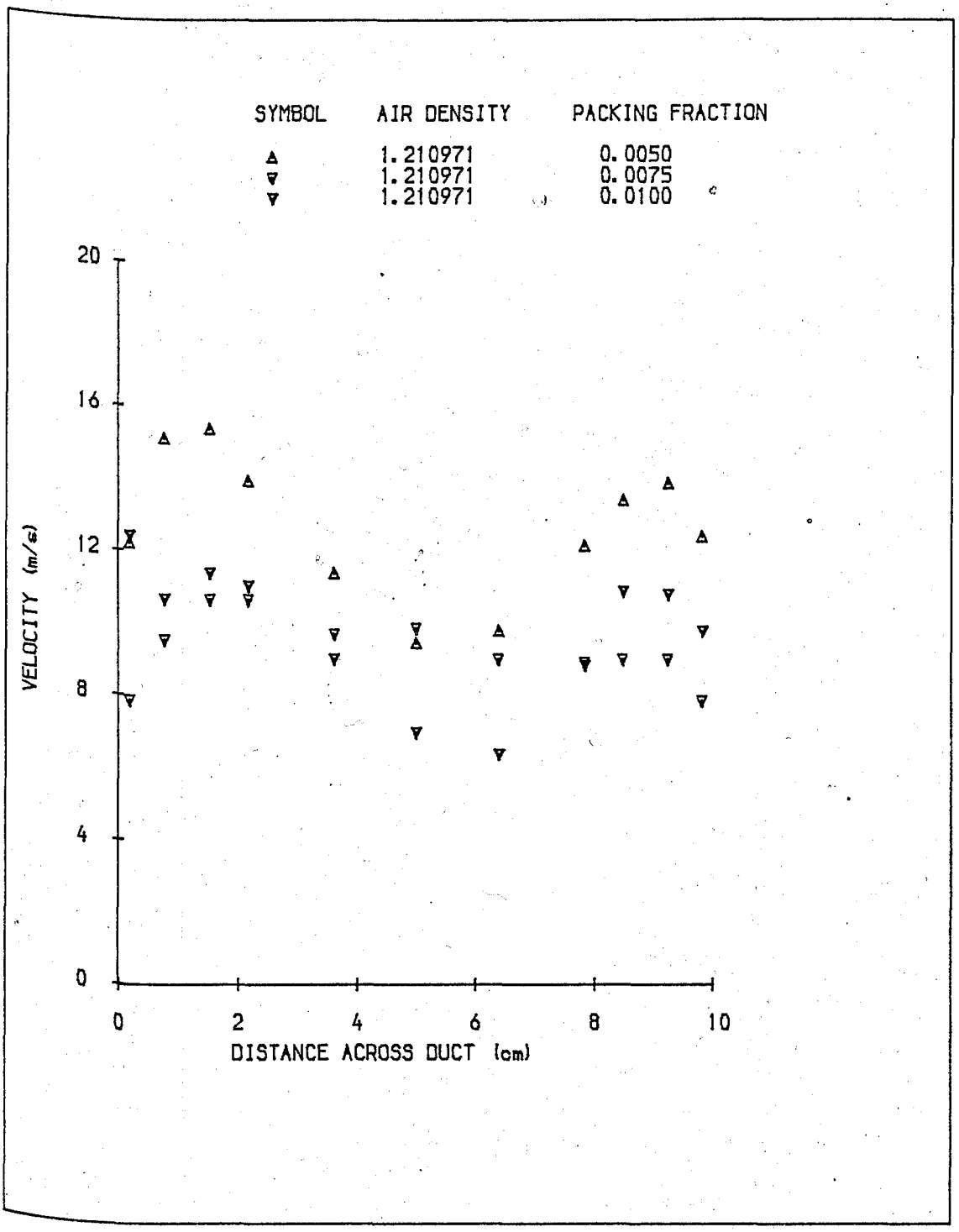

FIG. 4.7: CORRESPONDING VELOCITY PROFILE (FOR FIG. 4.6)

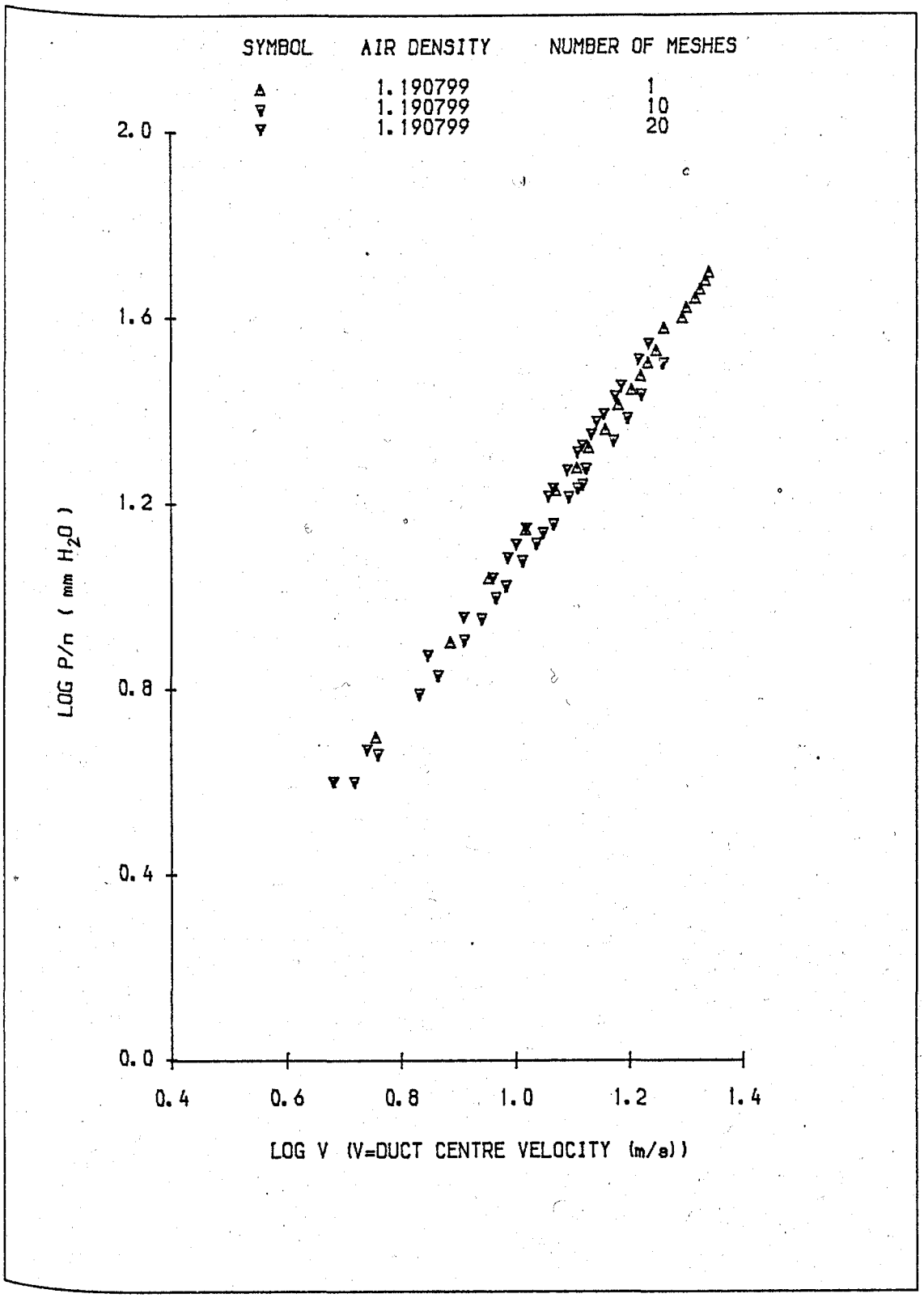

FIG. 4.8: PRESSURE DROP FOR WOVEN WIRE FILTER

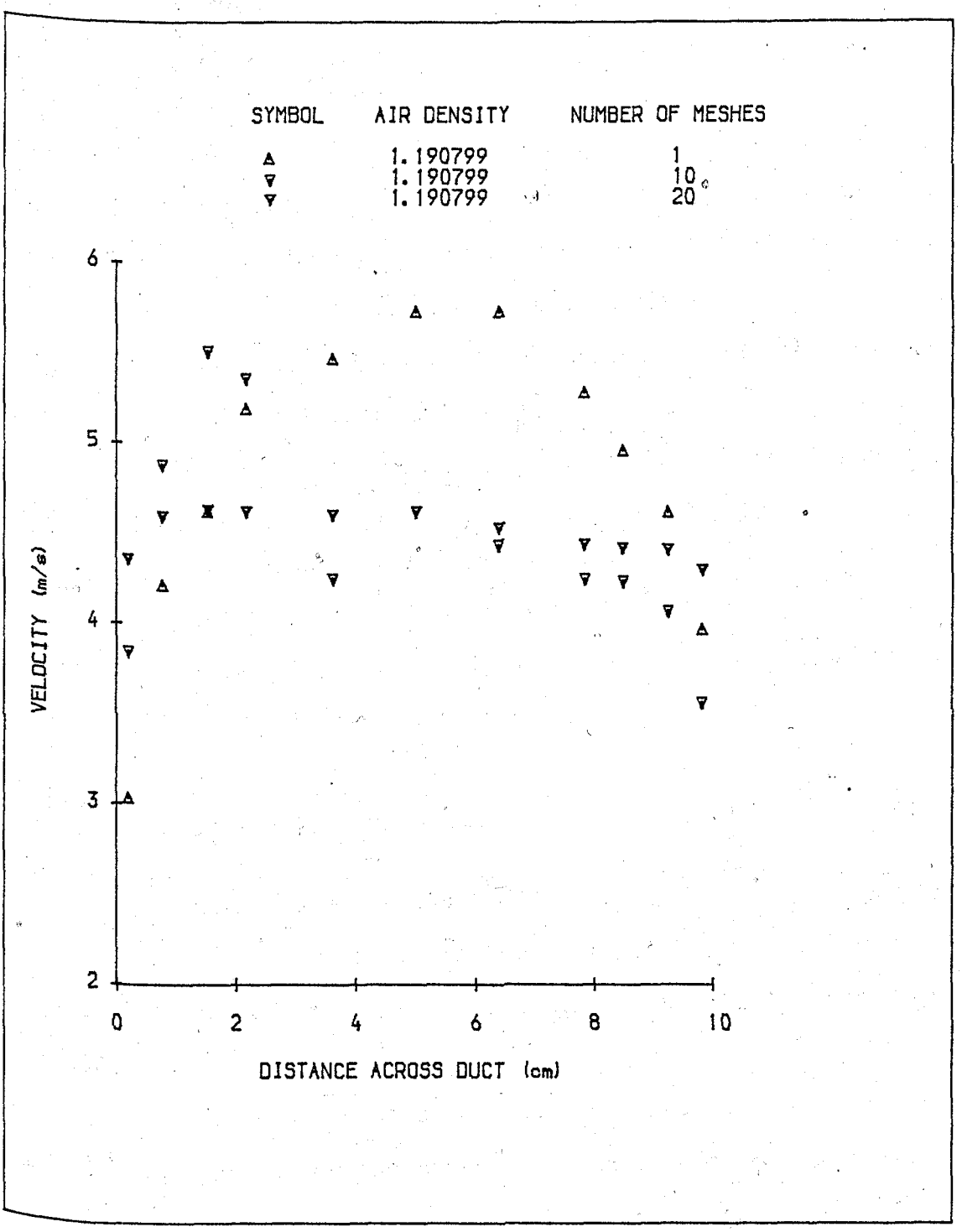

FIG. 4.9: CORRESPONDING VELOCITY PROFILE (FOR FIG. 4.8)

obvious from the plot that the following relationship exists.

$$\nabla P_{20} = 2x\nabla P_{10} = 20X\nabla P_1$$

This expression arose due to the fact that the pressure drop in a fan model filter is a function of both solid volume fraction and the ratio of average distances between neighbouring wires. Hence, for meshes of the same pore and wire sizes packed in the same matrix, their resistance tend to add up in series. A linear regression of the experimental data groups shown in Figure 4.8 produced a good correlation and high effectiveness factor. Details of the results of fitting straight lines through the data points are given in Table 4.3. A single specific expression to predict the mean pressure drop for the whole set of the experimental data takes the form:

$$\frac{\nabla P}{n} = S_s^x \, 1.699V - 0.602 \qquad (4.19)$$

which is similar to equations (4.17) and (4.18). S_s represents the screen solidity, which is the ratio of the blocked area over the total area of the mesh. For this particular case, S_s is 0.478.

The results of the woven wire filters also support the above explanation for the scatter of the data of random wires. In this particular case, because the wires are ordered, the unaccounted errors in the system are those due to equipment and their readings, as the error from random packing is drastically reduced. This is apparent in both Figure 4.8 and 4.9.

So, for a filter designer who is interested in predicting the power requirements of a randomly packed filter, equations (4.17) and (4.18) will be very useful. The first may be used for filter length upto 10cm, while the second is for 15cm and above. The resistance of well ordered woven wires of different mesh sizes can be predicted with equation (4.19) provided that the solidity is known.

An alternative form of the presentation of the above data was produced by plotting the experimental coefficient of drag as a function of flow Reynolds number. As already discussed in the formulation of the drag coefficient above, this approach models the entire filter as banks of cylinders that are perpendicular to the flow direction. The expectation is that the correlated experimental results must approach that of infinitely long cylinder. For random filters, the drag coefficients were calculated with equations (4.13) and (4.14) and are shown in Figures 4.10 and 4.11. These correspond to the data of Figures 4.4 and 4.6. Although Figure 4.10 shows a high scatter of the points, the data tended to asymptote at about a drag coefficient of 2.2. Higher packing of Figure 4.11 showed a better correlation with Re becoming independent of C_d at about the value 2. This lower C_d for longer filter is in tune with equation (4.13), which shows the drag coefficient to be indirectly proportional to the filter length. This practically means that the pressure drop across the shorter filter was increasing more rapidly with increased flow Reynolds number than the longer filter. Hence, producing earlier independence of C_d from the wire Re in Figure 4.11; or in other words, the earlier occurence of the asymptote.

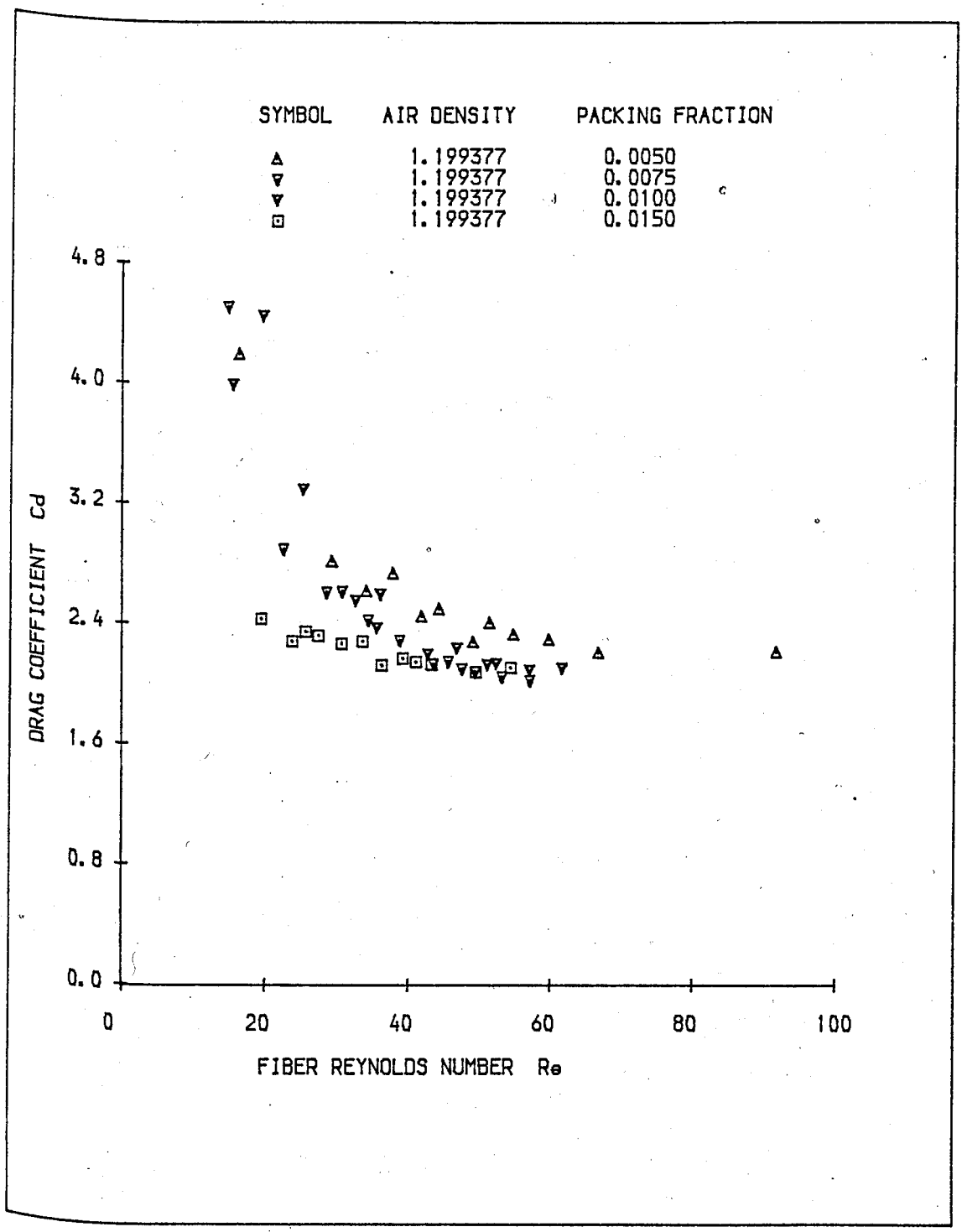

FIG. 4.10: CD - RE PLOT FOR A FILTER LENGTH OF 5 CM AND WIRE DIAMETER OF 50 MICRONS (RANDOM WIRES)

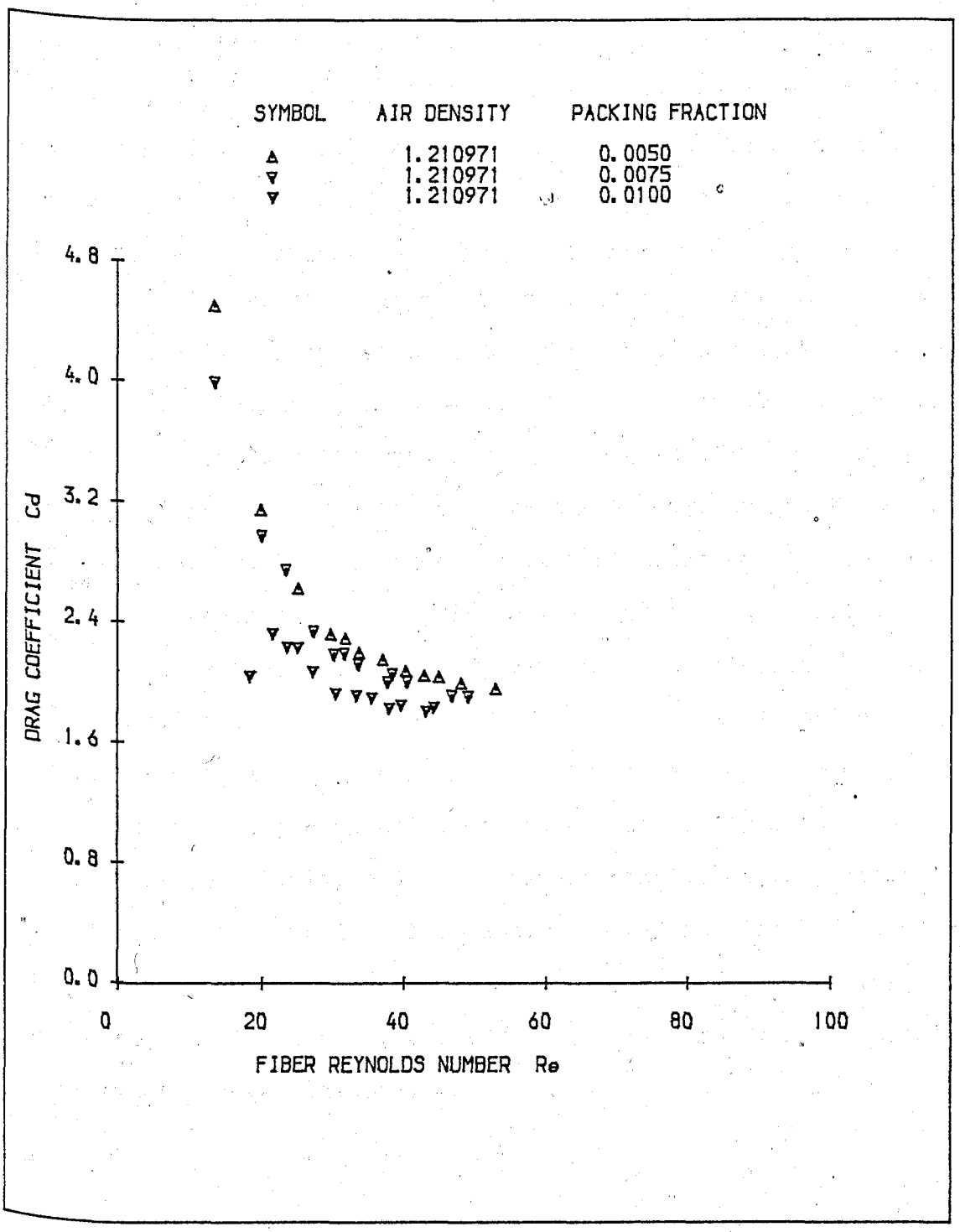

FIG. 4.11: CD - RE PLOT FOR A FILTER LENGTH OF 15 CM AND WIRE DIAMETER OF 50 MICRONS (RANDOM WIRES)

A combination of both results is shown in Figure 4.12 for easy comparison. Analysis of the woven wire data (Figure 4.13) corresponding to that of Figure 4.8 produced the best fit with C_d tailing off at about a drag coefficient of 1.8 which compares better with that of a single cylinder at the same range of Re. The difference between the values of C_d obtained from both random and woven wire filter may partly arise from the values of frontal areas used in the two models. In the case of woven wires, A_e was accurately calculated, while a statistical estimate was applied for random wire arrangement. Also in the case of woven wires, the mean solidity of each of the screen that make up the filter was almost constant. Hence, errors in filter resistance which arose from the randomness of the wire alingnment in individual filters were less. Lastly, the scale of turbulent intensity in the random filter would have been more because of the wire orientation; thus, resulting to a correspondingly higher pressure drop. The advantage of the presentation of the results in this form is that only the flow velocity and main characteristics of the filter is sufficient to predict the coefficient of drag of similar filtering systems. Hence the power (pressure drop) requirements can be determined without resorting to very expensive experimental investigation.

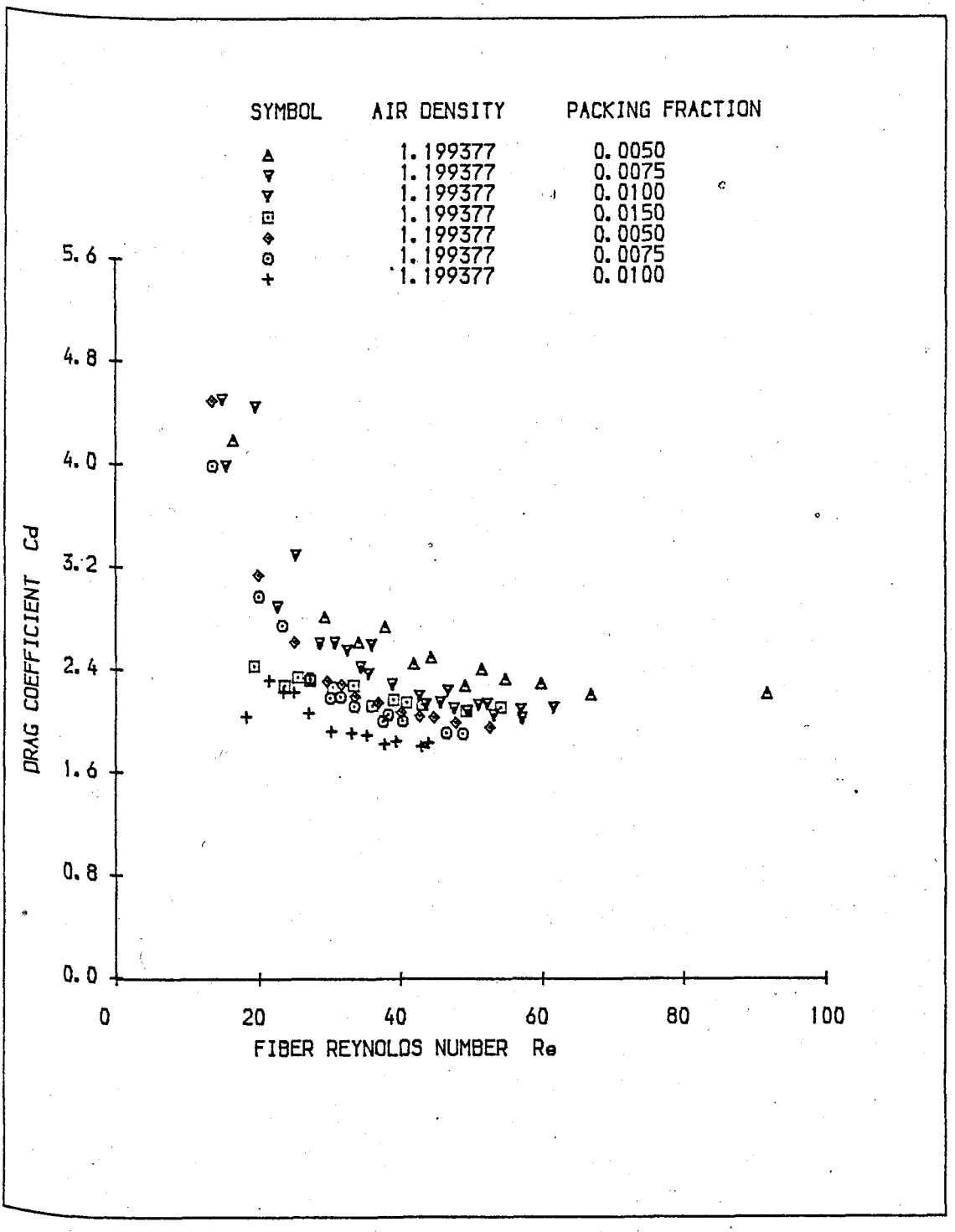

FIG. 4.12: CD - RE PLOT FOR FIGS 4.10 AND 4.11 COMBINED

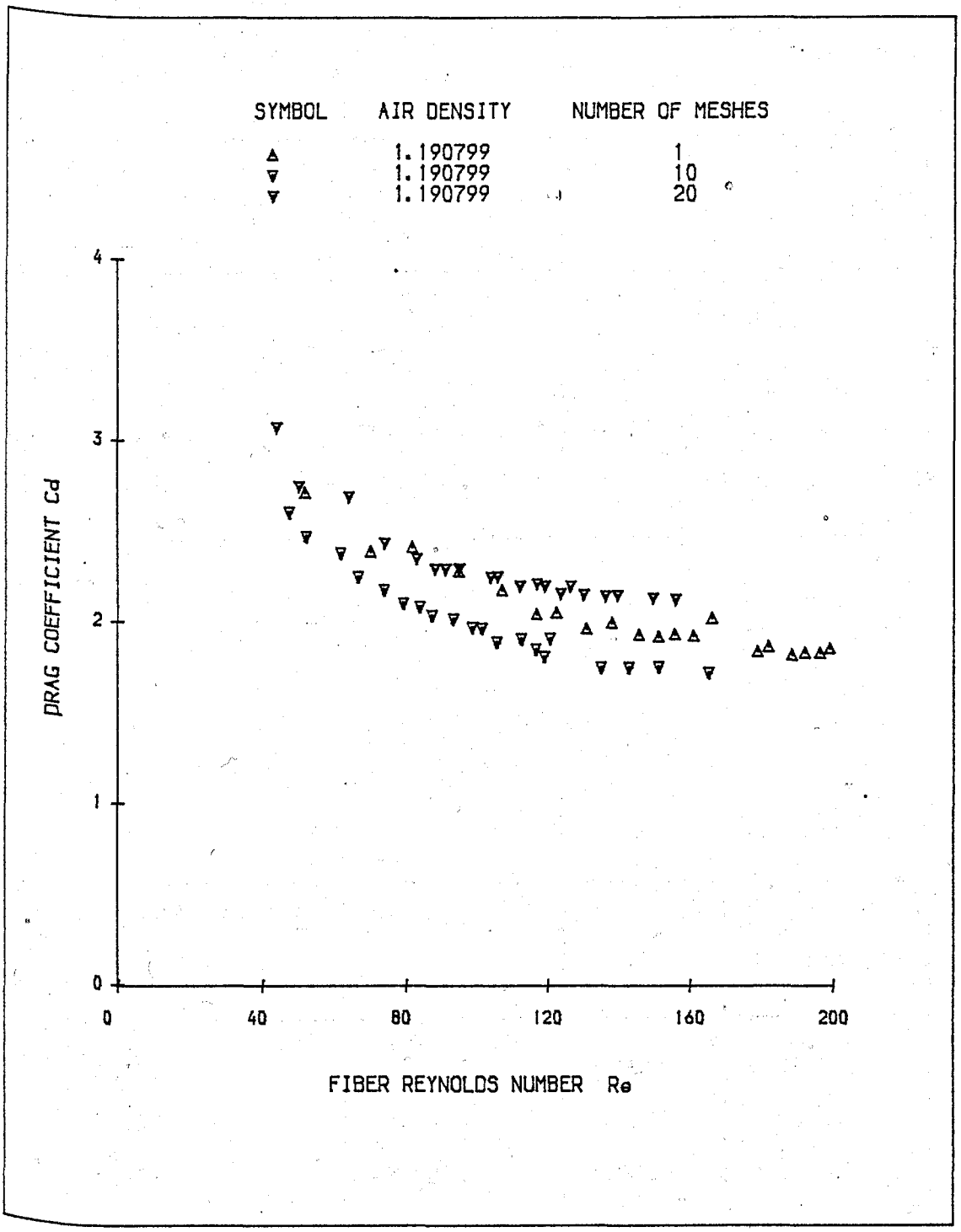

FIG. 4.13: CD - RE PLOT FOR WOVEN WIRES (400 MICRONS PORE SIZE)

Table 4.1

Packing Fraction	Interception	Gradient	Correlation Coefficient
0.0050	-0.4580	1.6300	0.9960
0.0075	-0.1430	1.4480	0.9950
0.0100	+0.0036	1.4270	0.9920
0.0150	-0.2960	1.8490	0.9995

Table 4.2

Packing Fraction	Interception	Gradient	Correlation Coefficient
0.0050	-0.3170	1.4080	0.9940
0.0075	-0.1790	1.4210	0.9960
0.0010	-0.4280	1.7400	0.9960

Table 4.3

Number of Meshes	Interception	Gradient	Correlation Coefficient
01	-0.6020	1.809	0.9990
10	-0.5980	1.337	0.9995
20	-0.6050	1.674	0.9990

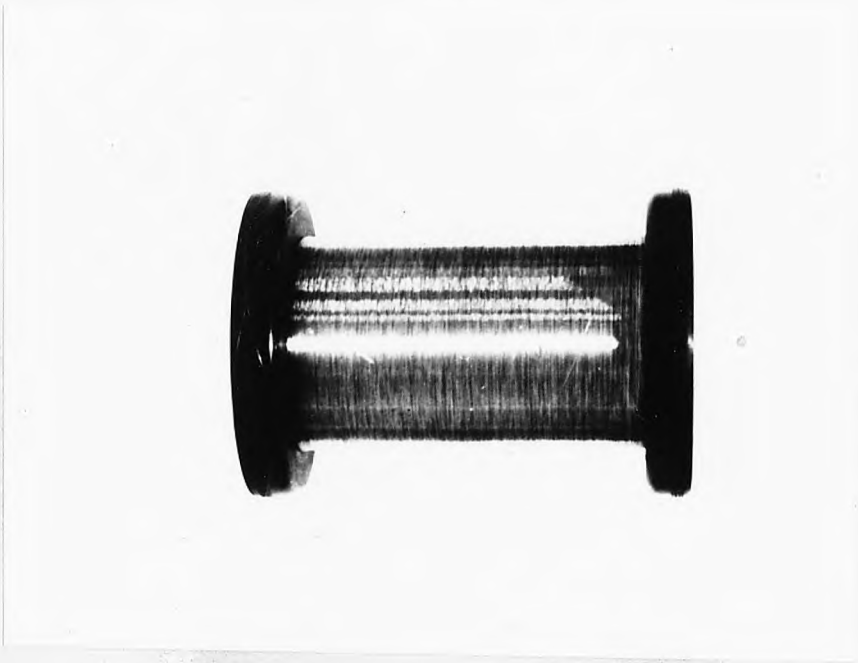

CURLED

LOOSE

PLATE 4.1: 50 MICROMETER DIAMETER STAINLESS STEEL WIRE USED IN THE FILTRATION TESTS (CURLED AND LOOSE)

PLATE 4.2: 10 x 10 CM FILTER MATRIX PACKED WITH STAINLESS STEEL WIRES (0.5% PACKING DENSITY)

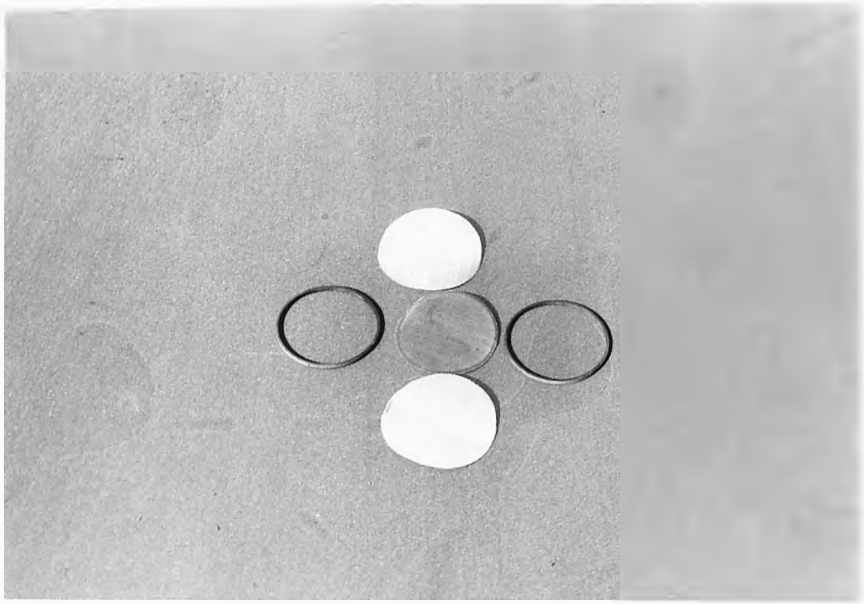

PLATE 4.3: GRADE OF WOVEN WIRE FOR FILTRATION WITH PVC SEPARATORS (400 MICRONS)

CHAPTER FIVE

THEORY AND MECHANISMS OF MAGNETIC FILTRATION

5.1 Single Fiber Efficiency

It is usually assumed in the quantitative description of the filtration process that once a particle touches a fiber it is captured and retained by either electrostatic, capillaric, or van der Waals adhesion forces [39]. The so-called "Single-Fiber" efficiency η_s, is given by the ratio of the number of particles striking the fiber to the number which would have struck had there been no deviation of the streamlines so far as the particles are uniformly dispersed. So if a fiber of diameter, s, removes all of the particles originally contained in a layer of thickness 2X far upstream of the fiber, the collection efficiency is given by :

$$\eta_s = \frac{2X}{2s} = \frac{X}{s} \qquad (5.1)$$

The main mechanisms that are present in gas filtration are given below:

5.2 Inertial Deposition

The presence of a body in a flowing fluid results in a curvature of the streamlines in the neighbourhood of the body as shown in Figure 1.2. The individual particles do not, due to their inertia, follow the curved streamlines but are projected against the body and may deposit on their surfaces. The intensity of this mechanism increases with increasing particle size and

velocity of the flow.

For particles with Reynolds number, Re, less than 1, mostly applicable to gas filtration, the single-fiber efficiency is a function of Stokes number, (inertial force divided by viscous force). The fiber diameter, (2s), is the characteristic dimension, and the Reynolds number with respect to the fibers determine the type of flow pattern around the fiber.

The fiber Reynolds number has a strong effect on the flow pattern and, therefore, on collection efficiency; two extreme cases have been investigated [40] : potential ($Re \rightarrow \infty$) and creeping flow ($Re < 0.2$) . Single-fiber efficiencies in these extreme cases, plotted against Stokes number for inertial deposition can be seen in [41]. Most of the calculations carried out for negligibly small s/b, predicted that there is a value of St for cylinders, below which no deposition occurs. The value generally quoted [42] is 0.125.

The single-fiber efficiency has direct application only in the case of relatively open filters, that is, at low packing densities, operated with high face velocities, up to Re = 10 or higher. In such cases, the case of fiber interference is not significant and the overall filtration efficiency due to inertia η_i of the filter can be related to the single-fiber efficiency η_s by an exponential expression in the following form [43]:

$$\eta_i = 1 - \exp\left[\frac{-4L}{\pi s}\,\frac{F}{1-F}\,\eta_s\right] \qquad (5.2)$$

where F is the packing density of the filter medium given by

F = Vol. of fibers/bulk vol. of the filter medium

L = filter length

Figure 5.1 shows the trend of inertial deposition with particle size.

5.3 Direct Interception

This mechanism involves the finite size of particles. A particle is intercepted as it approaches the collecting surface to a distance equal to its radius. A special case of this mechanism is the so-called sieve effect, which occurs if the distance between fibers is smaller than the particle diameter . Whilst interception can be simply included in the primary separation mechanism such as inertia or diffusion, it is customary to consider it separately.

The efficiency of interception is defined by those streamlines that pass within $X \leq (s+b)$ at $Y = 0$. For potential flow, the interception efficiency is given by [41] as :

$$\eta_d = (1 + R) - \frac{1}{(1 + R)} \qquad (5.3)$$

where $R = b/s$

Figure 5.1 shows η_d as a function of Re for small Reynolds number.

5.4 Diffusion Deposition

The probability of separation of sub-micron particles is increased by their random zig-zag motion due to Brownian bombardment by gas molecules. In their random movement, particles close to the surface of the fiber hit the surface and stick to it, thus reducing the particle concentration in the immediate

vicinity. A net diffusion flux towards the fiber develops as a result, and this brings new particles to the surface of the fiber. Diffusion effects increase with smaller particles and lower gas velocities.

Most of the literature correlations for a single-fiber efficiency due to diffusion η_{dd} indicates that it is proportional to Peclet number, Pe, raised to power -2/3 (i.e $Pe^{-2/3}$). Friedlander [44] showed that for Re = 0.1:

$$\eta_{dd} = 1.75\ Pe^{-2/3} \tag{5.4}$$

5.5 Gravity Deposition

Sedimentation due to gravity plays a relatively minor, often negligible, part in most practical gas filters. The effect of gravity may be represented by the Froude number Fr, which relates the external forces to the internal forces on particles [45]. The single-fiber efficiency due to gravity of a cylinder transverse to the gas flow is simply:

$$\eta_g = \text{Stokes No.} \times \text{Froude No.} \tag{5.5}$$

which is identical to :

$$\eta_g = \frac{V_t}{V} \tag{5.6}$$

where V_t is the terminal settling velocity of the particle and V the gas velocity.

Equation (5.6) indicates that gravity settling becomes significant only in the separation of heavy particles at low filtration velocities. An example of such a case is filtration in

granular packed beds [46] which gives higher efficiency for large particles if the gas flow is in the downward direction.

5.6 Electrostatic Deposition

Both the particles and the fibers in the filter may carry electric charges. Deposition of particles on the fibers may take place because of the forces acting between charges or induced forces.

Adhesion and cohesion of dust particles: Adhesion forces between the dust particle and the filter medium also affect the dust collection process. Collisions occur during displacement of the dust particles, which because of the adhesion forces can lead to coagulation. Such an effect favours dust collection in all dust separators. Adhesion forces are particularly high in electrical and filtration dust collectors, as the separation efficiency largely depends on the forces retaining the separated dust particles at the precipitation electrode or on the porous filter material.

Although all adhesion forces between dust particles are ultimately of electrical origin, they can be sub-divided into three groups from the microscpic view point and without reference to chemical bonding forces. These are:

(i) Van der Waals Forces [47]: forces acting between the molecules or atoms, other than chemical bonding forces.

(ii) Capillary adhesion forces [48]: in the presence of humidity, is provided by

capillary condensation from the surroundings. Liquid bridge form between the adhesion partners.

(iii) Coulomb adhesion forces [49]: forces due to charging of particles by collision, abrasion and friction. (This force is far smaller than the van der Waals forces except when particles are very highly charged as in the electrical dust collectors).

5.7 Combination Of Separation Mechanisms

Whilst most of the separation mechanisms discussed earlier take place simultaneously, the predominant effects in practical filters are those of inertial impaction, interception and diffusion. The relative importance of these three mechanisms varies with the filter type, but generally the efficiency due to diffusion decreases with particle size whilst that due to inertia and interception increases (for a give filtration velocity). The superposition of these conflicting trends results in a local minimum on the efficiency curve, (Figure 5.1); thus leading to the well known concept of the most penetrating size. The relationship between penetration and filtration efficiency is given by:

$$P = 1 - E \tag{5.7}$$

The actual shape of the efficiency curve, and subsequently the value of the most penetrating size depends on the filter type. The most penetrating size ranges from 0.5 to 1 micron. The theoretical superposition of the separation mechanisms are expressed as if they take place in series [50], so

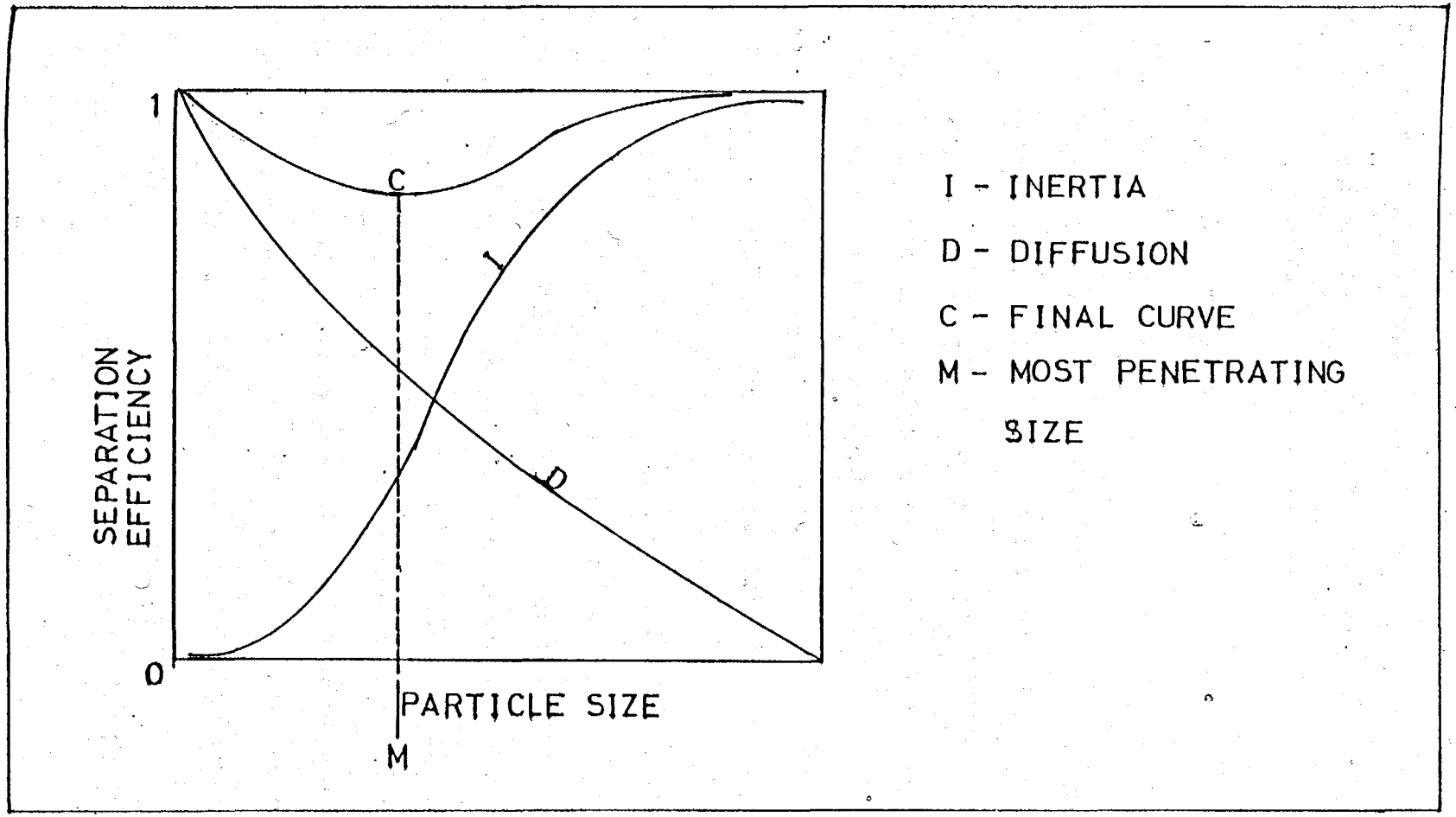

FIG. 5.1: SUPERPOSITION OF DIFFERENT MODES OF FILTRATION

that only the particles not collected by one mechanism is collected by the others. Thus for inertial, interception, and diffusion, the total efficiency become:

$$\eta_{i,d,dd} = \eta_i + \eta_d + \eta_{dd} \qquad (5.8)$$

5.8 Mathematical Modelling of HGMF Process

Predictions for the collection of particles in High Gradient Magnetic Separation (HGMS) have concentrated on the modelling of the collection process on a single cylindrical fiber. It involves the determination of the path followed by a particle passing through a magnetic field under the simultaneous action of magnetic and other forces. This is an Initial Value Problem (IVP) requiring for its solution complete specifications of the particle's initial conditions like location, size, shape, density, permeability and initial velocity, and a knowledge of magnetic and other forces as a function of position and time. The single wire model is then generalized to predict the collection efficiency of a completely " neat " filter matrix. A number of different models have been presented to explain the capture of paramagnetic particles by the matrix element of a high gradient magnetic separator. The first of these were based on the work of Zebel [51] who investigated electrostatic collection systems. Subsequently, Bean [52], Oberteuffer [53] and Watson [54] calculated critical capture trajectories using modifications of Zebel approach.

The approach considered here follows the usual treatment of conventional filtration, with the particle

considered to be spherical, uniformly distributed in the fluid stream, and moving at the same velocity as the fluid upstream of the collector. This can approximately be described as a monodisperse system. The basic element of the filter is a clean, cylindrical wire of radius s, oriented so that its axis was perpendicular to the flow direction.

The first model of HGMS published by Lawson [55] considered only magnetic force and drag forces to be acting on the spherical particle approaching the wire, but his subsequent work [56] extended the model to include inertial and gravitational effects. The present work is based entirely on this model and is applied to the magnetic filtration of particles from a gaseous stream.

Consider a small particle near a ferromagnetic cylinder which is in a magnetic field (Figure 5.2). The part taken by the particle depends on the gravitational, inertial , drag, and magnetic forces acting on it (Figure 1.2). In the following sections the equations for each of these forces and a general form of Newton's equation is developed for the motion of a single particle approaching the wire under the influence of these forces. The main objective of the exercise is to determine the portion of the fluid stream from which particle are removed as the fluid flows past the wire. This is achieved by analysing the trajectories of particles which approach the region of influence of these forces. The collision radius of the wire, X, is defined by the initial position of the particle whose trajectory just touches the wire. The critical collision radius, X_c , is that distance which separates those trajectories that intersect from

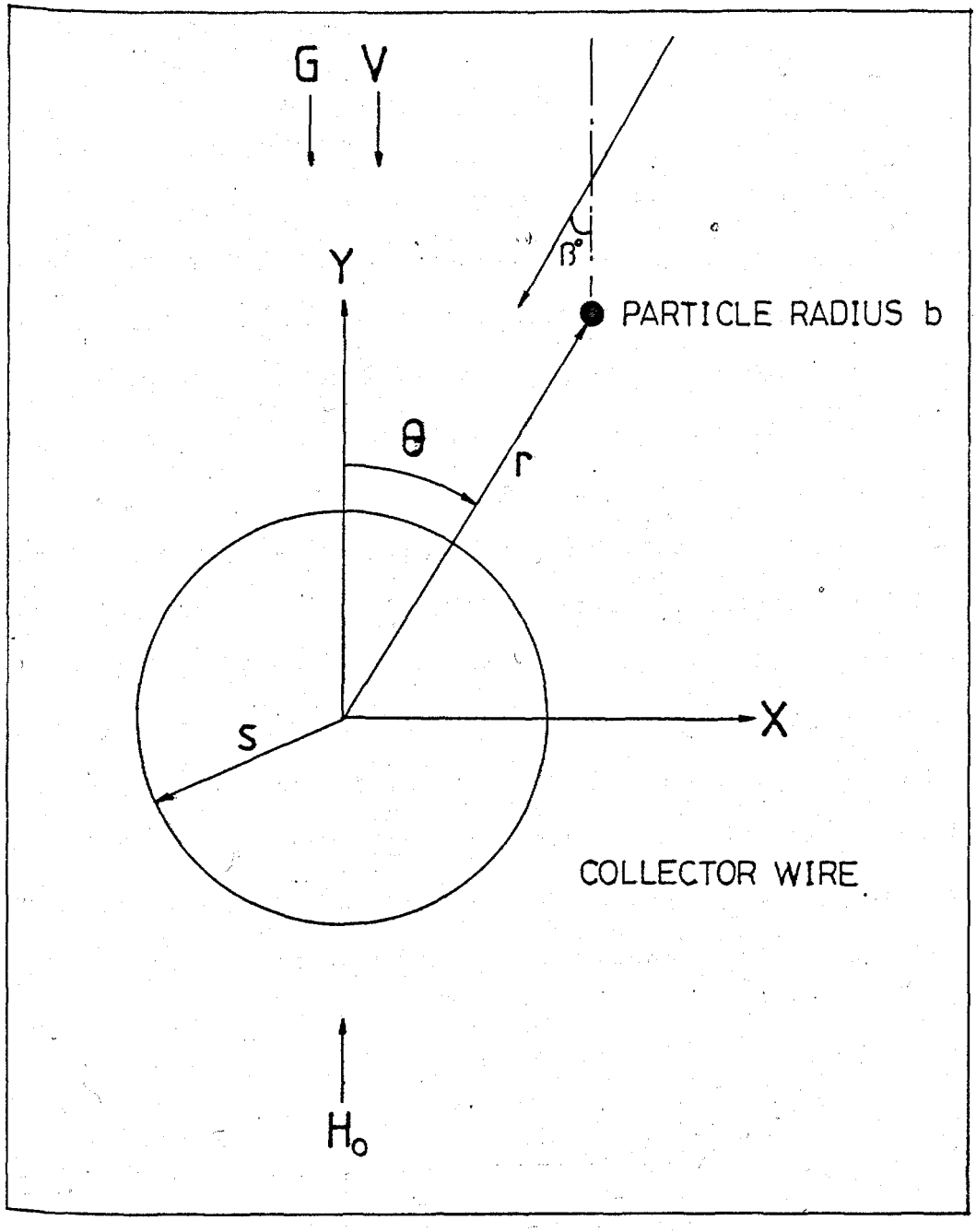

FIG. 5.2: ILLUSTRATION OF SINGLE WIRE SINGLE PARTICLE MAGNETIC SEPARATION

those that miss the wire.

5.8.1 The Magnetic Force

In a monodisperse system where particulates are randomly dispersed, (Newtonian fluid being assumed), the magnetic force exerted on a single small particle depends on the magnetization of the particle M_s and the fluid, the applied field, the particle shape, and the concentration of the particles.

The applied field, H_o , magnetizes the wire which inturn induces a magnetic field which is superimposed on the uniform field. (The capture regions in a strong magnetic interaction is shown in Figure 5.3) This combination of uniform and induced fields magnetize the particle. The fluid medium is considered to be non-magnetic and therefore is treated as free space. From the magnetic form of Gauss's law, which states that the flux of a vector B across any closed surface is zero, it follows that:

$$\int_s B \, ds = 0 \qquad (5.9)$$

or in a divergent form

$$\int_v \nabla \, B \, dv = 0 \qquad (5.10)$$

where ∇ is the volume enclosed by the surface. Therefore for areas inside and outside the wire surface

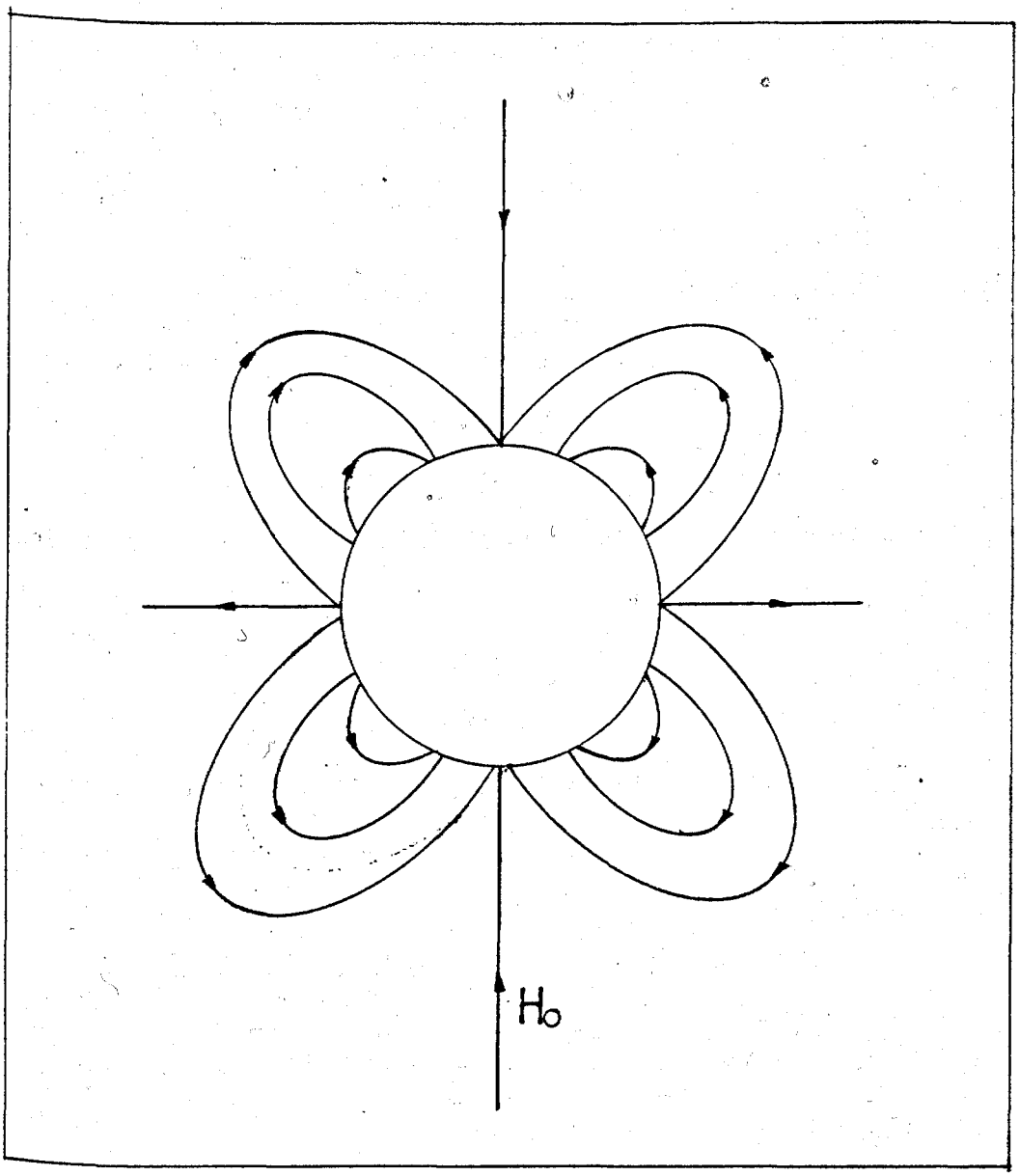

FIG. 5.3: PARTICLE CAPTURE ZONES ON A MAGNETIZED WIRE

$$\nabla \cdot B = \nabla \cdot H = 0 \tag{5.11}$$

Since the only source of the induced magnetic field is the magnetic dipole distribution and there are no currents, equation (5.11) can be written as:

$$\nabla \cdot H = 0 \tag{5.12}$$

Thus, the magnetic field, H, can be represented by a scalar magnetic potential ϕ, such that

$$H = -\nabla \phi \tag{5.13}$$

Substituting equation (5.13) into equation (5.11) results to:

$$-\nabla^2 \phi = 0 \tag{5.14}$$

a Laplace's equation from where the potential can be determined when appropriate boundary conditions are applied.

Note that

$$\nabla = \frac{\partial}{\partial r}\bar{r} + \frac{1}{r}\frac{\partial}{\partial \theta}\bar{\theta} + \frac{\partial}{\partial z}\bar{z}$$

in cylindrical polar-coordinates; $\bar{r}$, $\bar{\theta}$, and $\bar{z}$ being unit vectors.

At the surface of the fiber, the normal components of the induction field, B, must be equal. At r = s, the tangential components of the magnetic field, H, must be equal. Since the induced field has a localized source, the effect of this field vanishes far from the wire. End effects can be neglected since the wire is assumed to be infinitely long. The field has no axial

components and is, therefore, indpendent of Z.

According to [55,56] the solution outside the wire is

$$\phi = - H_o \, r \cos\theta + \frac{2 \pi M_s}{r} \cos\theta + \text{constant} \qquad (5.15)$$

The total field outside the wire is obtained by taking the divergence of equation (5.15), i.e.

$$H = H_o + H_i = \frac{\partial \phi}{\partial r} r + \frac{1}{r} \frac{\partial \phi}{\partial \theta} \theta \qquad (5.16)$$

which gives:

$$H = (H_o \cos\theta + \frac{2\pi M_s \cos\theta}{r^2} \bar{r}) + (H_o \sin\theta - \frac{2\pi M_s}{r^2} \bar{\theta})$$

$$= H_o (\cos\theta \, \bar{r} + \sin\theta \bar{\theta}) + \frac{2 \pi M_s}{r_2} (\cos\theta \, \bar{r} - \sin\theta \bar{\theta}) \qquad (5.17)$$

The induced magnetic field H_i is given by

$$H_i = \frac{2\pi M_s}{r_2} (\cos\theta \, \bar{r} - \sin\theta \, \bar{\theta}) \qquad (5.18)$$

In a uniform field H_o , the magnetization of a paramagnetic sphere was derived by Jackson [57] and is given by

$$M = \frac{X}{(1 + \frac{X}{3})} H_o \qquad (5.19)$$

where X is defined as the ratio of magnetization of paramagnetic body to the field inside the body. This is called the magnetic susceptibility.

For a very small particle , the field induced by the magnetization outside the wire is the same as that caused by a line dipole of moment

$$M_o = M\ V_o \tag{5.20}$$

where V_o is the volume of particle. Jackson [57] showed that the force on a dipole is given by

$$F_m = \mu_o\ (M_o \cdot \nabla)\ H \tag{5.21}$$

where μ_o is the fluid vacuum permeability.
Combining equations (5.19), (5.20) and (5.21) gives:

$$F_m = \frac{\mu_o\ V_o\ X}{(1 + \frac{X}{3})}\ (H \cdot \nabla\ )\ H \tag{5.22}$$

$$= \mu_o\ V_o\ X^*\ (H \cdot \nabla_o)\ H \tag{5.23}$$

where $X^* = \dfrac{X}{1 + \frac{X}{3}}$. Introducing equation (5.17) into (5.23) gives:

$$F_m = \frac{16\ \pi^2\ X\ M_s\ b^3\ s^2}{3\ r^3}\left[\frac{2\ \pi\ M_s\ s^2}{r^2} + H_o\ \cos 2\theta\right]\overline{r}$$

$$+\left[\frac{16\ \pi^2\ x\ M_s\ b^3 S^2}{3\ r^3}\sin\ 2\theta\right]\overline{\theta} \tag{5.24}$$

5.8.2 The Hydrodynamic Force

Practical cylinder diameters and bulk flow rates with Reynolds number, Re, in the region of 0.1 to 40.0 (where viscous

and inertial fluid body forces cannot be neglected) have been studied extensively. In this range, viscous and inertial fluid body forces cannot be neglected. Hence, there is no purely analytic solution of the full Navier-Stokes equation even for a simple cylindrical shape [58]. Therefore, viscous forces are accounted for by superimposing a boundary layer upon the solution for potential flow. The boundary layer thickness may be calculated as a function of Re (decreasing as $1/\sqrt{Re}$) [59]. Flow within the boundary layer is reduced by a factor which is a function of both Re and the distance of the cylinder. Numerical analysis and experimental data of fluid flow at moderate Re [60] show that the absolute velocities in the wake immediately behind the cylinder are small relative to the bulk flow. Since only a few particle trajectories enter this region (if at all), and do so in a region of high magnetic force close to the cylinder, the model assumes zero flow velocity in the wake directly behind the fiber.

As the relative velocity between the particle and the fluid is moderately small except just before impact and the particle's Re is assumed to be less than 1, the Stokes formula is used to calculate the drag force. Thus, the drag force acting on a sperical particle is given by:

$$F_d = - 6 \pi \mu b \left(\frac{dr}{dt} - V\right) \qquad (5.25)$$

where b is the particle radius, ν is the coefficient of viscosity of the fluid, V is the velocity of the fluid at r, and $\frac{dr}{dt}$ is the particle velocity. Therefore ($\frac{dr}{dt}$ - V) is the velocity of the particle with respect to the fluid. The use of equation (5.25)

assumes that the Stokes regime around particle is true as long as $(\frac{dr}{dt} - V)$ is small; this is the case for small particles that essentially follow the stream lines. The fluid flow field can be described by either potential or laminar (creeping) flow models. The former being a more realistic expression at large distances from the cylinder but very poor at a close range, and will be adopted throughout for the theoretical calculations of critical radii. Assumption of laminar flow model over estimates the critical radii.

For Re larger than unity, the flow can be approximated by irrotational flow.

$$\nabla \times V = 0 \tag{5.26}$$

where V is the fluid velocity vector. V can be represented by the gradient of a scalar potential field

$$V = - \nabla \phi \tag{5.27}$$

where the negative sign signifies the decrease of velocity potential towards the cylinder. By continuity:

$$\nabla \cdot V = 0 \tag{5.28}$$

Hence the substitution of (5.27) into (5.28) yields Laplace equation for the velocity potential

$$- \nabla^2 \phi = 0 \tag{5.29}$$

ϕ as obtained by Lawson [55] is:

$$\phi = V r \cos\theta + \frac{V s^2}{r} \cos\theta + \text{constant} \tag{5.30}$$

from where V can be obtained from

$$V = - \nabla \phi = - V \left(1 - \frac{s^2}{r^2}\right) \cos\theta \, \bar{r}$$

$$+ V \left(1 + \frac{s^2}{r^2}\right) \sin\theta \, \bar{\theta} \qquad (5.31)$$

For completeness, when laminar flow model is assumed, Lamb's equation as used by Zebel [51] is given by:

$$V = - c_1 \left(\ln(r) - 0.5 \left(1 - \frac{1}{r^2}\right)\right) \cos\theta \, r$$

$$- c_1 \left(\ln(r) + 0.5 \left(1 - \frac{1}{y^2}\right)\right) \sin\theta \, \theta \qquad (5.32)$$

where

$$c_1 = \frac{1}{\ln 7.4 \; / \; (\rho_f \; V \; 2 \; s/v)}$$

It should be noted, however, that an angle β called the approach angle could be added to θ (Figure 5.2), to simulate the effect of varing the direction of the approaching particle on capture for both Potential and Laminar flow Models [61].

5.8.3 The Gravitational Force

The weight of the particle abated by its buoyant force produces the effect of gravity. The gravitational force acting on a single particle is given by

$$F_{gp} = \rho_p \; V_f \; g \qquad (5.33)$$

while the buoyant force of the fluid on the same particle can be represented as:

$$F_{bf} = \rho_f V_f g \tag{5.34}$$

where ρ_p and ρ_f are particle and fluid mass densities respectively.

The net gravitational force acting on the particle in the y-axis is therefore given by:

$$F_g = F_{gp} - F_{bf} = m g \left(1 - \frac{\rho_f}{\rho_g}\right) \tag{5.35}$$

In cylindrical polar coordinates, equation (5.35) becomes:

$$F_g = \left[m g \left(1 - \frac{\rho_f}{\rho_g}\right) \cos\theta \right] \bar{r} - \left[m g \left(1 - \frac{\rho_f}{\rho_g}\right) \sin\theta \right] \bar{\theta} \tag{5.36}$$

5.8.4 The Force Balance

Having established analytical expressions describing the various forces acting on the particle at any point relative to the cylinder, the particle trajectory may be described by considering a piece-wise linear path. Over each increment, the balance between inertial, magnetic, hydrodynamic, and gravitational forces is written as [56].

$$m \frac{d^2r}{dt^2} = F_m + F_d + F_g \tag{5.37}$$

In dealing with very small particles, the mass of the particle can be considered small enough that inertia can be neglected and the force balance becomes [62]

$$0 = F_m + F_d + F_g \tag{5.38}$$

although all the present analysis is based on equation (5.37). In cylindrical coordinates the inertial term can be written as:

$$m \frac{d^2r}{dt^2} = \left[m \frac{d^2r}{dt^2} - m\, r \left(\frac{d\theta}{dt}\right)^2 \right] \bar{r}$$

$$+ \left[m\, r\, \frac{d^2\theta}{dt^2} + 2\, m \frac{dr}{dt} \frac{d\theta}{dt} \right] \bar{\theta} \tag{5.39}$$

Substituting the analytical forms of F_m, F_d, F_g, as derived previously into equation (5.37) together with equation (5.39) give after some re-arrangement the radial, tangential, and axial components of the force balance as:

$$m \left[\left(\frac{d^2r}{dt^2}\right) - r \left(\frac{d\theta}{dt}\right)^2 \right] =$$

$$- \frac{16\, \pi^2 \, X \, M_s \, b^3 \, s^2}{3\, r^3} \left[\frac{2\, \pi \, M_s \, s^2}{r^2} + H_o \cos 2\theta \right]$$

$$- 6\pi\mu b \left[V\left(1 - \frac{s^2}{r^2}\right)\cos\theta + \frac{dr}{dt}\right]$$

$$- m g \left(1 - \frac{\rho_f}{\rho_g}\right)\cos\theta \qquad (5.40)$$

$$m\left[r\frac{d^2\theta}{dt^2} + 2\left(\frac{dr}{dt}\right)\left(\frac{d\theta}{dt}\right)\right] =$$

$$- \frac{16\pi^2 X M_s b^3 s^2}{3 r^3}\sin 2\theta$$

$$- 6\pi\mu b\left[V\left(1 + \frac{s^2}{r^2}\right)\sin\theta - r\frac{d\theta}{dt}\right]$$

$$+ m g \left(1 - \frac{\rho_f}{\rho_g}\right)\sin\theta \qquad (5.41)$$

$$m\frac{d^2z}{dt^2} = - 6\pi\mu\frac{dz}{dt} \qquad (5.42)$$

Since equation (5.42) is independent of radial and tangential motion, it can be solved separately. The result [62] shows the magnitude of the initial velocity to decrease exponentially to zero with time, so that initial Z-velocity can be set to zero without any damaging effect in the solution accuracy. As a result, all motion is in a plane normal to the axis of the wire and only equations (5.40) and (5.41) are required to determine

the particle motion.

To eliminate the effect of geometry of the system, it is necessary to transform the position vector r, and time t into dimensionless time τ and position R defined by:

$$R = \frac{r}{s} \tag{5.43}$$

and

$$\tau = \frac{V}{s} \cdot t \tag{5.44}$$

Where $\tau = 1$, represents the time required for the free stream flow to travel a distance of one wire radius. Introducing R and τ into equations (5.40) and (5.41) give:

$$\left[\left(\frac{d^2R}{d\tau^2}\right) - R\left(\frac{d\theta}{d\tau}\right)^2\right] = -\frac{2\,A\,W}{R^3}\left[\frac{A}{R^2} + \cos 2\theta\right]$$

$$-\frac{1}{K}\left[\left(1 - \frac{1}{R^2}\right)\cos\theta + \frac{dR}{d\tau}\right] - G\cos\theta \tag{5.45}$$

$$\left[R\,\frac{d^2\theta}{d\tau^2} + 2\left(\frac{dr}{dt}\right)\left(\frac{d\theta}{d\tau}\right)\right] = \frac{-\,2\,A\,W\sin 2\theta}{R^3}$$

$$+\frac{1}{K}\left[\left(1 + \frac{1}{R^2}\right)\sin\theta - R\,\frac{d\theta}{d\tau}\right] + G\sin\theta \tag{5.46}$$

The four dimensionless parameters used above are:

$A = \dfrac{2\pi M_s}{H_o}$, the relative magnitude of the induced

magnetization in the ferromagnetic wire due to the applied field, H_o

$W = \frac{\mu_o \chi^* H_o^2}{\rho_p V^2}$, dimensionless magnetic force parameter (a ratio of magnetic to inertia force).

$K = \frac{2 \rho_p V b^2}{9 \mu s}$, Stokes number, a dimensionless viscous force parameter (a ratio of inertia to viscous forces).

$G = \frac{s g}{V^2} (1 - \frac{\rho_f}{\rho_p})$, dimensionless gravitational force parameter.

Equations (5.45) and (5.46) represent the complete dimensionless form of particle motion in cylindrical form. These can be split into four first order differential equations with the introduction of two new dependent variables Γ and Ω resulting to:

$$\Gamma = \frac{dR}{d\tau} \tag{5.47}$$

$$\Omega = \frac{d\theta}{d\tau} \tag{5.48}$$

$$\frac{d\Gamma}{d\tau} = R \Omega^2 - \frac{2 W A}{R^3} \left[\frac{A}{R^2} + \cos 2\theta \right]$$

$$- \frac{1}{K} \left[(1 - \frac{1}{R^2}) \cos\theta + \Gamma \right] - G \cos\theta \tag{5.49}$$

$$\frac{d\Omega}{d\tau} = -\frac{2\Gamma\Omega}{R} - \frac{2WA}{R^4}\sin 2\theta$$

$$-\frac{1}{KR}\left[R\Omega - (1+\frac{1}{R^2})\sin\theta\right] - \frac{G\cos\theta}{R} \qquad (5.50)$$

5.9 Extention of the model to polydisperse systems

Polydisperse mixtures are defined here as mixtures of particulates which comprise distribution of particle size, density, and susceptibility. Other distributions such as shape may exist but their role are usually considered to be secondary, therefore they are not included in the analysis below. If polydisperse mixtures involve nonsteady motion of the type defined by equation (5.37), the description of their flow pattern can be obtained by the solution of modified version of the sets of differential equations given in equations (5.47) to (5.50) [63]. However, the simultaneous existence of all three distributions may render the system excessively complex. The following assumptions are made for such systems:

(i) Particles are spherical and uniformly displaced in the fluid.

(ii) No interaction order than hydrodynamic and magnetic forces occur between particles.

(iii) Effect of collision if they exist, is neglected.

(iv) Flow system comprising fluid and polydisperse mixtures is Newtonian.

(v) Hindrance to the motion of particles depends on the total fractional volume occupied by the mixture.

Assuming the polydisperse mixture to have density and susceptibility distributions, they can be represented as

$$\rho_\zeta = \zeta \, \overline{\rho}_p + (1 - \zeta_f). \tag{5.51}$$

where

$$\overline{\rho}_p = \int_0^\zeta \rho_p \, d\psi(\rho) \tag{5.52}$$

and

$$X_\zeta = \zeta \, \overline{X}_p + (1 - \zeta) \, X_f \tag{5.53}$$

where

$$\overline{X}_p = \frac{1}{\zeta} \int_0^\zeta X_p d\psi(X) \tag{5.54}$$

ζ is the total fractional volume occupied by the mixture , $\psi(\rho)$ and $\psi(X)$ are distribution functions related to the density and susceptibility, respectively. By definition, each distribution should satisfy

$$\zeta \int d\psi(G) \tag{5.55}$$

where $G = \rho$ or $G = X$

Let the following density and susceptibility differences be defined by

$$\rho^* = \rho_p - \rho_f \tag{5.56}$$

$$\chi^* = \chi_p - \chi_f \tag{5.57}$$

If $\rho^* < 0$, $F_g < 0$ and if $\chi^* < 0$, $F_m < 0$.

The existence of density and susceptibility distribution give rise to conditions where change of direction of forces exerted on lighter and less susceptible particles may occur.

Particles which exhibit positive susceptibilities in the $0 < \chi_p < \chi_f$ range may still be rejected and forced to move away from zones of higher field intensities due to magnetic, gravitational or their combined effects. If in a polydisperse mixture "I" uniform fractions can be defined, then the description of particulates, flowing across a single magnetized wire, requires "I" simulteneous pairs of equations of the same type as (5.47) to (5.50). This is given by:

$$\frac{d^2R}{d\tau^2} - R\left(\frac{d\theta}{d\tau}\right)^2 = -\frac{2A_iW_i}{R^3}\left(\cos 2\theta + \frac{A_i}{R^2}\right)$$

$$-\frac{1}{K_i}\left(V_r + \frac{dR}{d\tau}\right) - G\cos\theta \tag{5.58}$$

$$R\frac{d^2\theta}{d\tau^2} + 2\left(\frac{dR}{d\tau}\right)\left(\frac{d\theta}{d\tau}\right) = -\frac{2A_iW_i}{R^3}\sin 2\theta$$

$$+\frac{1}{k_i}\left(V_\theta - R\frac{d\theta}{d\tau}\right)\} - G\sin\theta \tag{5.59}$$

where i = 1, 2, 3, ..., I is the ith fraction and

$$A_i = \frac{2 \nu H_o}{M_s}$$

$$K_i = \frac{2 (\rho_p + \rho_f) V_{fo} b_i^2}{(9 s \mu_f^*)}$$

$$W_i = \frac{\mu_o \chi^* H_o^2}{(\rho_p + \rho_f) V_{fo}^2}$$

$$V_r = V_{fr} - (1 - \frac{1}{R^2}) \cos(\theta + \beta) \qquad (5.60)$$

$$V_\theta = V_{f\theta} - (1 + \frac{1}{R^2}) \sin(\theta + \beta) \qquad (5.61)$$

$$V_r = V_{fr} - C(\ln R - 0.5 (1 - \frac{1}{R^2})^2) \sin(\theta + \beta) \qquad (5.62)$$

$$V_\theta = V_{f\theta} - C(\ln R + 0.5 (1 - \frac{1}{R^2})^2) \cos(\theta + \beta) \qquad (5.63)$$

Where V_{fr} and $V_{f\theta}$ are the radial and azimuthal components of the fluid displaced due the motion of particulates. The velocity of the displaced fluid, and consequently its radial and azimuthal component is evaluated by :

$$V = \frac{1}{(1 - \phi)} \sum_{i=1}^{n} V_{pi} \psi_i \qquad (5.64)$$

$$V_{pi} = \left(\frac{dR}{d\tau}\right) \bar{r} + R \left(\frac{d\theta}{d\tau}\right) \bar{\theta} \qquad (5.65)$$

$\bar{r}$ and $\bar{\theta}$ are unit vectors in the radial and azimuthal directions, respectively. Equations (5.64) and (5.65) comprise a set of 'I' simultaneous pairs of differential equations required to determine the trajetories of particles in a polydisperse system.

Smaller, lighter, and less magnetizable particles are likely to be affected most by the rest of the distribution and the displaced fluid. If V is large enough as compared to other velocity terms in the equations of motion of such particles they may be slowed down considerably and their direction of motion even be reversed. It follows that the behaviour of particles in polydisperse mixtures depends on the characteristics of the particle size, density, and susceptibility distributions. Sedimention tests carried out with polydisperse mixtures $1.0 < s < 600$ microns (at more than 1.0 % fractional volume), showed that particles less than 61 microns in diameter are not affected by the presence of other particles. Hence, its application to the test dust which has all its particles less than 2 microns would be inadequate. This point was further supported by trajectory calculations using both models. The results obtained portrayed no significant difference between the two models over the relevant particle range under consideration.

CHAPTER SIX

NUMERICAL SOLUTION OF THE GOVERNING EQUATIONS

6.1 Choice of Theoretical Model

There are two models presented in Chapter Five for the determination of critical capture radius. These are the monodisperse and polydisperse models. The choice for this particular application is the monodisperse system. It was chosen because of the low concentration of the particles in the experimental investigation. This means that the influence of the particles on each other is minimal and therefore can be neglected. The calculation of the trajectories of several particles simultaneously would give almost the same result for the same number of particles calculated individually with the monodisperse system. Therefore, all the critical capture radii and other particles' trajectories shown here were performed with the monodisperse system.

6.2 Particle Initial Conditions

The solution of the equations developed above requires some initial conditions. These comprise previous history of the particle in terms of its original position with respect to the wire, its velocity in relation to the fluid , and the influence of the magnetic force on the particle far from the wire.

These parameters have strong influence on the particle trajectory. There are two ways by which the particle's initial position on the Y-axis (Figure 5.2) can be determined. These are

starting the particle from infinity or assuming the particle to be located far upstream, that the effect of magnetic force is negligible. The motion of a particle approaching from infinity towards the collector, takes the following form:

$$X_o\, e_x + \infty\, e_y \tag{6.1}$$

where e_x and e_y are unit vectors in X- and Y- directions respectively.

It is assumed that at this distance from the collector the magnetic effects are neligible. Therefore, there is a finite value of Y, say Y^*, such that the particle will pass through

$$X_o\, e_x + Y^*\, e_y \tag{6.2}$$

with a known terminal velocity. This value of Y^* would be established later in the Chapter.

Terminal velocity is the steady velocity the particle attains when it is acted upon by the gravitational and viscous forces before coming under the influence of the magnetic field and when it is in an unperturbed region of the flow field. It is given by:

$$U_t = -(1 + KG)\, e_y \tag{6.3}$$

This is obtained by setting the acceleration and magnetic terms in the equations of motion (5.45) and (5.46) equal to zero, thus yielding:

$$\frac{1}{K}\left[(1 - \frac{1}{R^2})\cos\theta + \frac{dR}{d\tau}\right] - G\cos\theta = 0 \tag{6.4}$$

$$\frac{1}{K}\left[\left(1+\frac{1}{R^2}\right)\sin\theta+\frac{dR}{d\theta}\right]+G\sin\theta=0 \qquad (6.5)$$

It is observed that the term $\frac{1}{R^2}<<1$, outside the perturbation of the streamlines caused by the wire. The terminal velocity interms of the dimensionless quantities is given by :

$$\frac{dR}{d\tau}=(1-KG)\cos\theta=U_t \qquad (6.6)$$

and

$$\frac{dR}{d\tau}=\frac{1}{R}\left[(1+KG)\sin\theta\right]=U_r \qquad (6.7)$$

for tangential and radial components of velocity.

In principle, an alternative approach to starting the particle at infinity, is to arbitrarily choose Y, and then check to ascertain how much the presence of the magnetic parameter has influenced the particle trajectory. This is achieved by matching the particle's instanteneous X-coordinate (X_t) with the original X-coordinate (X_o) ; that is $X \simeq X_o$. For any set of applied values if the magnitude of ($X_o - X$) is large, then Y is incremented. All the trajectory calculations performed in this study assumed the particles to be initially located at a fixed position of some wire radii away in the Y-axis. The initial X-axis location was rather variable and depended entirely on the choice of particle to be monitored. The real location of the particle was determined using Pythagoras theorem with available X_i and Y_i as below.

$$R_i = (X_i^2 + Y_i^2)^{1/2} \tag{6.8}$$

The angle of orientation is obtained by finding the inverse of the tangent formed by the two coordinates. Thus:

$$\theta_i = \tan^{-1}\left[\frac{Y_i}{X_i}\right] \tag{6.9}$$

The initial tangential and angular acceleration are determined by solving an approximated version of the governing equations. The resulting equations are given below.

$$\Gamma_i = \frac{X_i}{R_i}(KG - 1) \tag{6.10}$$

$$\Omega_i = \frac{Y_i}{R_i^2}(1 - KG) \tag{6.11}$$

The final specifications needed for the determination of a unique trajectory are the initial coordinates (X_i, Y_i) and the four dimensionless parameters, W, K, G, and A.

6.3 Integration Of Governing Equations

The behaviour of many physical processes, particularly those in systems undergoing time-dependent changes can be defined by ordinary differential equations as shown in the model developed in Chapter five. Some of these equations can be solved by well known analytical techniques; but a greater number of them are too complex to be similarly solved, hence their solutions are usually generated numerically.

Most common numerical algorithms for solving first order differential equations are based on either indirect use of Taylor's expansion of the solution function, or the use of open or closed integration formulae. These various procedures can be classified roughly into two groups, the so-called one-step and the multi-step methods [64]. One-step method permits the calculation of the next discrete step given the information at the previous step only, while the multi-step requires in addition, several previous values usually outside the integration interval under consideration. The main disadvantage of this method is that subsequent values which are not known are usually required to start , hence, another self-starting method is usually initially applied. Multi-step methods however, require considerably less computation compared with the one-step methods to produce results of comparable accuracy.

6.4 Solution Algorithm

The coupled non-linear differential equations governing the behaviour of particles' trajectories in a uniform magnetic field have been solved by different numerical techniques. For example, Cummings et al [62] used Runge-Kutta (single-step) method Lawson [55] used Adam-Moulton predictor and Hamming corrector methods.

For this analysis, the forth-order Adam-Moulton and Modified Euler methods were applied. These comprised selected open and closed formulae with comparable order for local truncation errors. The open formula, the predictor, was used to estimate a particular step based on information from the previous

step, while the closed formula, the corrector, was used to obtain a better approximation. The corrector can be iterated but it has been known to have very little effect in the final solution.

A self starting modified Euler method was used to predict and correct the initial four values of the solution. The two Euler equations used are given in Appendix A.

Having obtained the initial first four values of the dependent variables at four given points, the numerical solution progressed by discrete prediction of approximate particle positions over the required range with the Adam-Moulten predictor and corrector; also given in Appendix A.

A fortran program was developed using the two solution methods to integrate the governing equations. The program is structured into several parts, each performing a complete task. The first part is concerned with reading in data, initial X and Y coordinates and the integration step. It must be observed that there is no mechanism for the variation of the step-size during calculation and no built in check for error monitoring. This is because the time step was chosen small enough to satisfy convergence criteria and ensure realistic solution in just one iteration of the corrector equations, while still large enough to minimize round off errors. Although, the mechanism for implimenting changes in step-size is not straight forward. The difficulty being that when the step size is changed, the necessary starting values for the predictor and corrector may not usually be available. Also to be selected at this stage is the fluid flow field, which are described by potential and creeping flow anologies. The initial tangential and radial acceleration

are also calculated before the analysis progressed.

The next step involves the actual calculation of the dependent variables. It entailed calculating the two functions, predicting the dependent variables with the values of these functions, and using the variables to calculate the values of the functions at the next step. When the particle has reached the surface of the fiber (checked with the diameter of the wire), a criteria that checks capture is used to confirm collection or escape. This was continued until the critical capture radius was determined for each of the operating parameters. In certain cases, calculations were still continued after X_c has been determined to obtain a family of trajectories.

The final part of the program plots the trajectories calculated from the above model. The structure of the program outlined in the form of a flow chart is given in Appendix B while Appendix C gives a listing of the program.

6.5 The (Critical) Radius of Trajectory

The physical system considered in Chapter five is characterized by a greater number of quantities than W, K, G, and A. Others include M_s, H_o and X . If two sets of these physical quantities have different values, but give the same numerical product, then their trajectories and capture distances found from the equations of motion will be the same provided the initial conditions are the same. Thus, the full mathematical content of the equation of motion can be obtained by varing the values of W, K, and A (G=0.0). As a result, the experimental values of these parameters were applied to obtain the equivalent critical capture

radii for the size range under study. Other authors in the past estimated these critical capture radii by extrapolating the curves of Log W versus Log K [55].

The first exercise carried out for the determination of X_c was to establish the accuracy of the numerical technique used. For this, the set of W, K, and A values used by Lawson [55] was selected and applied (W = 250.00, K = 0.10, A = 0.88 and G = 0.00). A family of such calculated trajectories is shown in Figure 6.1. This compared favourably with Lawson's family of trajectories (Figure 6.2), giving confidence in the numerical method used. The plot shows the trajectories of particles moving in a gas stream flowing downwards with a variation of the trajectories as related to the approach distance Y_o from the X-axis. The approach trajectories are set in multiples of the wire diameter of 1.0-1.8. For constant W, K, and A (with G = 0.0) values, there exists a trajectory, X_c , that separates those trajectories which intersect from those that miss. It was found to be about 4.3 particle radii away from the stagnation line (Y-axis) for this particular group of physical parameters. Thus, in general, the critical cross-section depends on W, K, and A, with G=0; and the model used to describe the flow field is enough to determine X_c .

Figure 6.1 also shows the negligible effect of magnetic field at a relatively far distance upstream. It could be seen that a particle originating from say $3e_x + 100e_y$ passed through $2.99e_x + 8e_y$ and finally arrived at $0.00e_x + 1.0e_y$. Such small deviation over a length of 92 radii provided convincing support for believing that $Y^* = 100$ was large enough for neglecting the

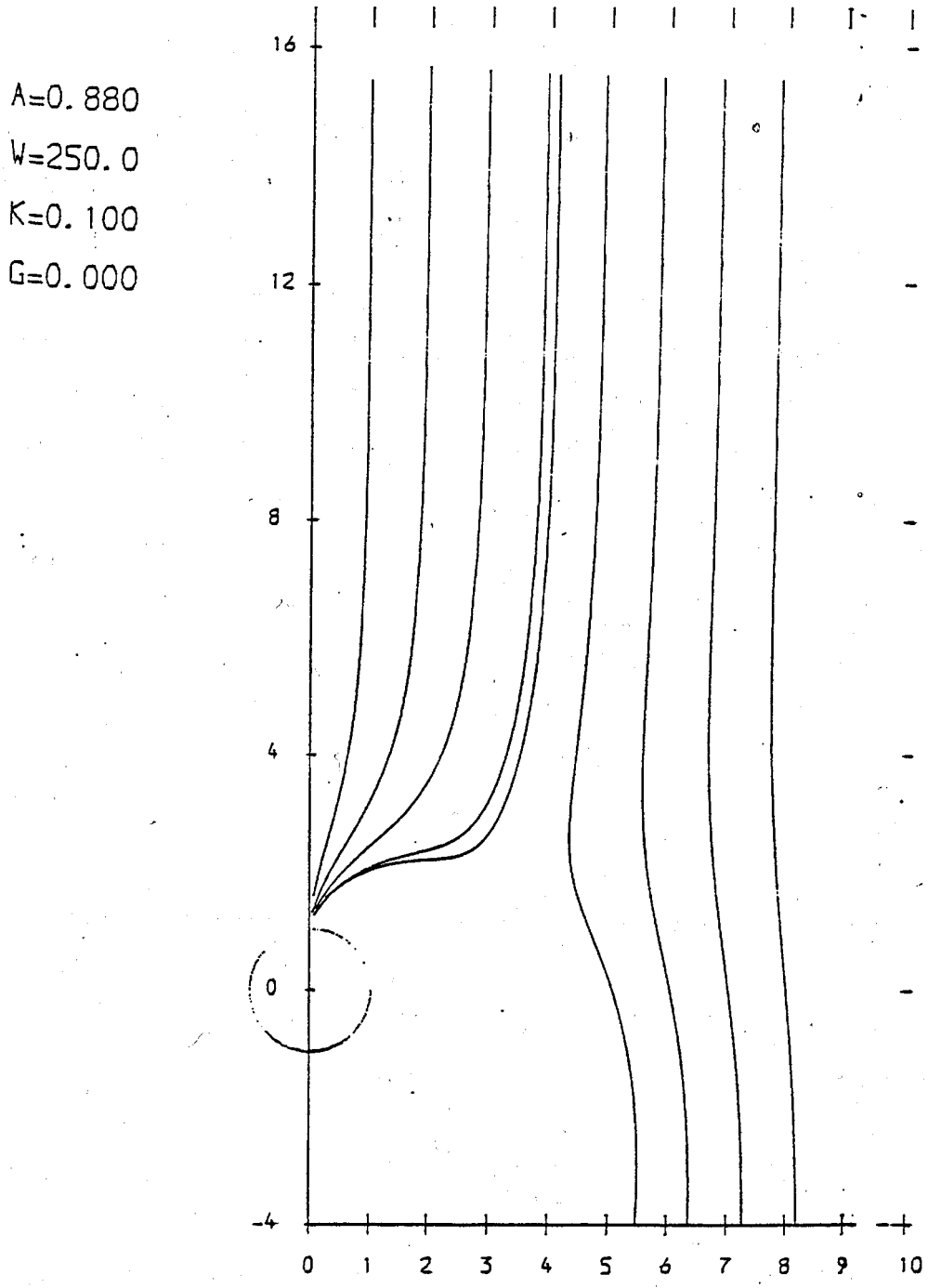

FIG. 6.1: FAMILY OF TRAJECTORIES ASSUMING A POTENTIAL FLOW MODEL (PFM) FOR VELOCITY FLOW FIELD

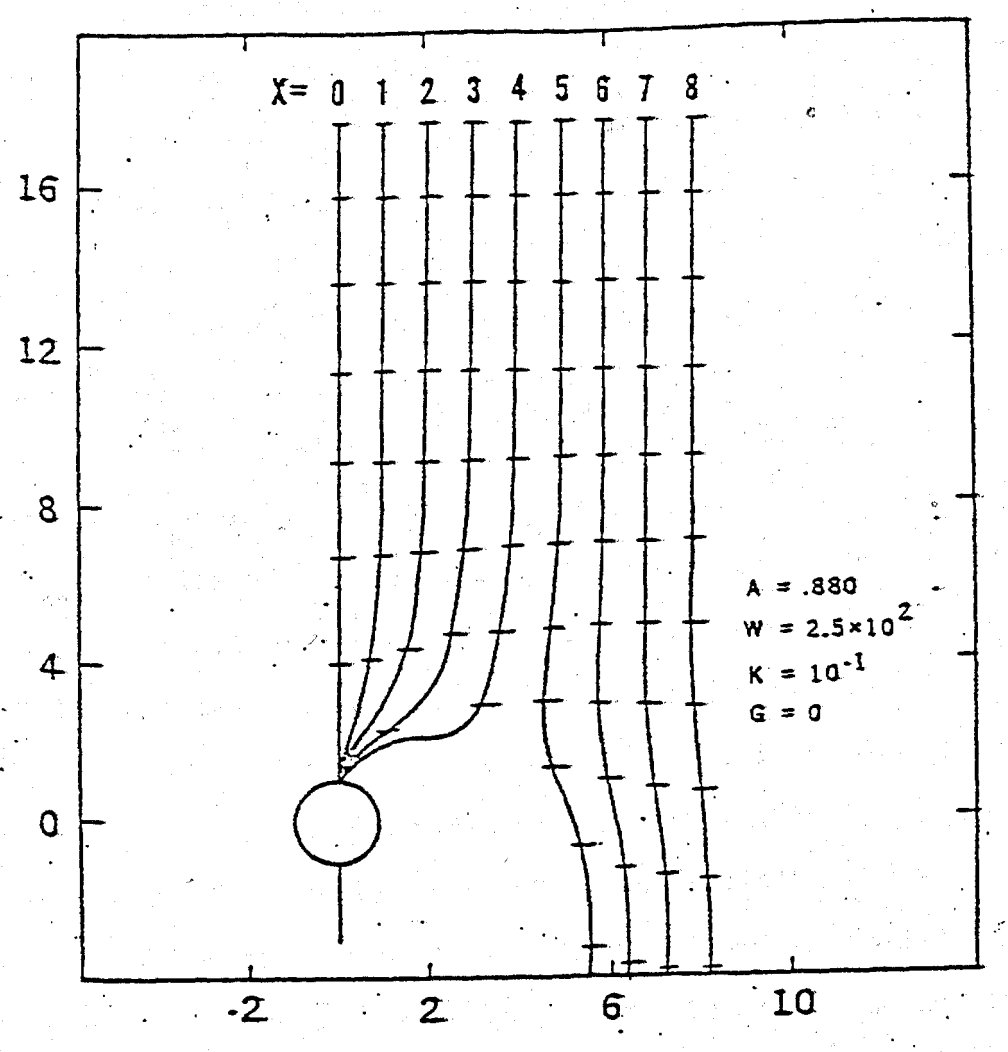

FIG. 6.2: A FAMILY OF TRAJECTORIES FROM LAWSONS INVESTIGATION

magnetic field. The field itself did not change appreciably from main stream flow until it was within R=5.

As already indicated, the flow field can be described by either a Potential Flow Model (PFM), or Creeping Flow Model (CFM). PFM has been adopted for this investigation. However, for completeness, calculations were also performed with CFM and both trajectories compared.

The use of PFM gave the results in Figure 6.3. As can be seen the particles follow trajectories which are almost parallel to the stagnation line (Y-axis) until about 5 collection raddi from the wire. At this point, the effect of magnetic force becomes significant. The intensity of this attractive force becomes progressively stronger until about 2 collector radii away when the particle was snatched away from its original direction to effect capture or pushed violently away. Figure 6.4 shows the result of the same system but with CFM applied. The superposition of both sets of trajectories (Figure 6.5) exhibits three notable differences. First, the particle at X = 4.5 which excaped capture when PFM was used was captured with CFM. This might be due to the initial no slip condition associated with the formulation of CFM which assumes a mass of nearly stagnant fluid accumulating in front of the collector. This makes the fluid to 'feel' the wire earlier than the case for PFM. Secondly, the slight displacement of CFM trajectories from previous directions indicate earlier effect of magnetic force. Finally, the presence of cusps associated with PFM capture as a result of inertia was less pronouced. Table 6.1 below contains calculated values of critical capture radii (using PFM) for the particle range of 0.24-1.80.

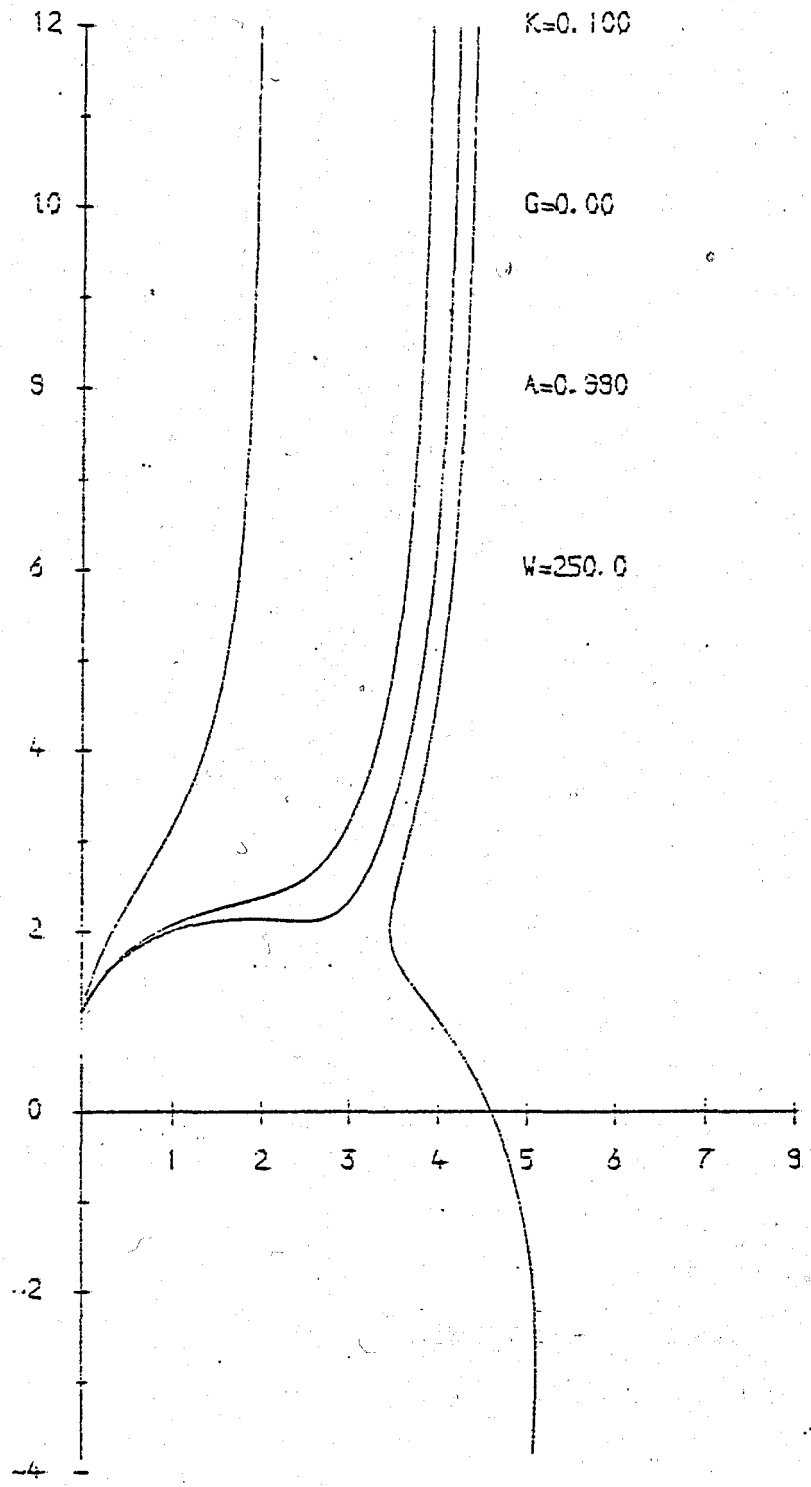

FIG. 6.3: FAMILY OF TRAJECTORIES ASSUMING POTENTIAL FLOW MODEL (PFM) FOR VELOCITY FLOW FIELD

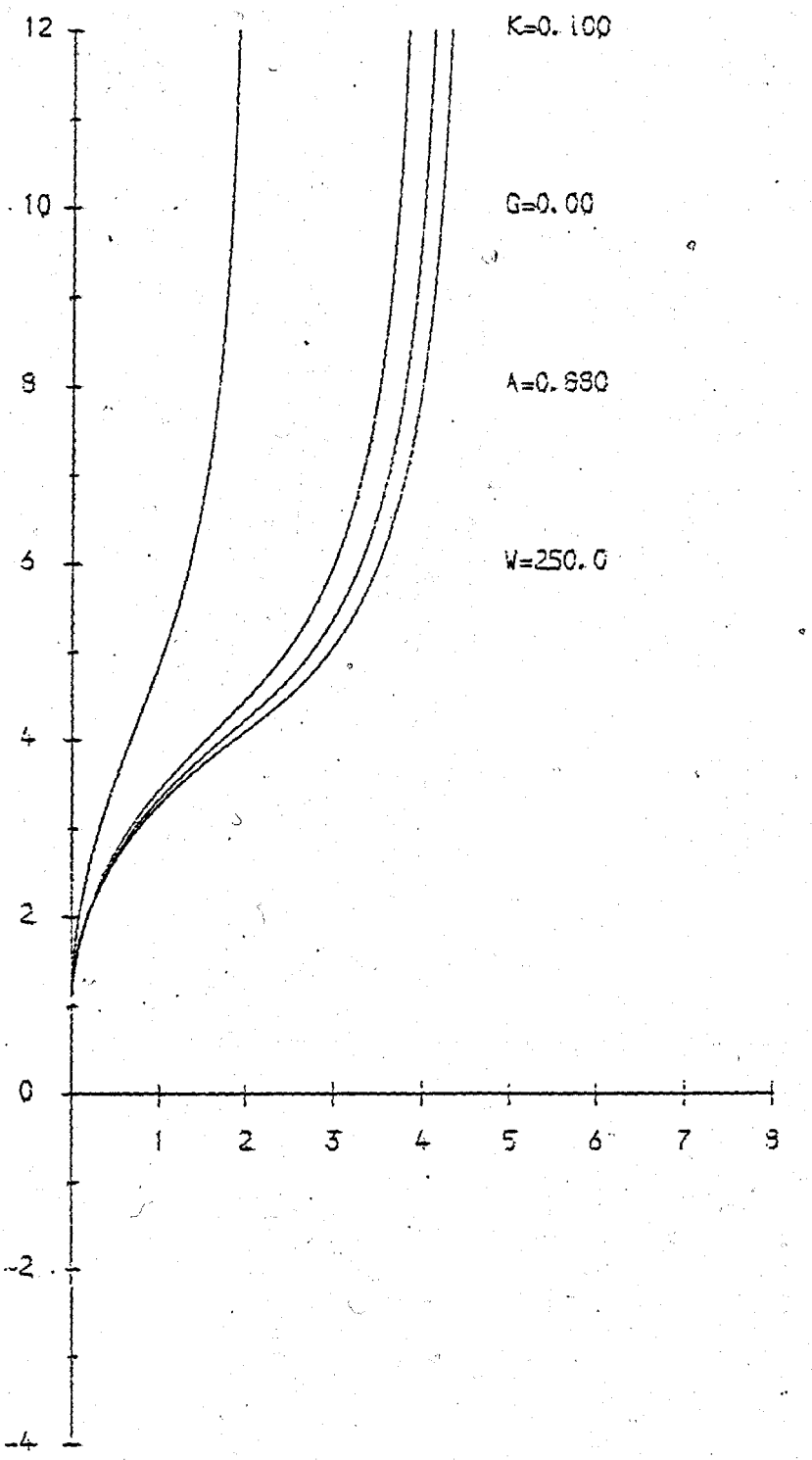

FIG. 6.4: FAMILY OF TRAJECTORIES ASSUMING CREEPING FLOW MODEL (CFM) FOR VELOCITY FLOW FIELD

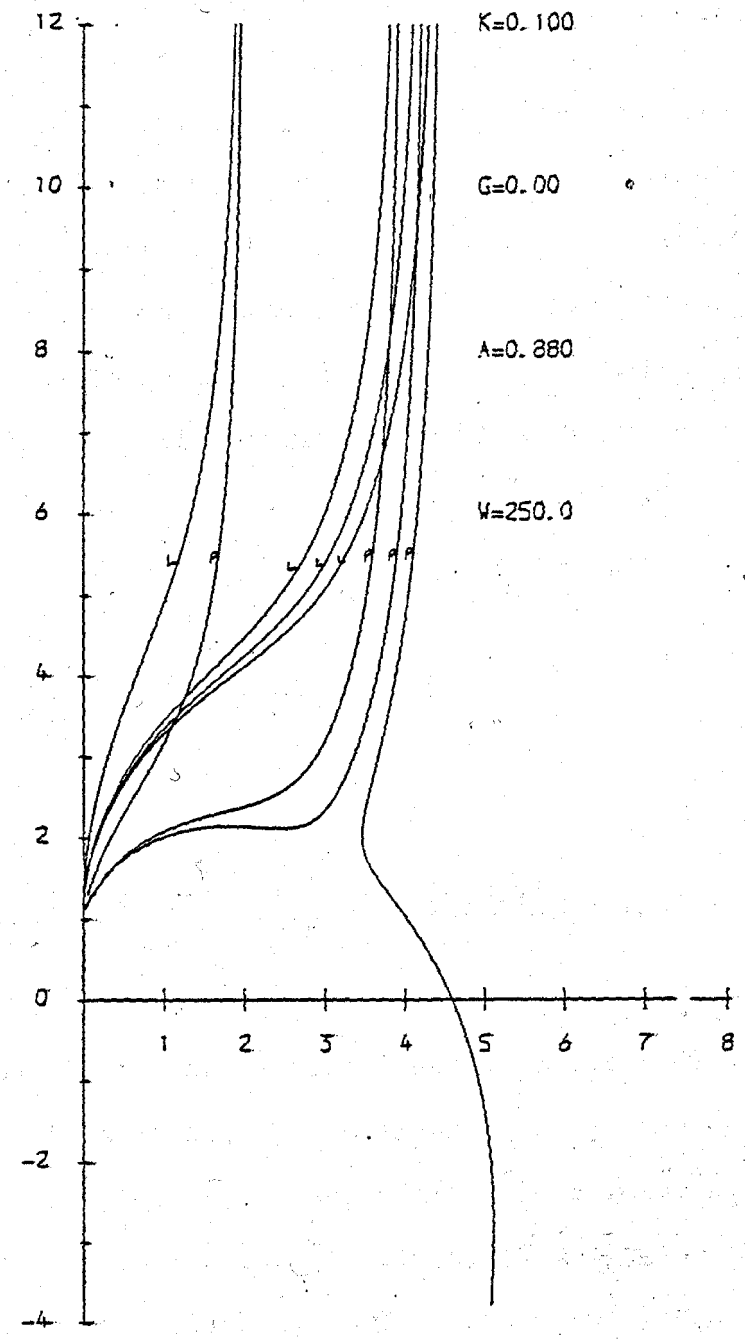

FIG. 6.5: COMBINATION OF PFM AND CFM (FIGS. 6.3 AND 6.4)

This is the range covered by the particle spectrometer selected for the entire experimental tests. The calculations were carried out only for magnetic field strength of 0.8 Tesla. The dimensionless parameters A, W, and K were calculated with the expressions derived in Chapter Five. M_s for the calculation of A was read off the magnetization curve of steel wool material [41]. Because K is a function of the particle diameter, it changes from one particle size to another and therefore is included in Table 6.1 for all particle sizes covered. A typical set of calculation for 0.8 Tesla is given below:

$$A = \frac{4\pi \times 10^{-7} \times 1.22 \times 10^{6}}{2.0 \times 0.8} = 0.96$$

And

$$W = \frac{4\pi \times 10^{-7} \times 2.41 \times 10^{-4} \times 636619.77^{2}}{2500.0 \times 6.6} = 1.57 \times 10^{-3}$$

6.6 Prediction of Collection Efficiency of a Total Filter

In this section, the model predicting the performance of magnetic stainless steel wool filter is developed. The model is akin to that of collection efficiency of a single fiber (η_s) ; which is defined theoretically as the ratio of cross-sectional area of the fluid stream from which particles of a given size are collected to the projected area of the fiber in the direction of the flow. Mathematically, this is equivalent to

$$\eta_s = \frac{N_c}{2\, s\, N_i\, V} \qquad (6.12)$$

where N_c = number of particles of a given size that are collected per unit length of fiber per unit time.

N_i = Number of particles per unit volume of a given size at upstream section.

The extension of the single fiber model to that of a total filter assumes that:

(i) There are no particle-to-particle or fiber-to-fiber interferences.

(ii) There is no magnetic interference in the filter unit.

Mass or number balance for particles of a single size in a total filter can be constructed in the following form:

Particle Flux In = Particle Flux Out + Particles Collected

Or mathematically:

N = (N + dN) + Particles collected per unit volume of the filter

where N = Number of particles per unit volume.

Consider a thin section of the filter taken perpendicular to the magnetic field and the fluid flow as shown in Figure 6.6. If the packing fraction of the stainless steel

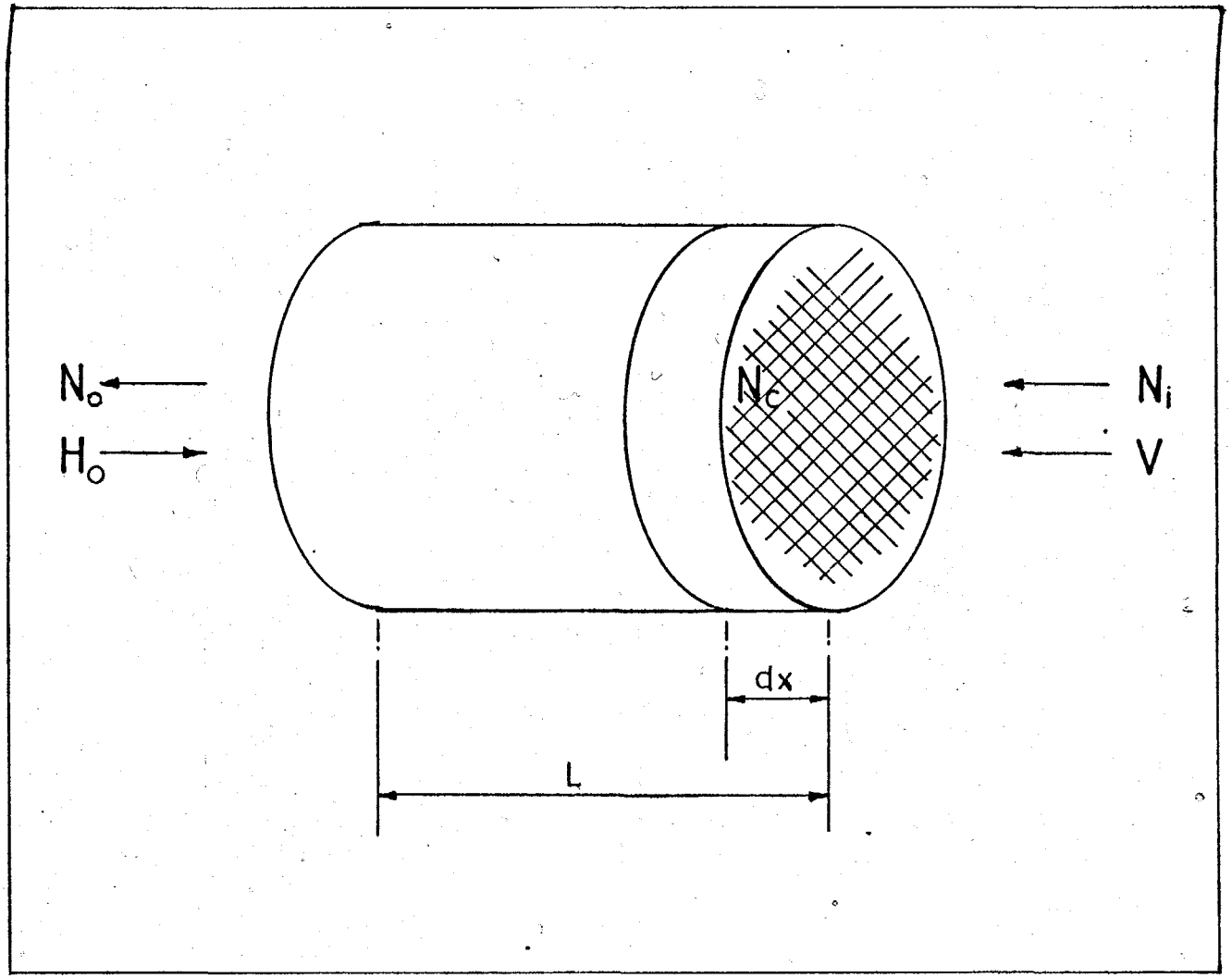

FIG. 6.6: A MATRIX SHOWING A SECTION OF THICKNESS DX WITH N PARTICLES/ UNIT VOLUME INCIDENT ON IT WITH A FLUID VELOCITY V

wire in the filter is F, then the length of the wire in a thickness of the filter is given by :

$$l_t = F \frac{dx}{\pi a^2} \tag{6.13}$$

For a capture cross-sectional area of $2 X_c a$ per unit length of wire and two thirds capturing surface, the effective area available to the fluid is given by :

$$A_e = \frac{2}{3} 2 s X_c \frac{F dx}{\pi s^2} = 4 F X_c \frac{dx}{3 \pi s} \tag{6.14}$$

Therefore the particles captured per unit volume is given by:

$$N_c = \frac{4 X_c F dx N}{3 \pi s} \tag{6.15}$$

Substituting in the mathematical representation above:

$$N = (N + dN) + \frac{4 X_c F dx N}{3 \pi s} \tag{6.16}$$

With some rearrangement equation (6.16) becomes:

$$dN = \frac{4 X_c F dx N}{3 \pi s} \tag{6.17}$$

Multiplication of equation (6.17) by the flow velocity gives:

$$V dN = \frac{4 X_c F dx N}{3 \pi s} V_a \tag{6.18}$$

where V is the fluid velocity and V_a the velocity of the fluid in the matrix.

V_a is slightly greater than the flow velocity because of the reduced flow area and it can be approximated by :

$$V_a = \frac{V}{(1 - F)} \tag{6.19}$$

Therefore equation (6.17) becomes:

$$dN = N \alpha \, dx \tag{6.20}$$

where $\alpha = \frac{4 X_c F}{3 \pi s}$

If the filter in Figure 6.1 is divided up into elements, the number of particles extracted in the first layer of thickness dx is dN_1 . Given mathematically as:

$$dN_1 = N \alpha \, dx \tag{6.21}$$

The number of particles extracted in the second layer is given by the probability of capture in the second layer multiplied by the probability of passage through the first layer. That is :

$$dN_2 = \alpha \, dx - \alpha^2 (dx)^2$$

$$= \alpha \, dx (1 - \alpha \, dx) \tag{6.22}$$

The number of particles captured in the n'th layer is given by :

$$dN_n = N \alpha \, dx (1 - \alpha \, dx)^{n-1}$$

$$= N \alpha \, dx \left[1 - (n-1) \alpha \, dx \right.$$

$$\left. + (n-1)(n-2) \alpha^2 (dx)^2 - \ldots \right] \tag{6.23}$$

Introducing a coordinate such that $m = \frac{X}{dx}$. Equation (6.23)

becomes :

$$dN_n = N \alpha \, dx \exp(-X\alpha) + 0 (dx)^2 \qquad (6.24)$$

If the filter is of length L, then the total particle per unit length extracted N_e is obtained, by integrating equation (6.24). This gives the concentration of particles extracted as:

$$N_c = \int_0^L N \alpha \exp(-\alpha X) \, dx$$

$$= N \alpha \left[\frac{\exp(-\alpha X)}{-\alpha}\right] = -N\left[\exp(-\alpha L) - \exp(0)\right] \qquad (6.25)$$

Therefore

$$N_c = N \left[1 - \exp(-\alpha L)\right] \qquad (6.26)$$

Equation (6.26) represents particles captured ; hence

$$N_i - N_o = N_i \left[1 - \exp(-\alpha L)\right] \qquad (6.27)$$

Dividing through with N_i gives the particle penetration as:

$$P = \frac{N_o}{N_i} = \exp(-\alpha L) \qquad (6.28)$$

Or

$$\frac{N_i - N_o}{N_i} = 1 - \exp(-\alpha L) \qquad (6.29)$$

Equation (6.29) can be re-written to give:

$$E = 1 - \exp\left(-\frac{L\ 4\ X_c\ F}{3\pi\ s\ (1-F)}\right) \qquad (6.30)$$

Where E is the collection efficiency of the filter. Equation (6.30) expresses the theoretical collection efficiency on a number bases. An Effectiveness Factor E_f can be incorporated in equation (6.30). The value of E_f is affected by the assumed mean wire sizes, by the validity of the assumed geometric orientation of the wires, and the assumption of no interference among neighbouring wires. In most cases, all these factors are different with respect to aerodynamic and magnetic phenomena, resulting in different values for E_f to correctly mimic the experimental results. This will be explored later. So in a more general form, equation (6.30) can be re-written as:

$$E = 1 - \exp\left[-L\ \frac{4\ X_c}{3\pi\ s}\ \frac{F}{(1-F)}\ E_f\right] \qquad (6.31)$$

Table 6.1 List of Theoretical Capture Radii

Channel Number	Size Range	Average Size	Stokes Number	Critical Radius(X_c^*)
1	0.24-0.29	0.265	0.120	0.40
2	0.29-0.34	0.315	0.170	0.42
3	0.34-0.40	0.370	0.234	0.51
4	0.40-0.50	0.450	0.346	0.52
5	0.50-0.63	0.565	0.546	0.54
6	0.63-0.81	0.720	0.886	0.49
7	0.81-1.05	0.930	1.479	0.43
8	1.05-1.26	1.155	2.280	0.40
9	1.26-1.40	1.330	3.024	0.38
10	1.40-1.50	1.450	3.594	0.35
11	1.50-1.56	1.530	4.002	0.33
12	1.56-1.62	1.590	4.322	0.31
13	1.62-1.68	1.650	4.654	0.28
14	1.68-1.74	1.710	4.998	0.29
15	1.74-1.80	1.770	5.355	0.30

X_c^* : Values calculated with A = 0.94, W = 1.57×10^{-3} and G = 0.0.

CHAPTER SEVEN

EXPERIMENTAL SET UP

The experimental rig comprises a centrifugal fan (F3642, Bryan Donkin Co Ltd., Chesterfield), a solenoid magnet, a dust generator, and a dust classification train (Figure 7.1). A fabric bag was also attached at the outlet of the fan to clean the dirty air before it is discharged into the atmosphere.

Tappings were made at both sides of the solenoid magnet for flow measurements. Sampling points were located both upstream and downstream of the solenoid and at the entrance to the duct were absolute and pre filters which removed any particles from the incoming air. The test rig is discussed in detail below under the following sub-headings: Ducting, Dust generator, Particle sampling train, and Compensated solenoid magnet.

7.1 Ducting

Copper duct of 98.4 mm (3.872 ins.) internal diameter and a wall thickness of 1.63 mm (0.064 ins.) was used in the construction of the main experimental rig. Copper was used because of its high electrical conductivity which helped to reduce the build up of electrical charges on the walls of the duct, and because of its resistance to corrosion. This property eliminated the formation of oxides that might distort the experimental results.

The total length of the duct excluding the entrance that housed the pre-filter (made of synthetic fibrous medium) and

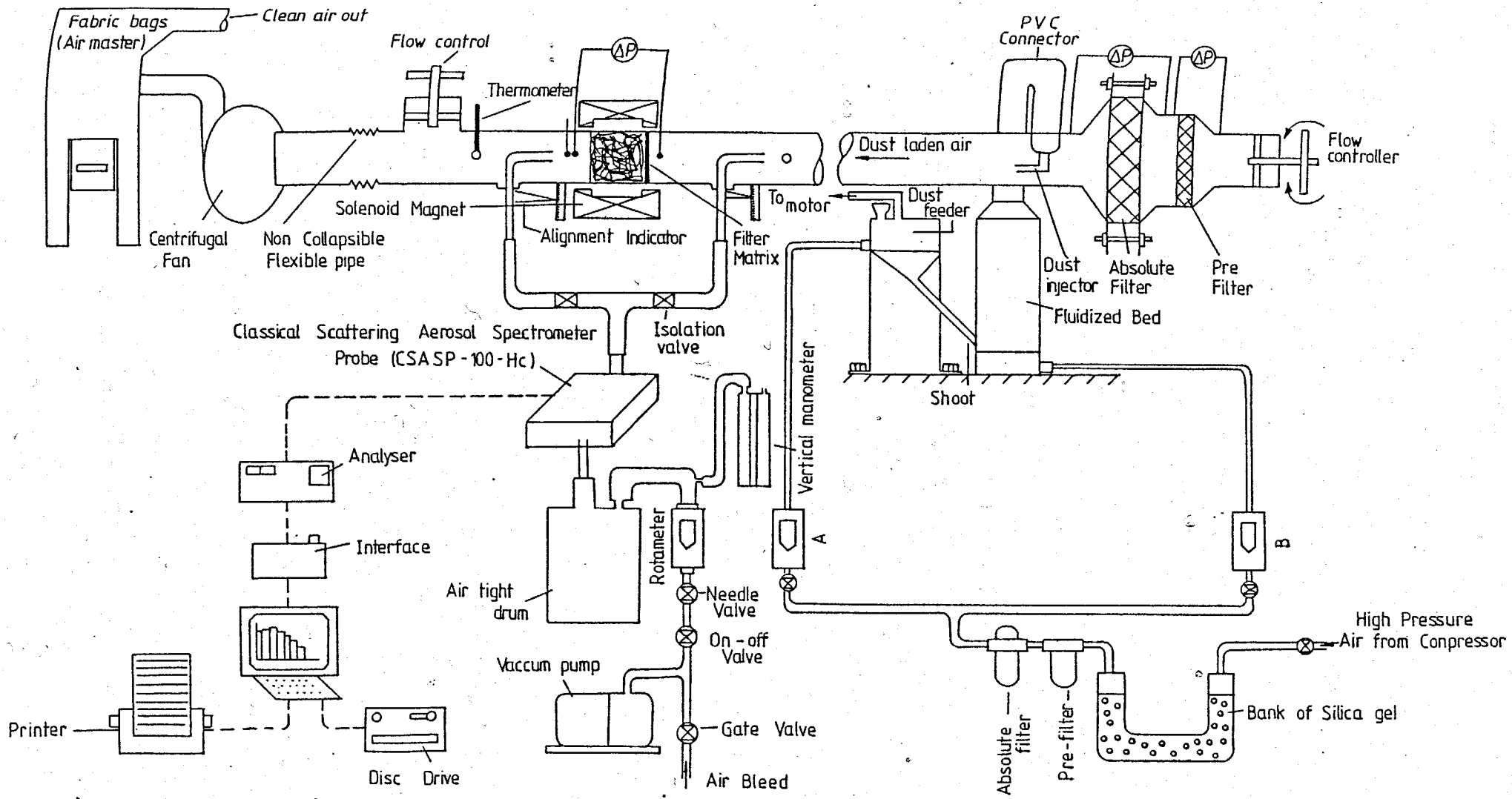

FIG. 7.1: SCHEMATIC DIAGRAM OF HCMF EXPERIMENTAL RIG

absolute filter was 8490mm. The long length of the duct up to the solenoid magnet zone was necessary to ensure a fully developed flow, and hence an even distribution of particle profile. For turbulent flows, minimum entrance length of about 10 pipe diameters is usually required. Figure 7.2 (a), shows the experimental velocity traverse taken at the upstream measuring zone, while those taken at the downstream of the filter zone is presented in figure 7.2 (b). As expected, the two profiles are similar; but this siezed to be the case when a filter was placed in the pipe as shown in Chapter Four. The presence of the filter had the effect of flattening the flow profiles. These changes in the flow profiles seem to be related to the packing density of the filter in that the denser the filter, the flatter the profile (Figure 4.9). This effect was previously used in monitoring the uniformity of wire packing in the filter matrix. Matrices with uneven wire packing showed a highly oscillatory velocity profile, thus signifying large flow channels in the matrix. Two U-tube manometers were used to monitored the change in the filter resistance. To achieve flexibility, a second flow control was introduced in the rig. For the range of the flow velocity required for the filtration tests, the number one control remained almost closed while the second remained completely open. Continuous adjustment of the first valve was however necessary throughout the experiment. The upstream measurements were made at between 57.3 and 65.65 pipe diameters from the entrance of the duct. These comprised four static pressure tappings and two ports at which the total horizontal and vertical pressures were measured. The static and total pressure tubes were

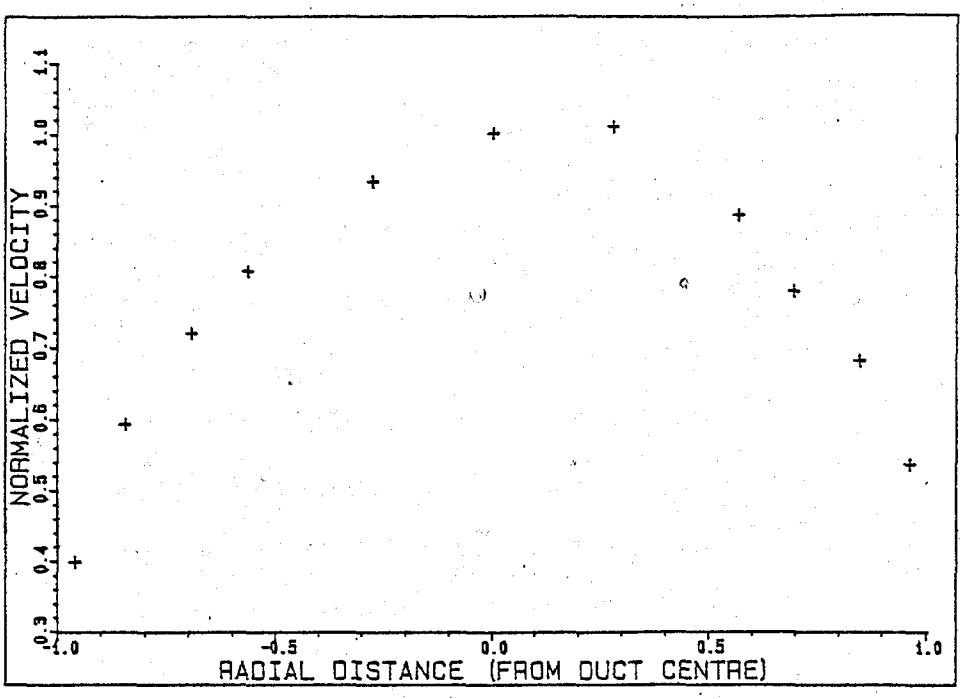

FIG. 7.2(A): UPSTREAM VELOCITY PROFILE OF MAIN DUCT

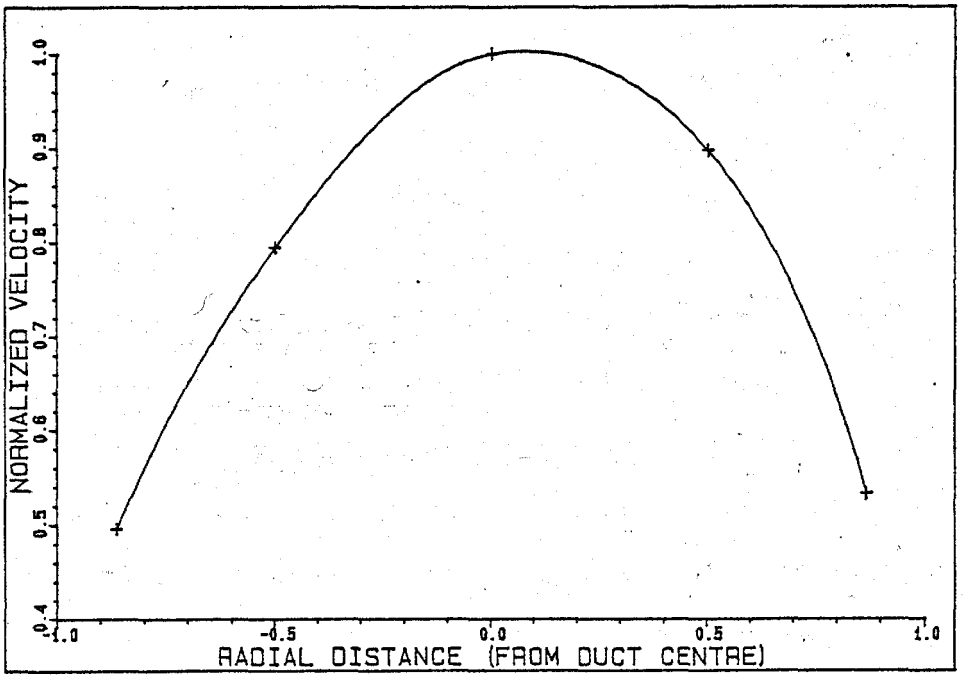

FIG. 7.2(B): DOWNSTREAM VELOCITY PROFILE OF MAIN DUCT

connected by a manometer which measured the difference in pressure. Four access holes each of 20mm diameter were drilled in this region to enable samples to be taken at different positions but at the same plane. These samples were passed through to the spectrometer for analysis. Beyond this region was the filter and solenoid zone which is discussed later. Downstream measurements of the parameters described above were carried out at between 70.33 and 87.65 pipe diameters. A thermometer was also inserted into the duct to measure the air temperature. A non-flexible collapsible tube at the end of the duct joined the copper tube to the inlet section of the fan. It also increased the lateral movement of the duct necessary for filter replacement. At both ends of the filter unit, were wall tappings to measure the pressure drop across the filter.

7.2 Dust Generator

The filtration tests required the introduction of completely de-agglomerated dust into the main test duct. It also required that the size distribution and concentration of the particles supplied be constant with time. There are a number of ways available for generating dust particles; these include blowing dust from a tube with a blast of air, feeding dust from the bottom of a hopper by a screw or by a vibrating hopper with a sieve at the bottom. But in this application, the dust was generated by a combination of shaking (Vibrating Feeder) and fluidizing (Fluidized Bed). In the process, a heavier and larger dust (in this case nickel) and the experimental dust (CuO) (PLATE 7.1) was allowed to mix before CuO was preferentially elutriated

and conveyed into the main duct. The vibrating feeder was incorporated because it was not possible to ensure that the fixed bed of the fine CuO was in quasi-brownian motion. Attempts to elutriate only the bulk dust resulted in the formation of air channels in the dust bed, which liberated agglomerated dusts. The use of fluidizing column helped by the rising gas bubbles in the fluidized bed. The gas bubbles carried upwards both the fine as well as the coarse particles through the fluidizing column. The mechanical impaction as well as the turbulent nature of the whole process (shearing of particles and violent eruption of bubbles) completely separated the particles from each other. The description of the vibrating feeder and the fluidizing bed is given below.

7.2.1 The Vibrating Feeder

The major parts of the dust vibrating feeder were a direct current motor (Fracmo, Shunt Winding), capable of producing 1/4 Horse Power and a copper receptacle. The motor had a variable speed control which enabled different torques to be placed on the drive shaft. The shaking action was controlled by either adjusting the motor speed or the position of the horizontal bracket needed to change the amplitude of the lateral movements.

The copper receptacle consists of an air tight chamber with an entraining air flow section, and a bottom chamber with a dust conveying tube to the fluidized bed (Figure 7.1). Inside the shaker were beds of steel balls separated by steel meshes. The steel balls prevented the dust from falling rapidly through the

shaker during operation. They also helped to provide a steady supply of dust when the shaker was saturated with CuO. About thirty percent of the flow of compressed air needed for elutriation was supplied to the fluidized bed through the feeder. The air was supplied to the feeder through 12 equally spaced nozzles of 0.75 mm diameter situated around the circumference of the top chamber. The air was first passed through a bed of silica gel before going through pre- and absolute- filters to remove any gel particles that may have been entrained. The rate of air flow was regulated from rotameter 'A' on the compressed air flow line. There were rubber mountings at the base of the receptacle to absorb flexible movements of the dust feeder.

7.2.2 The Fluidized Bed

The fluidized bed consists of a 100 mm diameter column of copper. The lower part of the column was made of plenum chamber separated by off-set metal clothes of nominal aperture 67.5 microns (G. Bopp & Co. Ltd., London). These prevented the nickel spheres from dropping into the base pot , and also acted as flow straighteners. Inside the column were nickel spheres of density 8910 kg/m^3 carefully sieved to give a fixed size range of 90-150 microns in diameter. During fluidization process, there was a constant mixing and agitation of both the nickel spheres and CuO particles. At the early part of the process, both dusts were entrained, but because of the larger difference in their sizes, the bigger sized nickel spheres fall back into the bed. The lighter CuO particles become conveyed into the main duct. The minimum fluidizing velocity or the maximum flow rate allowed

through the column for this effect is calculated below. Kunii and Leverspiel [65] gave the following equations for obtaining the minimum fluidizing velocity.

That:

$$\frac{\rho_f V_{mf} b}{\mu} = \left[33.7^2 + 0.0408 \frac{b^3 \rho_f (\rho_p - \rho_f) g}{\mu^2} \right]^{0.5} - 33.7 \qquad (7.1)$$

where V_{mf} = minimum fluidizing velocity

The terminal velocity of the particles also given by [65] are:

$$U_t = \frac{g\,(\rho_p - \rho_f) b^2}{18\,\mu} \quad \text{for } Re < 0.4 \qquad (7.2)$$

$$U_t = \left[\frac{4}{225} \frac{(\rho_p - \rho_f)^2\, g^2}{\rho_f\, \mu} \right]^{1/3} b \quad \text{for} \quad 0.4 < Re < 500 \qquad (7.3)$$

$$U_t = \left[\frac{3.1\,(\rho_p - \rho_f) b}{\rho_f} \right]^{1/2} \quad \text{for} \quad 500 < Re < 200{,}000 \qquad (7.4)$$

where U_t is the terminal velocity of the particle.

For a particle size of 150 microns in diameter, the minimum fluidizing velocity V_{mf} is obtained by applying equation (7.1). That is :

$$V_{mf} = \frac{18.12 \times 10^{-6}}{1.239 \times 150 \times 10^{-6}} \left[33.77^2 - K \right] = 0.065 \text{m/s}$$

where

$$K = \left[\frac{0.0408x(150x10^{-6})^3 x1.239x(8910-1.239)x9.81}{18.12x10^{-6^2}}\right]^{0.5}$$

$$= 45.413$$

Assuming a Reynolds number of between 0.4 and 500 (i.e $0.4 < Re < 500$), the terminal velocity of the smallest nickel sphere of 90 microns diameter is given by equation (7.3):

$$U_t = \left[\frac{4}{255}x\frac{(8910-1.239)^2x9.81^2}{1.239x18.12x10^{-6}}\right]^{1/3} x90x10^{-6}$$

$$= 1.085 m/s$$

Checking the Reynolds number assumption made above:

$$Re = \frac{1.239x1.82197x90x10^{-6}}{18.12x10^{-6}} = 11.2$$

Therefore the assumption made above was correct.

The minimum air flow rate required to fluidize the largest nickel spheres Q_c was given by the cross sectional area of the column multiplied by the minimum fluidizing velocity of the column. Hence,

$$Q_c = \frac{\pi}{4}x(100x10^{-3})^2 x0.065x10^3 = 30.63 \text{ L/min}$$

The terminal velocity of the maximum diameter of CuO dust (2 microns) is given by equation (7.2) with an assumption that the flow $Re < 0.4$.

Therefore:

$$U_t = \frac{9.81(2500-1.239)x(2x10^{-6})^2}{18x18.12x10^{-6}} = 3.006x10^{-4}m/s$$

This shows that the column velocity of 0.065 m/s needed for the largest nickel spheres should elutriate the CuO dust.

The size of nickel spheres that has the terminal velocity of 0.065 m/s is given by equation (7.3). It is calculated below as:

$$b = \frac{0.065}{\left[\frac{4}{255}x\frac{(8910-1.239)^2}{1.239x18.12x10^{-6}}\right]^{1/3}}$$

$$= 17.045x10^{-6}m \quad (17 \text{ microns})$$

17 microns represents the diameter of the nickel spheres that has 0.065 m/s as their terminal velocity. Since there are no spheres below 90 microns inside the column, the nickel spheres can never be elutriated. A sample of the filtrate collected on a filter paper (PLATE 7.2) showed no trace of nickel particles.

7.3 Particle Sampling Technique

This embraces the measurement of the physical parameters characteristic of, or particularly important as regards dust, dust distribution and dust collection. Different available method for particle size and concentration analysis for air-borne aerosol system fall into two general categories. In the first group, direct measurements are made on samples collected from original gas stream to determine their sizes, concentration, or in some applications for both; while in the second, stream of

particles are viewed directly without any prior collection.

7.3.1 Sampling In Gaseous Flows

Sampling in principle consists of taking a partial flow from a moving medium without disturbing the flow streamlines. The purpose of this being either to make the samples available at a more convenient location for optical analysis or to be collected on membrane filters for gravimetric analysis. The major errors that arise from this exercise are:

(i) Effects of anisokinetic sampling

(ii) Shape of the nozzle on the sampling tube

(iii) Deposition of the particles on the walls of the sampling tube

BS 893 [66] illustrates and explains the system of sampling in cylindrical ducts. Usually the total pressure of the flow is determined by pilot tube while the static pressure is determined from the tappings on the wall of the tube; thus, the velocity of the main gas flow can be calculated. The values for setting the partial flow velocity, that is the velocity in the probe can be obtained either from an orifice-plate measurement or a rotameter.

For the partial flow to provide representative sample, the gas velocity in the probe must meet certain requirements. A sample corresponds to the actual state in the main gas stream if the stream diameter σ_s shown dotted in Figure 7.3a and 7.3b. enters the probe. Extensive research by Noss [67], Dennis [68], Davis et al [69] and Ruping [70] postulates that this condition

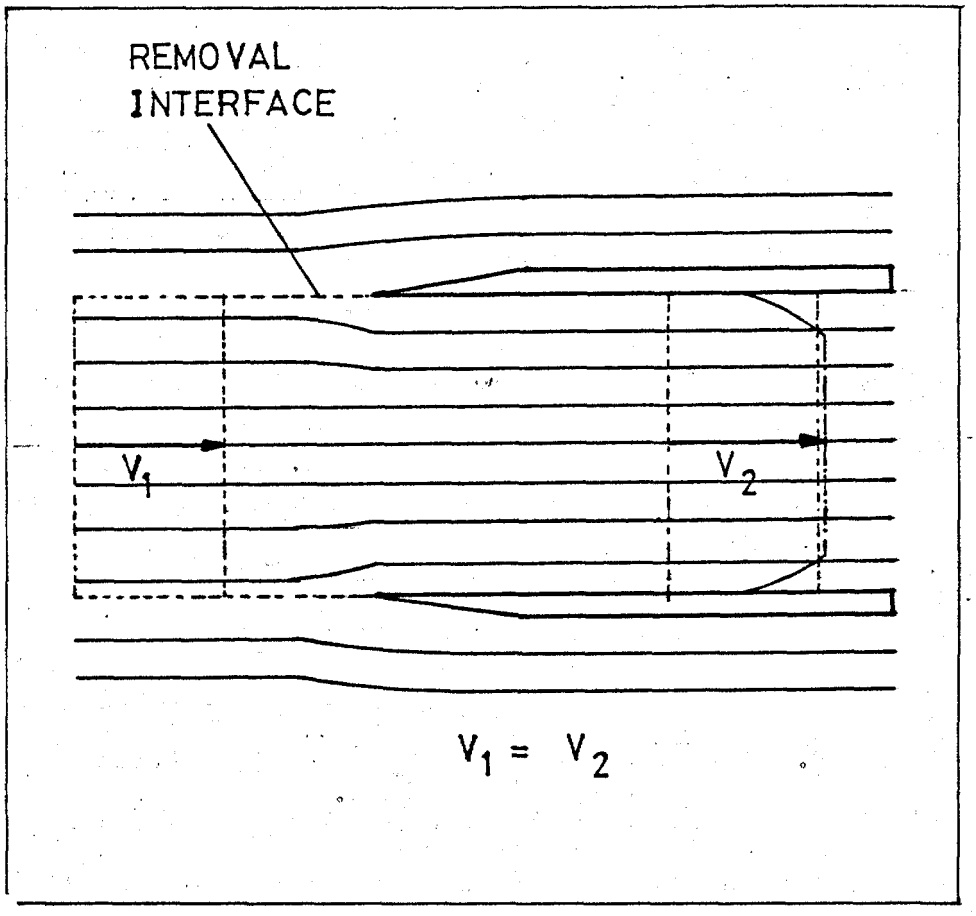

FIG. 7.3(A): ILLUSTRATION OF ISOKINETIC SAMPLING

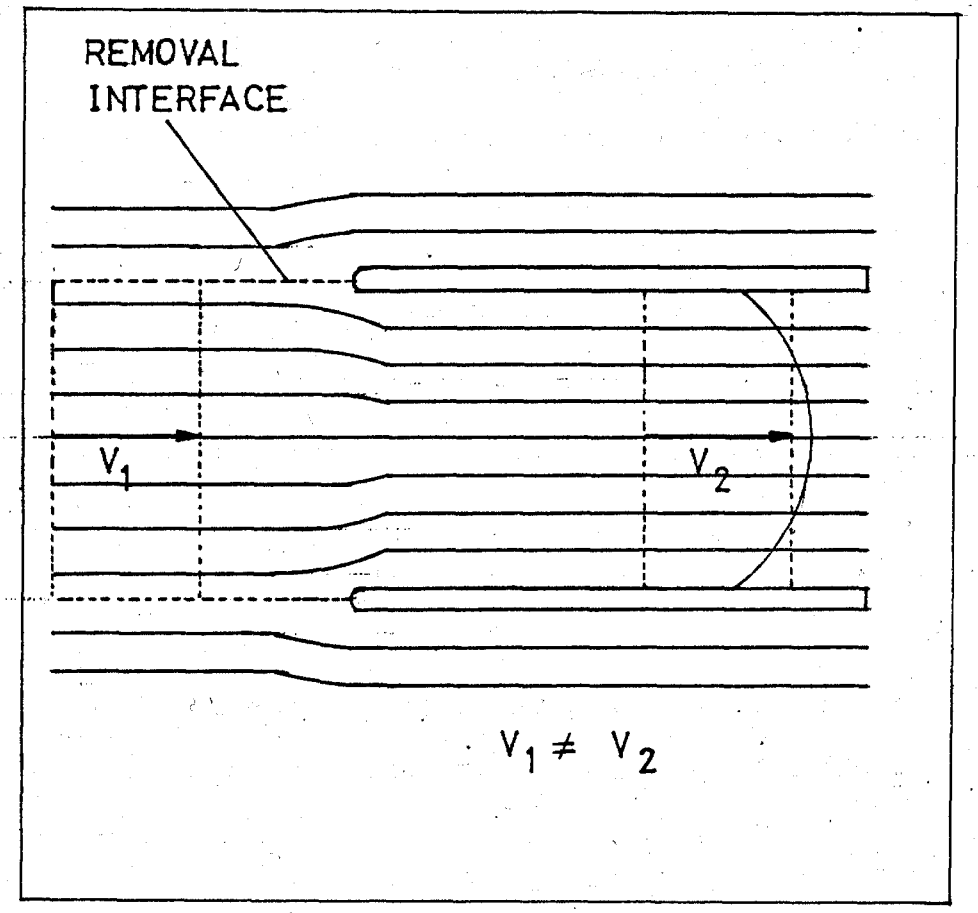

FIG. 7.3(B): ILLUSTRATION OF ANISOKINETIC SAMPLING

is fulfilled if the velocity of the fluid in the main duct is equal to the velocity of the partial flow, that is $(V_1 = V_2)$; this is called Isokinetic Sampling. Other works like Walter [71], however, indicated the requirement $V_2 > V_1$, and this is called Anisokinetic Sampling. Both sampling may be correct, as it can be shown that the required $\frac{V_1}{V_2}$ ratio is dependent solely on the shape of the profile or the definition of the partial gas flow.

If it is assumed that the partial gas flow starts at a sufficiently far distance upstream instead of the inlet to the probe, then the partial gas stream is correctly defined when there is no transition of dust particles between it and the main gas flow at the removal interface. This is the case when the removal interface does not exhibit any curvature in the flow direction and leads into the front end of the probe, as shown in Figure 7.2. Under these conditions all the particles remain in the main and partial gas flows respectively. It is therefore the shape of the probe which defines the partial flow cross-section. With the knowledge of the main flow velocity, the volume of air to be withdrawn via the probe is calculated. In the arrangement shown in Figure 7.1, this volume of secondary air is set by the needle valve. Therefore, it becomes a question of convenience whether to control sampling via the partial flow volume , or the partial gas velocity. On this premise therefore, isokinetic sampling applies to the case of the very sharp-edged tappered probe (Figure 7.2a) and a parallel flow arrangement.

In the case of Figure 7.2b, V_2 must be smaller than V_1 [72]. It must be emphasized that both approaches does not take into account the effect of molecular and turbulent diffusion,

which apply when there is a concentration gradient running across the direction of flow.

One further question arising from sampling of a flowing medium, is the number and distribution of the measurement points required in a duct in order to obtain representative samples. The large number of possible parameters to monitor, such as velocity, concentration and particle size distributions over a given plane compound the problem. However, this can be resolved on the basis of tests and statistical analysis of the test data.

Figure 7.1 also illustrates the sampling arrangement used for the tests. A 6mm sampling probe (Figure 7.4) introduced through the upstream and downstream sampling ports allowed particle sampling. The flow of air in the sampling line was obtained by means of a suction pump. Attached to the probe were alignment indicators which showed the position of the probe in the duct. The alignment arm was also used to ensure that the probe arm was perpendicular to the flow direction.

7.3.2 Particle Analysis

The particle number count and classification (analysis) was achieved by using a Classical Scattering Aerosol Spectrometer (CSA SP-100-HC) which is capable of detecting particles between 0.2 to 7.0 microns in diameter. The total size range of the instrument is divided into three overlapping ranges. Each being capable of further classification of the particles into 15 channels with every channel recording the number of particles counted within its size range.

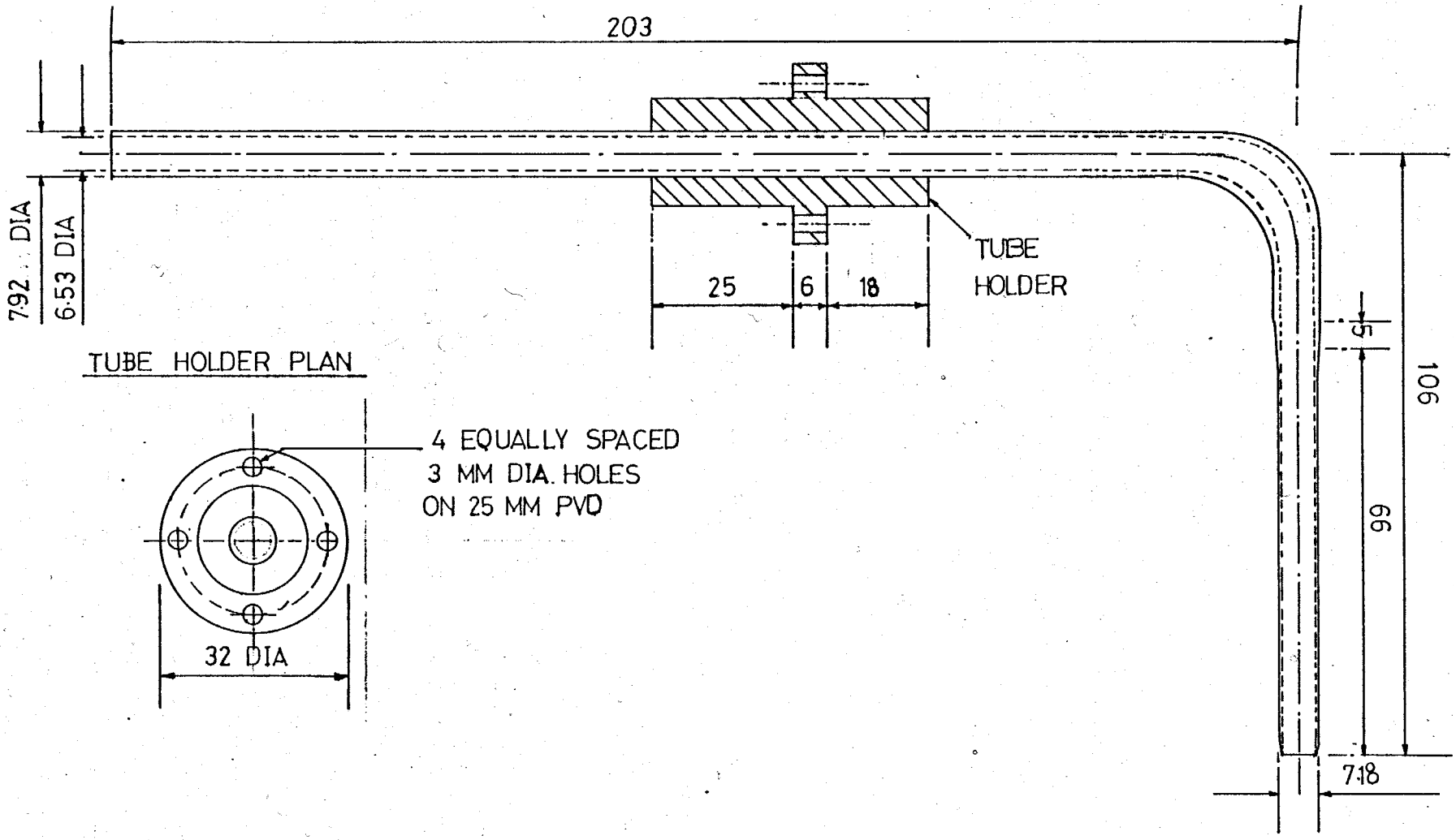

FIG. 7.4: TYPICAL ISOKINETIC SAMPLING PROBE

The operational specification of the spectrometer is given below:

Laser	80-5T 5 mW
Depth-of-Field	0.15 mm @ 30X
Beam Width (Astigmatic)	0.17 mm Length
	0.067 mm Width
Effective Beam Width	0.026 @ 30X
*Sample Area	1.95×10^{-3} mm^2 @ 30X
Flow Rate (Sample Point)	2 m/s to 10 m/s
Sampling Volume	Sample Area x (1.16 x Av. Flow Rate)
Maximum Concentration	>350,000 with correction
Power Requirements	230 VAC

SIZE	RANGE	INTERVAL
0	1.5 - 6.0	0.3
1	1.5 - 6.0	0.3
2	0.5 - 2.0	0.1
3	0.3 - 0.9	0.04

(All Dimensions in μm)

* (1/2 x Depth of Field x Effective Beam Width)

The information from the spectrometer was fed directly into the Data Acquisition System (PMS Data Acquisition System DAS-32) . Accumulated data based on the selected sampling time were displayed on a small VDU on the front panel of the analyser. Data from the analyser were fed to the computer through an interface described below. This arrangement made it possible to monitor the real time efficiency of the filter and also to extend

the length of time over which data can be acquired. The analyser was only capable of accumulating information for a period of hundred seconds. Attached to the computer was a printer and a disc drive which provided permanent storage for the accumulated data for future reference. Immediately beyond the spectrometer can be seen a large air-tight drum. Its main function was to dampen the oscillations in the flow created by the suction pump. It also enabled the condensation of the analysed particles following classification. Valves located along the flexible pipes were used to regulate the air flow. The rotameter nearest to the drum, gave the air flow rate in the sampling train.

7.4 BBC to Spectral Analyser Interface

The circuit diagram for this interface is shown in Figure 7.5. Components FF1 to FF5 in the diagram are JK type flip-flops, arranged to form a ring counter. The configuration forms a device that pass a logic 1 state through the counter in a cyclic fashion with it appearing at the Q output during operation. The flip-flop sets the $\overline{Q}$ (or the complimentary Q) output to a logic 0 when the Q output is at logic 1. It is this that enables the byte buffers, and allows data to be presented to the computer input port. In the initial setting of the counter, FF1 has the logic 1 at its Q output while the remaining FFs' (FF2-FF5) are set to logic 0 at their own Q outputs.

The 32 bit connector from the output of the spectral analyser is separated into four groups of 8 bits (a byte) before being presented as inputs to their respective buffers. The initiation of the input cycle to the computer is triggered by the

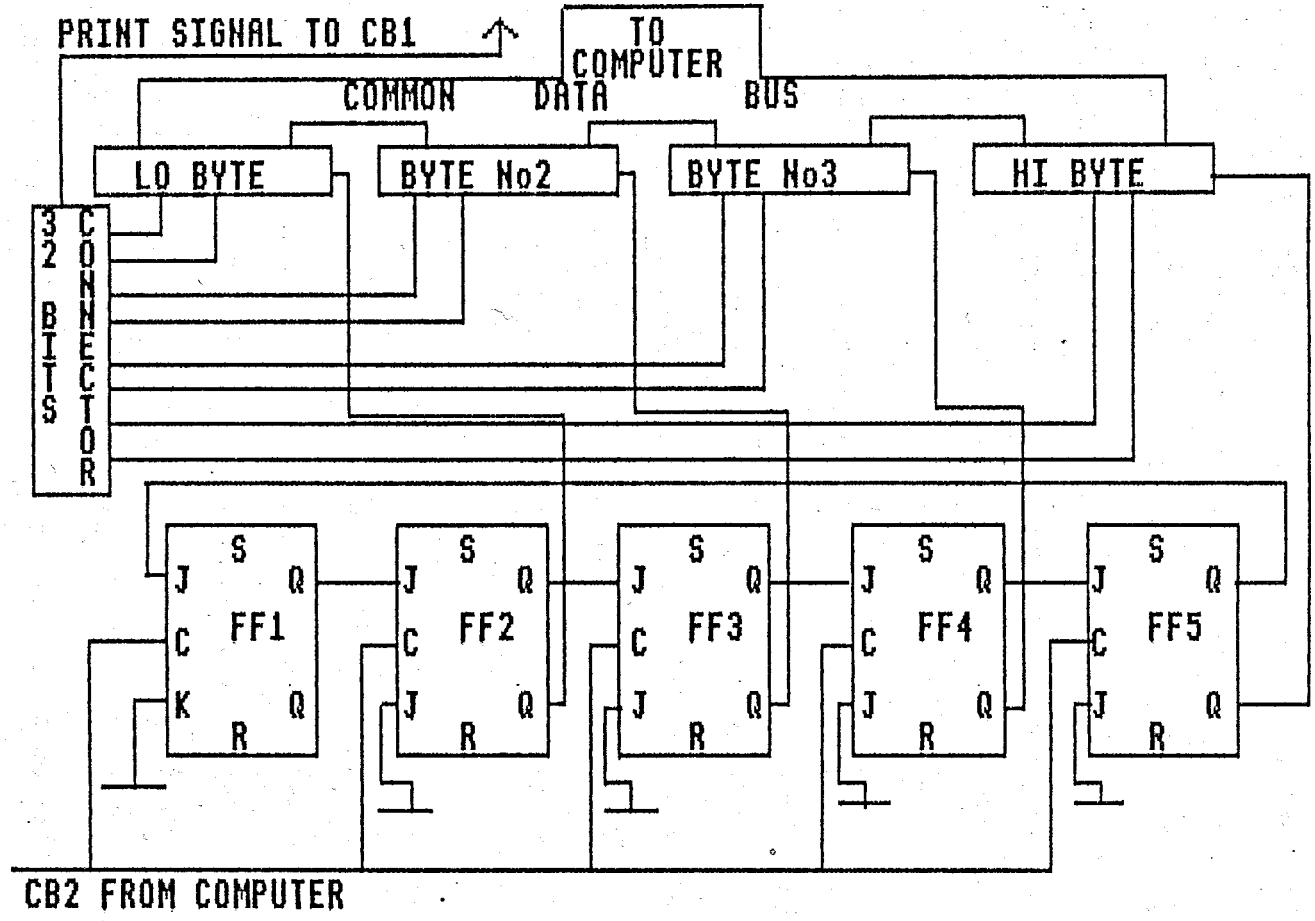

FIG. 7.5: BBC TO SPECTRAL ANALYSER INTERFACE

"print" signal from the spectral analyser. This activates the computer software (listed in Appendix D), which then takes over the control of activities of the interface by providing signals for the counter at the appropriate time to store the byte of data in the computer memory. This can then be displayed on the Visual Display Unit (VDU) or stored in floppy disks. At the end of each data transfer, the software returns the interface to its initial state, ready for the next "print" signal.

7.5 The Compensated Solenoid Magnet

One of the most important criteria for magnetic filtration is the provision of a uniform background of magnetic field through the entire length of the HGMF filter. This can be achieved by either the use of permanent magnets as in most early magnetic separators already discussed, or solenoid magnets as used in this study.

A water cooled compensated solenoid was used for the experiment. The solenoid was compensated to improve the field homogeneity. The solenoid was constructed out of 7.35mm square copper tubes with a wall thickness of 1.63mm. The inside diameter of the solenoid measured 113mm while the outside diameter measured 245.8mm. The overall length of the solenoid, including the compensated coil in the middle, was 315mm. It contained about 424 turns of insulated copper tubes capable of generating upto 0.8147 Tesla. The current necessary to produce this background magnetic field was obtained using a welding rectifier with a maximum continuous rating of 1200 Ampere at 45 Volts. A minimum of approximately 28.5 lit/min of water was required for cooling,

at an inlet water gauge pressure of 2.76×10^5 N/m^2 (40 psi).

7.6 Test Procedure

Each test was initiated by setting each of the operating parameters. These included the background field, the flow velocity, the sampling velocity, the motor speed and the compressed air pressure. Tests were carried out for increasing field strength to obviate the effect of hysteresis. The flow velocity was determined from the total and static pressure readings from the digital manometer. Adjustments to the flow were accomplished by using the number one flow control. Isokinetic sampling was achieved by adjusting the needle valve and monitoring the flow rate on a rotameter. The speed of the motor required to shake the feeder was obtained by adjusting the current supply to it. The high pressure air from the compressor was controlled by the valves located beneath rotameter 'A' and 'B'.

The filters were contained in the detachable filtering zone of the rig. In the case of cylindrical wires they were packed evenly in the matrix and weighed in conjuction with the detachable duct before final placement on the rig. The woven wire screens used were either stacked together in the duct section and locked at both sections with a PVC ring, or packed with separators in between them. At the end of each test, the detachable section was removed and weighed again to determine the mass of the dust collected.

Before each test the monitoring program was loaded into the computer. The program enabled the computer to accept signals

from the analyser, via the interface, for a specified time interval and then ignore the information received for another specified period. At the end of each test the solenoid magnet was usually switched off last. This was to prevent the re-entrainment of captured particles from the filter.

PLATE 7.1: CUPRIC OXIDE DUST ON A FILTER PAPER

PLATE 7.2: SAMPLES OF CuO DUST COLLECTED FROM THE EXPERIMENTAL DUCT SHOWING NO TRACES OF NICKEL PARTICLES

CHAPTER EIGHT

DISCUSSION OF FILTRATION RESULTS

8.1 Introduction

A comprehensive result obtained from the application of fibrous stainless steel wires as a filter in the presence of a magnetic field is presented. Table 8.1 shows the ranges of each of the important operating parameters used during the test. The experimental investigation was divided into two major parts. The first deals with randomly packed filters while the second deals with well ordered woven filters. Experimental results shown are those that elucidate trends or those that show significant differences from expected patterns of behaviour. The effect of various physical and hydrodynamic factors were investigated. Range three of the aerosol spectrometer was selected for sampling throughout the test. This covered the particle size in the range of 0.267-1.77 microns and was appropriate for the entire experiment.

8.2 Loadability Results for Random Filters

The loadability of a filter indicates the amount of filtrate a particular filter can hold before its arrestance deteriorates. In industrial use, this usually gives indication of the length of operational time of the filter. In most cases it is usually given as the ratio of mass of particles collected over the mass of filter.

The results of the loadability tests are presented for clarity in three plots (a), (b), and (c) in each of Figures 8.1 to 8.15. The first set of curves (a), applies to the smallest size range of 0.265 to 0.565; the second (b) to the mid-range of 0.72-1.45, while the last (c) applies to the largest size range of 1.53 to 1.77 microns. The mass of dust collected normalized by the mass of the material of the filter for each particular run is shown beneath the largest size range (c).

8.2.1 Effect of Magnetic Field on Loadability

Figure 8.1 to 8.4 show the loadability tests carried out for a constant packing fraction of 0.0075 and increasing field strength from 0.0 to 0.8 Tesla. For no-field investigation, Figure 8.1 shows the variation of filtration efficiency with time. In this test the only mode of particle capture is inertial deposition and direct impaction, which was enhanced by the surface adhesion forces of both the wires and that of the particle. Another possible effect that could have been present was mechanical capture. This is mainly the lodging of particles in between the interstices of crossed wires. The effect of this is less pronounced and therefore de-emphasized because of the low intensity of filter packing. The average initial collection efficiencies were 50%, 75% and 70% for the lowest, medium, and largest size ranges respectively. This initial high collection of the particles was due to the strong presence of surface adhesion forces on the clean wire. But as the filtration progressed , the wire surfaces become contaminated, thus reducing the coefficient of restitution of the wire. The progressive deterioration of the

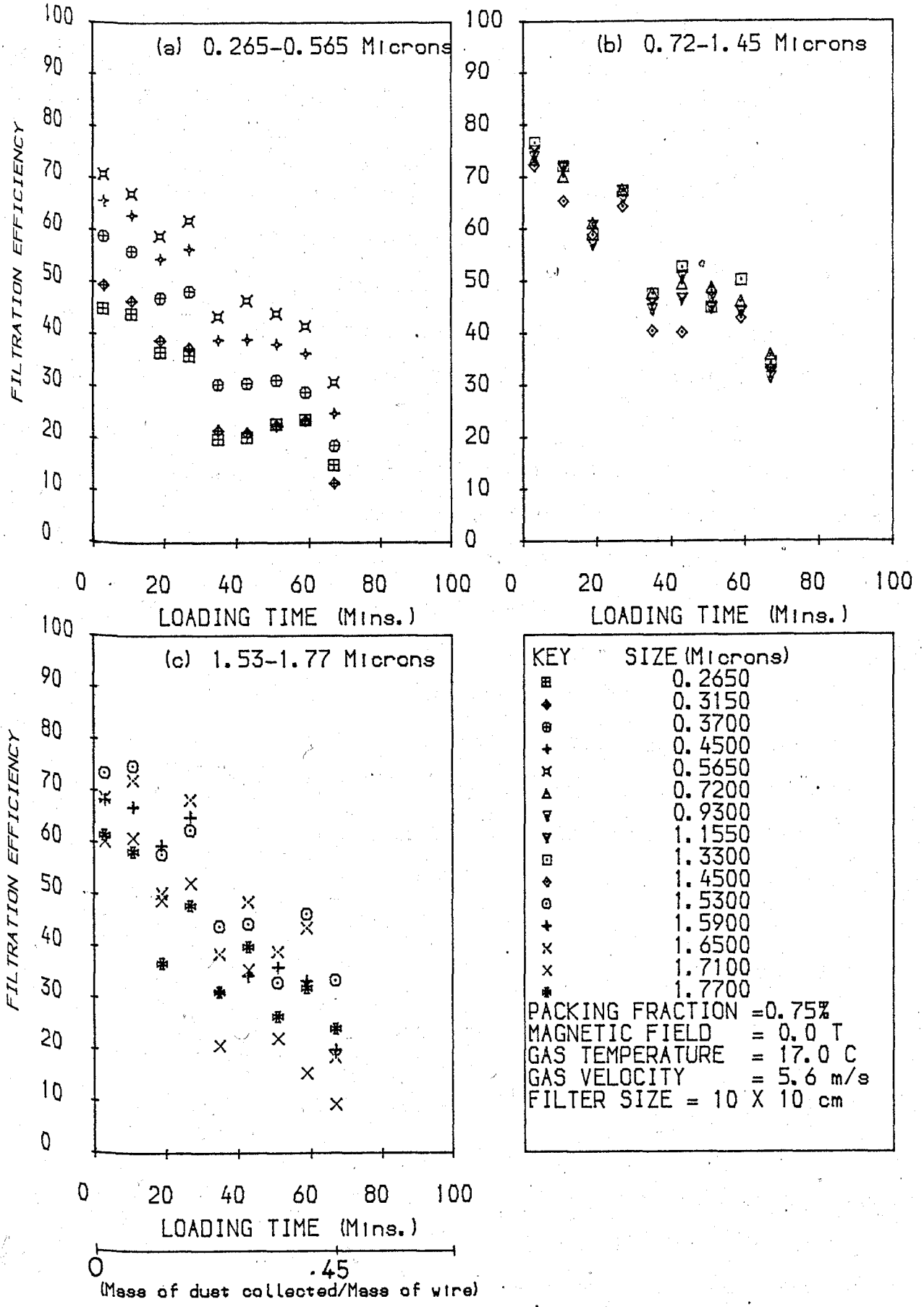

FIG. 8.1: EXPERIMENTAL MATRIX LOADABILITY AT ZERO FIELD

matrix can be partly attributed to this effect. The capture of particles this time rely more on them being trapped in between already captured particles. This has benefited the mid range particles because of their average momentum. The collection of the smallest size range particles was continuously exacerbated by their following the fluid streamlines. The largest particles possessed such a high momentum that instead of being trapped they bounced off the the wire, and in some cases sheared off already captured particles.

The results in Figure 8.2, (0.1 Tesla), which are slightly better than the previous one has a superior retentivity. For example, in the first part (0.265-0.565 microns) the initial results compared favourably with that obtained with no field but after about an hour of the test time has elapsed, the collection efficiency was still maintained at almost 50%, unlike that of no-field which had dropped by about 30%. The curves for the mid-range particles (0.72-1.45 microns), are smoother than those in Figure 8.1, indicating better retentivity as a result of magnetic field. But the erratic behaviour in the previous result for the largest particles is still present. This can only mean that the balance between the magnetic and hydrodynamic forces is still unfavourable.

The next test performed at 0.4 Tesla (Figure 8.3) produced the best loadability so far. Like the previous two graphs, the smallest particles have almost the same initial efficiencies, but quite unlike the two graphs, after about an hour of the filtration time the collection efficiency was minimally reduced. For mid-range particles, the benefits of the

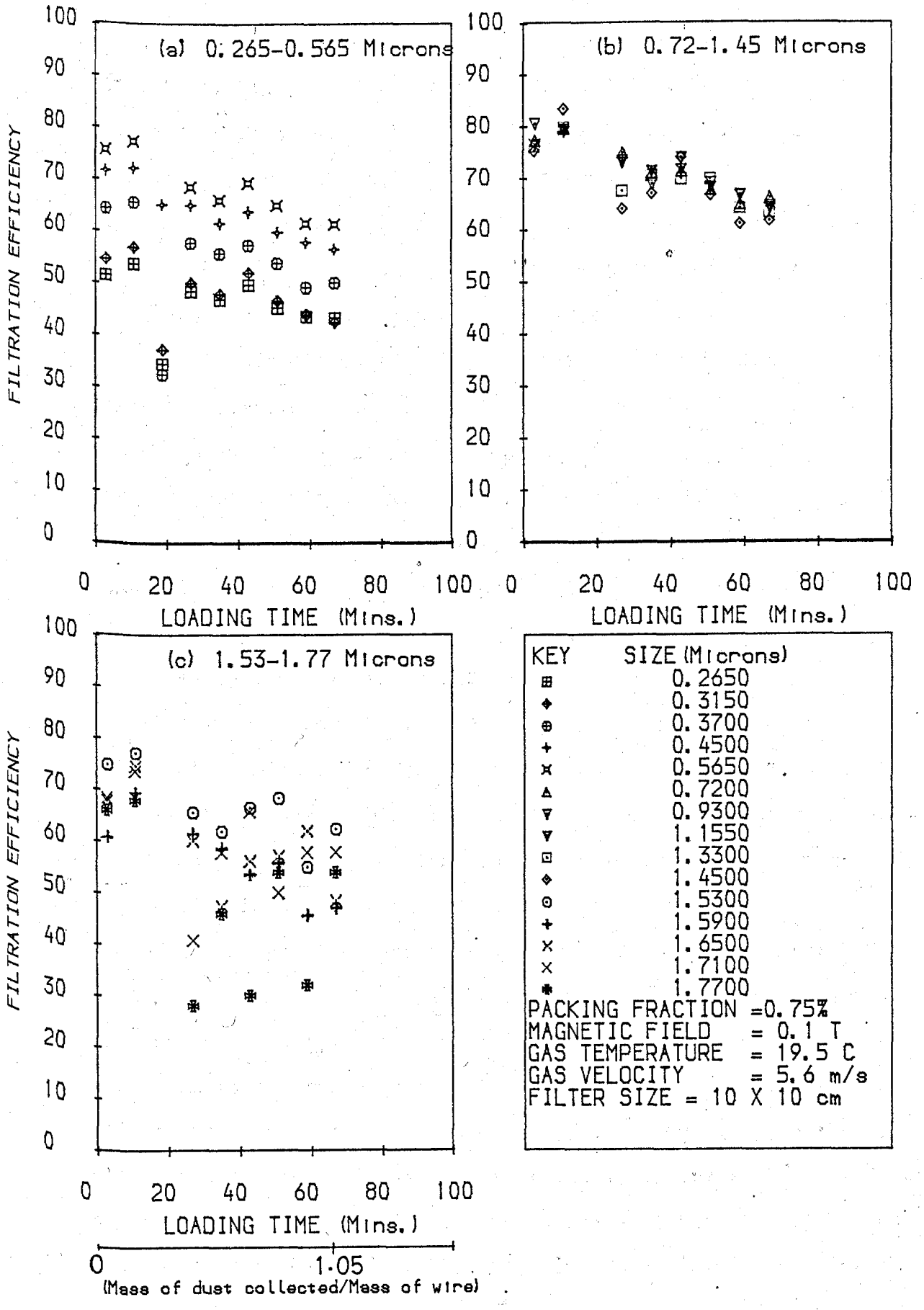

FIG. 8.2: EXPERIMENTAL MATRIX LOADABILITY AT 0.1 TESLA

increased field is much more detectable after about thirty minutes as compared to Figures 8.1 and 8.2. The most striking distinction is found in the plot for the largest particles, which maintained a collection efficiency of about 75% throughout the experiment. The effect of particle bounce off being completely eliminated. Figure 8.4 shows the same test carried out at twice the former field strength of 0.8T. As expected and supported by results already discussed, there is a substantial increase in the initial collection efficiency of all particle sizes because as CuO is paramagnetic, it never becomes saturated, hence increasing the magnetic field strength enhances the chances of more particles being trapped. This high efficiency is sustained for particles whose diameter are above 0.37 microns although the rate of deterioration is much higher for all sizes less than 0.565. A particularly unusual effect can be seen in the first set of results which show that the filter has become less effective after thirty minutes, compared to that obtained for 0.4T over the same length of time. This is puzzling because besides random error due to wire packing, variation in dust characteristics, fluctuation in the dust feed rate and of course human errors, there is no physical, magnetic, or hydrodynamic explanation for this effect. One of the explanations that was supported later by the ordered woven wire results is the realignment of the filter wires due to the magnetic field. This causes some surfaces of the wire to be attracted to each other, thus reducing potential effectiveness. The initial high performance of the filter was due to high receptivity of the wires because of the high field and the CuO dust being equally highly susceptible. The other

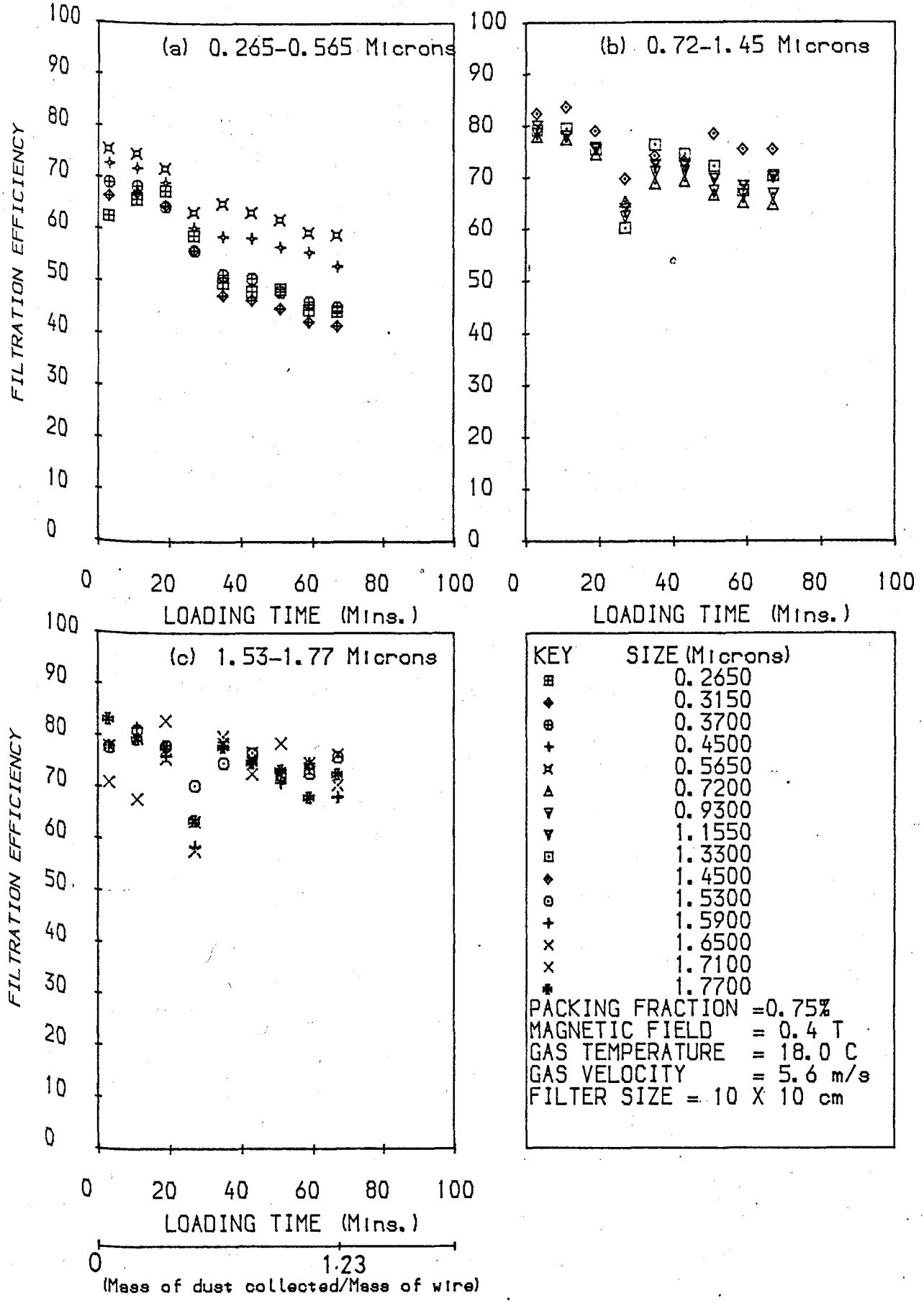

FIG. 8.3: EXPERIMENTAL MATRIX LOADABILITY AT 0.4 TESLA

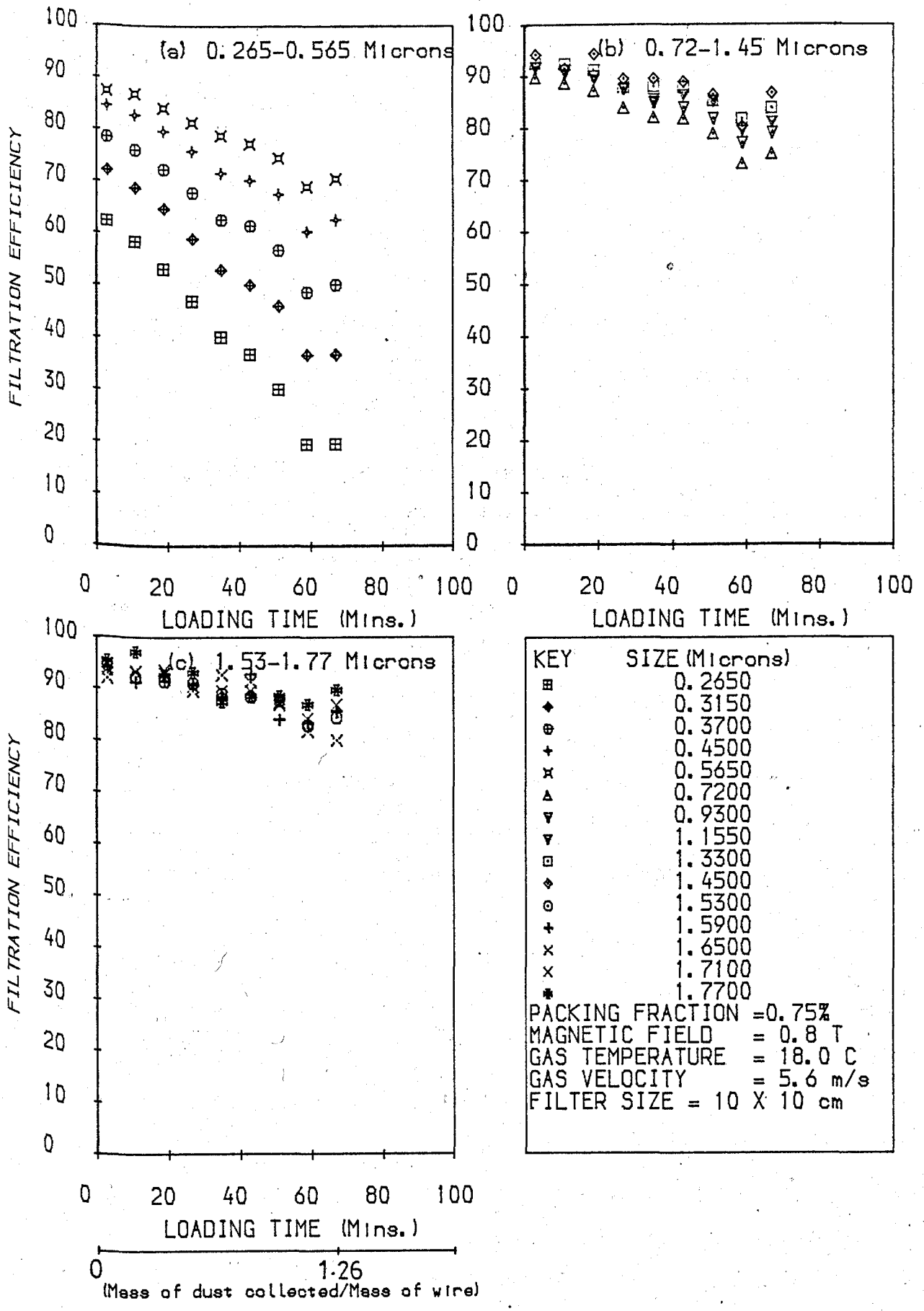

FIG. 8.4: EXPERIMENTAL MATRIX LOADABILITY AT 0.8 TESLA

possibility is wire-to-wire interference which tends to create zones with zero magnetic tractive forces and low magnetic gradients.

Figure 8.4A gives a summary of the effect of increasing the magnetic field on matrix loadability. As expected, increasing the number of the magnetic field improved the total mass of dust collected. However, the curve indicates a significant gain up to about 0.2T. These results presented so far, provides conclusive evidence that HGMF is beneficial to the filtration of paramagnetic dust, but this advantage is somewhat reduced by the re-alignment of the wire at field strength of up to 0.8T and the saturation of the stainless steel at about 0.2T. The re-alignment of the wires manifested in the form of increased flow channels that allowed the submicron particles to pass through the filter at much higher rate than for lower fields; while the wire after saturation contributes a little to a better collection as the magnetic field is increased. Nevertheless, the mass ratio (mass of dust collected over the mass of wire used) recorded for the highest field strength tested was still the largest.

8.2.2 Effect of Packing Fraction on Loadability

Figures 8.5 and 8.6 show results obtained from packing fractions of 0.5% and 1.0% respectively; all tested at a field strength of 0.8T. The improved collection efficiency is obvious when the two diagrams are compared. An interesting observation is made when Figures 8.4 and 8.6 are compared. There is very little or none of the improvement in Figure 8.6 which is expected with higher packing. This indicates that there is a limiting ratio of

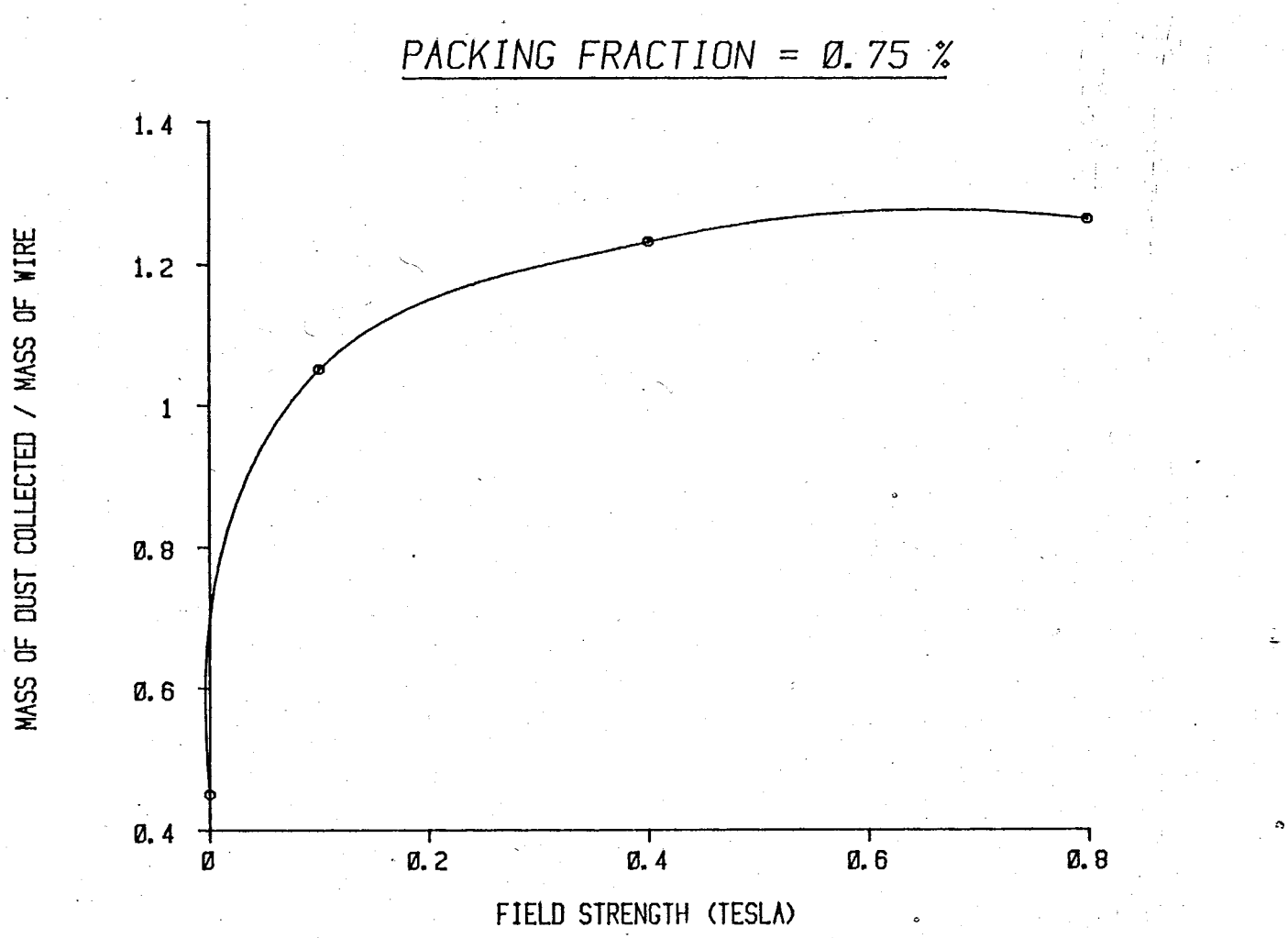

FIG. 8.4A EXPERIMENTAL MATRIX LOADABILITY AT 0.8 TESLA

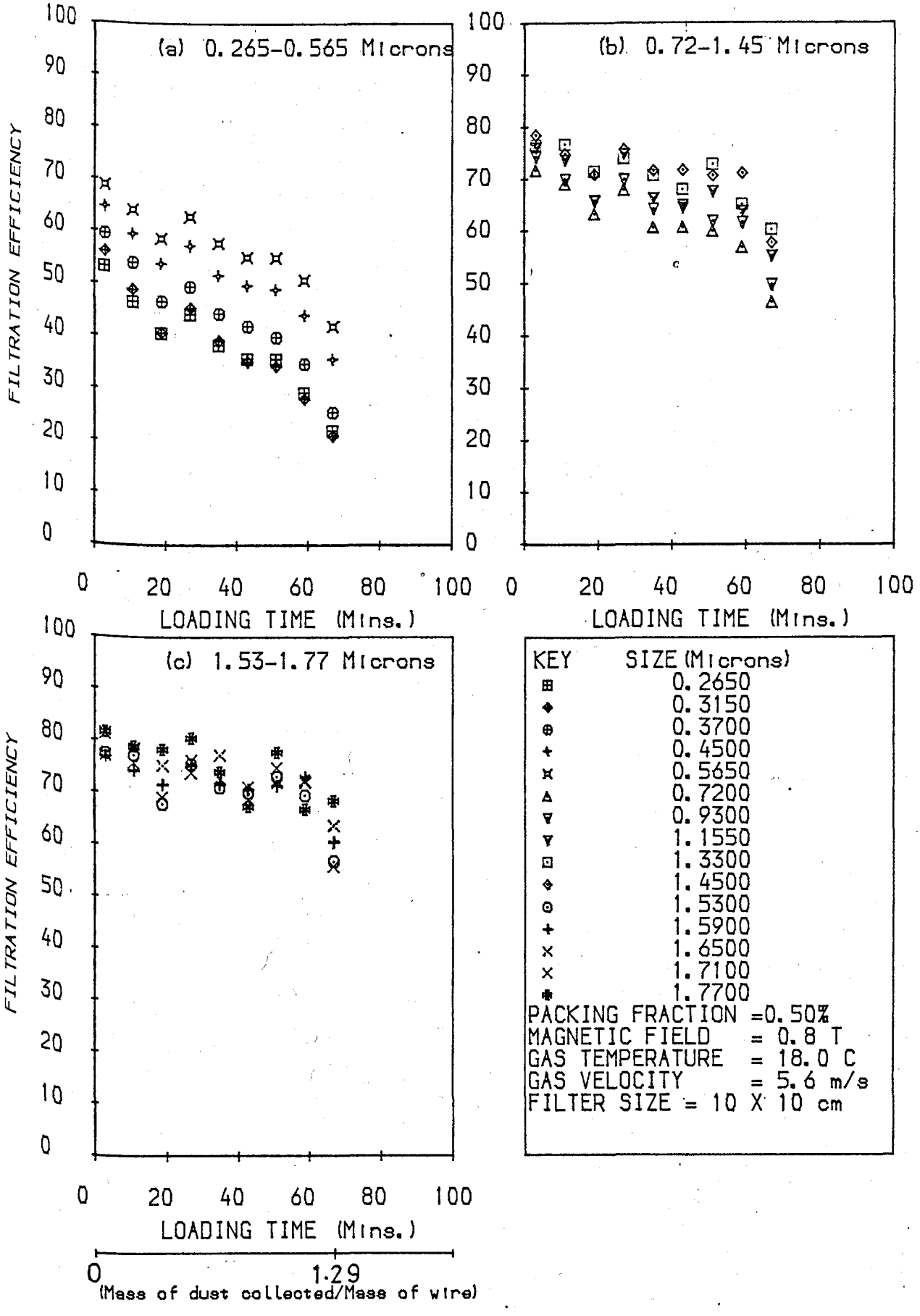

FIG. 8.5: EXPERIMENTAL MATRIX LOADABILITY AT 0.5 PACKING FRACTION

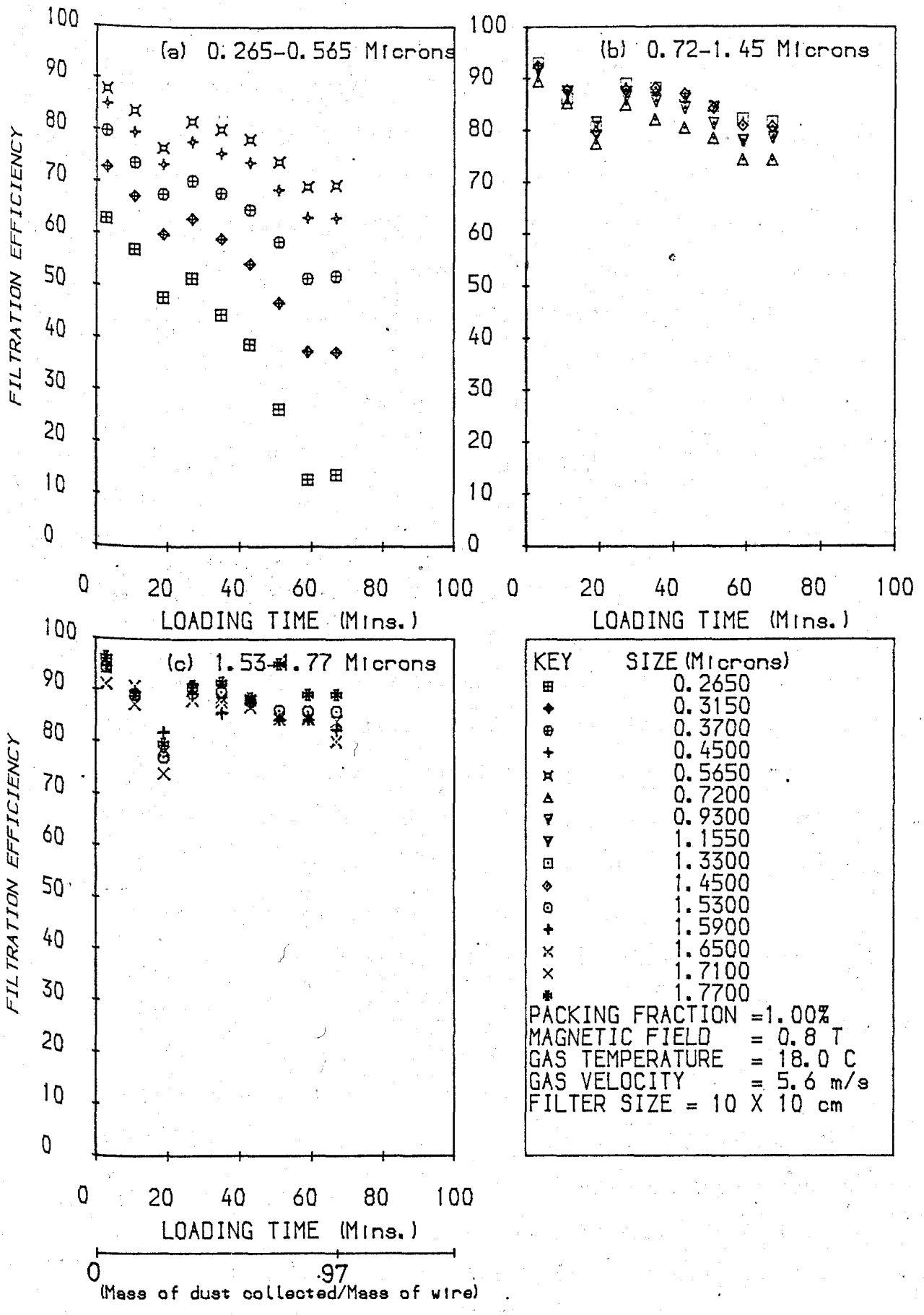

FIG. 8.6: EXPERIMENTAL MATRIX LOADABILITY AT 1.0 PACKING FRACTION

mass of wire over volume of the matrix above which favourable results are drastically affected. Figure 8.6A amplifies this point by portraying a gradual reduction in the mass ratio of the dust collected with increased packing fraction. Interpretation of both the loadability plots and Figure 8.6A together is necessary for a filter designer who has to make a decision of either designing for high collection efficiency with relatively high packing fraction or for economy. A superposition of Figures 8.4A and 8.6A gave an optimum design point of about 0.8% packing fraction at a field strength slightly less than 0.45T (Figure 8.6B).

It can be suggested that both the magnetic and fluid interferences may have combined to reduce the effectiveness of the matrix at high loading. There are two components of the magnetic force, both of different orders of magnitude. The long range component, most likely to interfere with each other (thus creating areas of reduced tractive force and magnetic gradients) is of the order of $\frac{1}{s^3}$, (where s is the wire radius), while the shorter range part is of the order of $\frac{1}{s^5}$. The hydrodynamic interference has an order of magnitude of $\frac{1}{s^2}$ and therefore most likely to be the first to affect the filtration process. If the filter matrix is modelled as a series of parallel square meshes of distance l_s apart (Chapter Four), the above interferences would only occur when their magnitudes fall in the average ranges of $\frac{l_s}{2}$. This represents the mean distance separating two wires in a filter matrix. Another source of interference arises from wires overlapping with each other, thus resulting in ineffective wire lengths. Although not quantified in this work, the increased

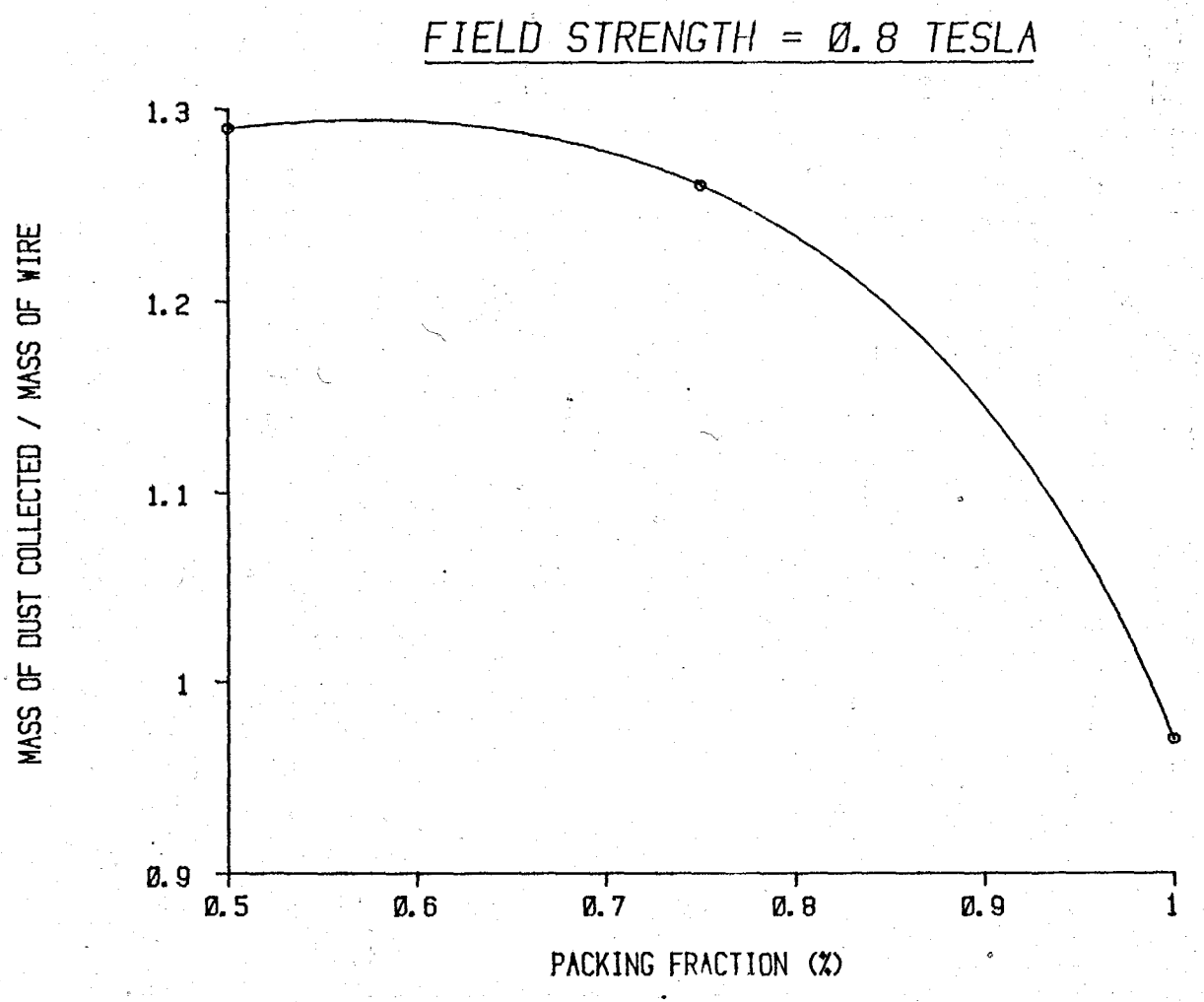

FIG. 8.6A EFFECT OF PACKING FRACTION ON MATRIX LOADABILITY (VELOCITY = 5.6 M/S)

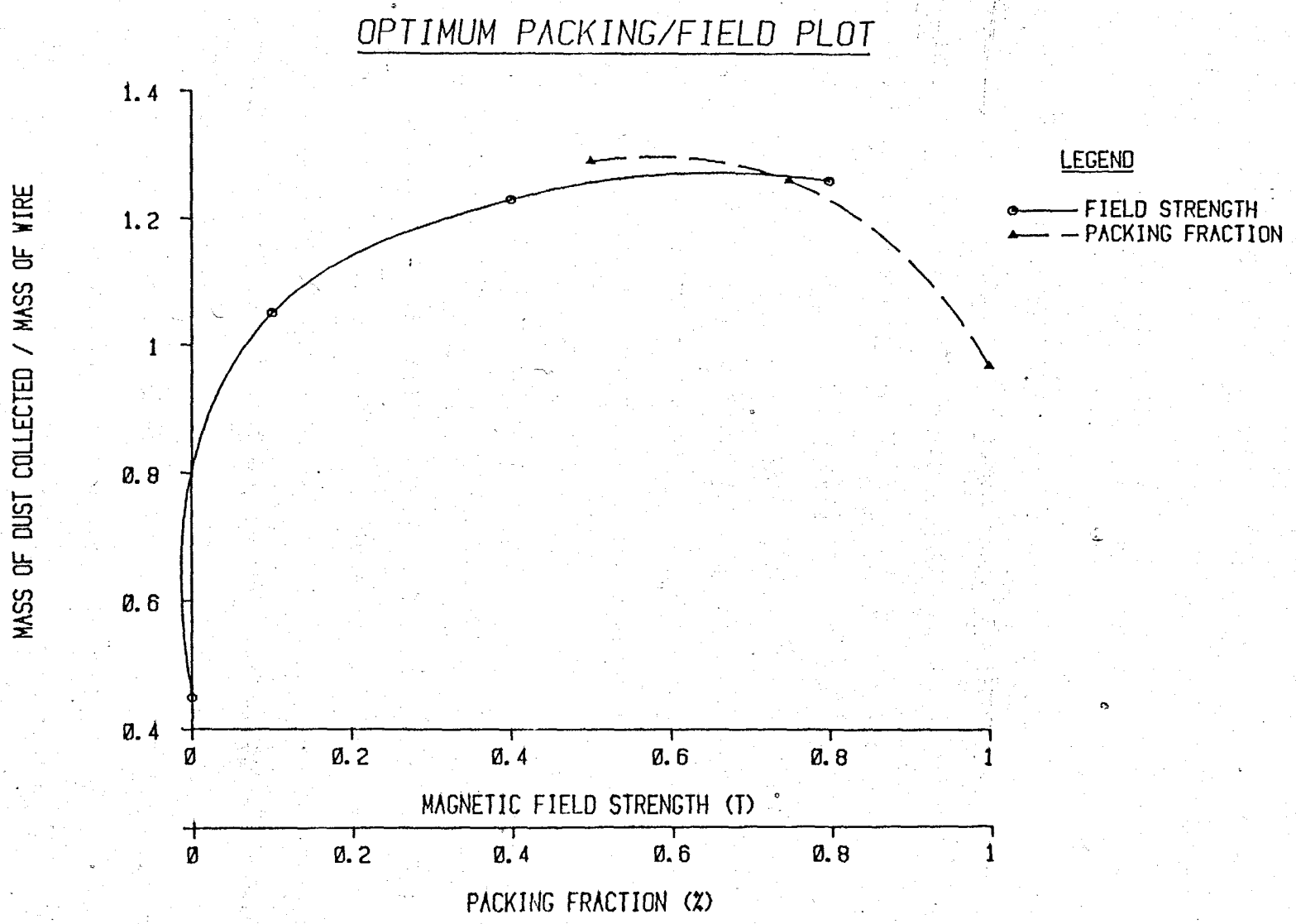

FIG. 8.6B CRITICAL DESIGN POINT FOR MAGNETIC FIELD STRENGTH AND PACKING FRACTION

interference effects are compensated for by the increased effectiveness of mechanical capture resulting from higher packing. Therefore, it can be concluded that after a critical value of packing fraction ($0.55<F<0.65$), the law of diminishing return sets in for any extra wire added.

8.2.3 Effect of Velocity on Loadability

The hydrodynamic effect of flow velocity is among the more complicated parameter in HGM filtration as it depends on a multitude of other physical factors of the filter.

All the previous results already discussed were performed at a flow velocity of 5.6 m/s. Figure 8.7 shows those obtained at a flow velocity of 7.6 m/s, field strength of 0.8T, and packing fraction of 0.75%. A comparison of this result with Figure 8.4, which was obtained for the same parameters except for different velocity, show some subtle differences, especially for particle sizes of less than 0.565 microns. While the initial collection efficiency is higher for the slower flow, the rate of deterioration of the filter, (Figure 8.4), is larger, resulting in a slight drop in collection efficiency at the end of the experiment. The most remarkable difference between the two (Figure 8.4 and 8.7) can be found in the size range of 0.265-0.565 . It shows that smaller particles (less than 0.565 microns) gave a sustained loading unlike that in Figure 8.4 through the course of the test. This is obviously as a result of increased inertial effect which has enabled larger (number of) particle flux to impinge on the wires. Otherwise, these small particles tend to follow the fluid streamlines. If the flow velocity is

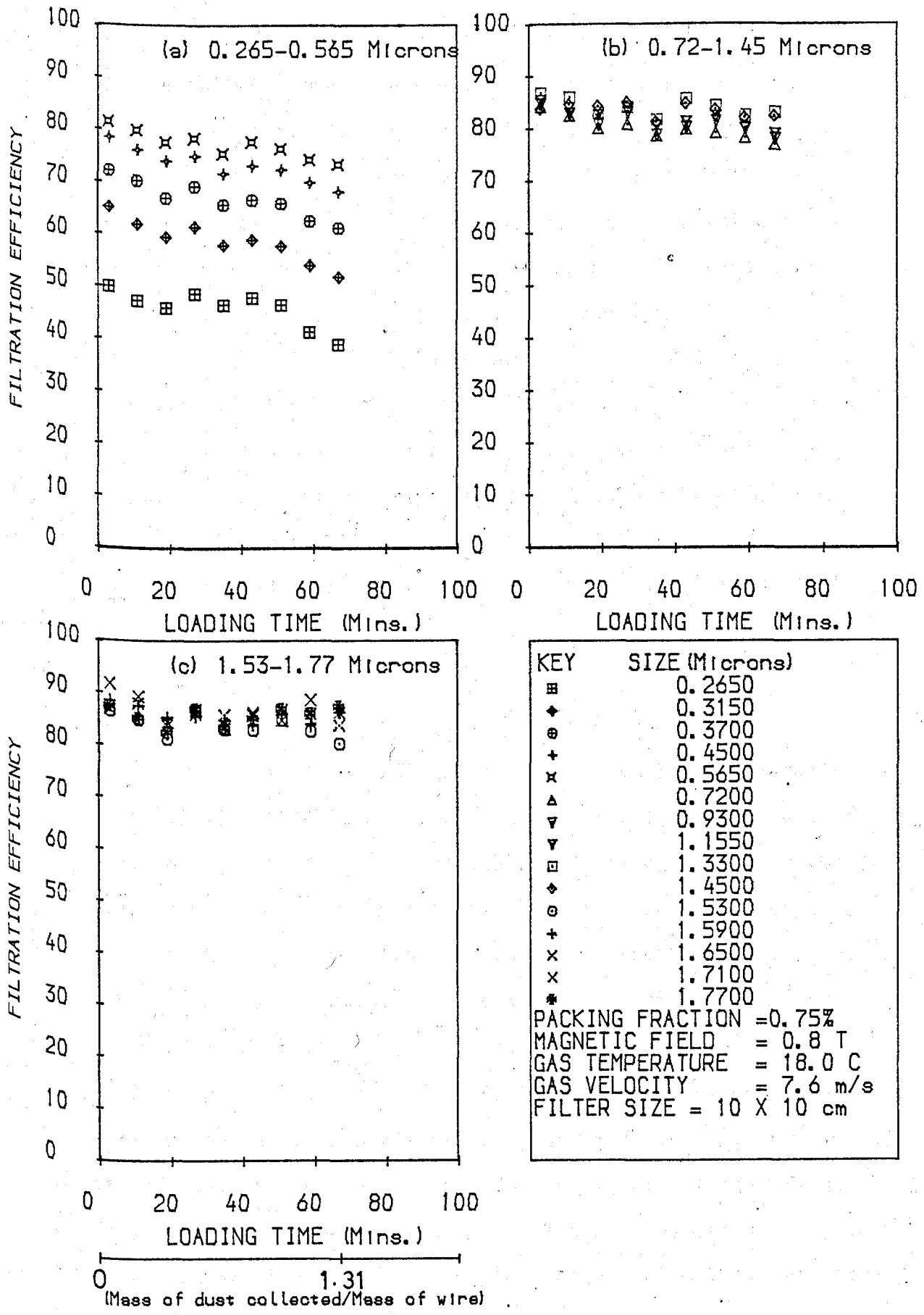

FIG. 8.7: EXPERIMENTAL MATRIX LOADABILITY AT 7.6 M/S

raised further, a point may be reached where it becomes detrimental to particle capture. At this point, the momentum of the bigger particles become high enough to neutralize the retentive forces on the surfaces of the wires created by the magnetic forces. In such circumstance, those particles already captured may be washed off the surface of the wires. This is the particle bounce off already discussed above.

There is obviously a larger amount of dust collected in this case of higher flow velocity as shown in Figure 8.7A. Although the plot was performed for only two experimental points, it amplifies the already stated advantage of HGMF over various other separation techniques, that very high rate of throughput can be obtained with well accepted particle collection rate for a relatively long time.

8.2.4 Effect of Filter Length on Matrix Loadability

Matrices of diameter 10cm with lengths 20cm (Figure 8.8) and 15cm (Figure 8.8A) were used for this test at a packing fraction of 0.5%. The magnetic field strength applied was 0.4T instead of 0.8T to avoid possible strong wire realignment. The same pattern of results were obtained except that there was an improvement in particle collection. Figure 8.8 shows the advantage of having a relatively longer filter. The better performance of this particular filter can be attributed to more wire surfaces being available for particle capture, low magnetic interference (as a result of larger volume), and mechanical capture due to wire orientation. The reduced field strength of 0.4T may have also helped in the high filtration efficiency

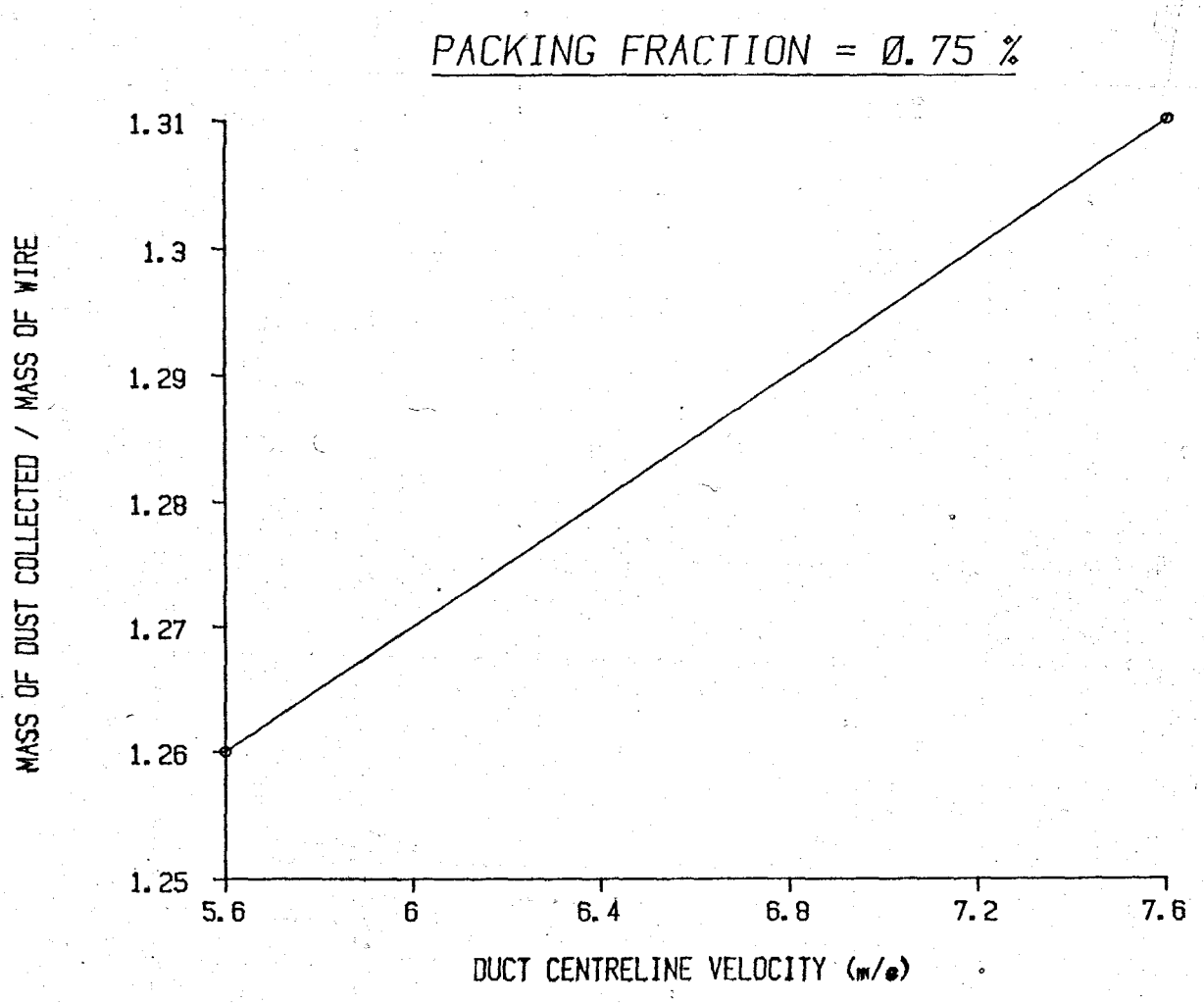

FIG. 8.7A EFFECT OF FLOW VELOCITY ON MATRIX LOADABILITY (FIELD STRENGTH = 0.8 T)

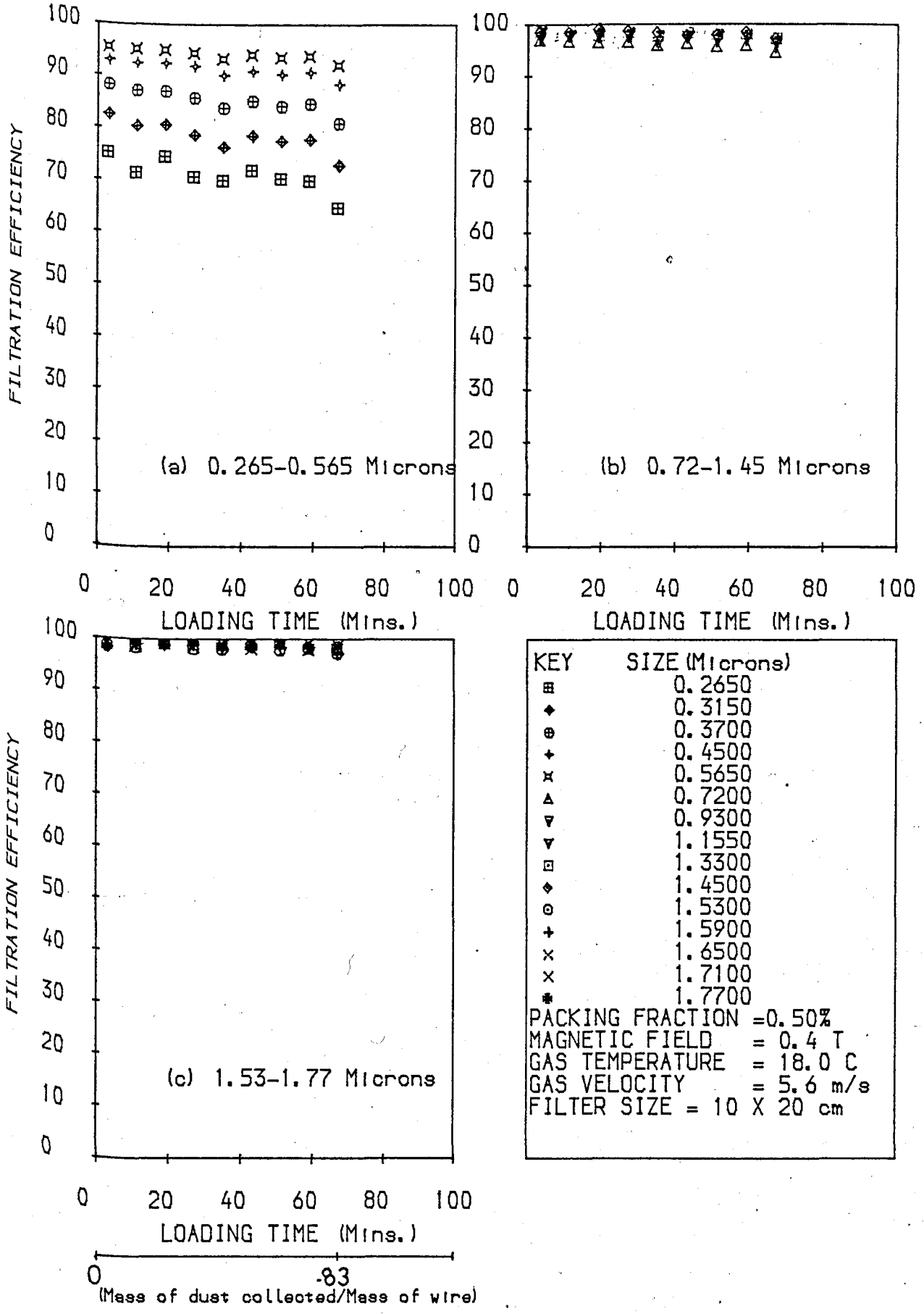

FIG. 8.8: EXPERIMENTAL MATRIX LOADABILITY WITH 20 CM LONG FILTER

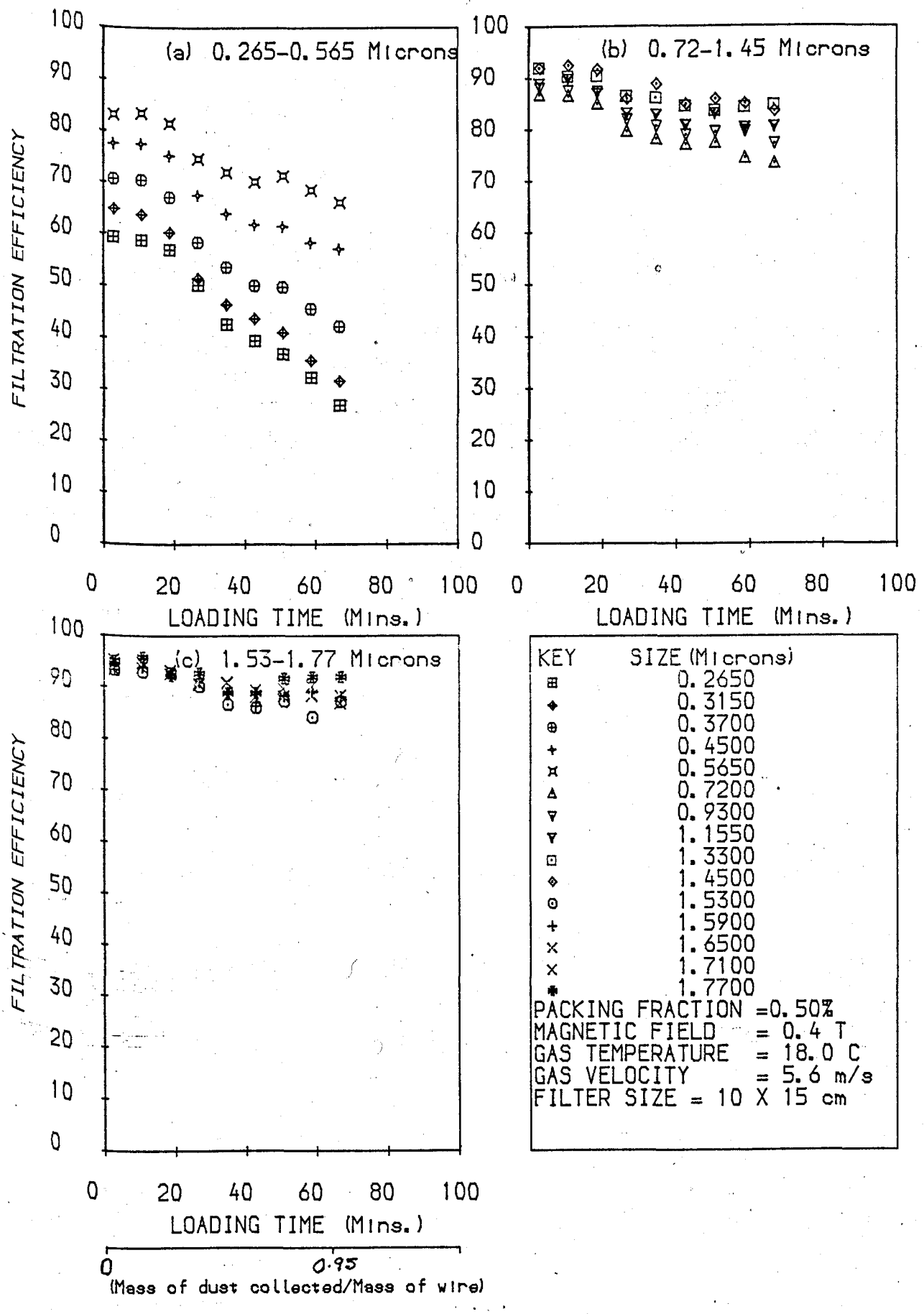

FIG. 8.8A EXPERIMENTAL MATRIX LOADABILITY WITH 15 CM LONG FILTER

obtained for the smallest particle size range, which in higher fields affected particle collection process. A visual inspection of the used filter revealed that most filtering occured at the front of the filter, while at the back, it remained virtually clean. This does not mean that the frontal part of the filter was most effective, but since particle density is higher at the front it got more loaded. These results therefore suggests that efficiencies above 95% are possible for magnetic filtration of paramagnetic dust with a relatively long filter, but at an added cost for overcoming its resistance.

The question of cost optimization can also be addressed here. For example, in Figure 8.8, although a high particle collection efficiency was achieved, the mass ratio of dust collected is lower than the same ratio for 0.0075 packing density at 0.4T (Figure 8.3) or 0.005 packing at 0.8T (Figure 8.6). From the values of these ratios, it is clear that to maintain a high particle collection efficiency (> 95%), it would cost more in terms of providing extra mass of wire which only provide a marginally better result.

8.3 Loadability Results for Woven Wires

Loadability tests were carried out with woven wires cut in the form of screens. These were packed in two different patterns; first with their faces touching, and with 5mm PVC rings separating them. The main objective for performing a test with the meshes separated was to optimize the filter configuration for possible application to binary mixtures.

The results obtained from these tests are supposed to

supplement those obtained from random filters. The most important advantage of applying woven wire being that the effect of matrix-to-matrix variation is completely eliminated. Figure 8.9 shows the result of a test performed with 16 screens at the same concentration of dust as in the random filters. The rapid decline of the filter is apparent. At about an hour after the starting of the experiment, the collection of the smallest particle range has dropped to less than 10%. This rapid drop is even present in the intermediate and the largest particles which in almost all the previous results were high. The effect of bounce off is also manifested in the scatter of the experimental points.

The mass ratio of dust collected was 0.92 which is much smaller than the value obtained for an equivalent test with random wire (Figure 8.4) that yielded a mass ratio of 1.26. This indicates that for the same dust concentration, that the use of the random wire arrangement is better. In subsequent tests carried out with woven wires, the concentration of the particles filtered was reduced to about half of its original value. This was to enable the investigation of the major operating parameters, which tended to be obscured at large dust concentrations.

Figures 8.10 and 8.11 show the loadability results obtained from the tests carried out for field strengths of 0.0 and 0.8 Tesla respectively at a reduced concentration. It is apparent by comparing the two sets of Figures that the presence of a magnetic field gives greater efficiency of dust collection. For a magnetic field of 0.8T (Figure 8.11), the collection efficiency of even the smallest particle exceeded 50% throughout

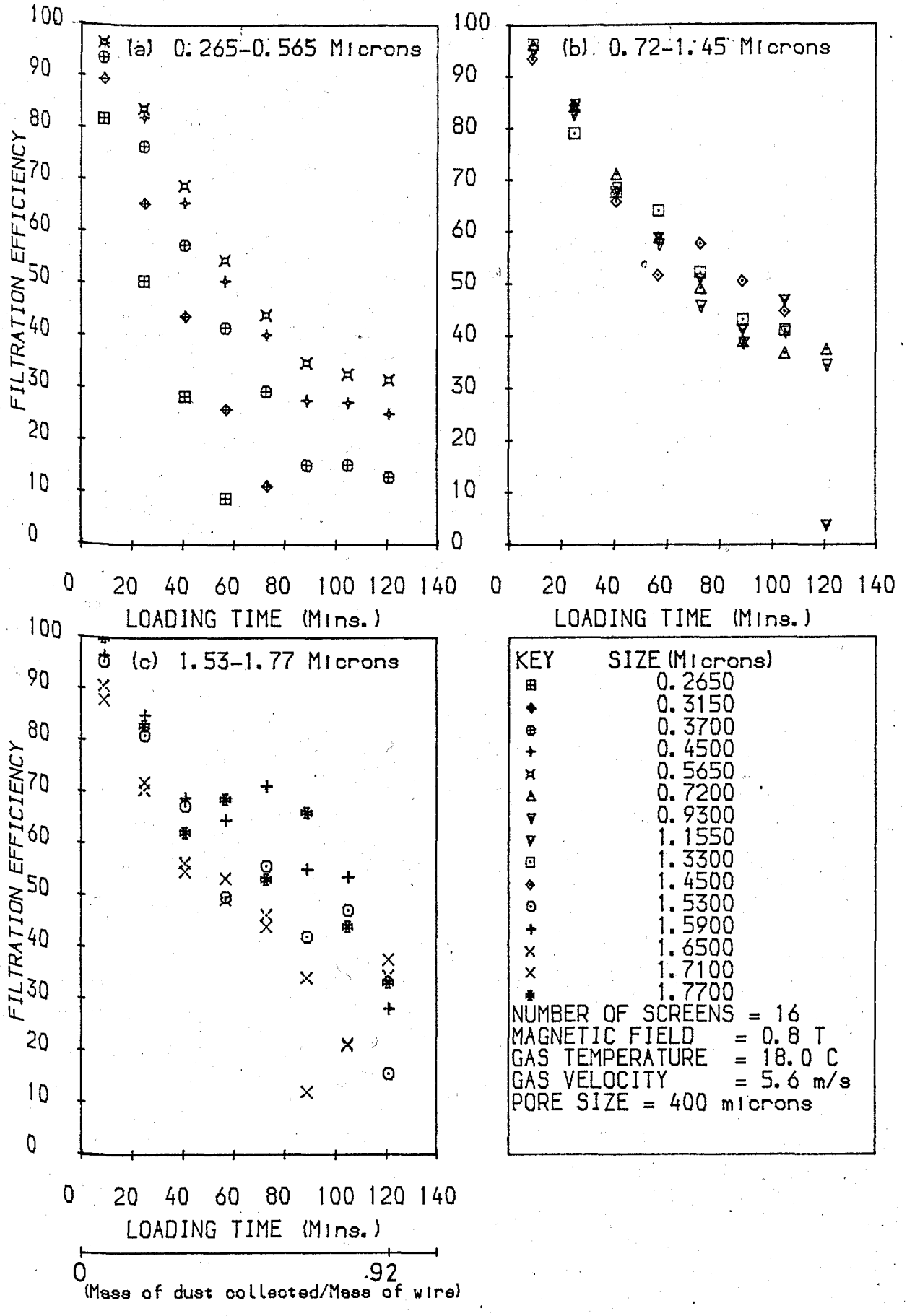

FIG. 8.9: EXPERIMENTAL MATRIX LOADABILITY AT HIGH CONCENTRATION WITH WOVEN WIRE

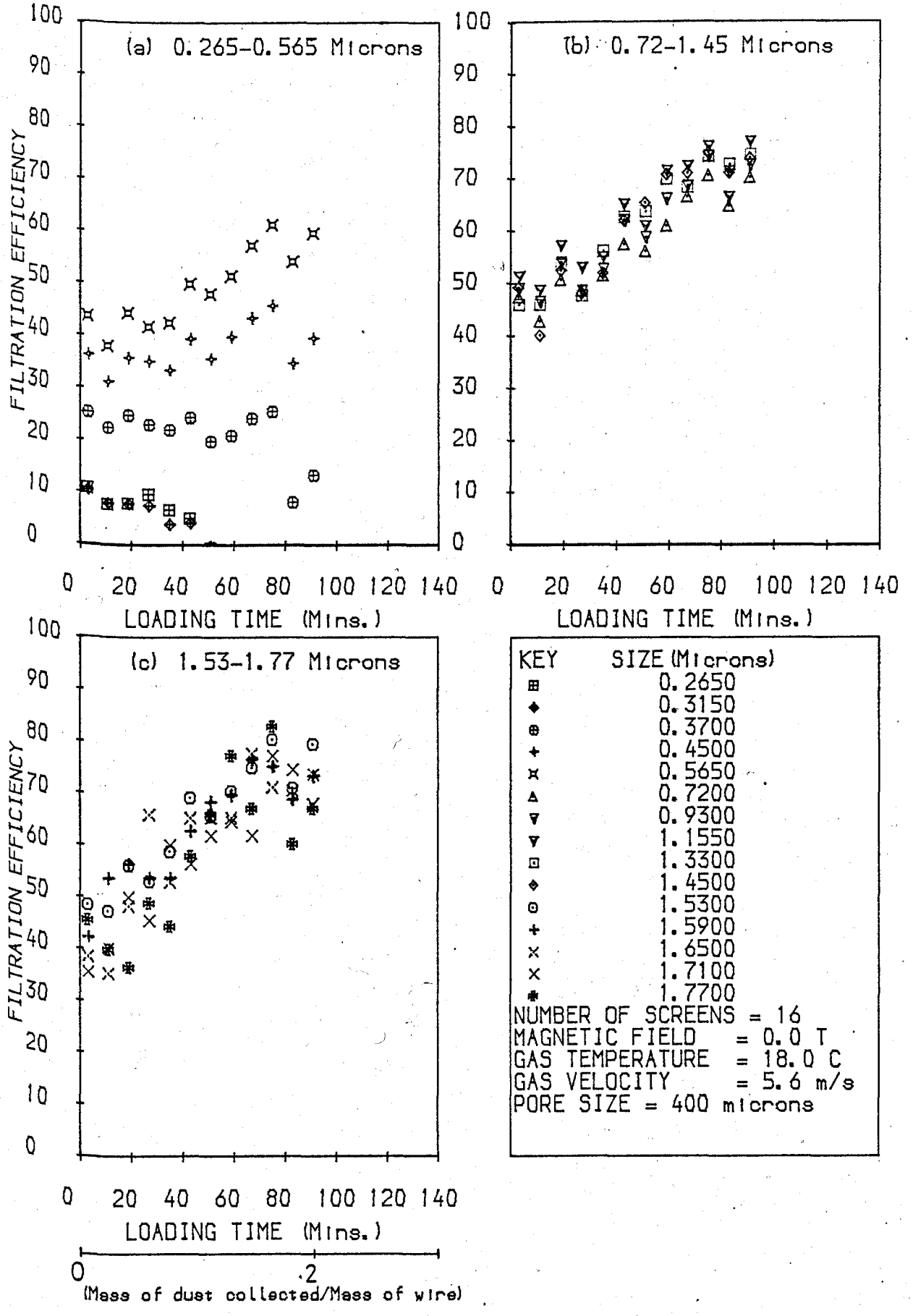

FIG. 8.10: EXPERIMENTAL MATRIX LOADABILITY AT ZERO FIELD (WOVEN WIRE)

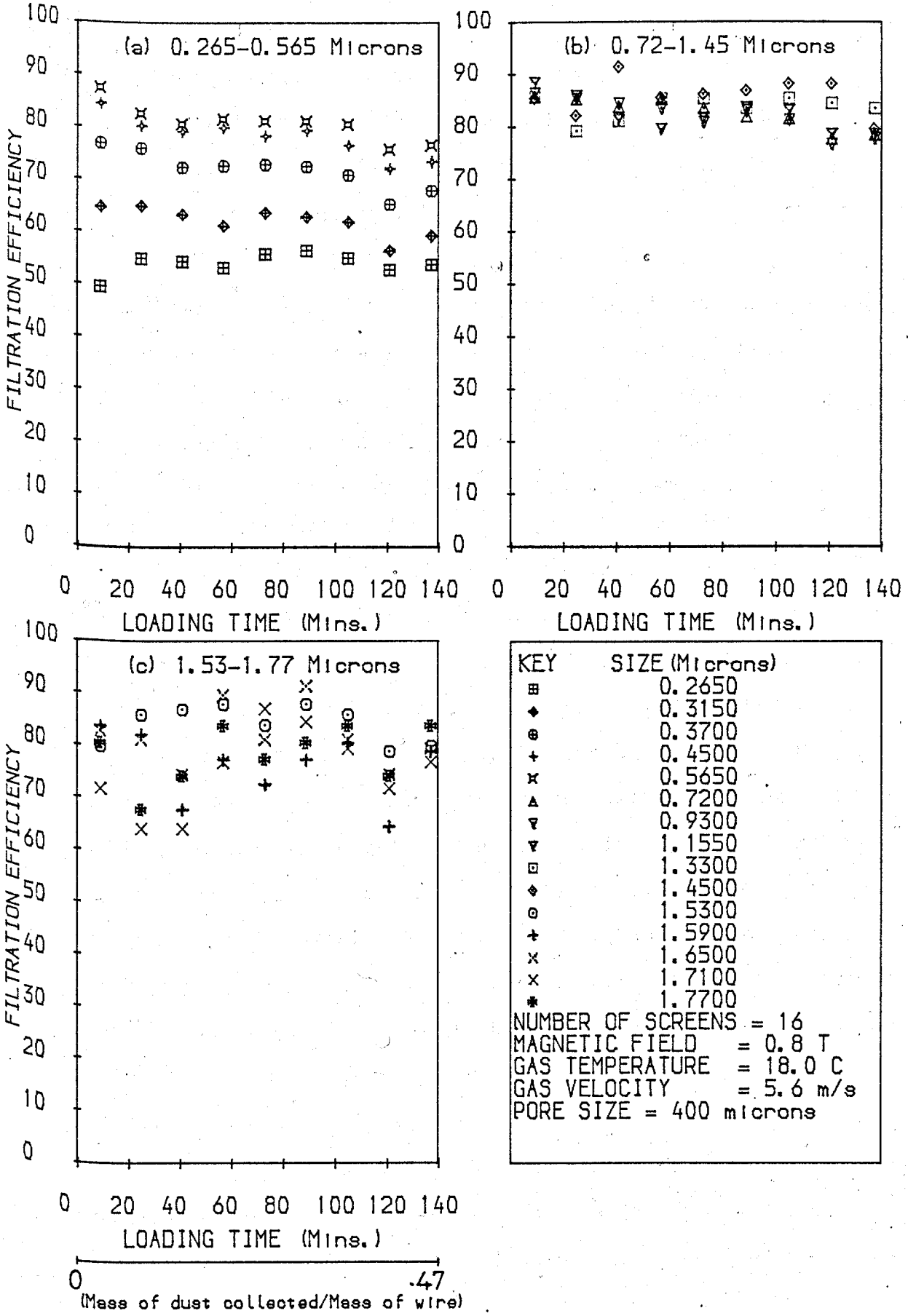

FIG. 8.11: EXPERIMENTAL MATRIX LOADABILITY AT 0.8 TESLA (WOVEN WIRE)

the course of the experiment. The efficiency of collection of the middle and largest ranges of particles was maintained at about 80%, and the performance showed no noticeable deterioration with time up to the end of the test. The mass of dust collected was 0.47 times the mass of the wire.

In the absence of the magnetic field it is clear that the collection efficiency for any particle size is always lower than that obtained for a field of 0.8T. Furthermore, after about fifty minutes the analyser indicated that washing off of the smallest particles was taking place. This can be seen in Figure 8.10(a) as a negative efficiency in the smallest size range. The test was however continued to investigate the continued increase in collection efficiency of the larger particles due to inertial impaction and particle interception. The progressive constriction of the filter pores (observed at the end of the test; PLATE 8.1) by the captured particles further sustained these modes of filtration, especially after forty minutes had elapsed. It must be noted that the maximum collection efficiency obtained was still approximately less than the minimum for 0.8T, thus highlighting the importance of magnetic field. The mass of dust collected for zero-field (0.0T) was 2.3g. The spurious pattern portrayed by plot 8.10(c) signifies that bounce off of larger particles occured. An average high collection can still be deciphered irrespective of the scatter of the experimental points.

The effect of increasing the number of screens can be seen by comparing Figures 8.11 to 8.13 (16, 9, and 21 screens respectively). The initial collection efficiencies for the

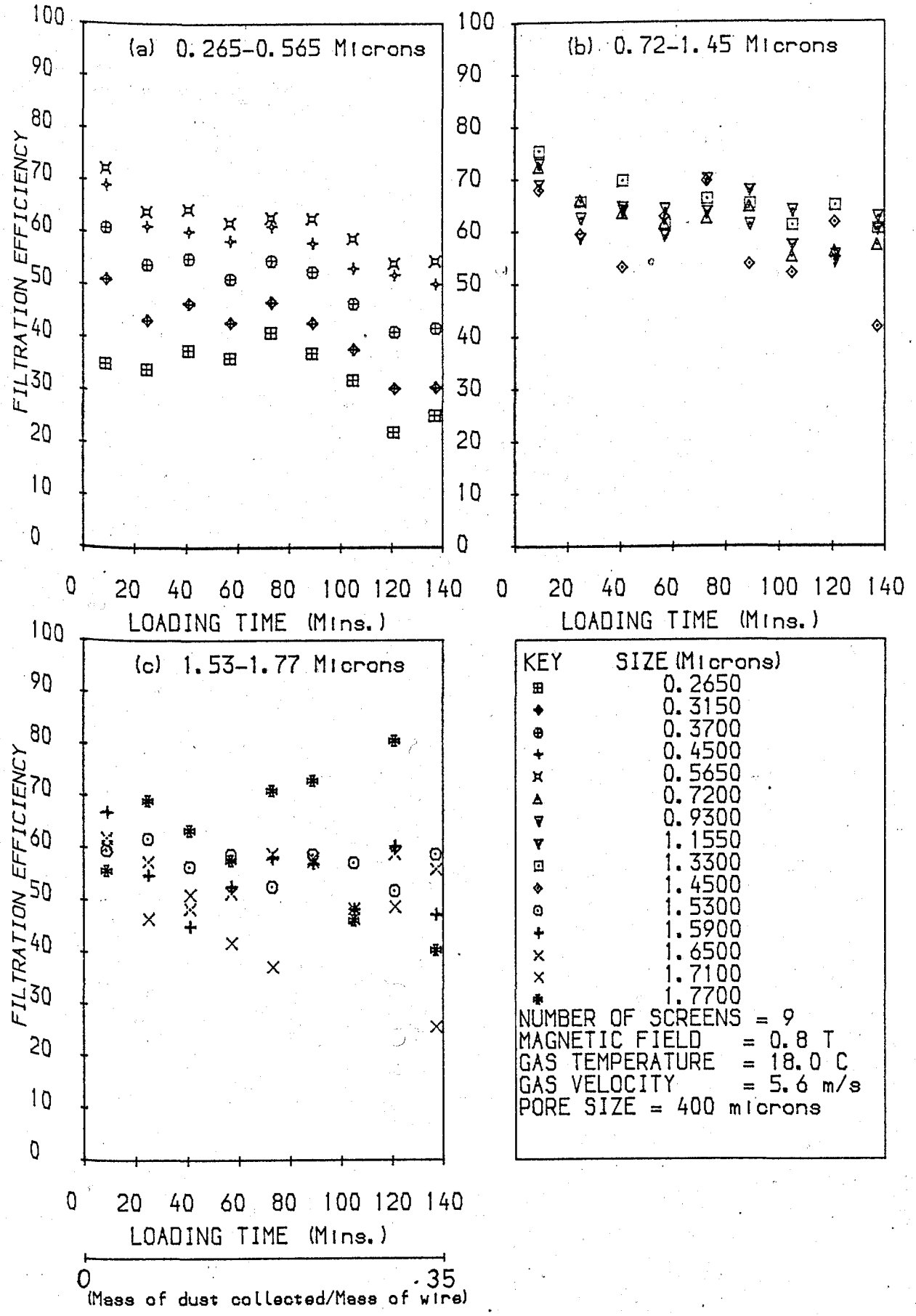

FIG. 8.12: EXPERIMENTAL MATRIX LOADABILITY WITH 9 SCREENS

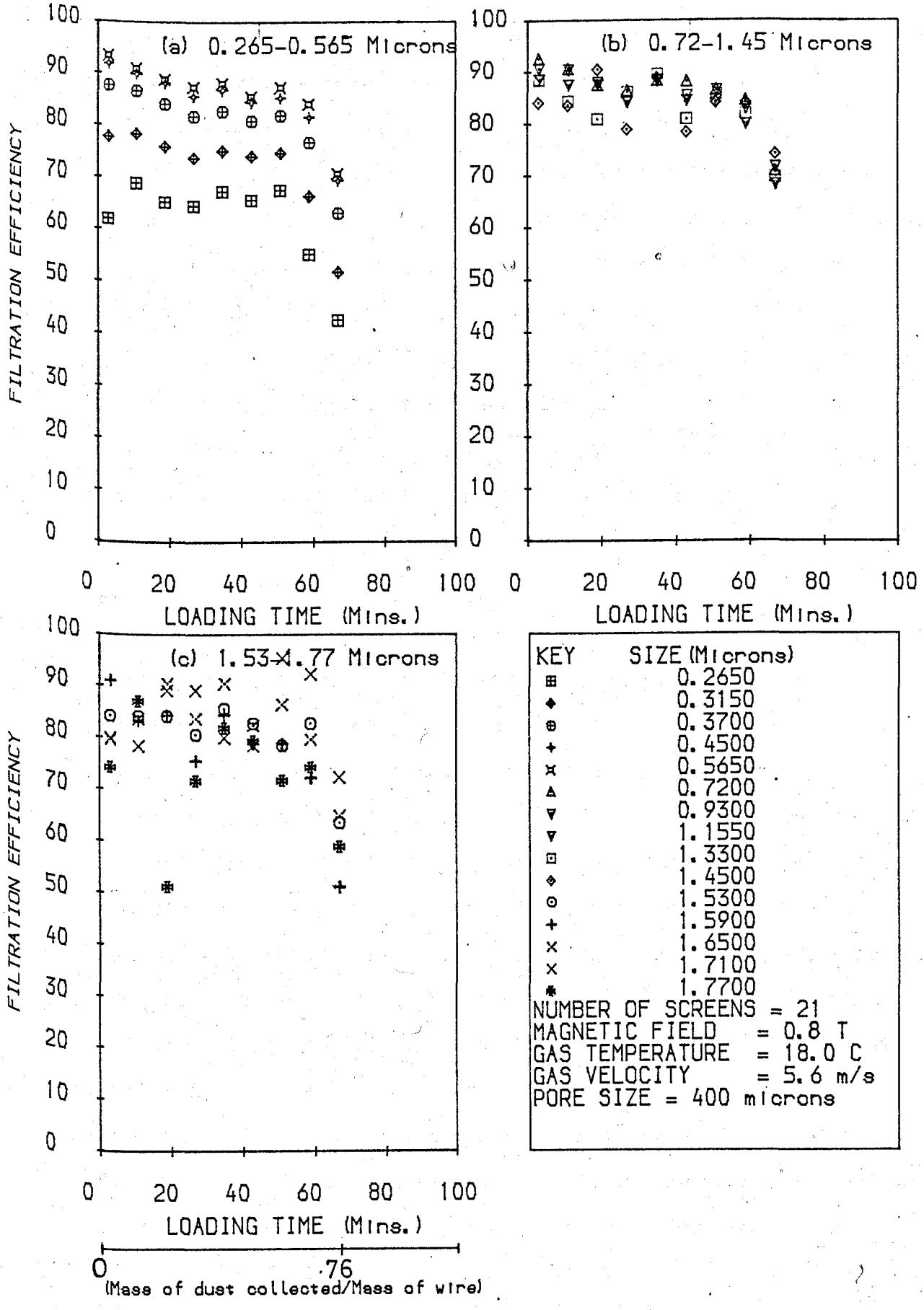

FIG. 8.13: EXPERIMENTAL MATRIX LOADABILITY WITH 21 SCREENS

smallest particles was about 20% greater when 9 screens were used. The larger gradient of Figure 8.12 compared with Figures 8.11 and 8.13 indicates a higher rate of deterioration in particle collection due to loading when fewer screens are used. The mass ratios of the dust collected for increasing number of wire screens are shown in Figure 8.13A. It shows a progressive benefit with the introduction of more meshes. This result is contrary to that obtained from random wires which showed a decreasing mass ratio for increasing packing fractions (Figure 8.6A). Perhaps, the orientation of the meshes helped in contributing to this better profile. However, using more screens does gave an average increase in pressure drop of 4 mm of H_2O per mesh.

The effect of performing the loadability test with 16 screens at the higher velocity of 7.6 m/s is shown in Figure 8.14, (5.6m/s). Comparing this result with Figure 8.11, it is seen that during the first part of the test, the efficiency of capture of the smallest particles was greater for the higher velocity flow. This is due to the increased momentum of smaller particles resulting in more impinging and sticking on the clean filter, although this advantage disappeared with continued loading. The reduced collection efficiency of the bigger particles (Figure 8.14(b) and (c)), is partly due to their relatively higher momentum which results in more particles bouncing off or missing the wires completely and some of those already captured being re-entrained. This was further enhanced by the poor surfaces provided by the captured CuO dust as a result of its low susceptibility. This particular test shows that an

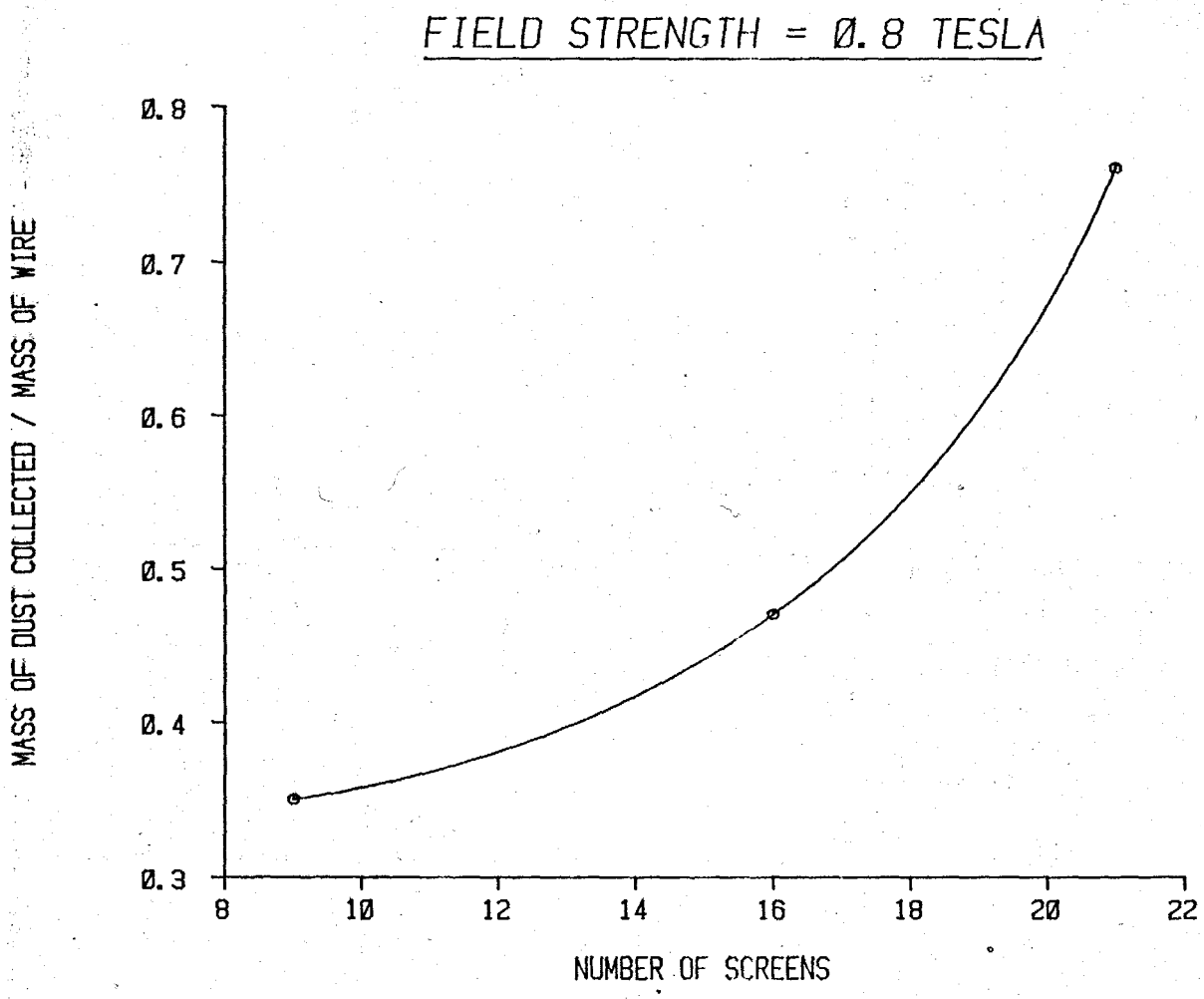

FIG. 8.13A EFFECT OF INCREASING NUMBER OF SCREENS ON MATRIX LOADABILITY (VELOCITY = 5.6 M/S)

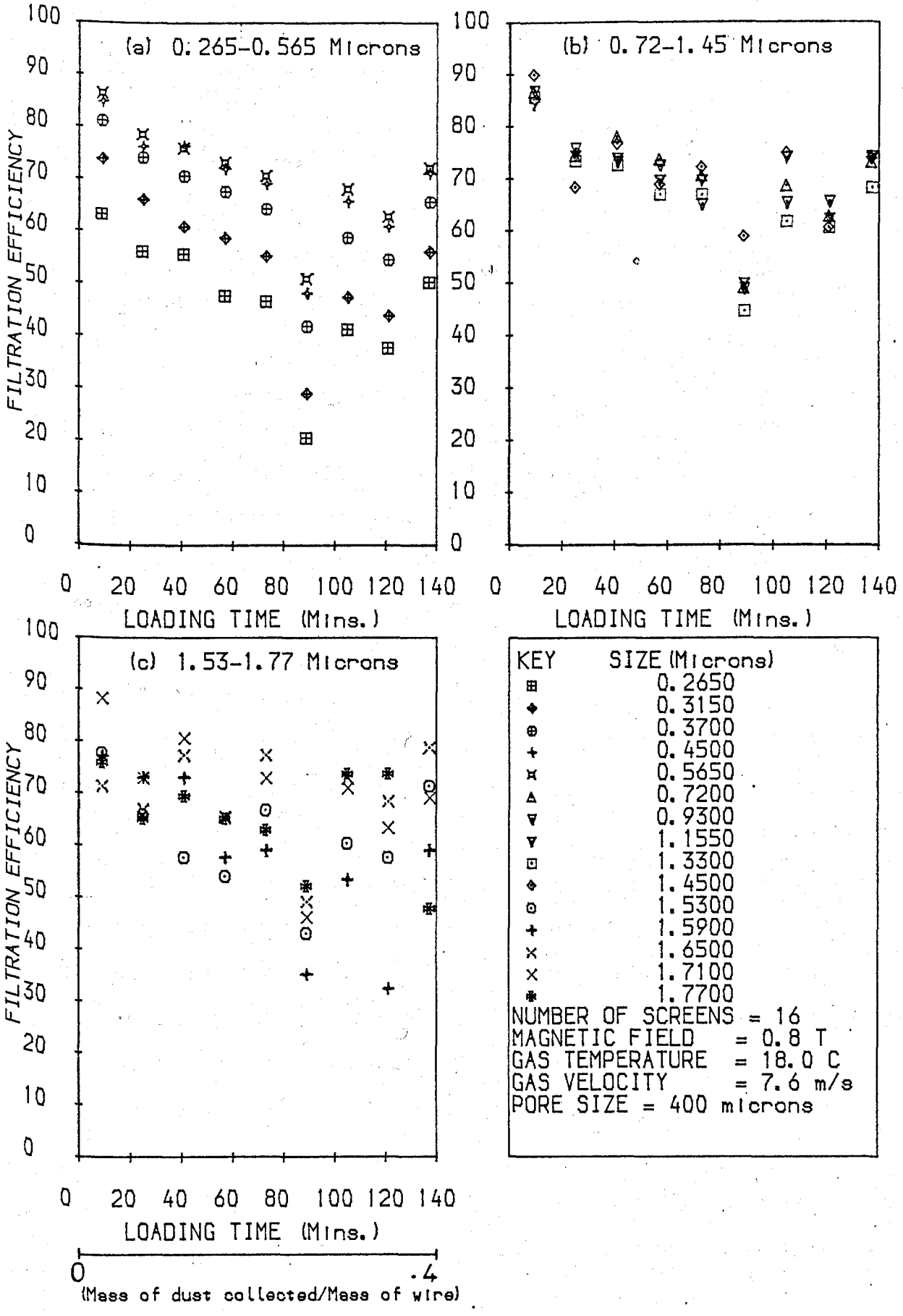

FIG. 8.14: EXPERIMENTAL MATRIX LOADABILITY AT 7.6 M/S (WOVEN WIRE)

increased flow velocity from 5.6 m/s to 7.6 m/s caused an overall decrease in dust capture.

8.4 Loadability of Woven Wire with PVC Separators

Another optimal loadability test conducted was to examine the effect of separating the meshes with 5mm PVC rings. This produced a very low collection efficiency (compared to Figure 8.11) as shown in Figure 8.15. The poor results obtained were probably due to re-dispersal of dust by the flow wakes behind the screens as opposed to the concentrated channelling effects of stacked filters which are in contact with each other. It is hoped that preferential separation of binary mixtures can use the above phenomenon, especially where a ferromagnetic material is to be separated from a paramagnetic one.

8.4.1 Experimental Capture Radius (X_e)

Experimental capture radii were calculated from the corresponding values of collection efficiencies already determined in the loadability tests for various ranges of major operating parameters. These were plotted against equivalent particles Stokes number (K), calculated from the expression given in Chapter Five. Before the use of the expression over the required range of particle size, (0.265-1.77 microns), it was necessary to check the validity of the expression over the range of the particle size under consideration. In the derivation of the equation of particle motion (equations 5.45 and 5.46), potential flow was used which required the wire Re to be greater than ten. Also, as the viscous force parameter on the particle is

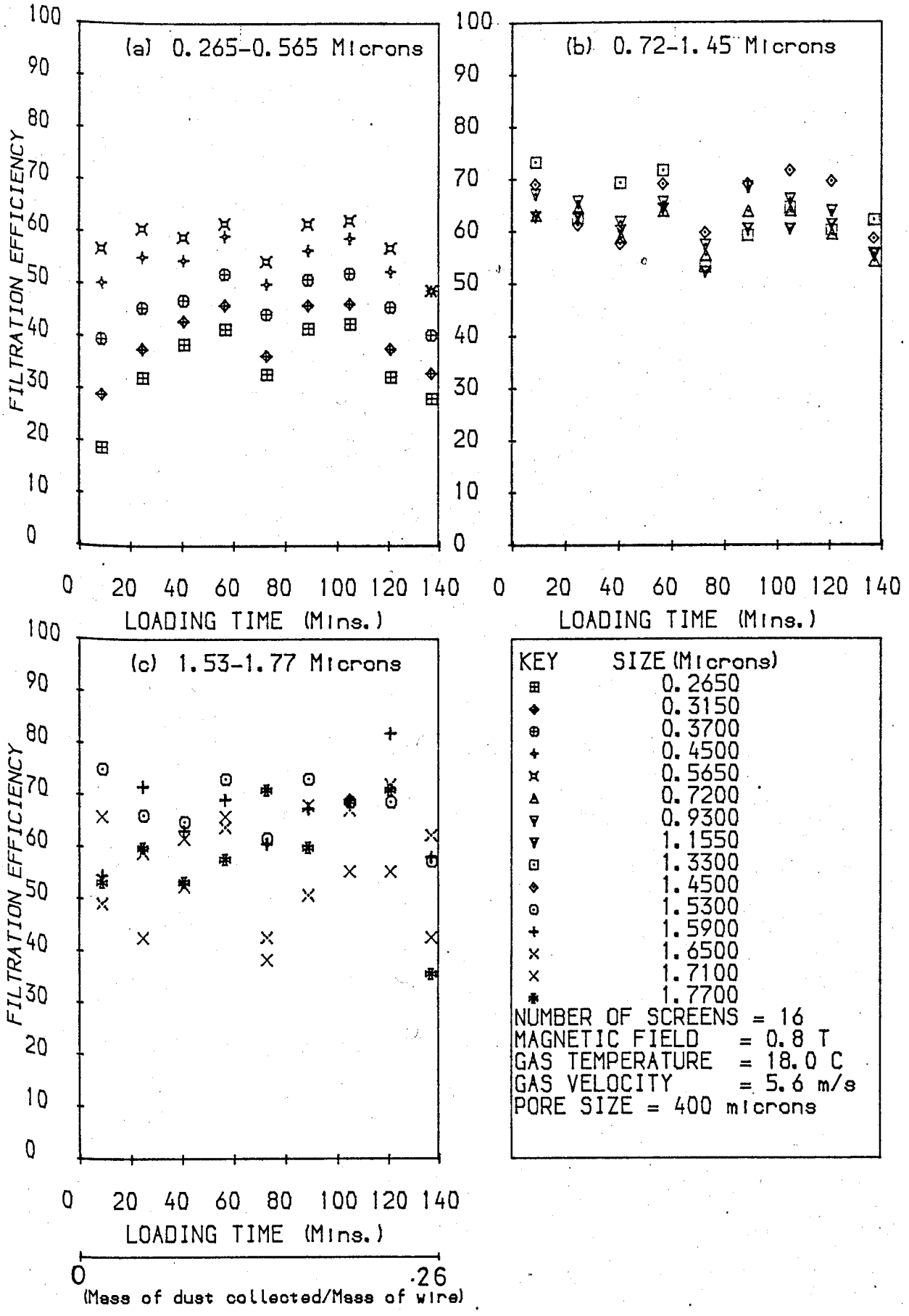

FIG. 8.15: EXPERIMENTAL MATRIX LOADABILITY OF WOVEN WIRE WITH 5 CM PVC SEPARATOR RINGS

based on Stokes law, it was imperative for the particle Re to be less than unity. For a wire of diameter 50 microns and flow velocity 5.6 m/s, the Re is given by :

$$Re = \frac{1.239 \times 5.6 \times 50\times10^{-6}}{18.12\times10^{-6}} = 19.15 \qquad (>10.0)$$

For a maximum particle size of 1.77 microns, and maximum flow velocity of 7.6 m/s , the Re becomes :

$$Re = \frac{1.239 \times 7.6 \times 1.77\times10^{-6}}{18.12\times10^{-6}} = 0.91 \qquad (<1.0)$$

Thus, the two conditions for using the expression above for K are satisfied. The maximum value of the ratio of the magnetic velocity to the fluid velocity in this study is 1.5×10^{-3} .

The expression used for the calculation of the experimental capture radii is given in Chapter Six (equation 6.31). A single E_f value of 0.35 was used to calculate the whole results. Figure 8.15A shows the X_e values for increasing field strength at a fixed packing fraction of 0.75%. The first observation is the increasing capture radius for increasing field strength or magnetic force parameter, W, at any given Stokes number, K, up to K=4. The benefit is most significant for the field of 0.8T. What is seen here is the dominance of magnetic force parameter over inertia. At k>4, (ie. low viscous force), the effect of particle inertia started to become significant because of the large particle sizes. This manifested in the scatter of the experimental points. In this region also, the effect of particle

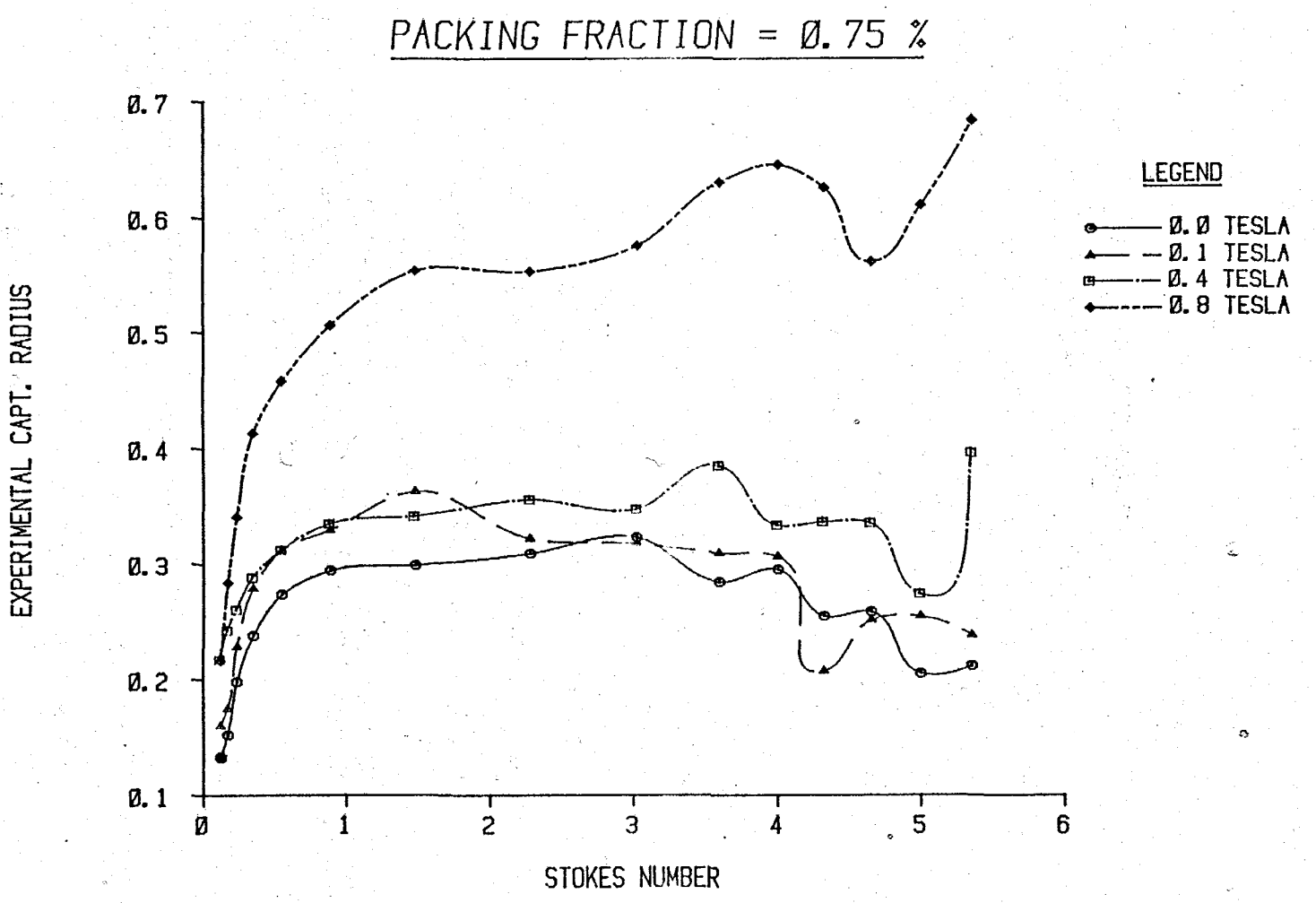

FIG. 8.15A EFFECT OF MAGNETIC FIELD ON EXPERIMENTAL CAPTURE RADIUS (V = 5.6 M/S)

previously pointed out. For increasing K at constant W and A, there is a remarkable increase of X_e for small ranged particles with almost no change in medium sized particles. This suggests that there is a range of sizes over which X_e was constant during the filtration process. There is no established pattern for the largest sized particles.

The effect of increasing the packing fraction at constant W is shown in Figure 8.15B. Contrary to what is expected, the addition of more wires in the matrix at constant K, is not necessarily beneficial as after a critical value (determined in Figure 8.6B), the wires become increasingly useless.

Varying K, but keeping F constant, produced similar results as obtained previously; that is significant gain in X_e in the low particle range, nearly constant X_e for mid range, and no pattern for the largest particles. Comparison of Figures 8.15A and 8.15B reveal that the change in F (ie. $\frac{l_s}{2}$) is more sensitive to X_e than W at low magnetic field strength. The low values of X_e for 1.0 % packing fraction is attributed to interference effect already pointed out in loadability discussion.

The effect of increasing fluid velocity is shown in Figure 8.15C. The lower velocity of 5.6 m/s gave higher X_e values, although the mass ratio of dust collected for it was lower than that obtained for 7.6 m/s. This can be interpreted as increased inertia which is supposed to give a better result as all values of X_e less than 1.0, but this is not the case in Figure 8.15C. The discrepancy arose from Figure 8.4 which gave higher initial efficiency than Figure for an initial period of

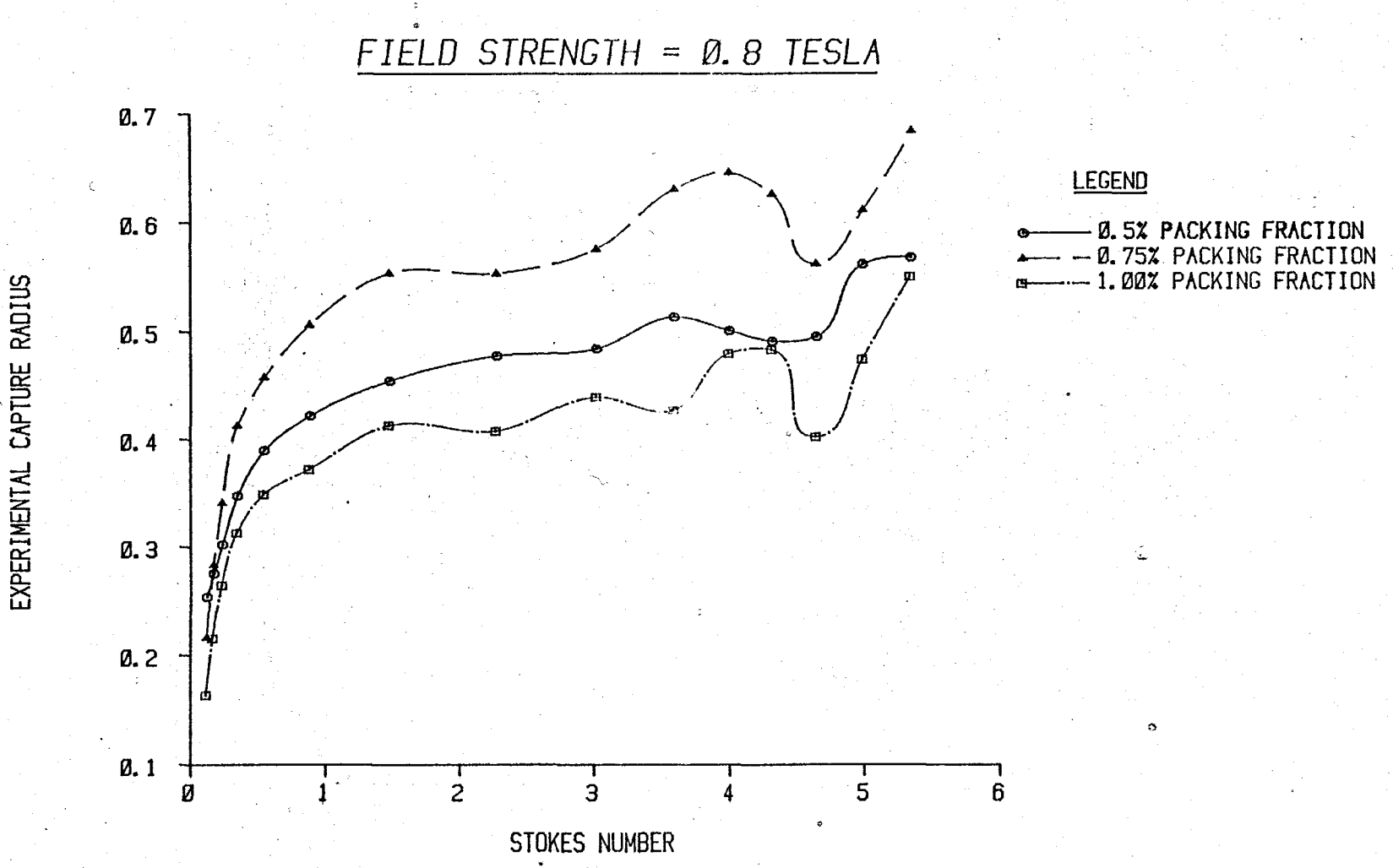

FIG. 8.15B EFFECT OF PACKING FRACTION ON EXPERIMENTAL CAPTURE RADIUS (V = 5.6 M/S)

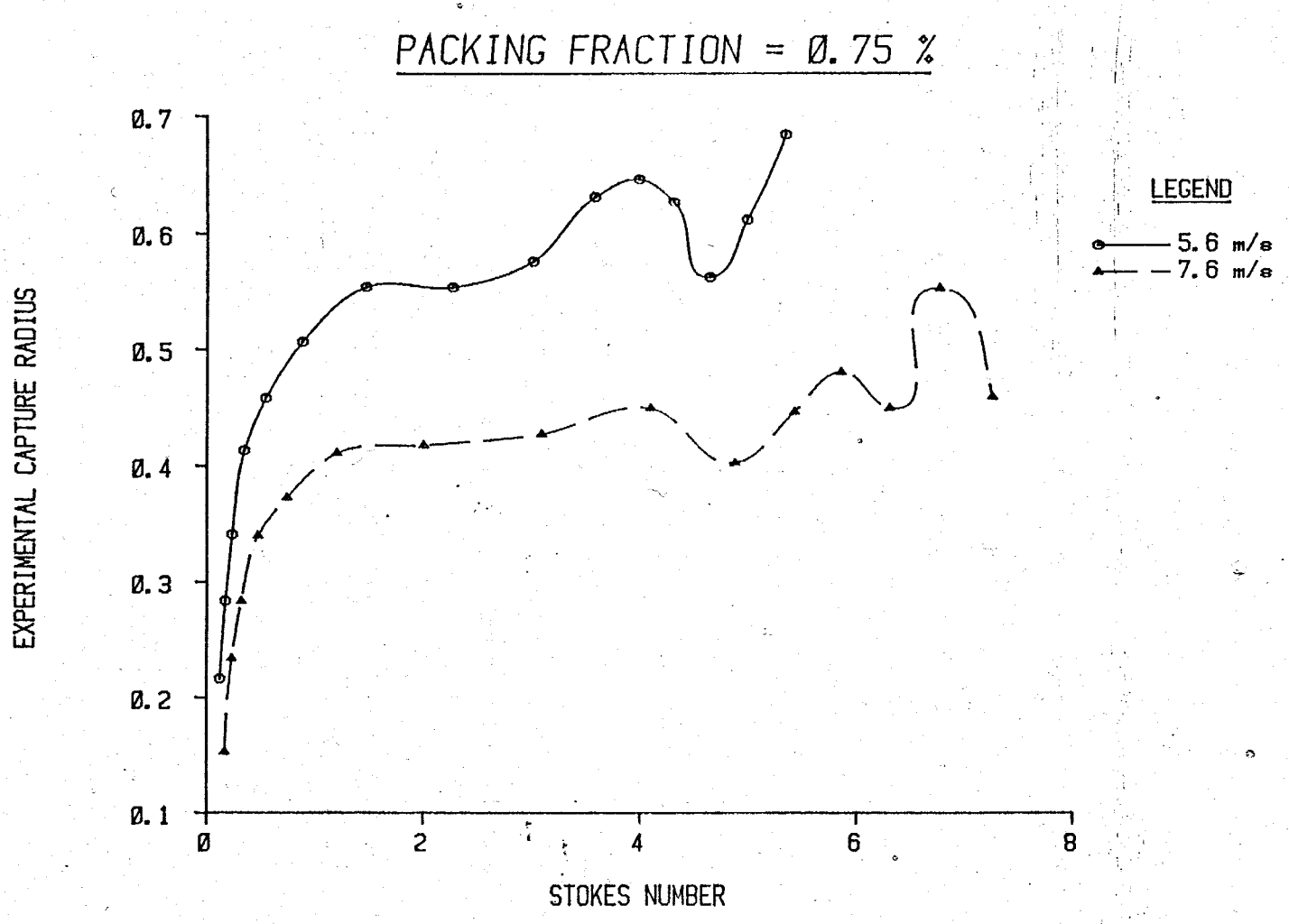

FIG. 8.15C EFFECT OF FLUID VELOCITY ON EXPERIMENTAL CAPTURE RADIUS (H = 0.8T)

about 20 minutes.

Comparison of the results obtained for two long filters of 15cm and 20cm at 0.4T show larger X_e for 20 cm filter (Figure 8.15D). This is because more wire surfaces are available for particle capture which in smaller matrix may be masked. The sharp increase in X_e values observed in the previous results are absent here, instead there is a progressive increase of X_e for all particles. Even the high oscillatory behaviour of the largest set of particles seem attenuated in this case. This can be explained by the particle reduced momentum at the rear end of the filter. It is possible that by the time the large particles arrived at the back of the filter they would have exhausted their kinetic energy and therefore, have more chance of being held before exiting from the matrix. This explanation particularly fits the reason for diminished particle bounce off. Another possible explanation, although less obvious lies in the flow velocity profile, which because of the length of the filter matrix comes out flat (see Chapter Four). This disperse the particles more, thus enhancing their chances of coming in contact with larger wire surfaces.

The values of X_e calculated from increasing number of wire screens are shown in Figure 8.15E. The profile of the curves are different to those already discussed. The only similarity is with the smallest range of particles which showed a handsome increase in X_e values. For particle sizes greater than 0.72 microns, their critical radius fell with increasing K in all the cases. Magnetic interference is believed to be the major reason for this unexpected behaviour because of the pattern of

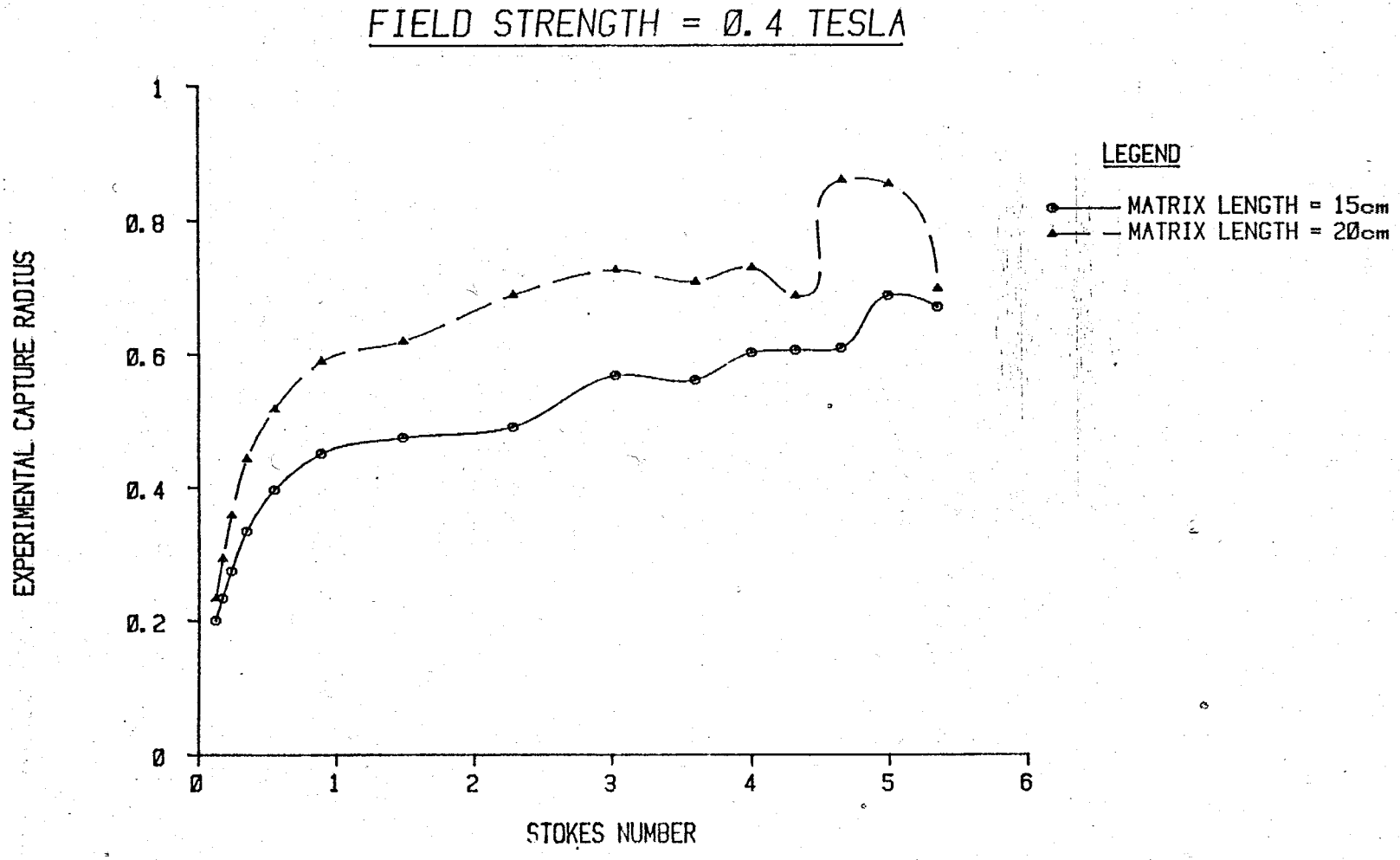

FIG. 8.15D EFFECT OF MATRIX LENGTH ON EXPERIMENTAL CAPTURE RADIUS (F = 0.5%)

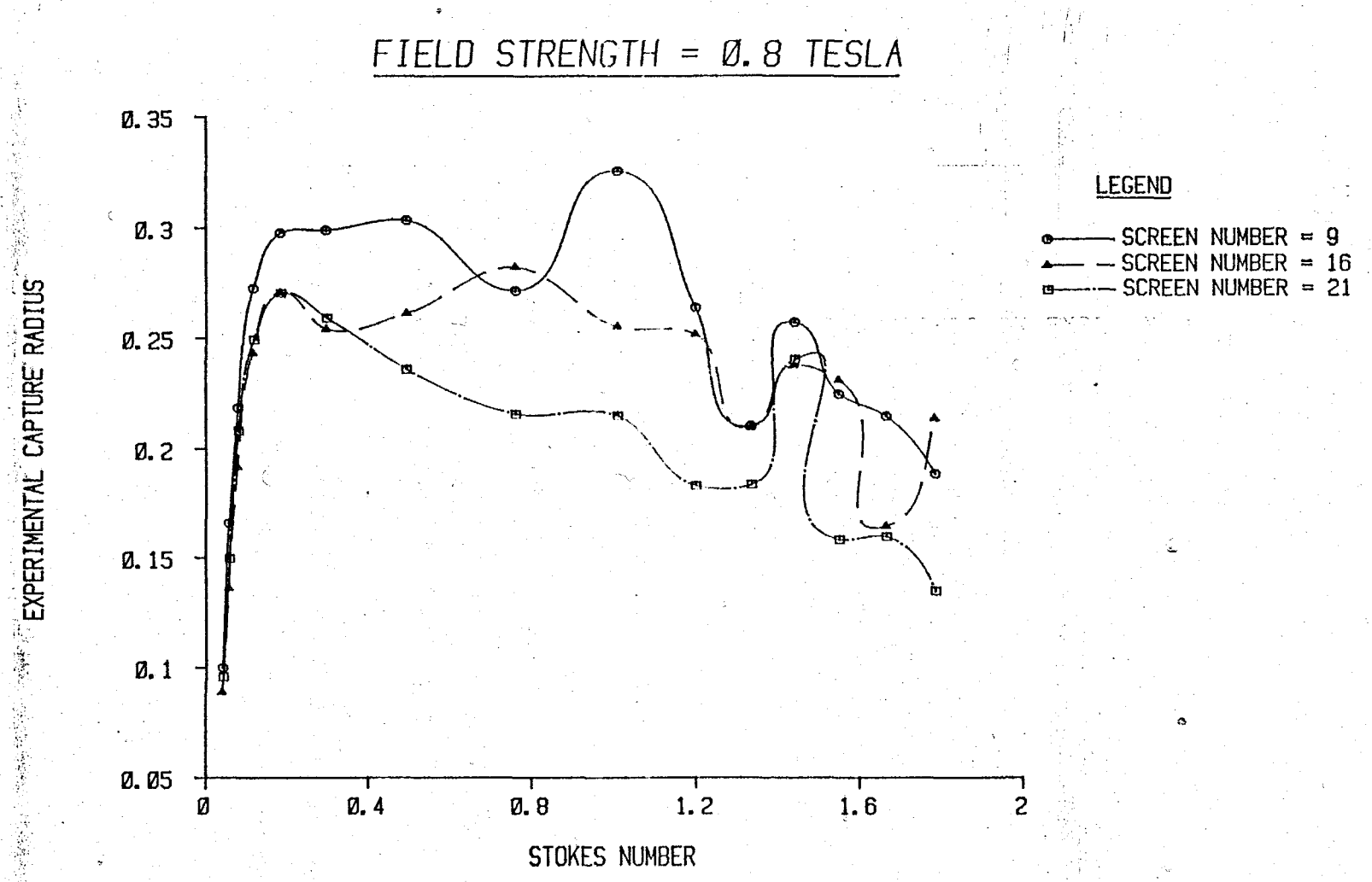

FIG. 8.15E EFFECT OF INCREASING NUMBER OF WIRE MESHES ON EXPERIMENTAL CAPTURE RADIUS (v = 5.6 M/S)

arrangement of the meshes in the matrix.

Unfortunately, none of the results above were compared with the theoretical capture radii published by Lawson [56] because the values of the magnetic force parameter used in this study are much smaller than his range of values.

8.5 Clean Filter Collection Efficiency

Presented below are results of clean filter collection efficiencies plotted against particle size range of 0.2650 to 1.7700 microns. These diagrams provide filtration information at the beginning of the experiment when the filter was still in its virgin state and 30 minutes later. The effect of three main operating parameters- packing fraction, magnetic field, and flow velocity- are illustrated. Besides providing information on the performance of the filter, it also helps in the verification of the filter collection model derived in Chapter Five to predict theoretical collection efficiencies. Some of these results may have been read from the loadability results from the previous plots, but to avoid any difficulty that might arise from following a particular trend, the results are re-plotted in this form.

The results obtained from varying the packing fraction over a range of magnetic field strength is shown in Figures 8.16 and 8.17. At 0.4T and flow velocity of 5.6 m/s (Figure 8.16), the difference between the curves are minimal, but increased after 30 minutes had elapsed. The filter with 0.005 packing density seems to have performed as well as that of 0.0075 packing density at the start of the test. The reason for this behaviour in this

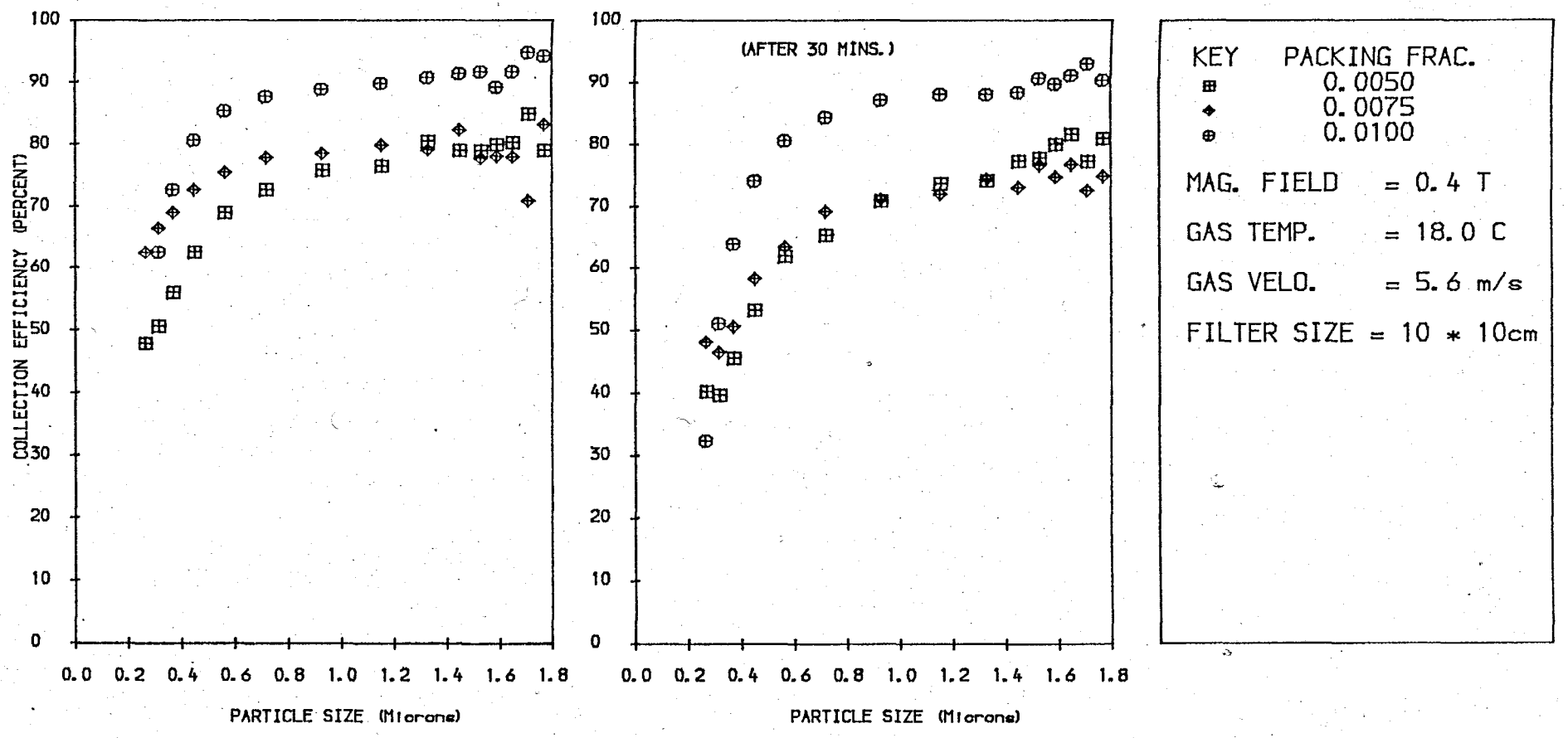

FIG. 8.16: EFFECT OF PACKING FRACTIONS AT 0.4 TESLA

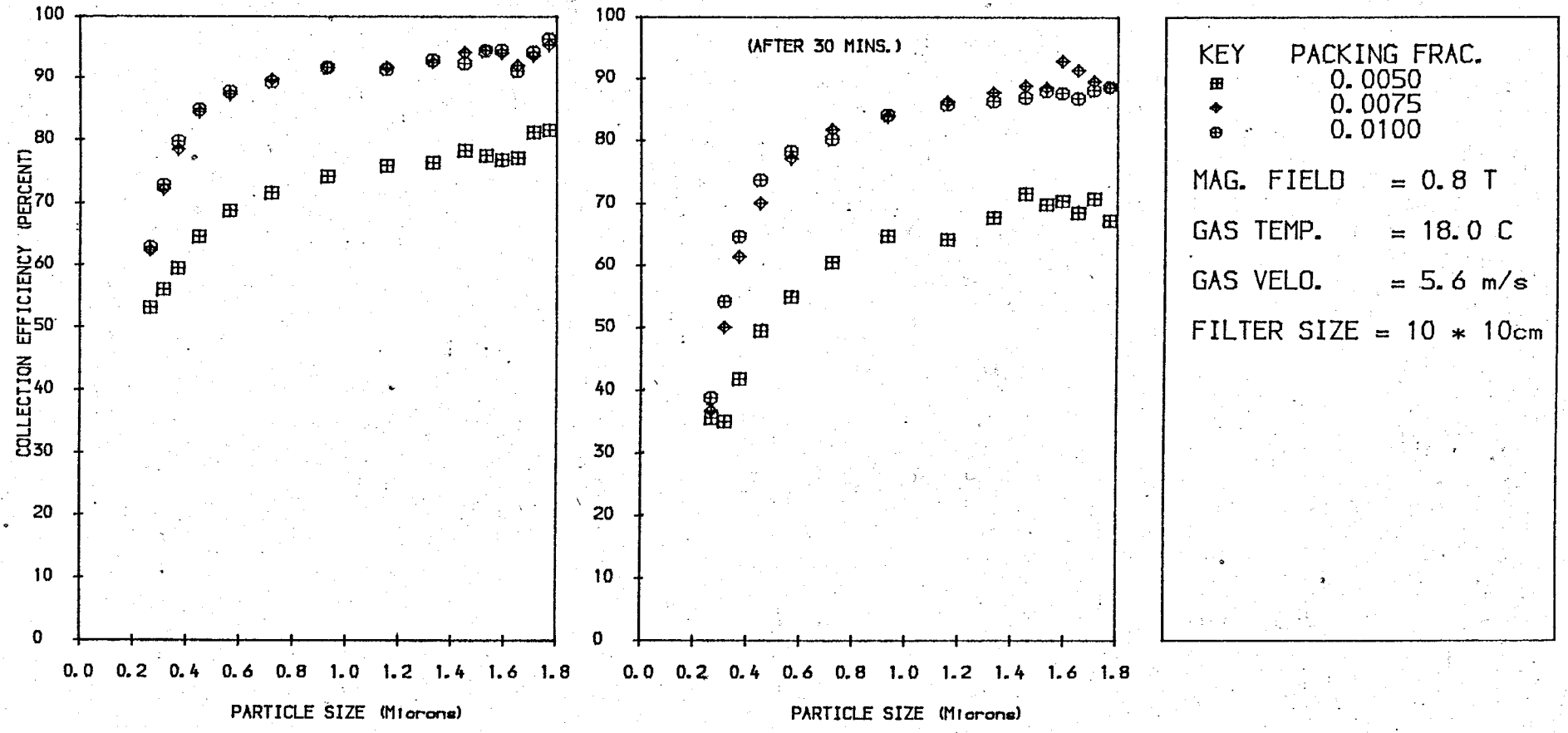

FIG. 8.17: EFFECT OF PACKING FRACTIONS AT 0.8 TESLA

particular run may have been due to a more uniform wire loading in the case of 0.005 packing density. A more familiar effect is observed from the results in Figure 8.17, where the magnetic field strength had been increased to 0.8T. Here, the application of the filters with 0.0075 and 0.01 packing produced similar results. This tend to support the previous explanation that there is a critical packing fraction for a given size of matrix above which additional wire becomes ineffective. There is also a noticeable drop in collection efficiency after 30 minutes. A remarkable sustained filtration efficiency of particles was also maintained. Although not presented, results of similar tests but with 0.0075 packing fraction at 0.4T and 0.8T are also available. At a much higher flow velocity of 7.6 m/s, Figure 8.18 shows a comparison of the three packing fractions used. When compared with Figure 8.17, the results are similar.

A comparison of the two flow velocities (5.6 m/s and 7.6 m/s) applied are shown in Figure 8.19 at a packing fraction of 0.010. As already pointed out in the discussion of the flow velocity on particle loadability, drawing firm conclusions are difficult. The results show no difference between the two tests in this case. This supports the fact that at relatively high packing fraction, the effect of velocity is not so obvious in these investigations. Results obtained from similar tests at other packing fractions varied within a margin of less than 10%.

It is also evident from these graphs that except for very low packing fractions, (about 0.5%), the initial collection of all filters tested are comparable. Hence, it may be economically viable to introduce variable power supply in HGMF

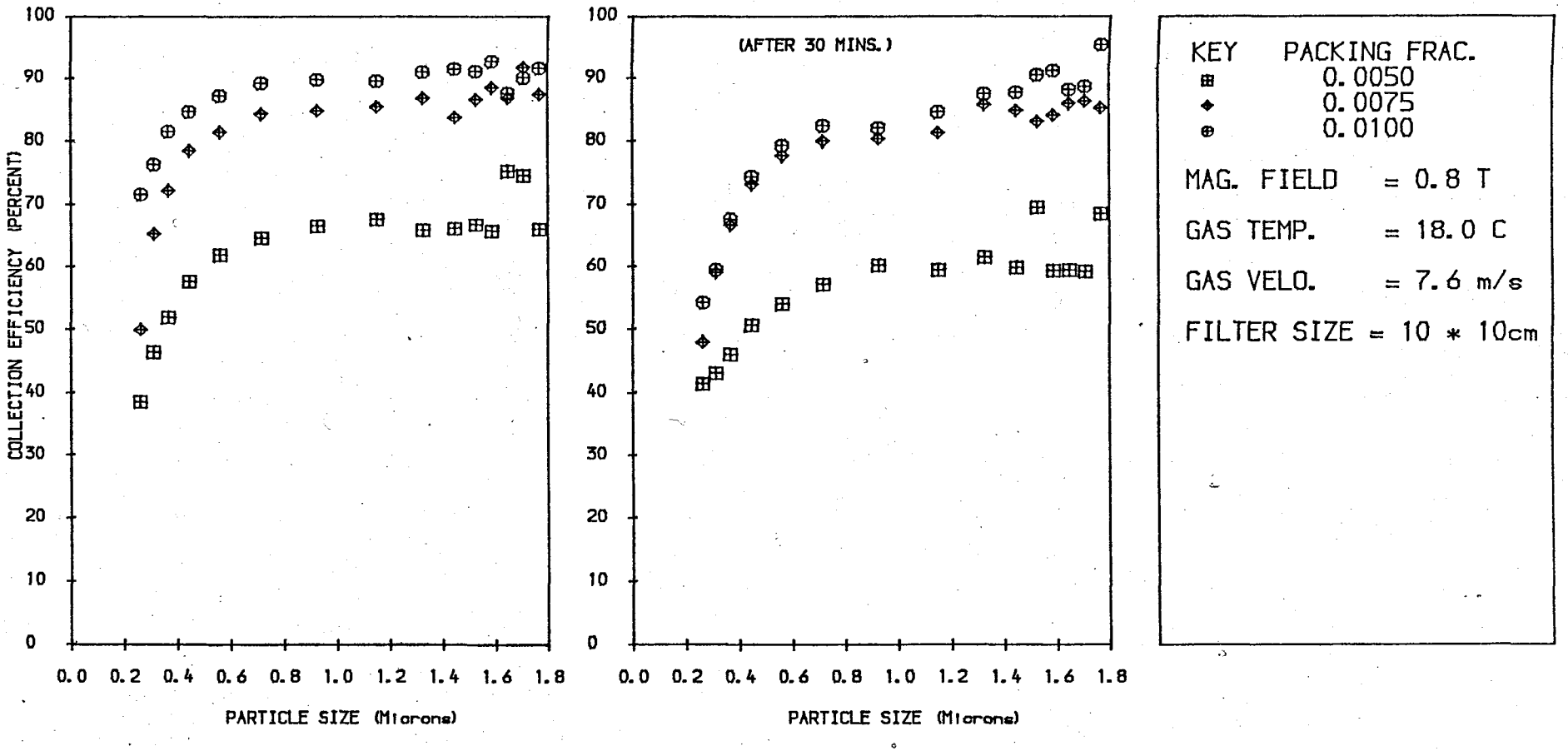

FIG. 8.18: EFFECT OF PACKING FRACTIONS AT A FLOW VELOCITY OF 7.8 M/S

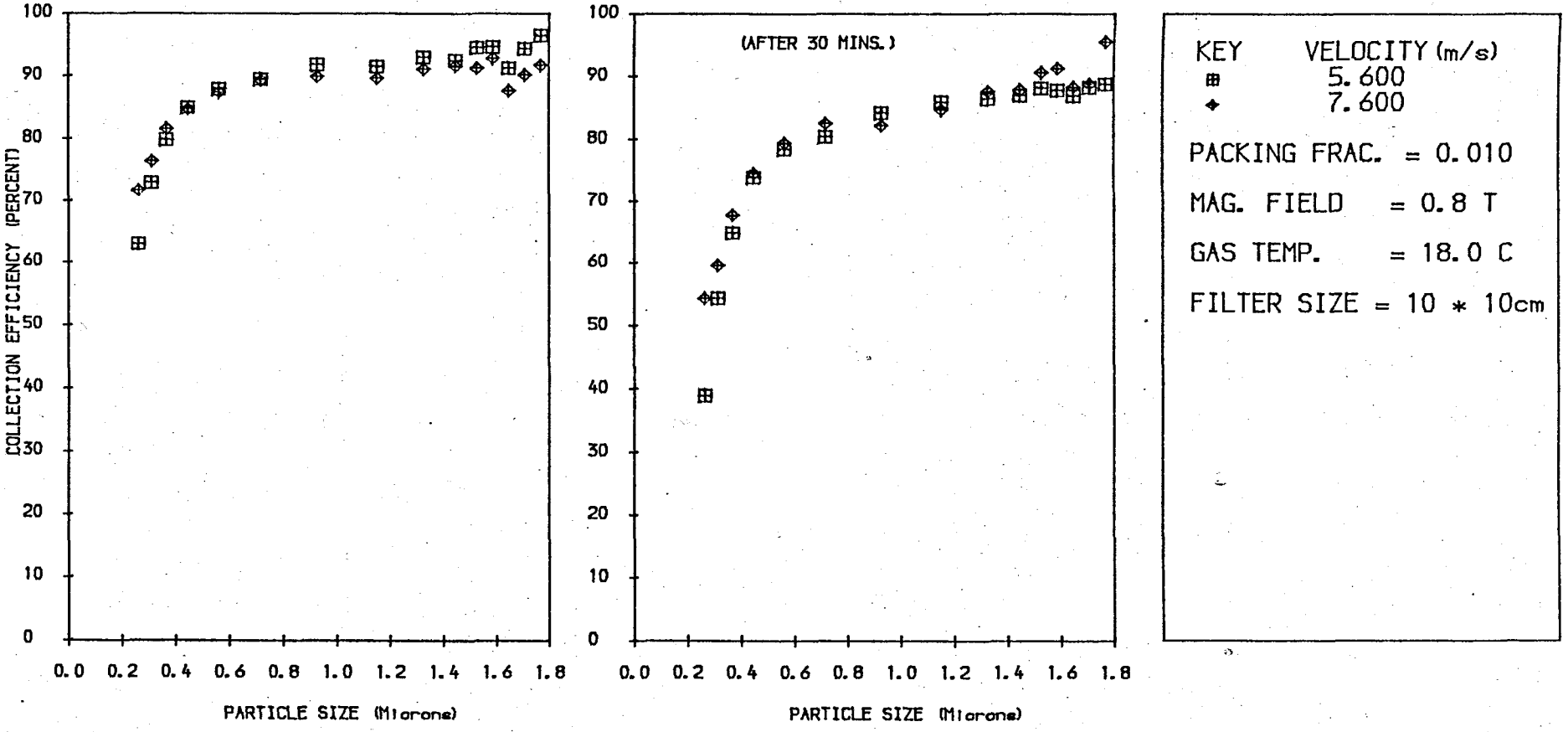

FIG. 8.19: EFFECT OF FLOW VELOCITY AT 0.01 PACKING FRACTION

installations during the filter loading up period.

The results obtained for an increasing number of screens at a magnetic field strength of 0.8T is shown in Figure 8.20. As expected, the results show better performance for an increased number of screens, although the difference between 16 and 21 screens was very small. This particular result will prove useful in the theoretical predictions of woven wire collection efficiency described in the next section.

8.6 Collection Efficiency Based on Total Particle Count

General industrial applications of HGMF require a less detailed specification of equipment. In this case, particle global collection efficiency defined within a known size range is a more suitable and convenient parameter. For this purpose, some of the loadability results were plotted in the form shown in Figure 8.21 for random wires and Figure 8.22 for woven wires. These Figures compare the filter collection efficiencies obtained from experiments performed at different magnetic fields and packing fractions. These efficiencies were computed from the total particle count from the spectrometer.

It must be emphasized that this form of presentation of particle collection efficiency can mask information and must be interpreted carefully. For example, the continual increase in collection efficiency of particles above 0.45 microns after 40 minutes as seen in Figure 8.10 is completely hidden in Figure 8.22. The effect of sloughing off of particles portrayed by the loadability curves is also not apparent. Instead, an average collection efficiency of about 22% was maintained throughout as

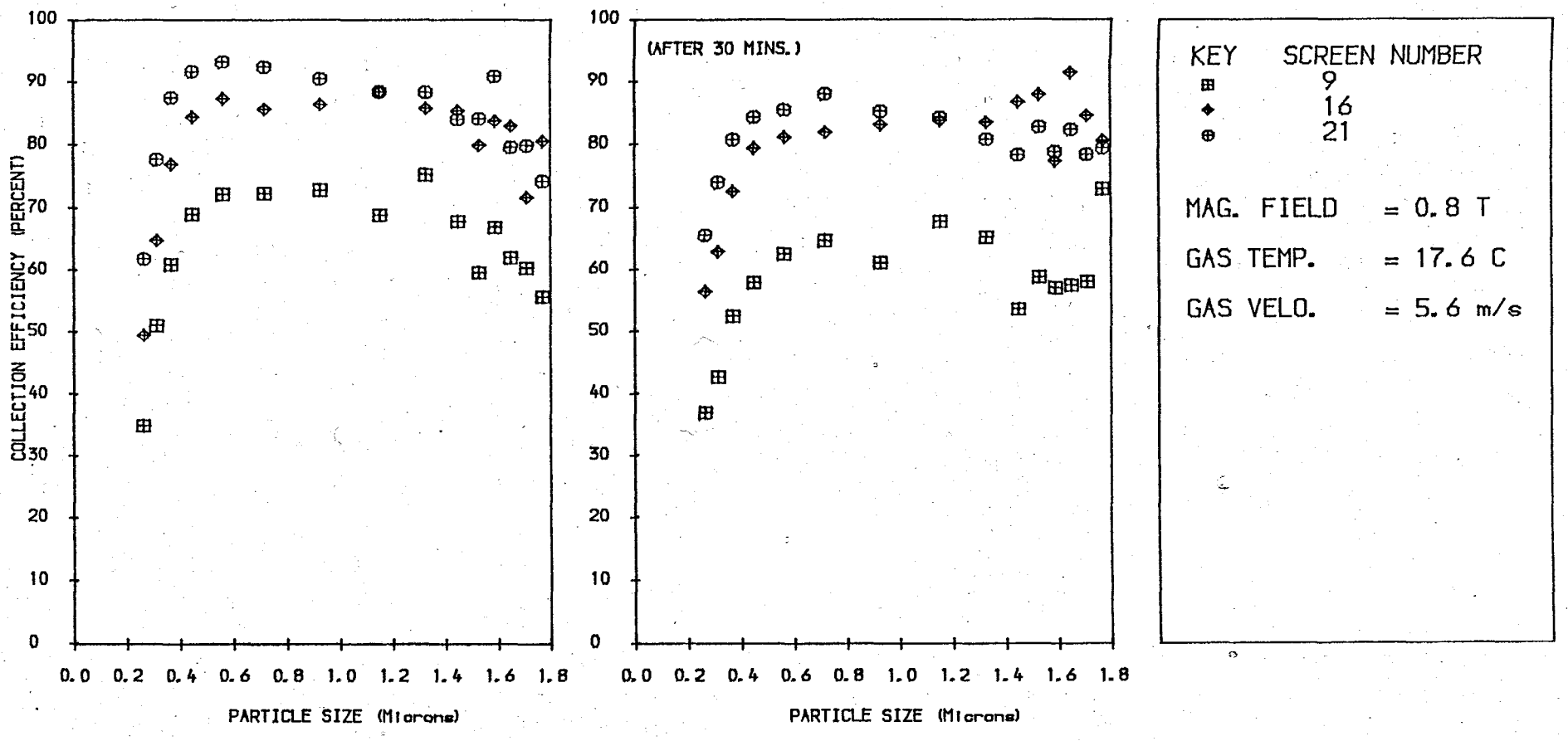

FIG. 8.20: EFFECT OF INCREASING NUMBER OF WIRE SCREENS AT 0.8 TESLA

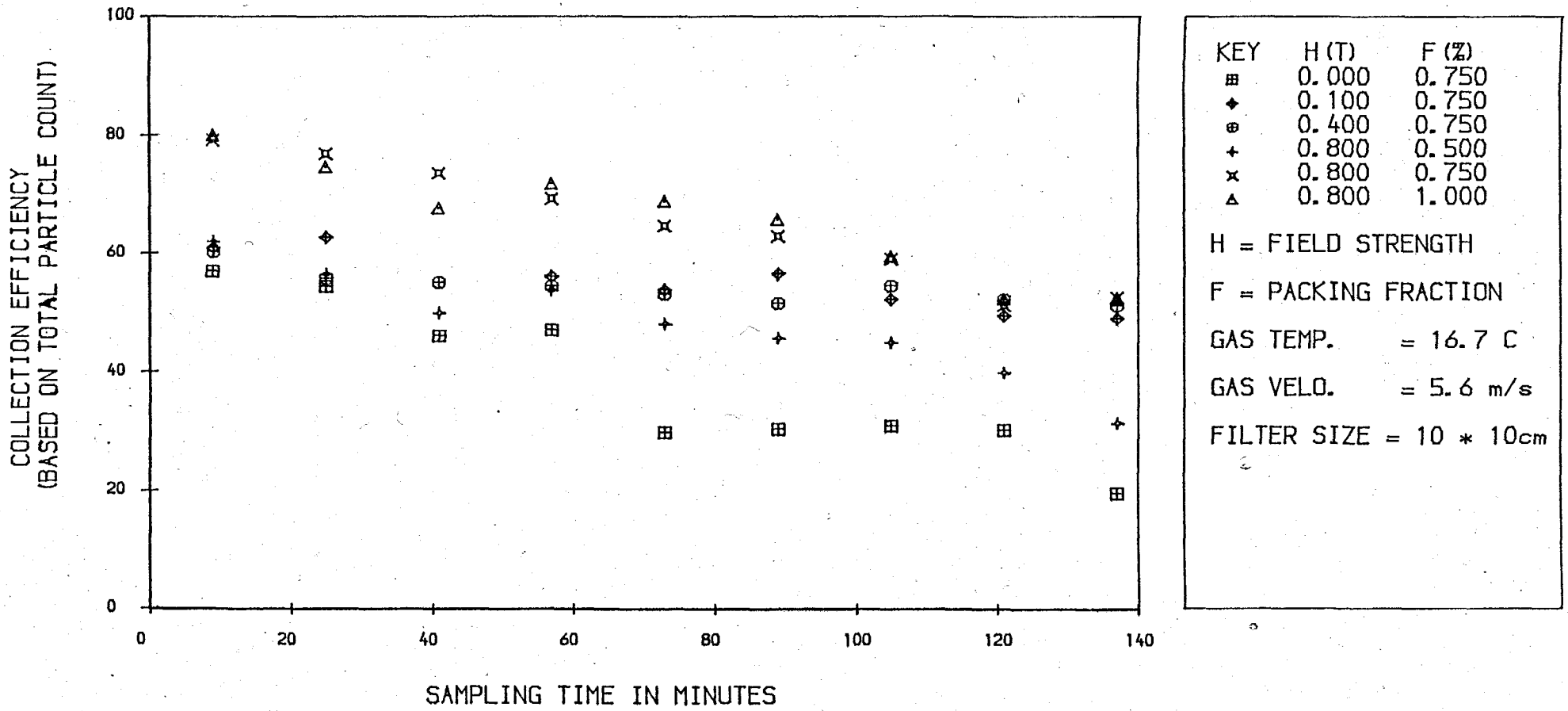

FIG. 8.21: COMPARISON OF PARTICLE COLLECTION EFFICIENCY BASED ON TOTAL PARTICLE COUNT (RANDOM WIRE)

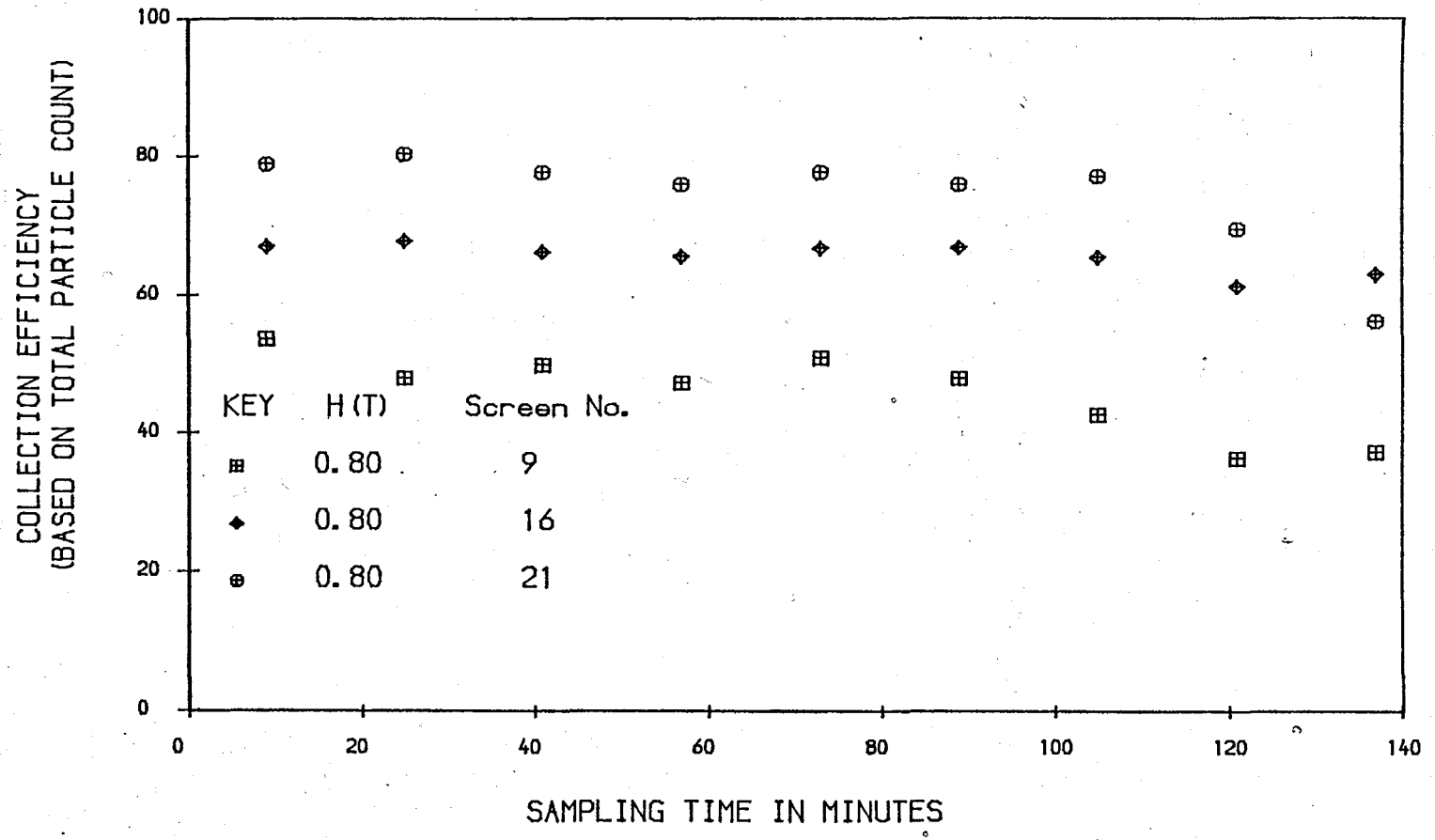

FIG. 8.22: COMPARISON OF PARTICLE COLLECTION EFFICIENCY BASED ON TOTAL PARTICLE COUNT (RANDOM WIRE)

shown.

8.7 Theoretical Collection Efficiency

The comparison between the theoretical study and experimental work can be made in two ways. The first is to calculate the experimental radii from the test data and compare them with theoretical predictions. The second is to calculate the efficiencies of particle collection based on the theoretical capture radii and compare them with those obtained from experiment. The later was adopted. This is because it offers a more practical approach and makes similarities and differences of both procedures more apparent. From these results, explanations can be sought that have obvious practical meaning.

Figure 8.23 shows the clean filter collection efficiency predicted with the model presented in Chapter Six. The curves are for a filter with 0.0075 packing fraction with a field strength of 0.80T and gas velocity of 5.6 m/s. The effectiveness factor, E_f , which was the only undetermined factor in equation (6.31) was the first optimized; that is varied until the best fit to the experimental data points were obtained. The values applied were 0.20, 0.22, and 1.00. E_f of unity predicted a 100.00% collection for almost all particle ranges under investigation. This is unrealistic when compared with experimental results obtained with the same parameters. The reduction of E_f to 0.22 predicted collection efficiency nearest to the experimental one. This is then compared with a similar result obtained from experiment (Figure 8.24). The most apparent difference lies in the larger particles (ie. 0.720-1.77) which have been under

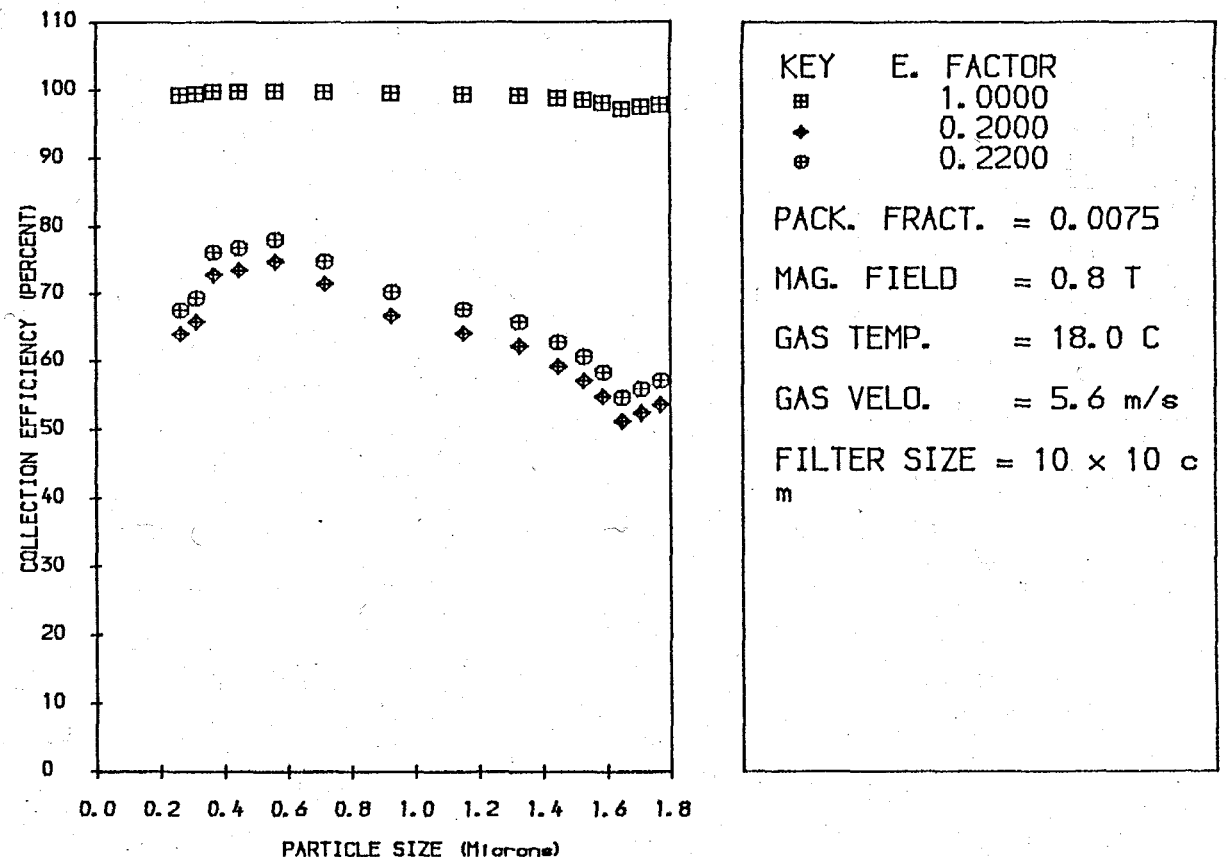

FIG. 8.23: THEORETICAL COLLECTION EFFICIENCY PREDICTED FROM ISOLATED WIRE MODEL (RANDOM WIRE)

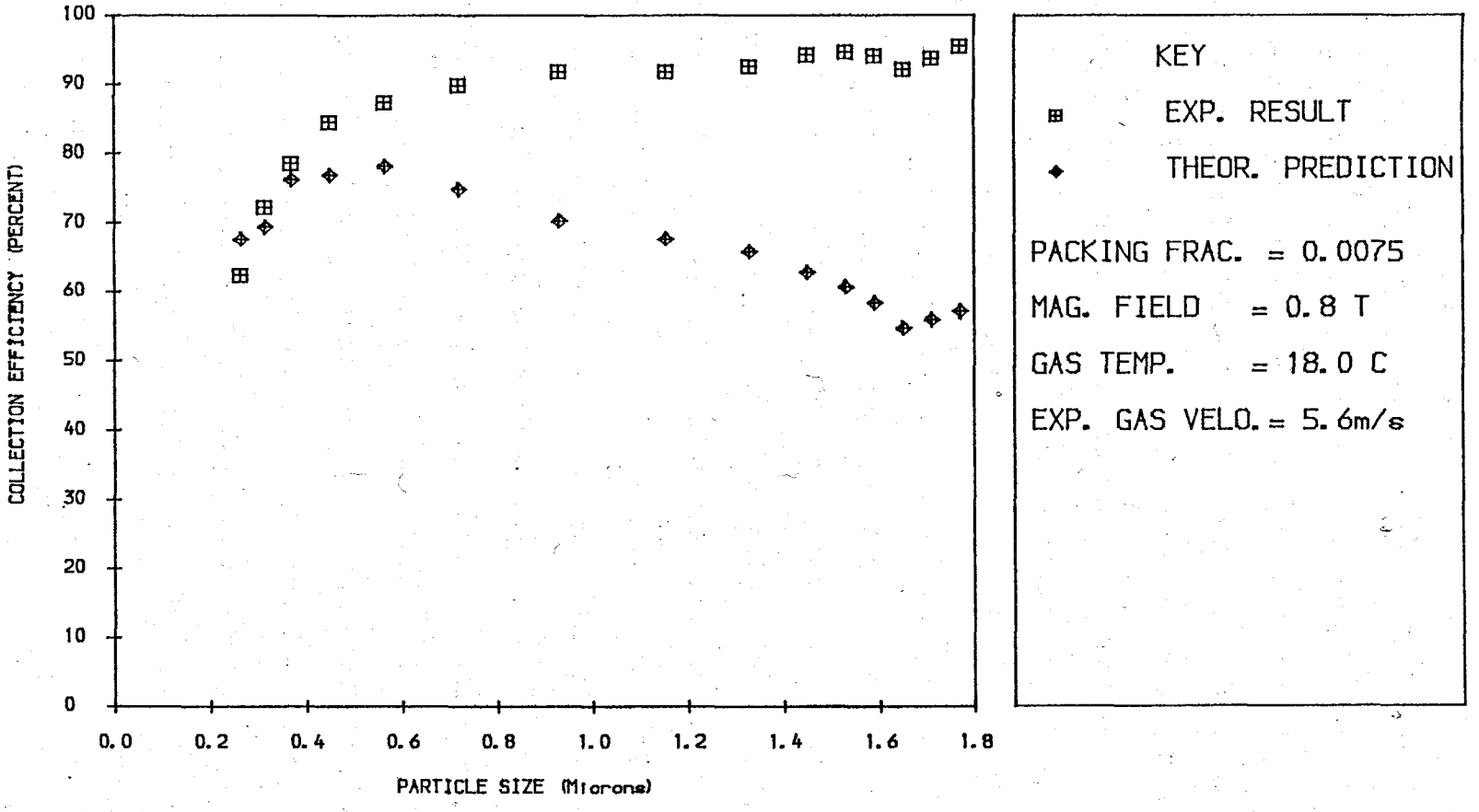

FIG. 8.24: COMPARISON BETWEEN THEORETICAL AND EXPERIMENTAL COLLECTION EFFICIENCY (RANDOM WIRE)

predicted by about 40%. The particle range of 0.265-0.565 agreed with the experimental results. Attempts to lift the collection efficiency of the larger particles resulted in the over prediction of the smaller ones. Some of the discrepancies in these results can be attributed to the assumed average diameter of the wires, the magnitude of the wire orientation factor and magnetic interference among neighbouring wires. Also the assumed approximate uniform particle density and concentration in the vertical layers of the filter may not have been satisfied in the experiment, therefore rendering the assumption unrealistic. Besides the points enumerated above , another important factor that may have affected the results in Figure 8.20 is the calculated critical radii shown in Table 5.1. A close look at the trend of X_e values expose the shape of the collection curves. They were predicted using the single-wire-single-particle model (or the so called isolated wire model), which can only give approximate theoretical efficiencies for highly porous filter matrix. The values of the dimensionless parameters used may have also contributed. For example, the value of the magnetic force parameter, W, was only 1.57×10^{-3} . This figure appears to be small in comparison with values used by other reseachers. (However, it must be pointed out that mostly they present results of conceptualized systems rather than attempt to simulate a given experimental situation). It was not possible to compare the critical radii calculated with those predicted by Lawson [65] because the values of his magnetic parameters were too large. On the other hand superimposing the points on his plot showed them lying outside the plotting area, in the low W zone. Since W is a

ratio of magnetic to inertia force, the explanation can only be that either the magnetic force is very small. Table 5.1 shows none of the critical capture radii to be up to unity. This means that in the absence of any adverse flow effect on any of these critical particles, they would be captured by direct impaction and the function of magnetic force in this case is preventing them from sliding off the surface of the wires. Particles in the shadow of the wire would, if small enough, be carried away by fluid streamlines unless the viscous forces are very small. Magnetic forces also oppose this forces and enhance capture.

Other differences in both results could lie in the susceptibility value of CuO which was 3.41×10^{-3} for the bulk dust. In the model it was assumed that this was uniform, but this may have completely broken down in actual practice. Another source of difference may have come from saturation magnetization, M_s , applied, which was used to calculate the A parameter. The M_s values were not measured but taken from the EPA [41] report on the application of HGMF to BOF dust.

It seems that given all these factors which are either approximated or assumed, that the present isolated wire model need several modifications before it can sensibly predict the performance of a complete filter unit.

Figure 8.25 shows the prediction of the collection efficiency of a similar system but with woven wire screens as the filter medium. The same E_f was used as in Figure 8.24. But for the smallest particle sizes, the results compared very well with that of experiment (Figure 8.26). The large drift present in Figure 8.24 for particles bigger than 0.37 microns is reduced,

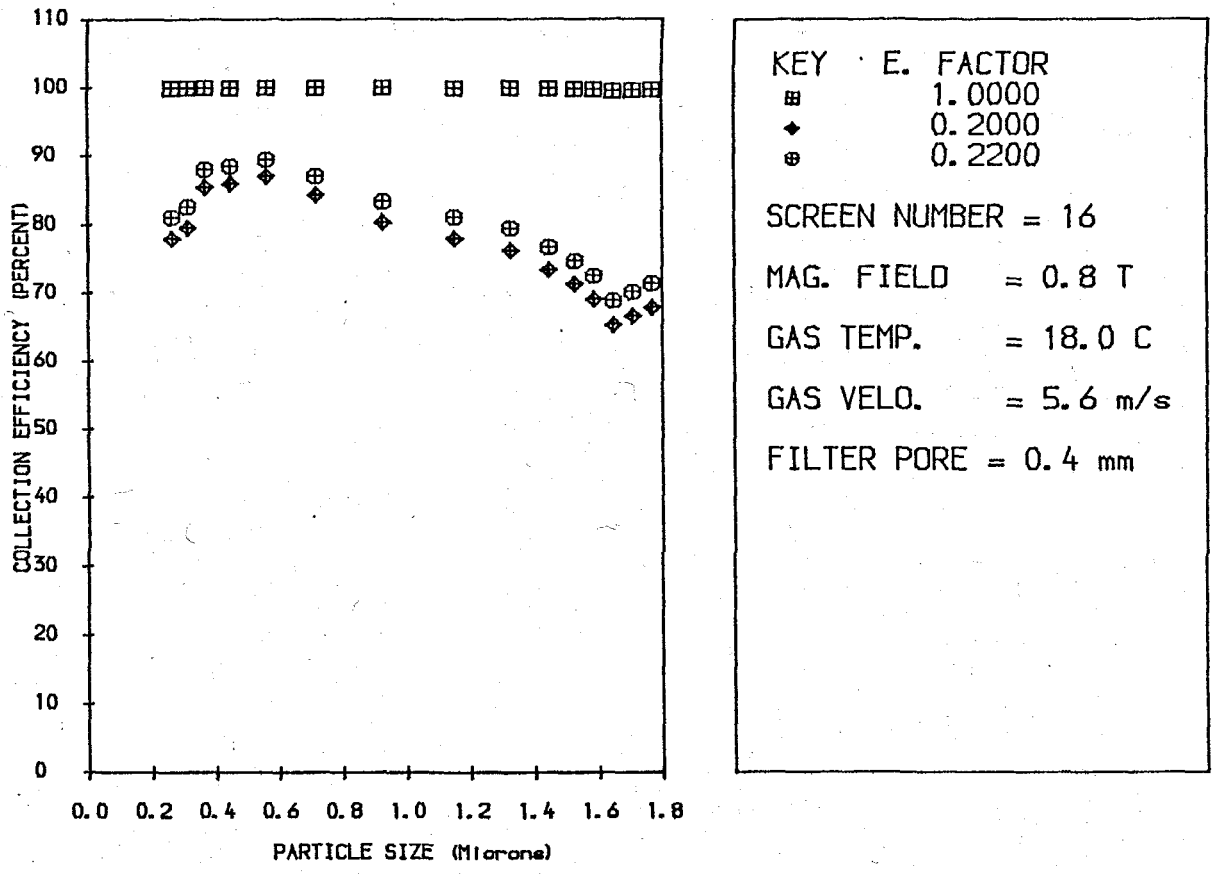

FIG. 8.25: THEORETICAL COLLECTION EFFICIENCY PREDICTED FROM ISOLATED WIRE MODEL (WOVEN WIRE)

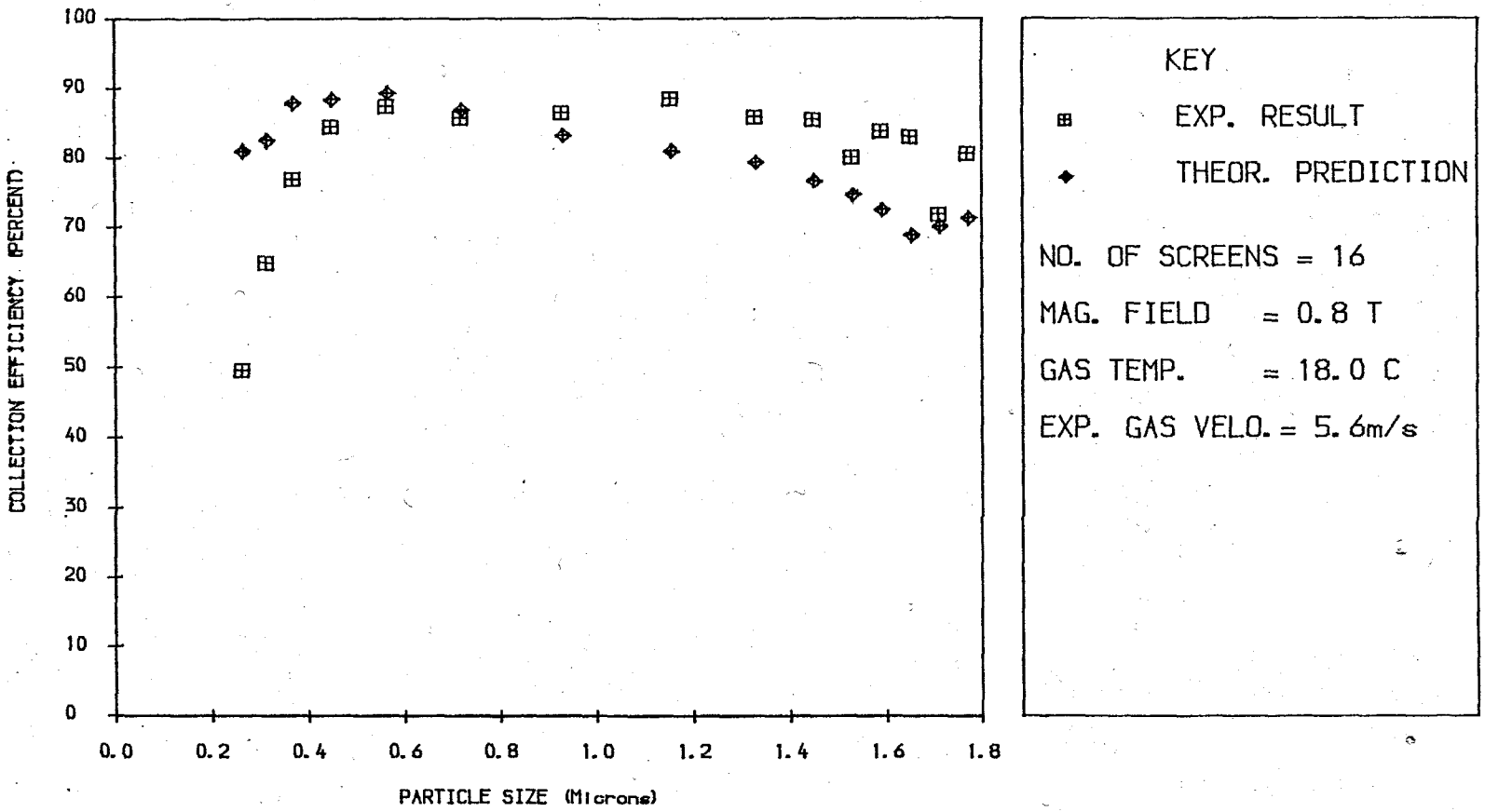

FIG. 8.26: COMPARISON BETWEEN THEORETICAL AND EXPERIMENTAL COLLECTION EFFICIENCY (WOVEN WIRE)

thereby making the similarities between the experimental and theoretical results much better in this case than those obtained from random wires. This might be due to a better quantification of the geometrical orientation of the whole filter matrix.

Table 8.1 Range of Operating Parameters

Magnetic Field (T)	0.0 - 0.8
Packing Fraction (%)	0.5 - 1.0
Number of Screens	9 - 20
Mean Wire Size (μ)	50
Screen Pore Size (μ)	400
Centre-line velocity (m/s)	5.6 - 7.6

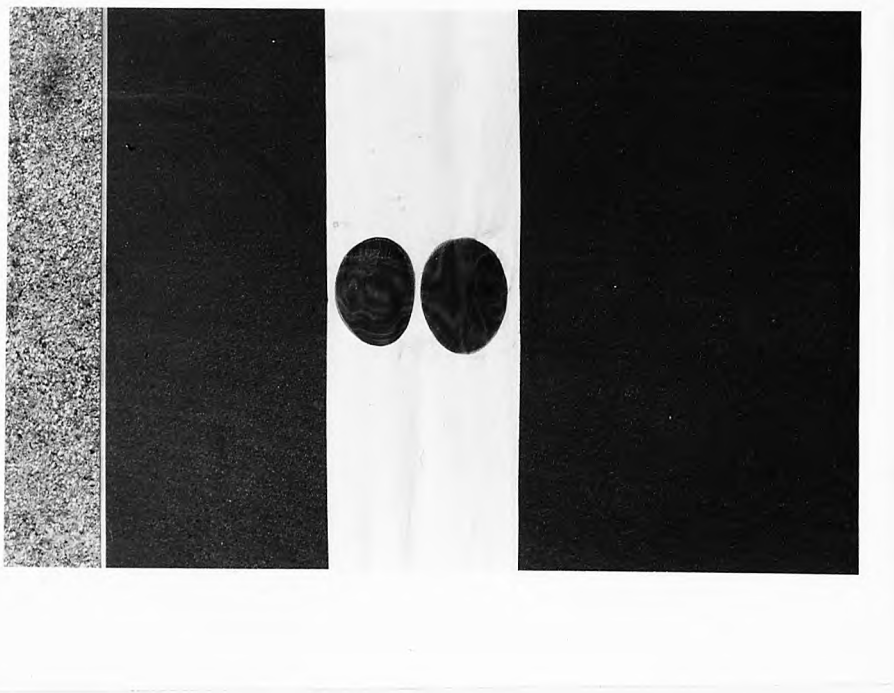

PLATE 8.1: WOVEN WIRE WITH CuO DEPOSITED ON THE SURFACES

CHAPTER NINE

APPLICATION OF FLUIDIC FLOW DIVERTER TO HGMF PROCESSES

9.1 Introduction

From the preliminary results obtained in the use of cylindrical and woven wires as filters, a maximum filtration efficiency of about 80% was obtained for particle size range of 0.5-1.77 microns. For particles of diameter 0.225 microns (the smallest detectable by the spectrometer), the filtration efficiency ranged from 40%-60%. This level of filtration efficiency has been achieved by using most favourable operating conditions which included high packing density, relatively high flow velocity, high background field and homogeneously packed cylindrical wires to increase magnetic gradients in the filter matrix. Therefore to effect a better performance, an ingenious optimization of one or more of these parameters needs to be performed.

9.2 Methods of Achieving High Collection Efficiency

9.2.1 Increasing The Magnetic Field

As the experimental dust (CuO) is paramagnetic, it never attains saturation unlike ferromagnetic particles such as Basic Oxygen Furnace dust. This means that increasing the background field, which in turn enhances the susceptibility of both the paramagnetic dust and the wire, will result in a higher retention of particles on the surfaces of the collecting wires.

However, there are some limiting factors. The first is cost, in that the power requirement will be too expensive to maintain. The second is an effect noticed in the preliminary tests carried out. It is the re-alignment of the randomly packed wires when the magnetic field was switched on. As a result, potential capture surfaces become attracted to each other and remain attached; thus, reducing available collection surfaces. Another limiting factor was the saturation magnetization of the wire. The final factor which is peculiar to this application was that the rectifier that supplied the current had a maximum rating of 200 Amp at a constant voltage output of 45 volts, producing a maximum field of about 0.8 Tesla.

9.2.2 Increasing Packing Density

This entails packing more wire in a given volume of matrix. There is a fraction over which extra increase becomes unprofitable. In the studies carried out by Boucher [73], he concluded that there is a better matrix loadability for 0.5% than 0.75% for ferromagnetic BOF dust. From the tests conducted so far for paramagnetic CuO dust, better collection efficiency was obtained with increasing wire mass. However, results obtained for 0.75% and 1% packing were barely discernible. Therefore the extra resistance involved in using higher packing fraction can be avoided without any significant reduction in particle collection efficiency. So in effect, a prohibitively high pressure drop with decreasing improvement in efficiency is the check against increasing packing density. Another very important factor that limits this is the wire interference, which drastically affects

the magnetic tractive forces that compel particles to migrate to wire surfaces.

9.2.3 Change In Flow Velocity

The flow velocity is an important parameter in particle filtration, although its influence is not well understood. The present studies show that flow up to 7.6m/s in random wire matrix sustained a relatively higher particle collection in the randomly packed filter. Above this value, the collection efficiency curves became spurious and on the average dropped, indicating that the hydrodynamic force is dominating and may have nullified the effect of the magnetic forces. Therefore if the flow can be manipulated to "stagnate" (come to rest momentarily) in the filter volume for a short time, the influence of the magnetic tractive forces may be much more effective. This is similar to sedimentation process [74], where particles are allowed to settle under the influence of gravitational forces except that in this particular case, the gravitational effect is replaced by the magnetic tractive force.

One of the acclaimed advantages of HGMS is the ability to maintain a relatively high filtration efficiency at a velocity far higher than conventional filtration methods, hence achieving larger throughput over a shorter period of time. So there is a need to design a HGMF system which can increase the flow residence time in the vicinity of the filter, whilst maintaining a relatively high superficial velocity. The new type of system involves the use of the Fluidic Flow Diverter.

9.3 Application of Fluidic Diverter to Dust Filtration

The flow diverter is a type of fluidic device that allows a stream of fluid, gas or liquid, to be diverted to one or two outlets without the use of obtrusive parts. The absence of hindrance to the flow streamlines is of particular importance in this application since the deposition of particles on such surfaces is much reduced, hence the original particle profile in the duct is very nearly maintained. In certain applications, three or more outlets has been used. Applications are usually in the process and nuclear industries. Some of these include the control of: liquid level in tanks, warm air heating, cement wagon loading and flexistor valve in mine ventilation. Others include the self cleaning bistable filter and the sorting and classification of solids and particles in the food industry.

9.3.1 Principles Of Operation

The basis of operation of a bistable flow diverter is the Coanda Effect [75]. Figure 1.3 shows this effect for a jet of fluid discharging from a nozzle into the atmosphere. Due to turbulent mixing, the jet entrains surrounding fluid and becomes wider and slower, and it transports more fluid as it moves further from the nozzle. The two walls tend to restrict the entrainment of the fluid so that the pressure at the walls is less than the surroundings. By geometrical design or random disturbance, the jet migrates closer to one wall than the other. The entrainment of the flow becomes more restricted there so that the pressure falls further; thus creating a pressure difference across the jet which tends to bend it even further until the jet

attaches and remains on that particular wall (Figure 1.3a). The jet can be made to attach at the opposite wall by the injection of compressed air through the control port on the jet side (Figure 1.3b). The underside of the jet is at low pressure, which is required to maintain jet curvature. It continues to entrain fluid most of which is provided by the jet returned when the jet strike the wall, the rest being sucked in through the control port.

These inherent features of the fluidic diverter is most suitable for its application to dust filtration. The two discharge openings can be connected to outlets containing filters (Figure 1.3). Filtrate can then be supplied to these two filter zones alternatingly. The frequency of this operation is dictated by the switching of the main flow (filtrate) with a small sample of compressed air.

In some applications, this switching of the jet is maintained by alternating closure and opening of both control ports to the atmosphere. The time required by the flow to completely flick to the opposite side is called the Switching Time. For optimum performance, this time has to be optimized, firstly to allow a suitable time for magnetic force to act and secondly to minimize the bulk of material used as will become apparent later. To achieve this, the average minimum distance between adjacent wires would be determined; and also the minimum Time Delay required in the filter matrix. Note that time delay here means the time it takes a particle to travel from its initial position to the capture surface of the wire.

In principle, a bistable flow diverter is capable of

dividing the main flow equally through the output pipes, but due to difficulties in achieving symmetry during construction, a diversion of 60% to 40% in the absence of control flow is considered a good design.

9.3.2 Determination of the Farthest Particle Location

The determination of the average farthest X-axis location of a particle in an array of randomly packed wires is achieved by the simple cubic lattice model described in Chapter Four. The model is based on the assumption that the entire matrix is made up of cylinders arranged in cubes (Figure 4.1), with two-thirds of the cylinders perpendicular to the flow. The remaining one-third are parallel to the flow and therefore considered ineffective. It is also assumed that the packing density of the matrix is relatively low to minimize wire-to-wire interference as has been the case in the previous tests. From Chapter Four, the unit length of the cube was given as:

$$l_s = \left(\frac{3a}{F}\right)^{0.5} \tag{9.1}$$

To remove the effect of geometry, equation (9.1) was divided by the wire diameter d. Given that

$$\frac{l_s}{d} = \left(\frac{3a}{F}\right)^{0.5} \frac{1}{d} \tag{9.2}$$

The diameter of the wire used was 50 microns, and the minimum packing fraction which will be employed has been established to be about 0.005. With this figure, the maximum side length of the cubic lattice l_s is calculated thus:

$$\frac{l_s}{d} = \frac{\left[3x(50x10^{-6})^2 x\pi\right]^{0.5}}{0.005x4} \quad x \frac{1}{50x10^{-6}}$$

= 21.7 Wire Diameters (22 d)

22d represents the average farthest position on X-axis an opposite wire can take. Therefore, the representative average distance between any two directly opposite wires is $\frac{l_s}{2} = \frac{22}{2} = 11$. This is represented in Figure 9.1.

The next task is to determine the time it will take a particle located at, say, the centre of the cube defined by the coordinate (11, 11) to reach the surface of the wire. It should be noted that this does not necessarily entail capture , since a particle at this position requires a large tractive force to be present before it can be pulled in and captured as was evident in the theoretical particle trajectories presented earlier. So, although a mean particle position has been determined, the effective X-distance used was the critical radius of capture (X_c) . However it is worth mentioning that it is not expected that a particle at X = 11 should arrive later than another nearer the wire as both have approximately the same Y-distance to travel.

9.3.3 Calculation of the Particle Capture Time:

The capture time of the particle was calculated using the monodisperse theoretical model describing the particle trajectory in the presence of Magnetic, Hydrodynamic, Gravitational, and Inertial forces developed in Chapter Five. The procedure involves the application of the values of independent

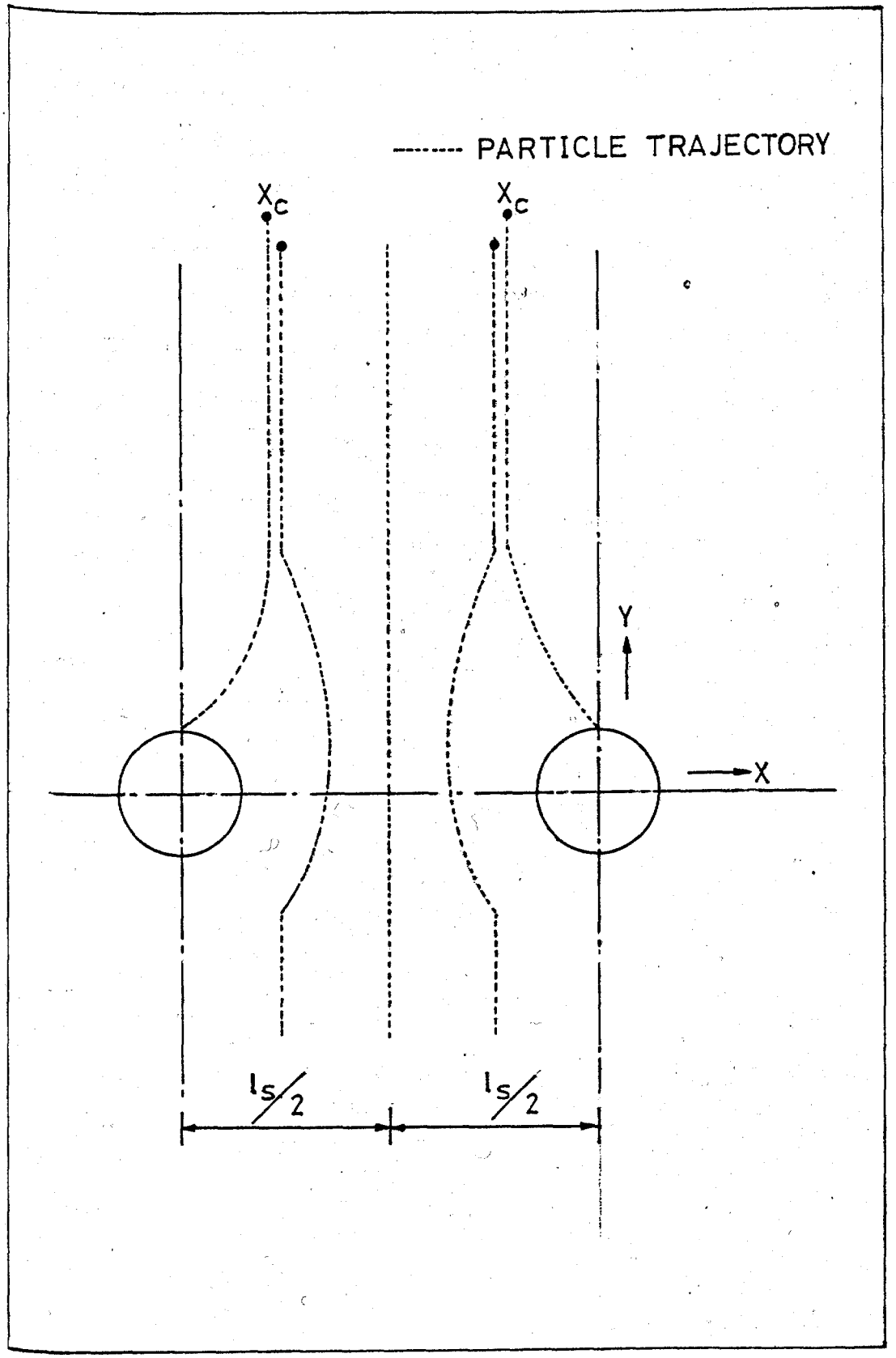

FIG. 9.1: LOCATION OF THE FARTHEST PARTICLE

parameters (W, A, K and G) to obtain the dimensionless particle position in space. The resulting corresponding dimensionless time τ required by the particle to reach the surface of the wire (for capture) or an equivalent distance (in the case of particle escape) was also calculated.

This was approached by assuming that the fluid is stagnant for the period in between switching, and then slightly modifying equations (5.45) and (5.46) before commencing integration. In this case, a different set of non-dimensionalizing parameters were chosen to exclude the fluid velocity. In the new equations, the non-dimensionalizing time parameter was $\frac{s^2 \rho_p}{\nu}$, instead of $\frac{s}{V t}$ used in the original set. The resulting set of governing equations are given below:

$$\left[\left(\frac{d^2R}{d\tau^2}\right) - R\left(\frac{d\theta}{d\tau}\right)^2\right] = -\frac{2 A W}{R^3}\left[\frac{A}{R^2} + \cos 2\theta\right]$$

$$-\frac{1}{K}\left[\frac{dR}{d\tau}\right] - G\cos\theta \qquad (9.3)$$

$$\left[R\frac{d^2\theta}{d\tau^2} + 2\left(\frac{dr}{d\tau}\right)\left(\frac{d\theta}{d\tau}\right)\right] = \frac{-2 A W \sin 2\theta}{R^3}$$

$$+\frac{1}{K}\left[R\frac{d\theta}{d\tau}\right] + G\sin\theta \qquad (9.4)$$

The four dimensionless parameters used above are:

$A = \frac{2\pi M_s}{H_o}$, the relative magnitude of the induced magnetization in the ferromagnetic wire due to the applied field, H_o

$W = \mu_o \chi^* H_o^2 \frac{\rho_p s^2}{\mu^2}$, dimensionless magnetic force parameter (a ratio of magnetic to inertia force).

$K = \frac{2 b^2}{9 s^2}$, Stokes number, a dimensionless viscous force parameter (a ratio of inertia to viscous forces).

$G = \frac{s^3 g \rho_p^2}{\mu^2}(1 - \frac{\rho_f}{\rho_p})$, dimensionless gravitational force parameter.

The calculation procedure involves:

(i) The choice of independent parameters

(ii) Calculation of the dimensionless time parameter (τ).

(iii) The use of τ to calculate the real time.

The real time obtained was 0.081 seconds. This is the minimum time required in the filter matrix for the particle to reach the wire surface. So, for the optimum performance of the fluidic diverter, the flow residence time in the filter must not be less than 0.081 seconds.

9.3.4 Design of a Suitable Diverter

A bistable flow diverter was designed to suit the configuration of the general test rig. There are several operational constraints which have to be taken into consideration in the preliminary part of the design work. The most important of these were:

(i) The nominal size of the two exit ducts must fit into the bore of the magnet which was 120mm.

(ii) Total length of the diverter unit must be less than 2m. (This is because of the limited space available)

(iii) The minimum switching period must be longer than 0.081 seconds (that is time to switch from side to side must be < 0.081 seconds).

The fourth necessity, although less important, was the need to retain the original form of the rig arrangement (Figure 7.1) so that direct comparison to previous results could be made when necessary.

For easy description, the diverter has been divided into three distinct sections, each comprising a complete unit:

Section 1 :- This comprises of the reducer and the method of joining to the upstream part of the duct. (Figure 9.2)

Section 2 :- This represents the main body of the diverter itself. Attached at the upstream part was the reducer; while at downstream was the third section.

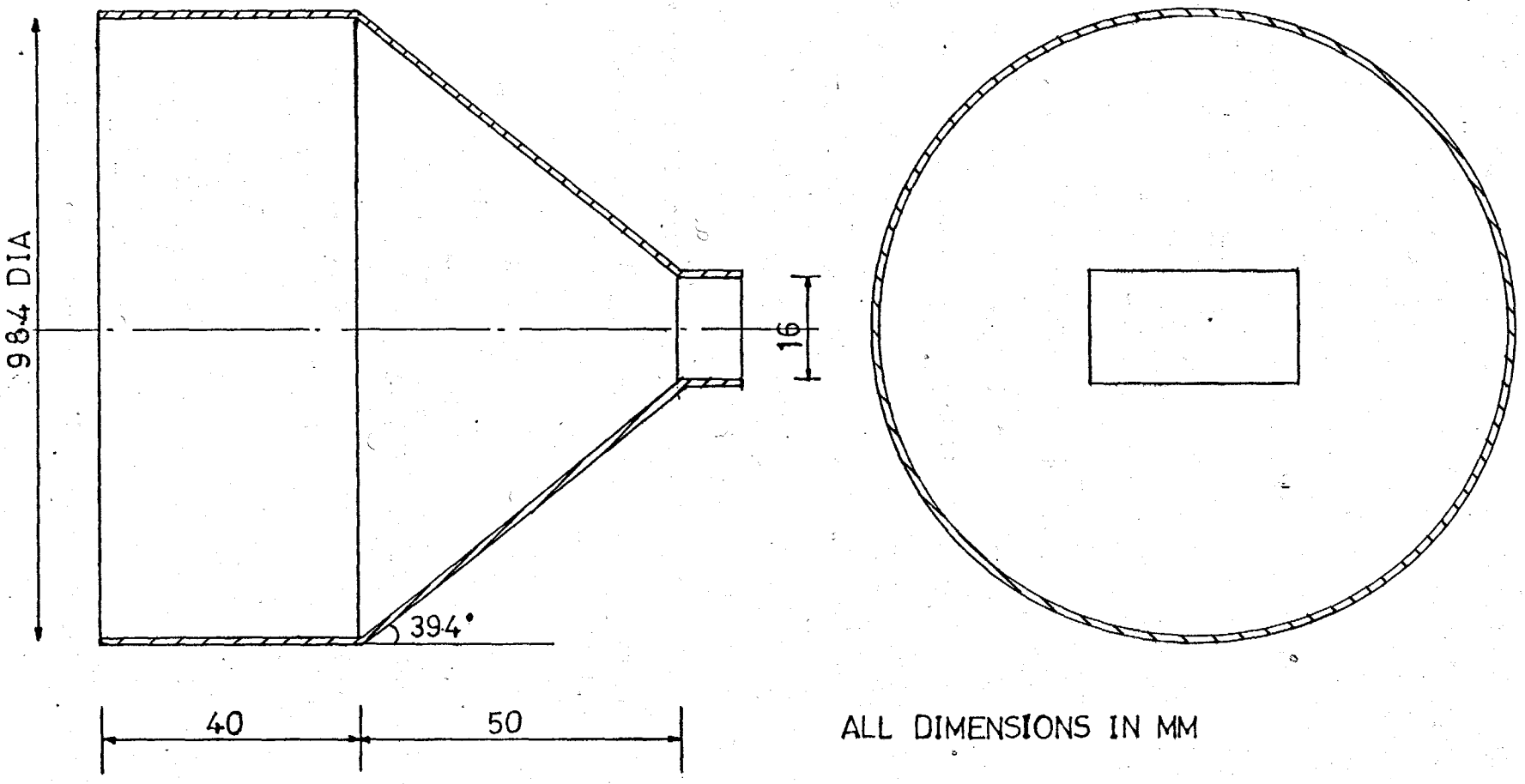

FIG. 9.2: SECTION OF THE INLET REDUCER TO THE FLUIDIC DIVERTER

(Figure 9.3)

Section 3 :- This contains a mixing chamber where flows from both arms of the diverter were discharged and subsequently a reducer for final connection to the main duct. (Figure 9.4)

Section 4 :- This describes the variable speed solenoid switching circuit used in achieving the diversion of the fluid in the diverter. (Figure 9.5)

9.3.5 Design Of The Reducer

The main pipe diameter was 99.4mm outer diameter. In order to channel the flow of air into the diverter, this size must be stepped down through a reducer to fit the nozzle dimensions. This is necessary because a sudden change in the duct diameter will cause a high loss of pressure. A smooth flow of the suspended particles which otherwise would have been deposited by impaction is achieved. The coefficient of pressure drop is normally given for a sudden change of area as [76].

$$K_1 = \frac{P_r}{\rho V^2/2g} = F_f\left(\frac{L_r}{D_n}\right) \qquad (9.5)$$

For minimum velocity head loss, the loss coefficient, K_1, is about 0.05 [76]. So adopting this value, equation (9.5) becomes:

$$K_1 = \frac{P_r}{\rho V^2/2g} = F_f \frac{L_r}{D_n} = 0.05 \qquad (9.6)$$

where P_r = pressure drop across the reducer

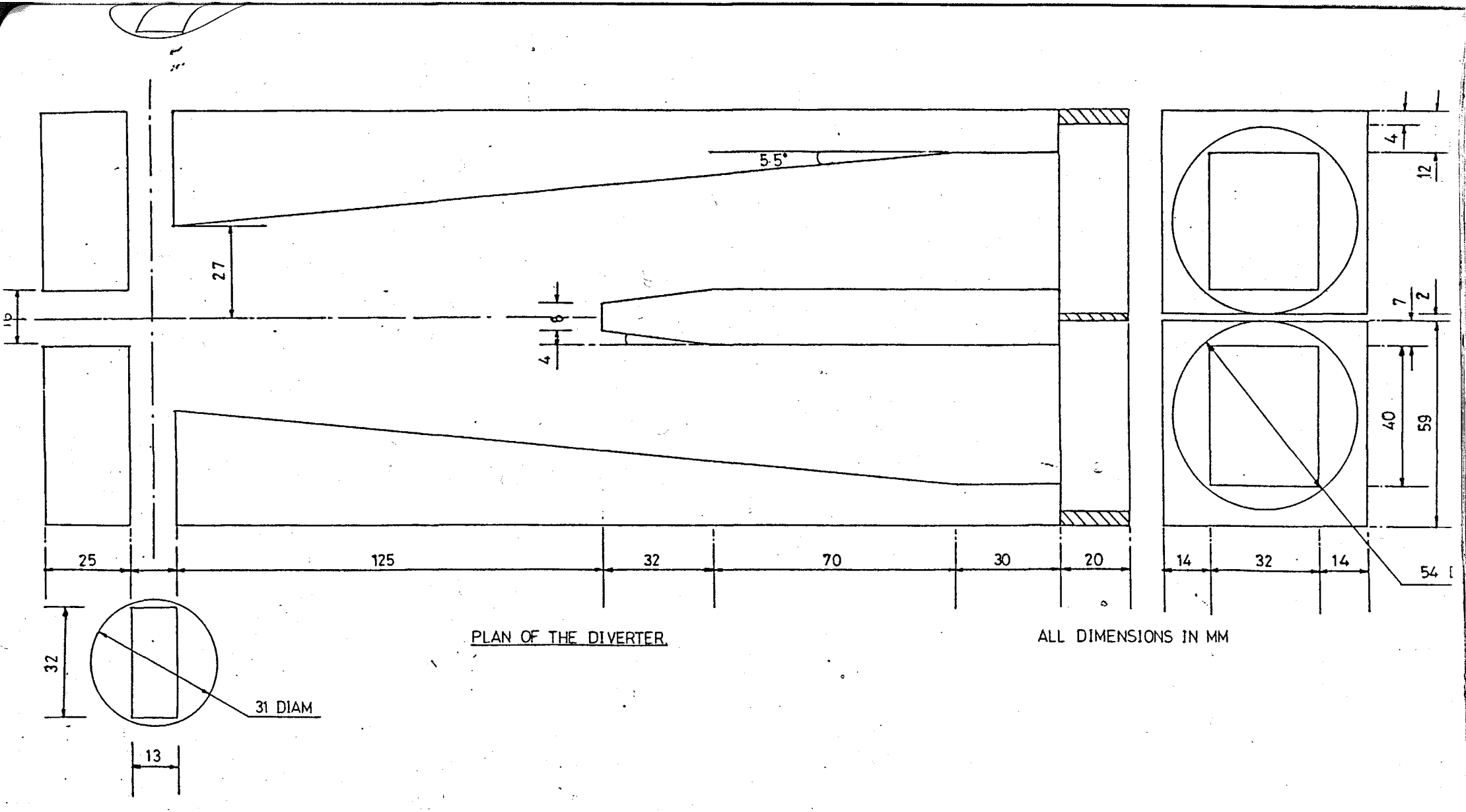

FIG. 9.3: SECTION OF THE FLUIDIC DIVERTER

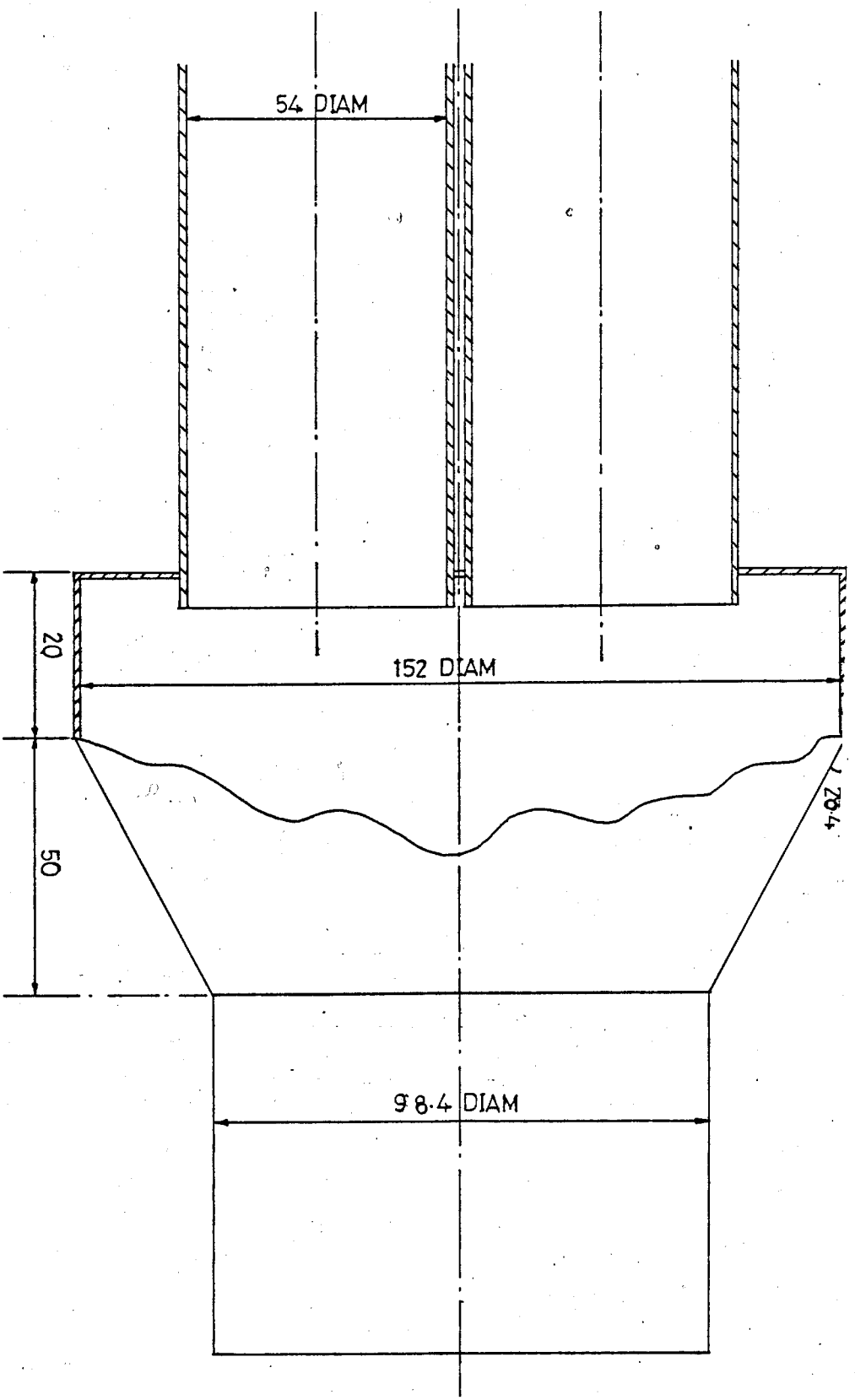

FIG. 9.4: SECTION OF THE MIXING CHAMBER WITH THE OUTLET REI

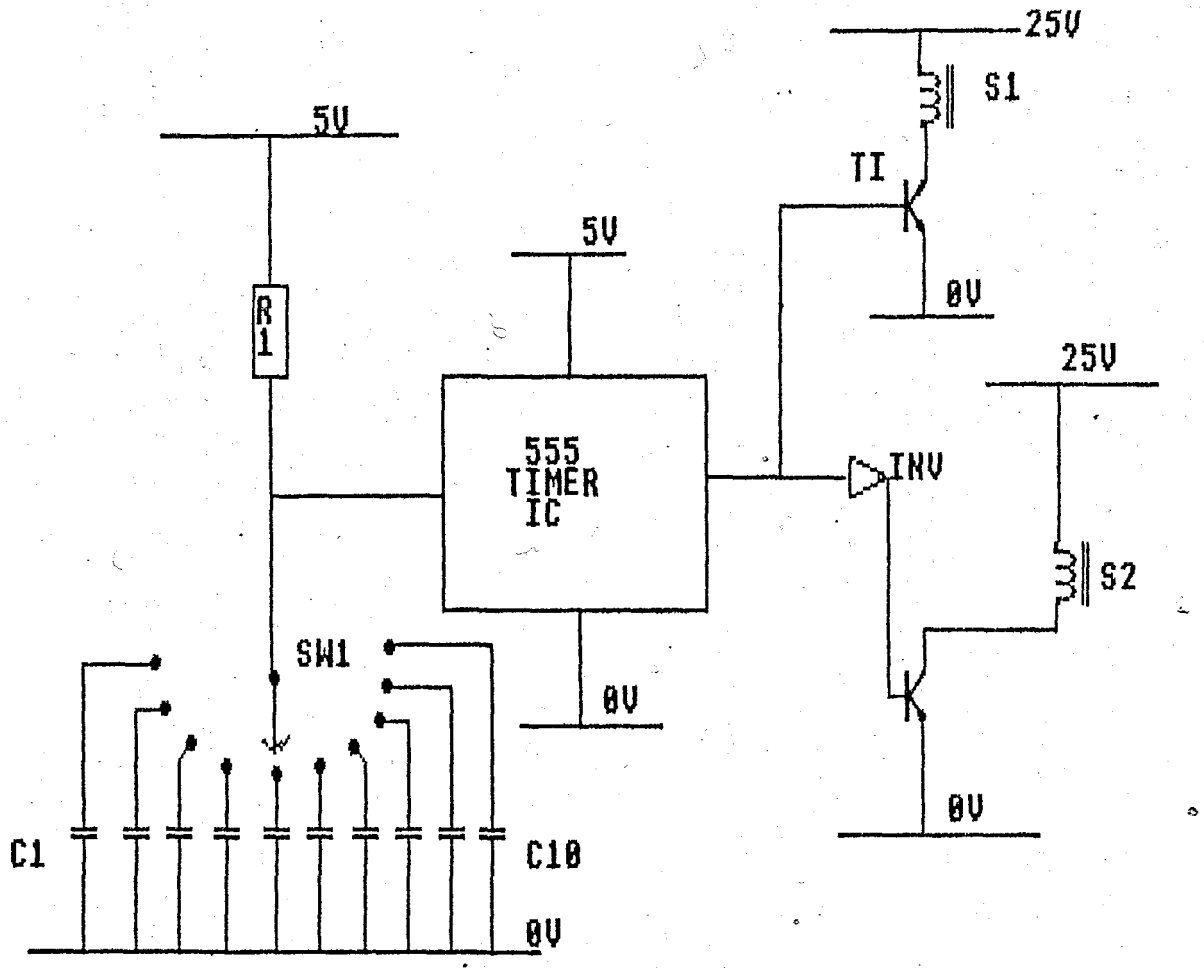

FIG. 9.5 VARIABLE SPEED SOLENOID SWITCHING CIRCUIT

L_r = Length of reducer

D_n = Nozzle diameter

F_f = Friction factor

With the knowledge of the flow Reynolds number, the friction factor, F_f, can be obtained from the Moody-Diagram [76]. Thus, for the minimum and maximum velocities, 5.6 and 7.6 m/s respectively, envisaged, their Reynolds numbers become:

$$Re_{min} = \frac{1.239 \times 9.6 \times 98.4 \times 10^{-3}}{19.12 \times 10^{-6}} = 3.77 \times 10^{4}$$

$$Re_{max} = \frac{1.239 \times 9.6 \times 98.4 \times 10^{-3}}{19.12 \times 10^{-6}} = 8.10 \times 10^{4}$$

Giving $F_{f(min)}$ and $F_{f(max)}$ as 0.21.
Substituting these values in equation (9.6) gives

$$L_r = \frac{0.05}{0.21 \times 15} = 3.57\text{mm}$$

which is impracticable.

An alternative arrangement was then adopted where a suitable length that fits into the available space was chosen and then using equation (9.6) the corresponding friction factor F_f was calculated as:

$$F_f = 0.21 \times \frac{50}{16} = 0.656$$

With the value of F_f, an estimate of the pressure drop across the reducer can be made using equation (9.5):

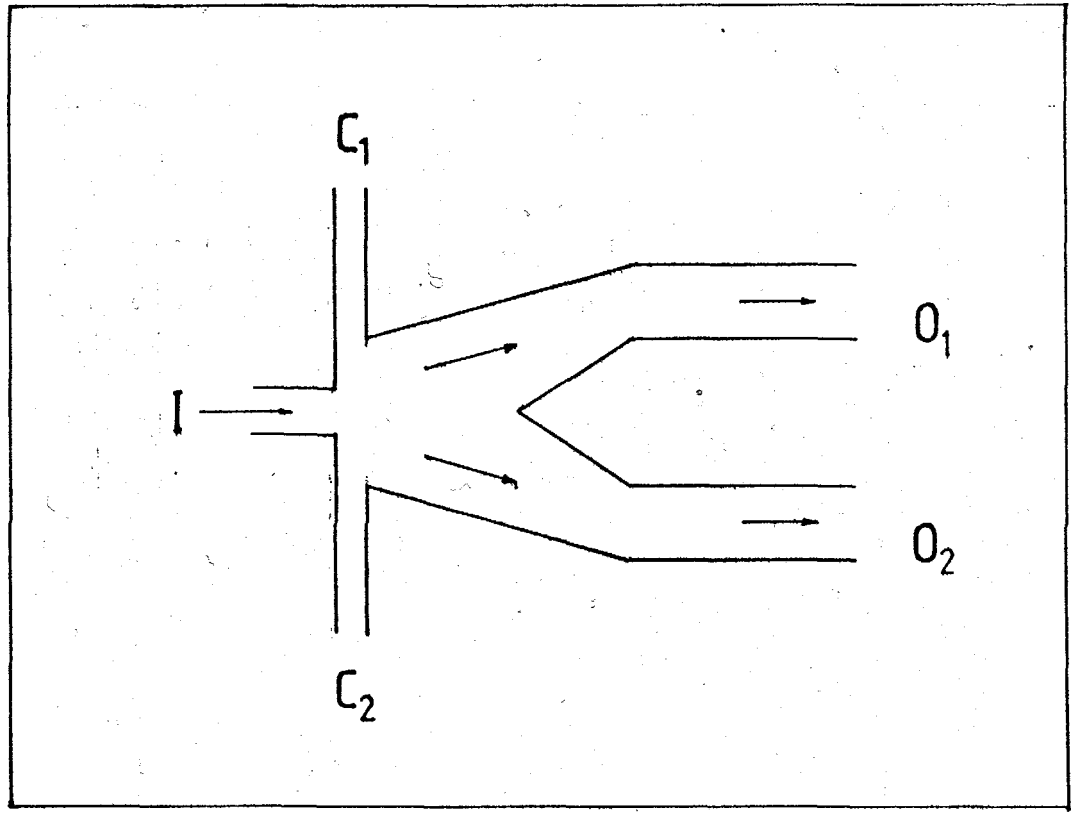

FIG. 9.6 CHARACTERISTIC GEOMETRY OF A FLUIDIC DIVERTER

$$0.657 = \frac{P_r}{\rho V^2/2g}$$

$$P_r = \frac{0.656 \times 1.239 \times 52^2}{2 \times 9.81} = 112\text{mm } H_2O$$

9.3.6 Design of the Flow Diverter Unit

The operational requirements of the bistable flow diverter to be constructed with duralumin are:

(i) It should deliver not more than one-filter-full of filtrate per switching

(ii) It should be capable of switching up to 100% of the filtrate for optimum performance.

(iii) The nozzle should be large enough to allow a reasonable flow rate.

(iv) The pressure drop should be reasonable.

(v) The device should be cheap and adaptable to other applications.

The principal geometrical variable in the design of this bistable flow diverter is the nozzle width, W_n [77]. This was chosen such that both the output ducts fit into the bore of the solenoid magnet (120mm in diameter) and also be able to supply not more than a filter full of the filtrate per switching. The device size was defined by a relationship linking the nozzle width and velocity to the switching time. The switching time T_s is the time lag between the switching of the flow from one side

to the other or the time for one filter to be filled. It is obvious that either doubling the velocity of the jet or halving the device size reduces the switching time by a factor of two. Therefore the following relationship exists for a diverter.

$$T_s \propto \frac{W_n}{V_n} \tag{9.7}$$

where W_n is the nozzle width and V_n the jet velocity .

Equation (9.7) represents the time it takes the jet to travel a distance of one nozzle width known as nozzle transport time T_t . Thus, removing the proportionality sign results in

$$T_s = S\ (\frac{W_n}{V_n}) \tag{9.8}$$

$$= ST_t \tag{9.9}$$

where S is called the switching or transient Strouhal number.

This constant (S) is a difficult parameter to determine and depends on the diverter geometry and how much flow is forced through the control port to cause the switching. Ignoring geometrical effects and taking the latter effect as the more important one, switching with a control flow in excess of the minimum necessary reduces switching time. [78,79]. Reduction of the switching time to a minimum is necessary as it reduces the filtration volume required to accommodate the flow when it is brought to rest. The ultimate advantage being the shortening of the length of the output pipes required. This necessitates the use of high flow in the control ports to effect switching. To

show how this affects the filtration volume, consider the diverter in Figure 9.6.

The switching time is given by :

$$T_s = S \frac{W_n}{V_n} \tag{9.10}$$

$$= S \frac{W_n}{V_n} \frac{A_n}{A_n} \tag{9.11}$$

$$= S \frac{W_n}{Q_n} A_n \tag{9.12}$$

But as the nozzle flow rate is constant, it follows that it is equal to the flow rate through one arm of the diverter (Q_f) at at any given switch, (i.e $Q_n = Q_f$).

But:

$$Q_f = V_f A_f = \frac{V_m}{T_f} \tag{9.13}$$

T_f being the time it takes to fill the matrix volume V_m .

Thus, equation (9.12) can be re-written as:

$$T_s = S \frac{W_n}{V_f} \frac{A_n}{A_f}$$

$$= S \frac{W_n}{V_m} A_n T_f \tag{9.14}$$

The volume of one side of the diverter is given by :

$$V_m = \frac{\pi D_f^2}{4} L_f \tag{9.15}$$

Substituting in equation (9.14) results to :

$$T_s = S \frac{4}{\pi} W_n A_n \frac{T_f}{L_f D_f^2} \tag{9.16}$$

For rectangular nozzle:

$$A_n = W_n(N_n W_n) = N_n W_n^2 \tag{9.17}$$

Therefore equation (9.16) becomes:

$$T_s = S\ N_n \frac{4}{\pi} W_n^3 \frac{T_f}{L_f D_f^2} \tag{9.18}$$

$$= N_n\ S \frac{4}{\pi} \left(\frac{W_n}{D_f}\right)^3 \frac{D_f}{L_f} T_f \tag{9.19}$$

Re-arranging gives:

$$\frac{T_s}{T_f} = N_n\ S \frac{4}{\pi} \left(\frac{W_n}{D_f}\right)^3 \frac{D_f}{L_f} \tag{9.20}$$

For best performance, the ratio $\frac{T_s}{T_f}$, must be less than one (i.e $\frac{T_s}{T_f} < 1.0$)), and the more it approaches zero the better the performance of the diverter and hence the filter. Of course the minimum time of 0.081 seconds already established would not be exceeded. The only envisaged restriction is the inertia of the jet or if the switching time becomes shorter than the response time of the flow at the largest possible control flow rate. The

pressure of the compressed air required at the two control ports is also governed by the specification of the two solenoid valves which can only withstand a gas pressure of up to 8.60 bar.

Therefore equation (9.20) can be re-written in the following form.

$$N_n \, S \, \frac{4}{\pi} \left(\frac{W_n}{D_f}\right)^3 \frac{D_f}{L_f} \ll 1 \qquad (9.21)$$

Most of the geometrical dimensions in equation (9.21) can be chosen for maximum efficiency. A good estimate of practical switching time for moderate pressure drop in the range of 20% of the supply flow and pressure is obtained by using S = 0.025. The following values are used for the other parameters.

W_n = 16mm

D_f = 52mm

L_f = 300mm

N_n = 2

Substituting in equation (9.21) results in :

$$T_f = \frac{T_s}{0.514} \qquad (9.22)$$

By choosing different values of diverter switching time, a range of filling periods can be computed from equation (9.22). These values are given in Table 9.1 for switching time of 0.1 to 1.0 seconds. However, it must be emphasized that for optimum performance the following conditions applies: $0.081 < T_f < 1.0$ second. This limits the switching time to only about 0.5 of a second.

9.3.7 Design of the Diverter Discharge Unit

The outlet unit from the diverter consists of two parts; a mixing chamber and a reducer (Figure 9.4). This form of arrangement is adopted as the combination of the two pipes is bigger than the main duct. The reducer is required for smooth transition of the flow back into the main duct. The dimensions of the chamber were chosen to fit the available space on the rig. The reducer is of the same type as the one used upstream but is slightly smaller. Figure 9.7 (PLATE 9.1) shows a diagram of the complete unit.

9.3.8 The Solenoid Switching Circuit

The variable solenoid switch circuit used for the fluidic diverter is shown in Figure 9.5. It comprised mainly of solenoid S1 and S2, energized by transistors T1 and T2 respectively. The switching signals T1 and T2 were derived from the 555 timer Integrated Circuit (IC), which is a square wave whose periodic time is dependent on the resistance R1 and the 10 position wafer switch, WS1. Since the capacitors C1 to C10 are of different values (C1 being the smallest), the position of SW1 alters the time constant of the resistor capacitor network, hence the periodic time of the output square wave. The component marked "INV" is an inverter whose function is to provide a phase change in the signal being applied to the bases of T1 and T2. This phase change ensures that when S1 is energized, S2 is de-energize and vice-versa.

Each position of the rotary switch SW1 varies with the square wave timing by 0.10 seconds. In position 1, the periodic

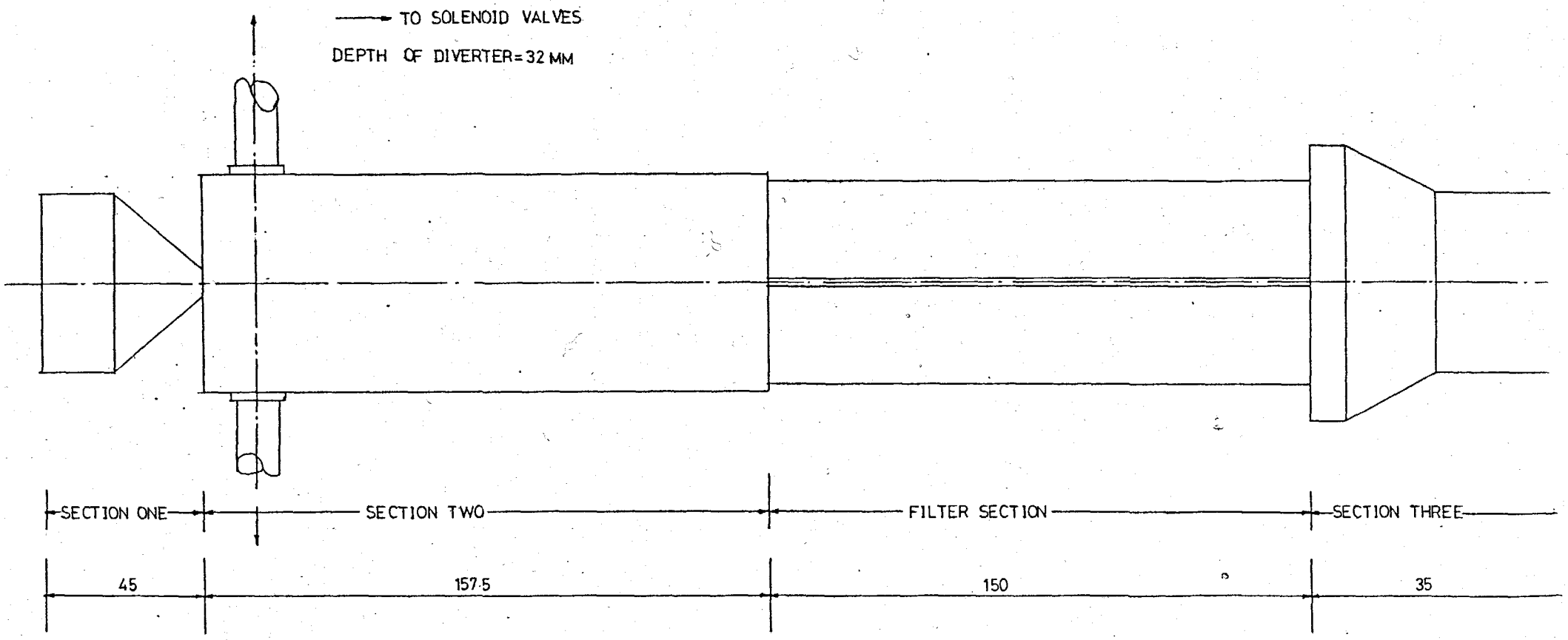

FIG. 9.7 SECTION OF THE COMPLETE FLUIDIC DIVERTER UNIT

timing of the square wave was 0.10 seconds, going up to 1 second in position 10. Therefore the amount of time that either solenoid was energized is PT/2.

9.4 Diverter Development Tests

Some initial development tests were performed on the diverter to determine the effects of relevant operating parameters that can affect filtration. These are the flow velocity profiles, dust profile, and the flow rates required at the control ports to effect complete switching during filtration.

9.4.1 Diverter Outlet Velocity Profiles

This was performed to determine the velocity profile of the flow in the pipe. This test is necessary because of an anticipated change in flow pattern resulting from the flow passing through the nozzle before being expanded into the diverter rectangular channels prior to discharge into either of the two output pipes (PLATE 9.2). This equipment consisted mainly a pitot-static tube, a stand, and a digital manometer. The stand has a calibrated lever on X and Y axis to enable traverses in both directions. Figure 9.8 shows a typical profile obtained when the jet lapped completely on one side and discharged into the atmosphere.

The second outlet velocity profile was taken after the mixing chamber has been attached. Initially the measurements were made without the presence of the filter. The resulting profile is shown in Figure 9.9, while Figure 9.10, shows the results obtained with 16 woven wire screens placed in the filtering zone.

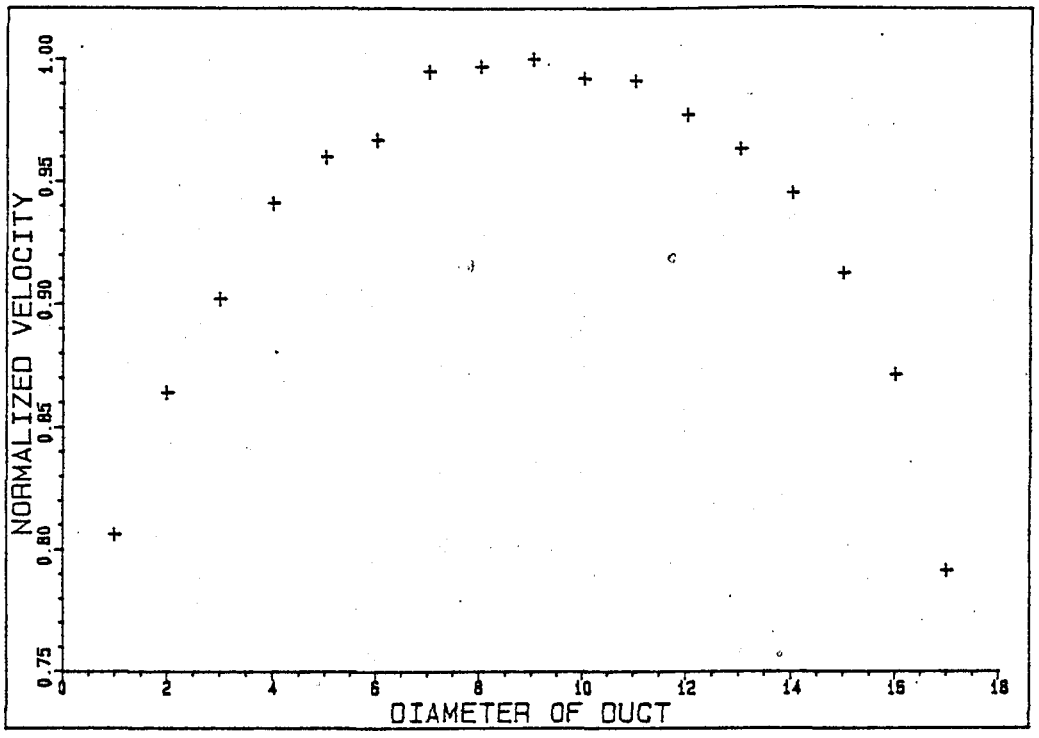

FIG. 9.8(A) FLOW PROFILE OF OUTPUT #0 SUB 1 # OF THE DIVERTER DISCHARGING TO THE ATMOSPHERE

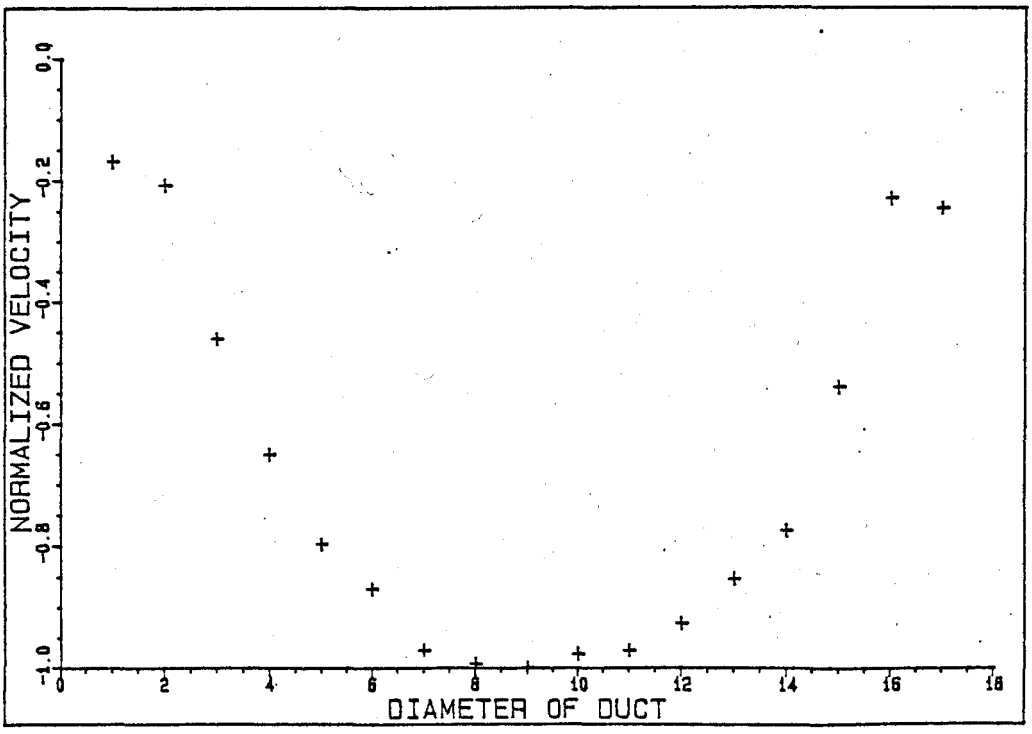

FIG. 9.8(B) FLOW PROFILE OF OUTPUT # 0 SUB 2 # OF THE DIVERTER DISCHARGING TO THE ATMOSPHERE

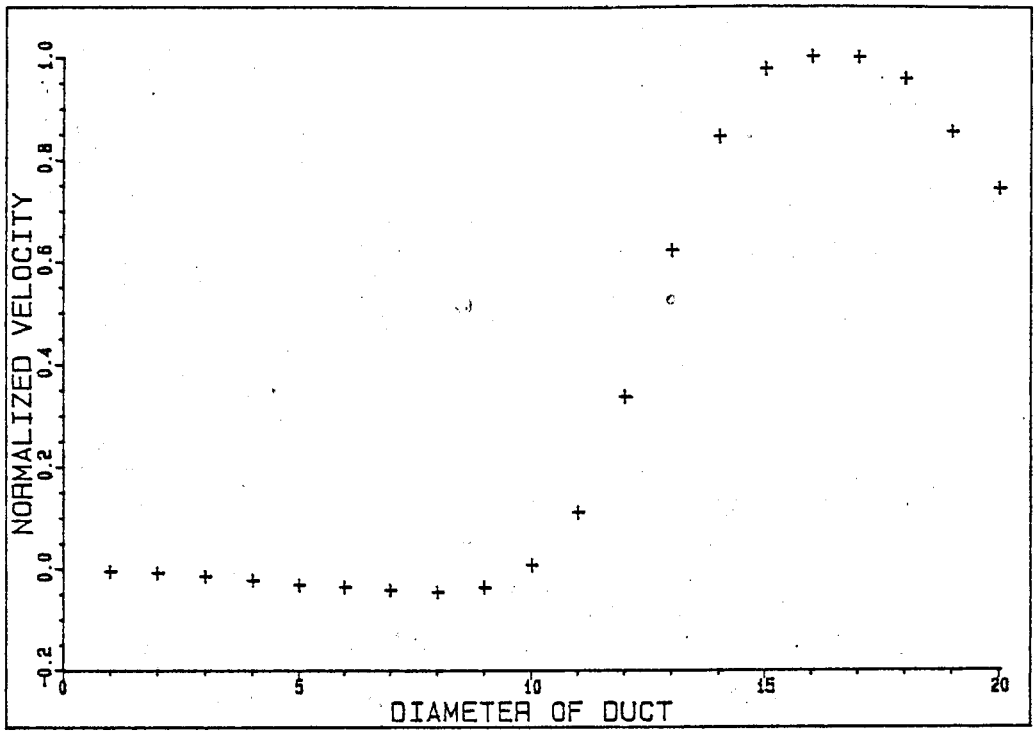

FIG. 9.9 OUTLET VELOCITY PROFILE WITH THE MIXING CHAMBER CONNECTED

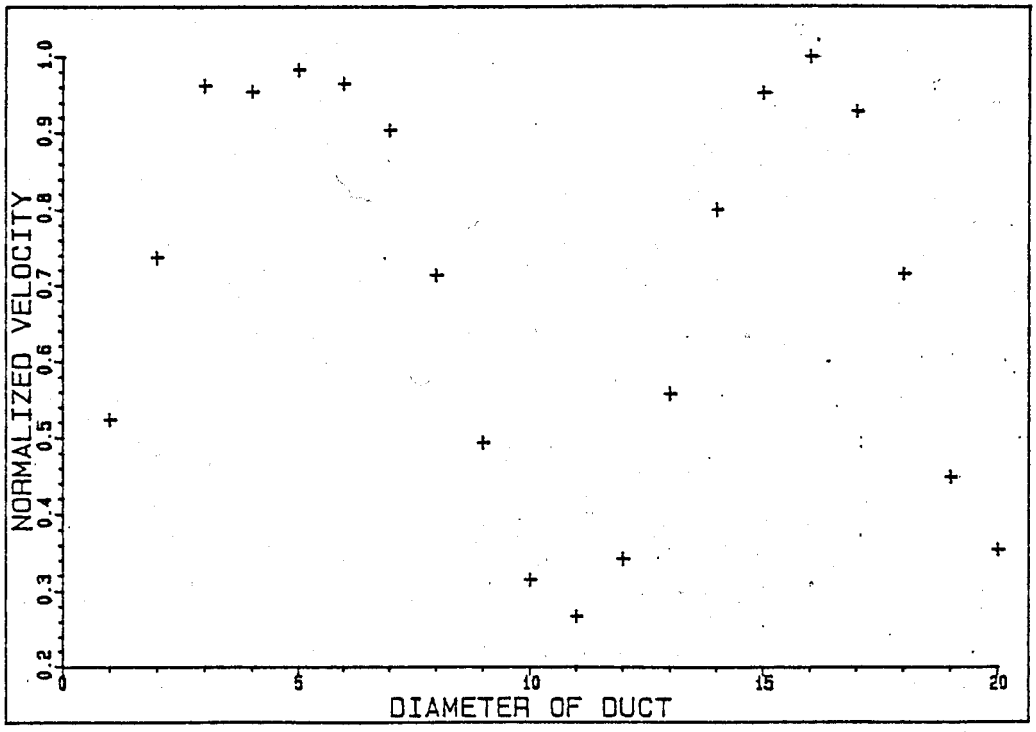

FIG. 9.10 OUTLET VELOCITY PROFILE WITH FILER

9.4.2 Particle Profile Measurement

Single iso-kinetic sampling had been adopted throughout this study because of the uniformity of the particles at any given plane in the duct. In this particular case, a preliminary sampling traverse was needed in order to implement such a procedure. Tests carried out with the diverter control ports plugged are shown in Figure 9.11, while those obtained with the ports operational is in Figure 9.12. These tests were necessary to investigate the effect of the extra volume of air being injected through the control ports.

9.4.3 Effect of Switching Time on Particle Count

There is a range of switching time over which the experiment was performed. In order to be certain that change in switching time does not affect particle analysis downstream samples were taken for 0.1, 0.5, and 1.0 seconds switching time. The resultant particle profiles obtained are shown in Figure 9.13.

9.5 Filtration Test Procedure

The procedure for carrying out a filtration test is the same as that previously discussed in Chapter Seven, except there were certain modifications incorporated in the rig to accommodate the diverter. For example, the second flow control valve previously near the centrifugal fan was removed and replaced by an adjustable flange, to make more space for the diverter. Another deviation from the previous practice was that samples were no longer taken upstream. This is expected to nullify any

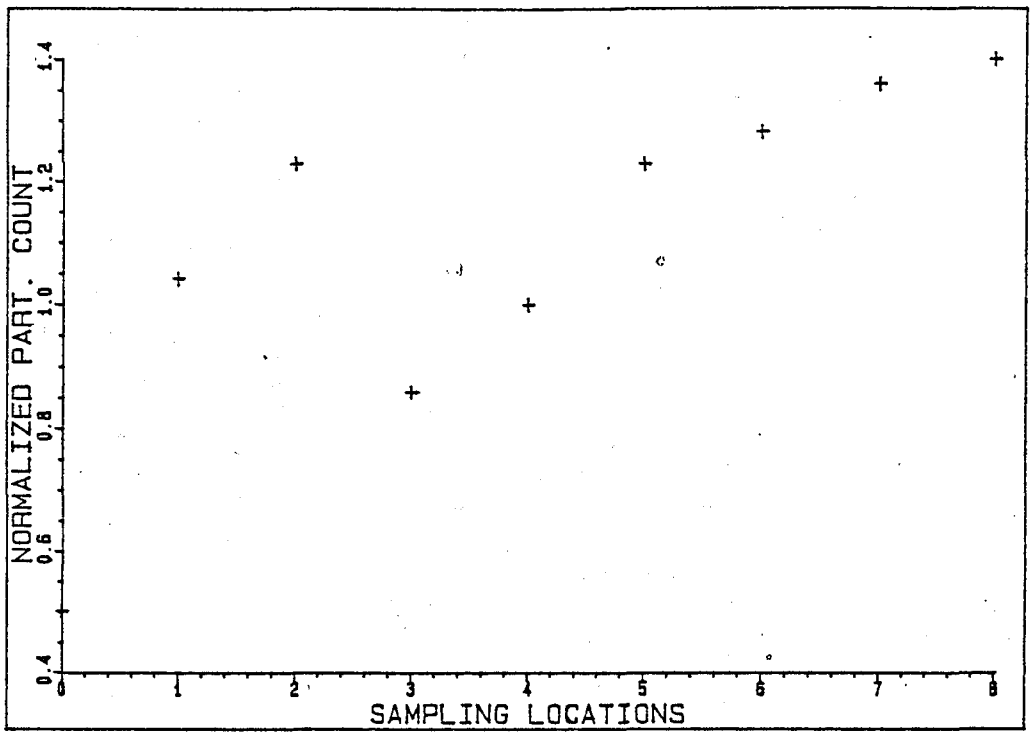

FIG. 9.11 PARTICLE PROFILE WITH CONTROL PORTS PLUGGED

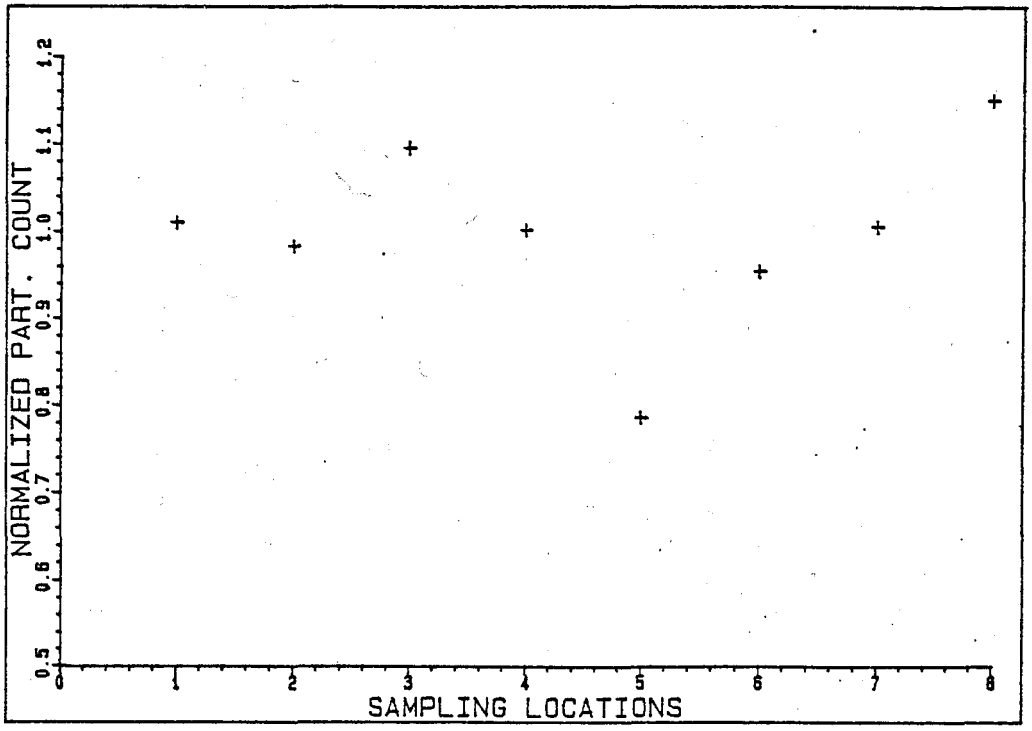

FIG. 9.12 PARTICLE PROFILE WITH DIVERTER SWITCHING

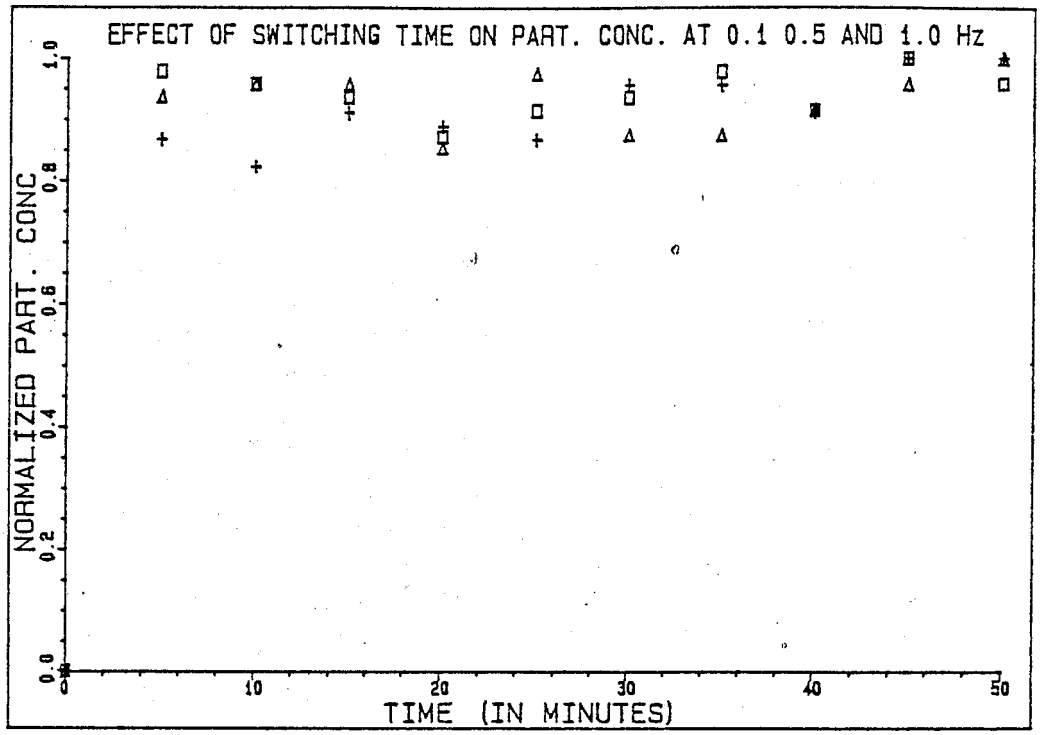

FIG. 9.13 EFFECT OF SWITCHING TIME ON PARTICLE CONCENTRATION

inaccuracies in particle count that may be caused by losses within the diverter itself.

9.6 Discussion of Diverter Results

Figure 9.14 shows the loadability results obtained when the fluid diverter was attached to the main experimental rig. The matrix packing fraction for the test was 0.0075 and the test was carried out with a magnetic field strength of 0.8 Tesla. The fluid velocity was 12.54 m/s. This was slightly less than twice the value previously applied. The reason for this is that for both results to be compared effectively, and the advantage of attaching the diverter isolated, the same throughput must be applied. For reduced pipe size (because of the geometrical constraint), the other variable option was the fluid velocity; hence the high fluid velocity. The frequency of the control flow switching was set at 10 Hz. It should be remembered that the flow residence time, (T_f) , is such that it must not be less than 0.081 second or larger than 1.0 second (ie. $0.081 < T_f < 1.0$)

There is a remarkably poor loadability for particle sizes of 0.265 and 0.315 for the first thirty minutes which recorded a zero collection efficiency of these particle sizes. The next three sizes showed a constant performance for about ten minutes before starting to rise. For the larger sized particles (Figure 9.14(b) and (c)), the effect is slightly different from that of the early part of the test. It showed a steady improvement through to the end. A comparison of these results with those in Figure 8.7 performed at a velocity of 7.6 m/s show different trends. While Figure 8.7 show the efficiency to

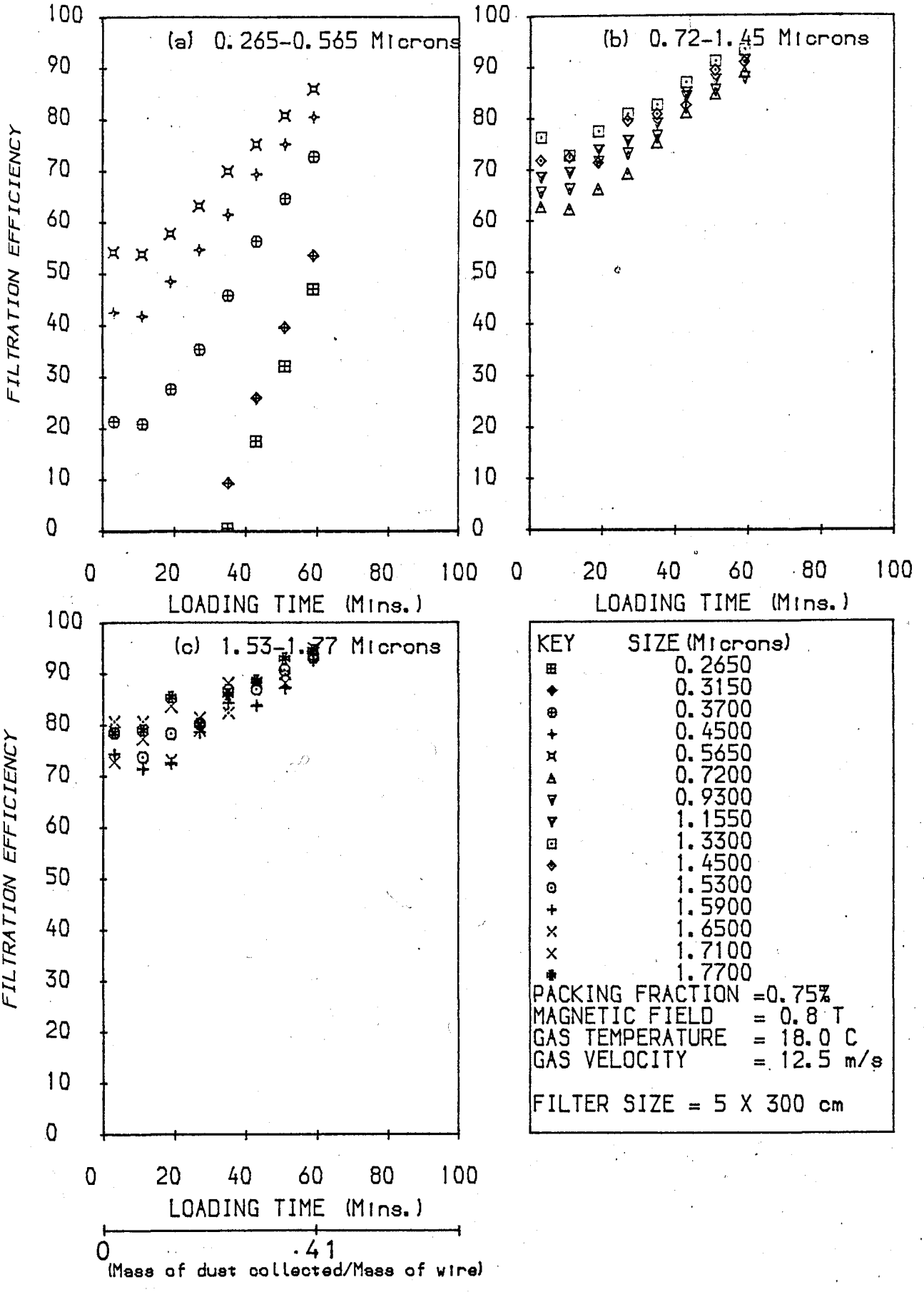

FIG. 9.14 EXPERIMENTAL MATRIX LOADABILITY AT 0.85% PACKING FRACTION (0.8 TESLA)

decrease with time, Figure 9.14 showed it to increase. This suggests that other modes of particle capture, like inertia and direct interception, were strong leading to bigger sized wires resulting from particle build up increasing the particles' chances of being intercepted as filtration progressed. The continual increase in particle capture could also be attributed to the stagnation of the filtrate in the filter volume. This allows more time and less drag for the particles migrating to the wire surfaces. Thus, as well as the magnetic forces increasing the particle retentivity on the wire surfaces, it also attracts those particles outside the swept volume of the wire. As for the very small particles, their poor removal may be due to the initial strong influence of the drag force which compels them to follow the fluid streamlines at the early part of the filtration process.

The clean filter collection efficiency plots are shown in Figure 9.15. Besides the minimal increase in particle collection portrayed after thirty minutes, they are similar to those already discussed.

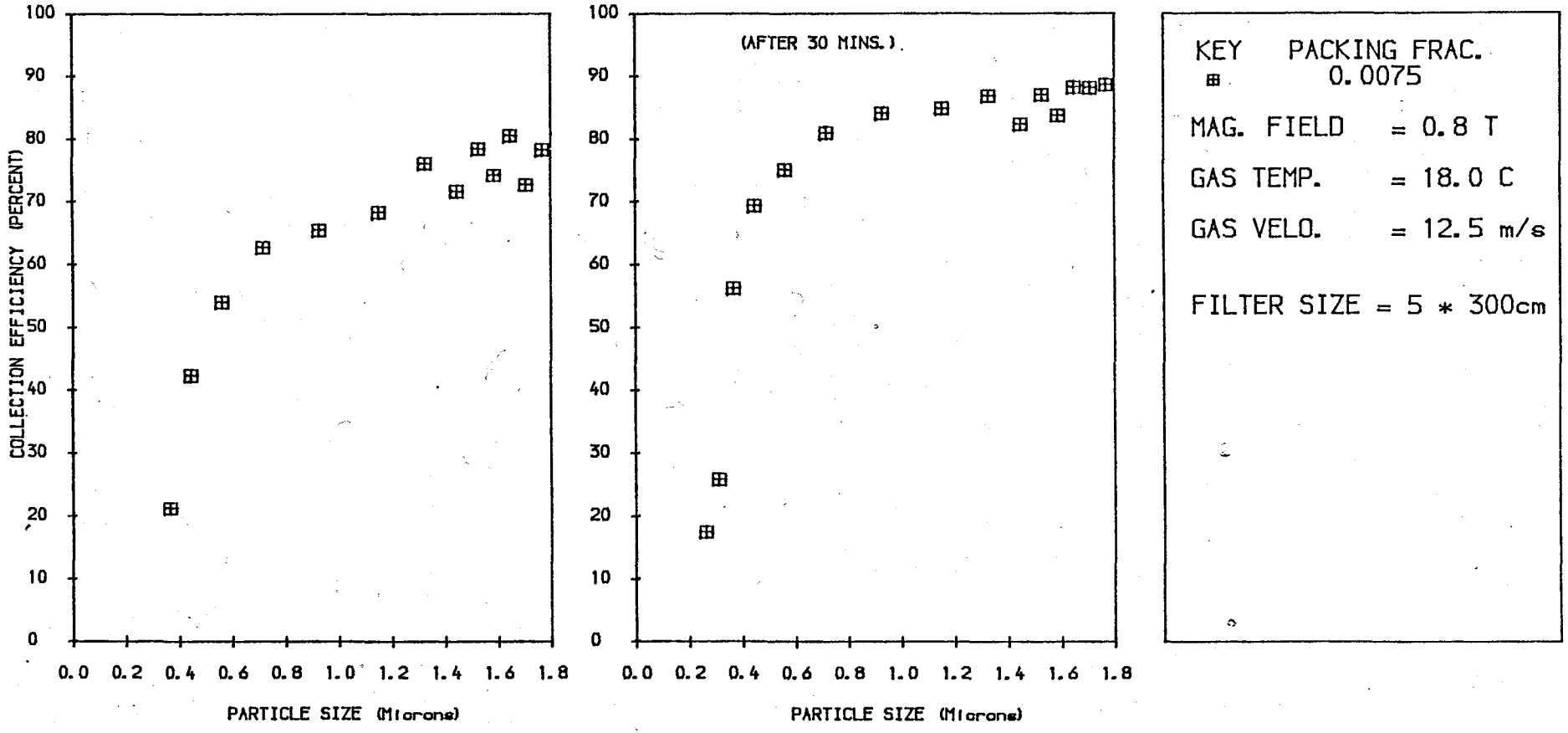

FIG. 9.15 CLEAN FILTER COLLECTION EFFICIENCY AT 13 M/S (0.8 TESLA)

Table 9.1

T_s	T_f
0.1	0.195
0.2	0.389
0.3	0.584
0.4	0.778
0.5	0.973
0.6	1.167
0.7	1.362
0.8	1.556
0.9	1.751
1.0	1.946

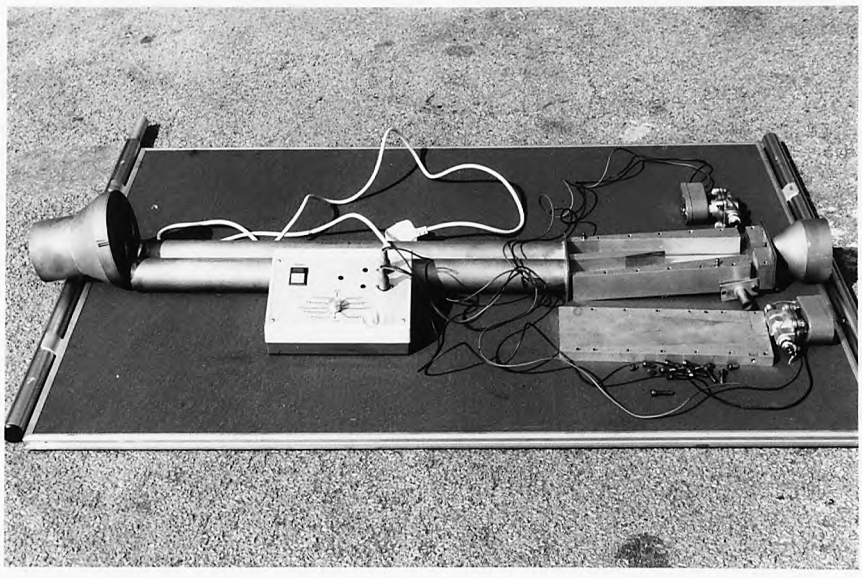

OPEN

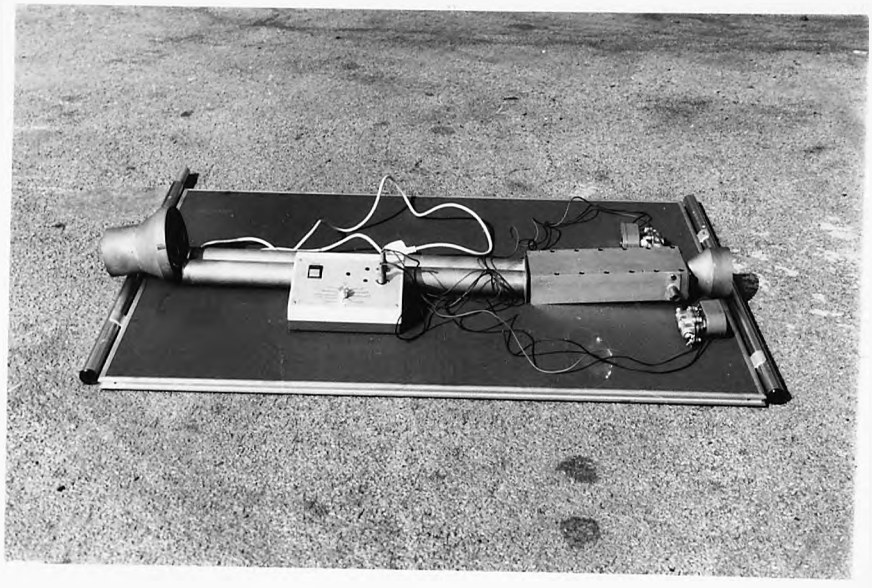

CLOSED

PLATE 9.1: THE DIVERTER UNIT WITH FILTERING ZONE AND OUTPUT CHAMBER (OPEN AND CLOSED)

PLATE 9.2: SET UP FOR VELOCITY PROFILE MEASUREMENT ON THE FLUIDIC DIVERTER

CHAPTER TEN

CONCLUSIONS

10.1 Pressure Drop Results

Pressure drop measurements were performed for both randomly packed and woven wire filters. Straight lines were fitted to each set of experimental data plotted. The gradients and quotient of these lines were calculated and presented. Expressions for predicting mean pressure drop were also prescribed for each group of data. However, they only serve as guides.

Corresponding velocity profiles for all the filters tested were shown. They helped in the understanding of the results by actually portraying the flow patterns after they have gone through the filter matrix. It also gave indication of the uniformity of wire packing in the matrix.

Relationships between the flow resistance and coefficient of drag (C_d) were derived for both random and woven wire filters. Plots of C_d versus Reynolds number were presented for both filters. The two results compared very well but were found to be slightly different from the C_d of a single wire. The difference might have been due to flow turbulence and wakes present in the filter. However, from the presented

results, an estimate of the filter resistance can be made for any given characteristic of a filter with known Reynolds number.

10.2 Experimental Filtration Results

The largest size of the experimental dust (CuO) was less than 2.0 microns. This was established with channel three of the analyser which has a particle size range of 0.265 - 1.770, and confirmed by independent measurements performed with two other different types of analyser.

Loadability tests were performed for two types of filters - randomly packed stainless steel wool (AISI 430) of 50 microns diameter, and well arranged stainless steel woven wire filters of 400 microns pore size. For easy comparison, the mass of woven wires applied were such to produce an equivalent pressure drop for random wire filter.

The test carried out for zero magnetic field with random wire filter showed an initial particle collection capacity, but this quickly vanished with time. Other tests performed with magnetic field present showed increased collection efficiencies. In certain cases like that of 0.1 Tesla, the initial particle efficiency was comparable with that of no field but as the experiment progressed, the benefit of the presence of magnetic field became apparent.

Application of a magnetic field of 0.4 Tesla produced a very good loadability with a relatively uniform curve maintained through the course of the experiment. An unexpected effect took place when 0.8 Tesla was used. This showed a relatively higher collection efficiency for all particles, but the rate of deterioration was much higher especially for particle sizes of 0.265 and 0.310 which fell lower than those of 0.4 Tesla. This cannot be attributed to particle saturation since CuO is paramagnetic. The reason must be because of re-alignment of the wires in the filter matrix that created flow channels which were larger than those in 0.4T filter, allowing the smallest sized particles to escape.

Obviously, as expected an increased packing fraction gave better filter performance. This tended to be untrue for high ratios of mass of wire over the volume of the filter because the gain in applying 1.00% instead of say 0.75% packing fraction for a given filter size was not worth the resistance associated with it. In this study therefore, it was reckoned that the critical packing density was between 0.75 and 1.00 percent for a filter of 10cm X 10cm.

Better filter performance was obtained for an increased gas velocity in the case of random wire. In this case from 5.6 m/s to 7.6 m/s. Very smooth curves were obtained, showing good loadability.

All the tests above were carried out with matrix length of

10cm. Increasing the filter length gave an improved collection. This is almost similar to increasing the matrix packing density in the previous test, but has a possible strong distinction of having less interference as a result of larger volume. Therefore, providing more surface area for a better performance. However, the mass ratio of dust collected was relatively low indicating that a high percentage of the wire were ineffective.

Experimental capture radius were computed from the corresponding values of collection efficiency already determined in the loadability tests, and then plotted against equivalent stokes number. The results were then interpreted interms of main dimensionless parameters.

The varing of major experimental parameters for wire screens produced effects similar to those obtained from the random wire filters, except that of velocity. In this particular application, an increased flow velocity produced a deleterious effect opposite to that obtained in the random wire case.

Filtration efficiencies were determined with screens separated with PVC rings. This was meant to investigate the possibility of separating a binary mixtures. An average of about 50% collection efficiency was obtained for the test. This suggests that if a ferromagnetic dust (which has nearly 100% collection efficiency in HGMF process) is mixed with

CuO on a 1:1 ratio, that it is possible to get a filtrate of ratio 0.05:0.5 respectively. This could be useful in separating very strong magnetic minerals from weak ones.

Most of the experimental loadability results presented show some scatter of the data points. In certain cases like the zero field and 0.1T results, the scatter may be attributed to the magnitude of the magnetic forces but this explanation may not be appropriate for relatively higher magnetic field like 0.4T and 0.8T. In such cases, particle bounce off has been explained to be the cause.

A range of results obtained were given for what is referred here as the clean filter collection efficiency to show how much the arrestance capacity of a filter could fall within 30 minutes. In most cases, the difference between those obtained at zero time and after 30 minutes has elapsed was not much as the filters had yet to collect enough mass of dust for them to deteriorate.

The test was performed for both randomly packed cylindrical wires and woven wires. The results were basically similar and self explanatory. Both results were compared with those obtained from theoretical predictions.

Total collection efficiency based on the total particle count presented as an alternative to loadability and clean filter collection efficiency was considered to be less

effective. This is because the details of the information obtained from experimental data tend to be lost when all the sizes of the particles counted are summed. However, this form of presentation of filtration results seems to be favoured by most industrial manufacturers of dust control equipments.

10.3 Theoretical Results

The non-linear second order simultaneous equations governing the behaviour of a particle in magnetic field (Monodisperse System) were derived in Chapter Five. Also presented were the same equations modified to predict polydisperse systems, but all predictions were performed with the monodisperse system of equations.

The above equations were solved by a combination of modified Euler and Adam-Moulten methods. System parameters equivalent to those used in the experimental work were used to determine critical capture radii.

The values of all the critical radii obtained was less than unity. This suggests that for these particles, in the absence of unfavourable hydrodynamic forces, would be captured by direct interception instead of by the attractive force of the magnetic field. One of the major functions of the magnetic field in this case would have been to supplement the van der Waals forces on the surfaces of the

wire.

Expressions predicting the total filter efficiencies for randomly packed filter and woven wire screens were derived in Chapter Six. The critical radii calculated were substituted together with other matrix geometrical characteristics to determine the total filter efficiency. The only undetermined factor was the effectiveness factor which was optimized for the best fit to the experimental curves. The value chosen was 0.22.

Large particles (> 0.8 microns) were under predicted. Giving the indication that perhaps the model was not suitable and therefore needed modifications. However, the predictions for woven wire filter performance were not entirely unsatisfactory as the error margin present in the random predictions were reduced.

10.4 Fluidic Diverter Results

The fluid velocity used in the fluctuating flow (Diverter application) was about 12.54 m/s which was slightly less than twice the highest velocity applied in the previous tests. The reason for applying double the previous velocity was to enable direct comparison with conventional filtration which had twice the diameter of the diverter filtering zone.The application of the fluidic diverter would only be advantageous if it gave better filtration at an equal throughput.

The clean fibre efficiencies gave very good collection efficiencies for the larger particles but poor results for the smallest size range. This was attributed to the high drag force acting on these small particles which pulled them along the fluid streamline. The bigger ones on the other hand proceeded to hit the wires as a result of inertia and direct interception.

A simple comparison can be made between the results obtained from temporarily bringing the flow to rest in the filter matrix and conventional filtration, to isolate the advantage of the diverter. The diverter produced results that improved as filtration progressed, contrary to what was observed from conventional filtration.

Surprisingly, the noticeable effect of particle bounce off observed in some of the previous results were absent. This may have been because of the filter length which enabled those particles missed or washed off at frontal parts to be captured at the rear of the matrix or increased residence time of the filtrate in the matrix.

CHAPTER ELEVEN

RECOMMENDATION FOR FUTURE WORK

Although high collection efficiencies were obtained from this investigation on paramagnetic dust, they were not comparable to the existing results for ferromagnetic dusts which were successfully filtered at efficiencies of above 99%. Only by using very long matrix (25 cm) were efficiencies of 95% obtained. Alternatively an increased packing density with the smaller matrix (used for most of the tests) was necessary in order to obtain such good results. An alternative approach to achieving a high collection efficiency for the same sized and packed matrix would have been to increase the magnetic field to far above 0.8 Tesla, the maximum capacity of the power generating set used. As paramagnetic dusts never in practice get saturated, an increasing field strength would only serve to enhance their chances of being captured.

The results obtained from these single species investigation is encouraging but there still remains a problem that may be encountered if another dust is present in the filtrate (Binary mixture). The results obtained for single species cannot be directly applicable to this situation. Hence, there needs to be an investigation carried out to determine the extent of the influence of both dusts on each other. The

problem in the case of say a paramagnetic and diamagnetic mixture lies in the diamagnetic particles getting lodged between the interstices of the wire (Mechanical capture). There is also the problem of particles getting captured mechanically at magnetic capture sites.

Some tests were performed with woven wire screens separated with PVC rings. This was additionally intended to be part of a fundamental study in separating paramagnetic and ferromagnetic dusts. Efficiencies of removal of ferromagnetic particles by HGMF for even low field strength and packing fraction is high. The use of the separators in conjunction with wire screens gave poor collection efficiency for CuO dust. So for a mixture of paramagnetic and ferromagnetic dusts the use of separated woven wire meshes would substantially extract the highly susceptible ferromagnetic dusts, while allowing the paramagnetic ones to pass through. This needs to be vigorously investigated

It has been shown that batchwise filtration (ie. the application of fluidic diverter) is possible in the Technology of HGMF. Further work to include the variation of major operating parameters needs to be done. This was not possible during this investigation because of the difficulty encountered in modifying the experimental rig.

The fluidic diverter application could also be very useful for directing the filtrate to a required filter matrix in a

filtration network, in order to carry out repairs or cleaning. The dynamic stability for this particular application needs to be investigated. That is a free running self oscillator is preferred to electrically driven valves, because moving valves are eliminated. Also, a loaded matrix presents a high resistance to the flow and can cause the jet to switch away spontaneously without a switching signal. This phenomena require accomodation in a fluid diverter design.

The theoretical predictions were quite different from the experimental result; indicating that the isolated wire model was not particularly suitable to mimic the performance of a real filter. However, the results obtained for woven wires were quite comparable. This suggests that a major part of the discrepancy between the experimental and theoretical results would have come from the simplifying assumption of a cubic lattice model and wire-to-wire interference because in a random matrix some wires are actually in contact. A thorough investigation needs to be carried out in the area.

The theoretical capture radii calculated in Chapter Six were all less than unity for the experimental parameters applied. Attempts to locate this on Lawson's Magnetic (W) versus Stokes (K) dimensionless numbers failed because they were too small. Another W - K chart is needed for very low dimensionless parameters usually comparable to experimental investigations, thus, excluding the errors involved in

extrapolating the available curves.

APPENDIX A

The higher order Euler equations used in Chapter Six is given below in a general form for a similar less complex equation like

$$\frac{d^2\phi}{dx^2} = F\ (\phi, X, \phi') \tag{B.1}$$

with initial conditions

$$\phi(0) = \phi_o \text{ and } \phi'(0) = \phi_o'$$

Where $\phi' = \frac{d\phi}{dx}$.

Rewriting equation (B.1) gives:

$$\frac{d\phi}{dx} = \zeta \tag{B.2}$$

$$\frac{d\zeta}{dx} = F\ (\phi, x, \zeta) \tag{B.3}$$

With $\zeta(0) = \zeta_o = \zeta_o'$ and $\phi(0) = \phi_o$

The modified Euler method gives:

For Equation (B.2) For Equation (B.3)

$$\phi^p_{i+1} = \phi_i + h\zeta_i \qquad \zeta^p_{i+1} = \zeta_i + hF_i$$

$$\phi^c_{i+1} = \phi_i + \frac{h}{2}(\zeta_i + \zeta^p_{i+1}) \qquad \zeta^c_{i+1} = \zeta_i + \frac{h}{2}(F_i + F^p_{i+1})$$

For similar equation as (B.1), the Adam-Moulten predictor and corrector are given respectively as:

$$\phi^{p}_{i+1} = \phi_i + \frac{h}{24}\left(55F_i - 59F_{i-1} + 37F_{i-2} - 9F_{i-3}\right)$$

$$\phi^{c}_{i+1} = \phi_i + \frac{h}{24}\left(9F^{p}_{i+1} + 19F_i - 5F_{i-1} + F_{i-2}\right)$$

Where h represents the step size.

APPENDIX B

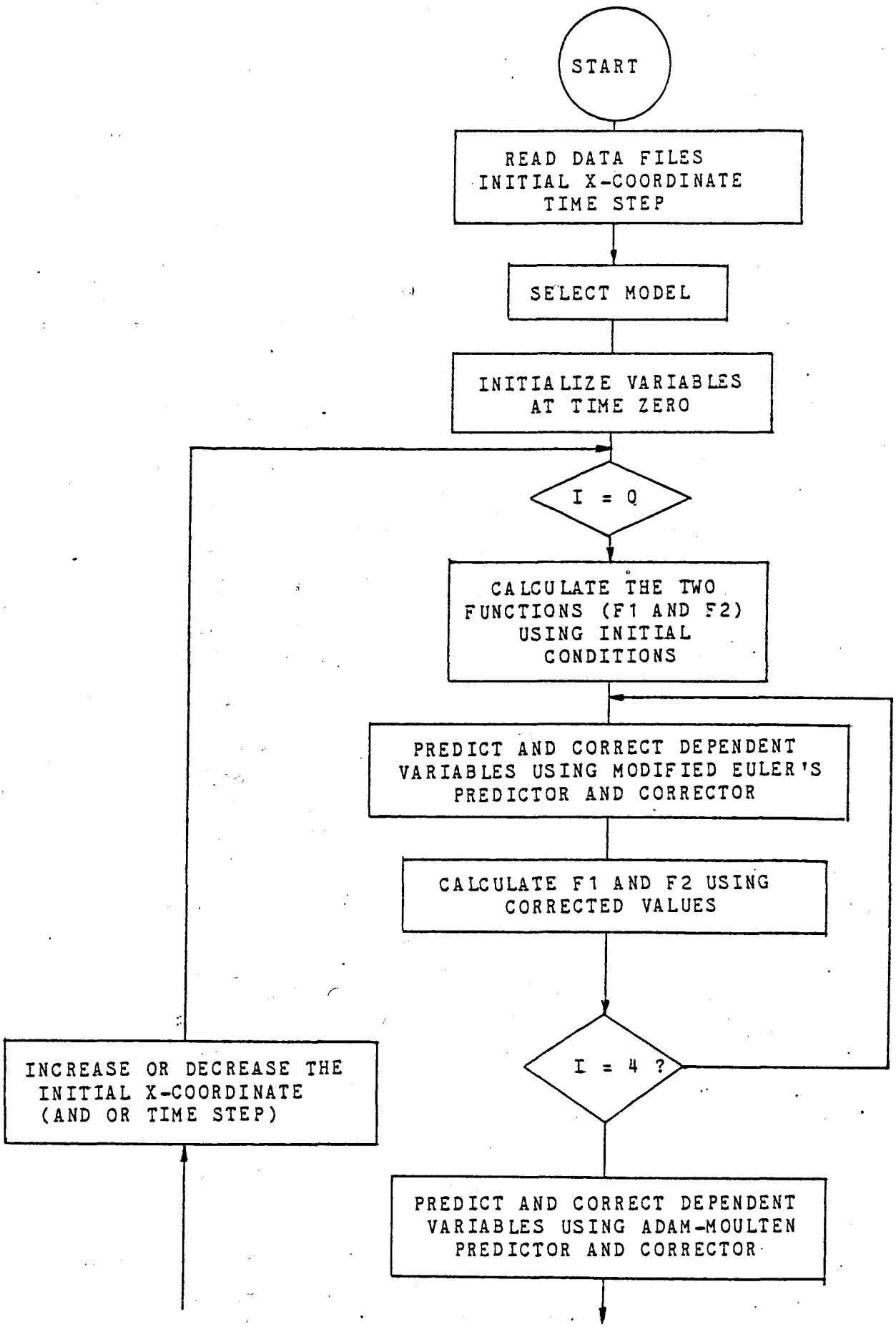
START
READ DATA FILES
INITIAL X-COORDINATE
TIME STEP
SELECT MODEL
INITIALIZE VARIABLES
AT TIME ZERO
I = 0
CALCULATE THE TWO
FUNCTIONS (F1 AND F2)
USING INITIAL
CONDITIONS
PREDICT AND CORRECT DEPENDENT
VARIABLES USING MODIFIED EULER'S
PREDICTOR AND CORRECTOR
CALCULATE F1 AND F2 USING
CORRECTED VALUES
I = 4 ?
INCREASE OR DECREASE THE
INITIAL X-COORDINATE
(AND OR TIME STEP)
PREDICT AND CORRECT DEPENDENT
VARIABLES USING ADAM-MOULTEN
PREDICTOR AND CORRECTOR

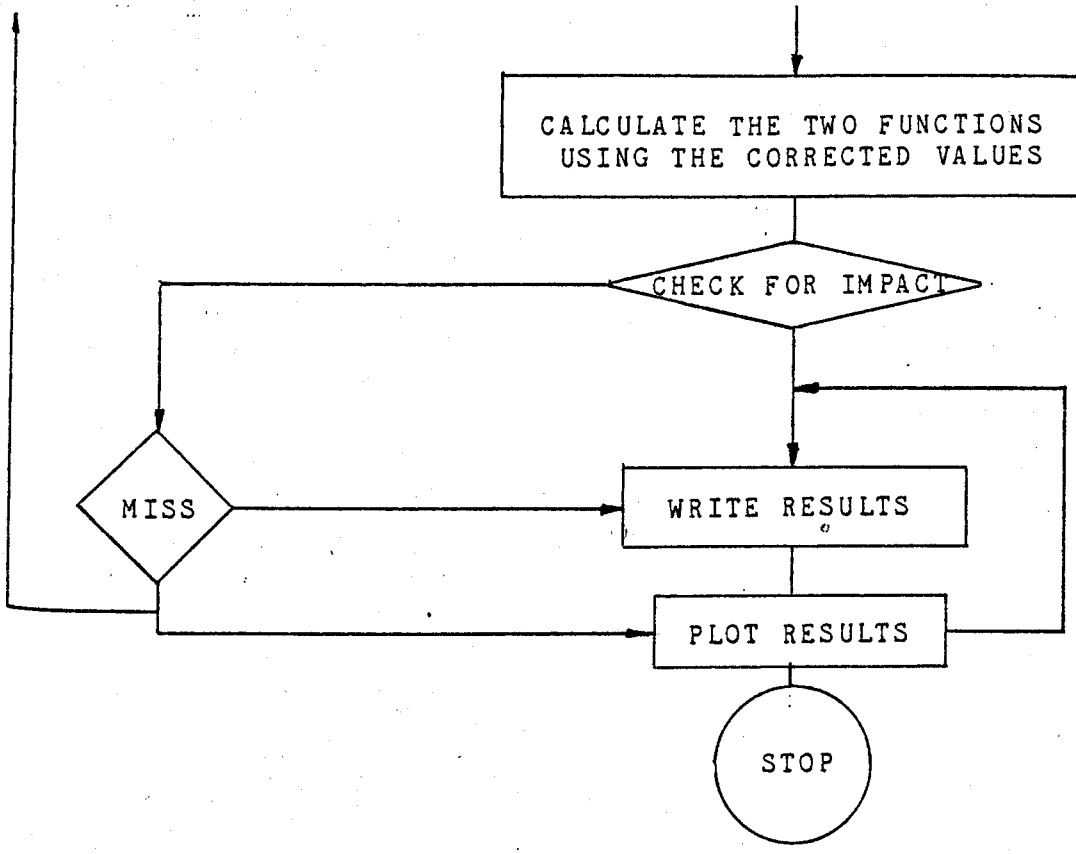
CALCULATE THE TWO FUNCTIONS USING THE CORRECTED VALUES
CHECK FOR IMPACT
MISS
WRITE RESULTS
PLOT RESULTS
STOP

```
CC::::PROGRAM TO CALCULATE (CRITICAL) PARTICLE TRAJECTORIES*
      PROGRAM ME2
      LOGICAL LPRINT
      DIMENSION PARTPC(20),GAMAC(20),TETAC(20),OMEGC(20)
      DIMENSION FC1C(20),FC2C(20)
      CHARACTER*8 FILE1,FILE2,FILE3,FILE4
CC::::PARTICLE AND FLUID DATA
      COMMON /VARIA/A,W,G,BK,Z,IFL
      DATA DT,MD/0.0,1000/
      OPEN(8,FILE='XVA')
      GO TO 74
      WRITE(1,1)
1     FORMAT ('ENTER X/Y-AXIS & TIME FILENAME')
2     FORMAT(A6)
      READ(1,2) FILE1
      OPEN(8,FILE=FILE1)
      WRITE(1,123)
123   FORMAT ('ENTER VELOCITY FILENAME')
      READ(1,2) FILE2
      OPEN(9,FILE=FILE2)
      WRITE(1,124)
124   FORMAT ('ENTER ACCELERATION FILENAME')
      READ(1,2) FILE3
      OPEN(7,FILE=FILE3)
      WRITE(1,333)
CC::::SPECIFICATION OF INITIAL CONDITIONS
333   FORMAT('ENTER YDW,DELTAT,IFL')
      READ(1,*)YDW,DELTAT,IFL
74    WRITE(1,233)
233   FORMAT('ENTER YDW')
      READ(1,*)YDW
      DELTAT=0.005
      IFL=0
      IF(IFL.EQ.0)THEN
      WRITE(1,12)
12    FORMAT('POTENTIAL FLOW MODEL')
      ELSE
      WRITE(1,13)
13    FORMAT('LAMINAR FLOW MODEL')
      END IF
      L=0
      I=0
      NPOINT=0
      XDW=50.0
CC::::DETERMINATION OF INITIAL POSITION WITH X- Y- VALUES
      TETAI=ATAN(YDW/XDW)
      PARTPI=SQRT(XDW*XDW+YDW*YDW)
      GAMAI=-1.0/PARTPI*((BK*G*YDW)+XDW)
      OMEGI=1.0/PARTPI**2*(YDW-(BK*G*XDW))
      CALL FUNC12(PARTPI,GAMAI,OMEGI,TETAI,F1C,F2C)
33    I=I+1
      DT=DT+DELTAT
CC::::APPLICATION OF MODIFIED EULER METHOD TO GENERATE THE FIRST FOUR
CC::::PARTICLE LOCATIONS
      PARTPP=PARTPI+DELTAT*GAMAI
      GAMAP=GAMAI+DELTAT*F1C
      TETAP=TETAI+DELTAT*OMEGI
      OMEGP=OMEGI+DELTAT*F2C
      CALL FUNC12(PARTPP,GAMAP,OMEGP,TETAP,FC1I,FC2I)
      PARTPC(I)=PARTPI+DELTAT/2.0*(GAMAI+GAMAP)
      GAMAC(I)=GAMAI+DELTAT/2.0*(F1C+FC1I)
      TETAC(I)=TETAI+DELTAT/2.0*(OMEGI+OMEGP)
      OMEGC(I)=OMEGI+DELTAT/2.0*(F2C+FC2I)
```

```
      CALL FUNC12(PARTPC(I),GAMAC(I),OMEGC(I),TETAC(I),FC1,FC2)
      FC1C(I)=FC1
      FC2C(I)=FC2
      PARTPI=PARTPC(I)
      GAMAI=GAMAC(I)
      TETAI=TETAC(I)
      OMEGI=OMEGC(I)
      F1C=FC1C(I)
      F2C=FC2C(I)
      IF(I.GE.4) GO TO 3
      GO TO 33
CC::::APPLICATION OF ADAM - MOULTEN METHOD
3     L=L+1
      LPRINT=(MOD(L,MD).EQ.0)
      DT=DT+DELTAT
      PATMP=PARTPC(4)+DELTAT/24.0*(55.0*GAMAC(4)-59.0*GAMAC(3)+
     +37.0*GAMAC(2)-9.0*GAMAC(1))
      GAMMP=GAMAC(4)+DELTAT/24.0*(55.0*FC1C(4)-59.0*FC1C(3)+37.0*
     +FC1C(2)-9.0*FC1C(1))
      TETMP=TETAC(4)+DELTAT/24.0*(55.0*OMEGC(4)-59.0*OMEGC(3)+
     +37.0*OMEGC(2)-9.0*OMEGC(1))
      OMEMP=OMEGC(4)+DELTAT/24.0*(55.0*FC2C(4)-59.0*FC2C(3)+37.0*
     +FC2C(2)-9.0*FC2C(1))
      CALL FUNC12(PATMP,GAMMP,OMEMP,TETMP,FCMP1,FCMP2)
      PATMC=PARTPC(4)+DELTAT/24.0*(9.0*GAMMP+19.0*GAMAC(4)-5.0*
     +GAMAC(3)+GAMAC(2))
      GAMMC=GAMAC(4)+DELTAT/24.0*(9.0*FCMP1+19.0*FC1C(4)-5.0*
     +FC1C(3)+FC1C(2))
      TETMC=TETAC(4)+DELTAT/24.0*(9.0*OMEMP+19.0*OMEGC(4)-
     +5.0*OMEGC(3)+OMEGC(2))
      OMEMC=OMEGC(4)+DELTAT/24.0*(9.0*FCMP2+19.0*FC2C(4)-
     +5.0*FC2C(3)+FC2C(2))
CC::::PARTICLE LOCATION ON A TWO DIMENTIONAL PLANE
      YAXIS=PATMC*SIN(TETMC)
      XAXIS=PATMC*COS(TETMC)
CC::::SPECIFICATION OF BOUNDARY CONDITIONS
      IF(XAXIS.LE.-1.50)GO TO 42
      IF(XAXIS.LE.0.80.AND.YAXIS.LE.0.50) GO TO 42
      IF(XAXIS.LE.0.80.AND.YAXIS.LE.-0.04) GO TO 42
      IF(XAXIS.LE.-4.00.AND.YAXIS.GE.YDW) GO TO 42
      IF(XAXIS.LE.-4.00.AND.YAXIS.LE.-YDW) GO TO 42
      IF(YAXIS.GE.6.0*YDW) GO TO 42
      IF(XAXIS.LT.6.0) MD=50
      CALL FUNC12(PATMC,GAMMC,OMEMC,TETMC,FC11,FC22)
C     WRITE(1,*)YAXIS,XAXIS,DT
      IF(XAXIS.LE.100.0)THEN
      IF(LPRINT)THEN
      NPOINT=NPOINT+1
      WRITE(1,*) YAXIS,XAXIS,DT
      WRITE(8,*) YAXIS,XAXIS,DT
C     WRITE(9,*) GAMMC,OMEMC
C     WRITE(7,*) FC11,FC22
      END IF
      END IF
CC::::RESET OF PARAMETERS FOR NEXT STEP OF CALCULATION
      GAMAC(2)=GAMAC(3)
      GAMAC(3)=GAMAC(4)
      GAMAC(4)=GAMMC
      OMEGC(2)=OMEGC(3)
      OMEGC(3)=OMEGC(4)
      OMEGC(4)=OMEMP
      FC1C(2)=FC1C(3)
      FC1C(3)=FC1C(4)
      FC1C(4)=FC11
      PARTPC(4)=PATMC
      TETAC(4)=TETMC
```

```
      FC2C(2)=FC2C(3)
      FC2C(3)=FC2C(4)
      FC2C(4)=FC22
      GO TO 3
42    WRITE(8,*)NPOINT
C     CALL PLOT(NPOINT)
      STOP
      END
CC::::CALCULATION OF MODEL FUNCTIONS
      SUBROUTINE FUNC12(PARTPO,GAMMA,OMEGA,TETAR,VALUE1,VALUE2)
      COMMON /VAR1A/A,W,G,BK,Z,IFL
      DATA BETAR/0.00/
      BETA=BETAR*Z/180.0
      CTE=COS(TETAR)
      STE=SIN(TETAR)
      CTE2=COS(2.0*TETAR)
      STE2=SIN(2.0*TETAR)
      PA1=2.0*W*A/PARTPO**3
      PAA=A/(PARTPO**2)
      PAU=1.0/(PARTPO**2)
      PA2=2.0*W*A/PARTPO**4
      POC2=2.0*GAMMA*OMEGA/PARTPO
      REN=0.10
      CON=1.0/ALOG(7.4/REN)
      IF(IFL.EQ.0)THEN
      RADV=(1.0-1.0/PARTPO**2)*COS(TETAR+BETA)
      TANV=(1.0+1.0/PARTPO**2)*SIN(TETAR+BETA)
C     RADV=0.0
C     TANV=0.0
      ELSE
      RADV=CON*(ALOG(PARTPO)-0.5*(1.0-1.0/PARTPO**2))*COS(TETAR+BETA)
      TANV=CON*(ALOG(PARTPO)-0.5*(1.0-1.0/PARTPO**2))*SIN(TETAR+BETA)
C     RADV=0.0
C     TANV=0.0
      END IF
      VALUE1=PARTPO*OMEGA**2-PA1*(CTE2+PAA)-1.0/BK*(GAMMA+RADV)-(G*ST
      VALUE2=-POC2-PA2*STE2-1.0/(BK*PARTPO)*(PARTPO*OMEGA-TANV)-
     +(G*CTE/PARTPO)
      RETURN
      END
CC::::PLOTTING OF RESULTS
      SUBROUTINE PLOT(NPOINT)
      DIMENSION YAXIS(5000),XAXIS(5000),DT(5000)
      REWIND 8
      READ(8,*)(YAXIS(I),XAXIS(I),DT(I),I=1,NPOINT)
      CALL INKPEN(2)
      CALL PAPER(1)
      CALL PSPACE(0.4,0.8,0.1,0.9)
      CALL CSPACE(0.0,1.0,0.0,1.0)
      CALL MAP(-2.0,2.0,-2.0,6.0)
      CALL AXESSI(1.0,1.0)
      CALL CURVEO(YAXIS,XAXIS,1,NPOINT)
      CALL PLOTCS(4.0,16.0,'A=0.754',7)
      CALL PLOTCS(4.0,14.0,'W=2.01',6)
      CALL PLOTCS(4.0,12.0,'K=0.52',6)
      CALL PLOTCS(4.0,10.0,'W=0.00',6)
      CALL GREND
      RETURN
      END
      BLOCK DATA
      COMMON /VAR1A/A,W,G,BK,Z,IFL
C     DATA A,W,G,BK,Z/0.754,2.01,0.0,0.53,3.14159/
      DATA A,W,G,BK,Z/1.54,.000391,0.0,0.695,3.14159/
C     DATA A,W,G,BK,Z/0.0157,7829294.829,2917.78,0.00142,3.14159/
C     DATA A,W,G,BK,Z/0.0157,7829294.829,0.00,0.00142,3.14159/
      END
```

```
>L.
  10REM ********************************
  20REM **                              **
  30REM **  Spectrometer Analysis     **
  40REM **           Program            **
  50REM **                              **
  60REM **                              **
  70REM **                              **
  80REM ********************************
  90MODE4
 100*KEY10 OLD:M
 110REM ONERROR GOTO 940
 120IER=&FE6E:rec=0:num=0
 130 rec$="ABCDEFGHIJKLMNOPQRSTUVWXYZ"
 1400SBYTE=&FFF4
 150A%=&97:X%=&6C:Y%=&FE:CALL OSBYTE
 160temp=&70:?temp=&00
 170DIM c10(10),c9(10),c8(10),c7(10),c4(10),c3(10),c2(10),c1(10),size(6,16)
 180DIM M% 100
 190FORopt%=0 TO 3 STEP 3
 200P%=M%
 210[
 220OPT opt%
 230.init SEI
 240LDA &206
 250STA oldv
 260LDA &207
 270STA oldv+1
 280LDA #int MOD 256
 290STA &206
 300LDA #int DIV 256
 310STA &207
 320CLI
 330RTS
 340.int LDA &FC
 350PHA
 360TXA
 370PHA
 380TYA
 390PHA
 400LDA &FE6D
 410AND #&90
 420CMP #&90
 430BNE exit
 440STA &FE6D
 450INC &70
 460.exit PLA
 470TAY
 480PLA
 490TAX
 500PLA
 510STA &FC
 520JMP (oldv)
 530.oldv EQUW 0
 540]
 550NEXT opt%
 560REM CALL init
 570 REM ? IER=&90 To enable Interupt
 580FOR opt%=0 TO 3 STEP 3
 590P%=&900
 600[
 610OPT opt%
 620LDA #&FF:STA &8D \ No of count in delay
 630LDA #&00:STA &8F \ Set COUNTERS
```

```
640STA &8E  \                to zero
650LDA #&97:LDX #&62:LDY#&00:JSR OSBYTE \ Sets port B to OUTPUT
660.pulse LDA #&97 \ Start of Routine
670LDX #&6C:LDY #&DE:JSR OSBYTE     \       CB2 set LOW
680JSR delay
690LDX #&6C
700LDA #&97:LDY #&FE:JSR OSBYTE \ Set CB2 HIGH
710JSR delay
720LDA #&96:LDX #&60:JSR OSBYTE  \ Input Data at Port B
730TYA     \ Transfer Data to A Reg
740LDY &8E:STA &80,Y \ load Y Reg with zero page offsett and store Data
750INC &8E:INC &8F \ increment offset     and increment count
760LDA #&04:CMP &8F \ check to see if
770BNE pulse \4 bytes have been input
780LDA #&97:LDX #&6C:LDY #&DE:JSR OSBYTE
790JSR delay
800LDA #&97:LDX #&6C:LDY #&FE:JSR OSBYTE
810RTS
820.delay LDA #&00
830 DEC &8D
840 CMP &8D
850BNE delay
860 RTS
870]
880NEXT opt%
890CLS
900PRINTTAB(5,5)"********************************"'TAB(5)"**
**"'TAB(5)"**    Spectrometer Analysis  **"
910PRINTTAB(5,8)"**            Program          **"'TAB(5)"**
**"
920PRINTTAB(5,10)"**        Written BY          **"'TAB(5)"**       Phillip Kennett
**"'TAB(5)"**                                **"
930PRINTTAB(5,13)"**      Mech Engineering      **"'TAB(5)"**    Electronics Workshop
**"'TAB(5)"**                                **"
940PRINTTAB(5,16)"********************************"
950INPUT"'TAB(5)"WHAT IS YOUR SAMPLING POINT ?"'TAB(5)"UPSTREAM OR DOWNSTREAM ? "dis
k$
960IF disk$="U" disk$="U.point":GOTO 990
970IF disk$="D" disk$="D.point":GOTO 990
980 GOTO 950
990INPUT"TAB(5)"WHAT IS YOUR RADIAL SAMPLING"'TAB(5)"POSITION....1 TO 9 ? "S$
1000disk$=disk$+S$
1010INPUT'TAB(5)"The Record Qualifier is < A >"'TAB(5)"Do you Wish To Change It Y / N "
num$
1015IF num$="N" THEN GOTO 1040
1020IF num$="Y" THEN INPUT'TAB(5)"Enter The New Qualifier ! "num$ ELSE GOTO 1010
1030num=ASC(num$)-&41
1040CLS
1050PRINTTAB(3,5)"Do You Require an Increased"'TAB(3)"Sampling Delay Y / N":PRINT
1060ques$=GET$
1070IF ques$="Y" THEN INPUTTAB(3,8)"Enter Delay Time In Mins  "delay:delay=delay*60:GO
TO 1100
1080IF ques$="N" THEN delay=0:GOTO 1100
1090GOTO 1040
1100PRINTTAB(3,11)"Do You Require a Continuos"'TAB(3)"Sampling Interval Y / N"
1110per$=GET$
1120IF per$<>"Y" THEN P%=0:GOTO 1160
1130IF per$="Y" THEN P%=1:INPUTTAB(3,15)"Give Time Interval In Mins  "period:period=perio
d*60 ELSE P%=0
1140INPUTTAB(3,18)"Enter the Spectrometer Sampling"'TAB(3)"Time in seconds... "tim
1150tim=period/tim
1160CLS
1170INPUTTAB(5,5)"Enter the Date !  eg. 7. March. 86     "A$:A=LEN(A$)
1180INPUTTAB(5,8)"Enter a test No if required             "B$:B=LEN(B$)
1190INPUTTAB(5,11)"Enter Your Name if required            "C$:C=LEN(C$)
1200CLS
```

```
1210REM VDU2
1220PRINT"Spectrometer Test No ";B$;SPC(40-(21+B))
1230PRINT"Test Initiated by ";C$;SPC(40-(18+C))
1240PRINT"Date  ";A$;SPC(40-(6+A))
1250PRINT;SPC(40)
1260VDU3
1270PRINTTAB(5,20);CHR$136;"Press any key to continue"
1280Z=GET
1290CALL init
1300? IER=&90
1310CLS
1320T=0:F=0:N=0:B%=0
1330REPEAT
1340IF P%=0 THEN PROCstart
1350IF delay>0 AND  P%=1 AND B%=0 THEN PROCsample
1360IF delay=0 THEN w=0:GOTO 1420
1370PRINTTAB(10,10)"AT DELAY"
1380FOR D=1 TO delay
1390w=INKEY(100)
1400NEXT
1410PRINTTAB(10,10)"END OF DELAY"
1420?&70=0
1430IF P%=1 THEN PROCsample
1440UNTIL w=&20
1450CLS:PRINTTAB(8,10)"PROGRAM TERMINATED"
1460END
1470DEFPROCstart
1480fin=0
1490PRINTTAB(8,12)"AT PROC START"
1500?&70=&00:I%=0
1510REPEAT
1520IF ?&70=&01 PROCinterupt:I%=I%+1
1530UNTIL I%=10
1540PROCprint:PROCdisk:PROCgraph
1550ENDPROC
1560DEFPROCinterupt
1570 CALL &900
1580N=N+1
1590?&70=0
1600c10(N)=?&80 DIV 16:c9(N)=?&80 MOD 16:c8(N)=?&81 DIV 16:c7(N)=?&81 MOD 16:c4(N)=?&82 DI
V 16:c3(N)=?&82 MOD 16:c2(N)=?&83 DIV 16:c1(N)=?&83 MOD 16
1610IF N=1 AND c10(1)<>15 THEN N=0:ENDPROC
1620CLS
1630IF N=10 THEN N=0:PROCtotal
1640ENDPROC
1650DEFPROCprint
1660REM VDU2
1670FOR G=1 TO 10
1680PRINT;~c10(G);:PRINT;~c9(G);:PRINT;~c8(G);:PRINT;~c7(G);"xx";:PRINT;~c4(G);:PRINT;~c3(G);:PRINT
;~c2(G);:PRINT;~c1(G);SPC(3);
1690F=F+1:IF F=10 THEN PRINT;SPC(27):PRINT SPC(40):F=0:T=0:NEXT:VDU3:ENDPROC
1700T=T+1:IF T=3 THEN PRINT;" ":T=0
1710NEXT
1720VDU3
1730ENDPROC
1740DEFPROCtotal
1750G=3:S=0
1760FOR I=1 TO 8
1770size(0,S)=c10(G)*1000+c9(G)*100+c8(G)*10+c7(G)
1780S=S+1
1790size(0,S)=c4(G)*1000+c3(G)*100+c2(G)*10+c1(G)
1800G=G+1:S=S+1
1810NEXT
1820IF size(0,0) > 1000 THEN mult=0.1
1830PRINT"Total No of Particles = ";size(0,0)
1840PRINT':TAB(10)"Breakdown of Particles"
```

```
1850IF size(0,0) > 99 AND size(0,0) < 1000THEN mult=1
1860IF size(0,0) < 99 THEN mult= 10
1870PRINT"SIZE 1  SIZE 2  SIZE 3  SIZE 4  SIZE 5"
1880PRINTTAB(1);size(0,1);TAB(9);size(0,2);TAB(17);size(0,3);TAB(25);size(0,4);TAB(33);size(0,5)
1890PRINT""SIZE 6  SIZE 7  SIZE 8  SIZE 9  SIZE 10"
1900PRINTTAB(1);size(0,6);TAB(9);size(0,7);TAB(17);size(0,8);TAB(25);size(0,9);TAB(33);size(0,10)
1910PRINT""SIZE 11 SIZE 12 SIZE 13 SIZE 14 SIZE 15"
1920PRINTTAB(1);size(0,11);TAB(9);size(0,12);TAB(17);size(0,13);TAB(25);size(0,14);TAB(33);size(0,15)
1930PRINT'
1940PRINTTAB(15)"Sample No";rec+1 '
1950ENDPROC
1960DEFPROCgraph
1970CLS
1980MOVE 40,20:DRAW 40,1020:MOVE 40,20:DRAW 1240,20
1990X=45:Y=20
2000FOR I=0 TO 15
2010MOVE X,Y:DRAW X,Y+(size(0,I)*mult):DRAW X+60,Y+(size(0,I)*mult):DRAW X+60,Y
2020X=X+75
2030NEXT
2040PRINT"          MULTIPLIER = ";mult
2050Z=INKEY(300)
2060CLS
2070ENDPROC
2080DEFPROCdisk
2090rec=rec+1
2100FOR I=1 TO 16
2110size(rec,I)=size(0,I-1)
2120NEXT
2130PRINT"PRESS SPACE BAR FOR MANUAL SAVE TO DISK"
2140Z=INKEY(300)
2150IF Z=&20 THEN GOTO 2170
2160IF rec<>6 THEN ENDPROC
2170*DR.0
2180num=num+1:num$=MID$(rec$,num,1):save$=disk$+num$
2190PRINT;CHR$(136);"SAVING ";save$;" TO DISK"
2200channel=OPENOUT (save$)
2210FOR rec=1 TO 6
2220FOR I=1 TO 16
2230PRINT# channel,size(rec,I)
2240NEXT
2250NEXT
2260CLOSE# channel
2270rec=0
2280IF num=25 THEN num=0
2290ENDPROC
2300DEFPROCsample
2310PRINTTAB(8,12)"AT PROC sample"
2320samp=0
2330?&70=&00
2340REPEAT
2350I%=0
2360samp=samp+1
2370REPEAT
2380IF ?&70=&01 PROCinterupt:I%=I%+1
2390UNTIL I%=10
2400PROCprint:PROCdisk:PROCgraph
2410UNTIL samp=tim
2420CLS
2430B%=1
2440ENDPROC
```

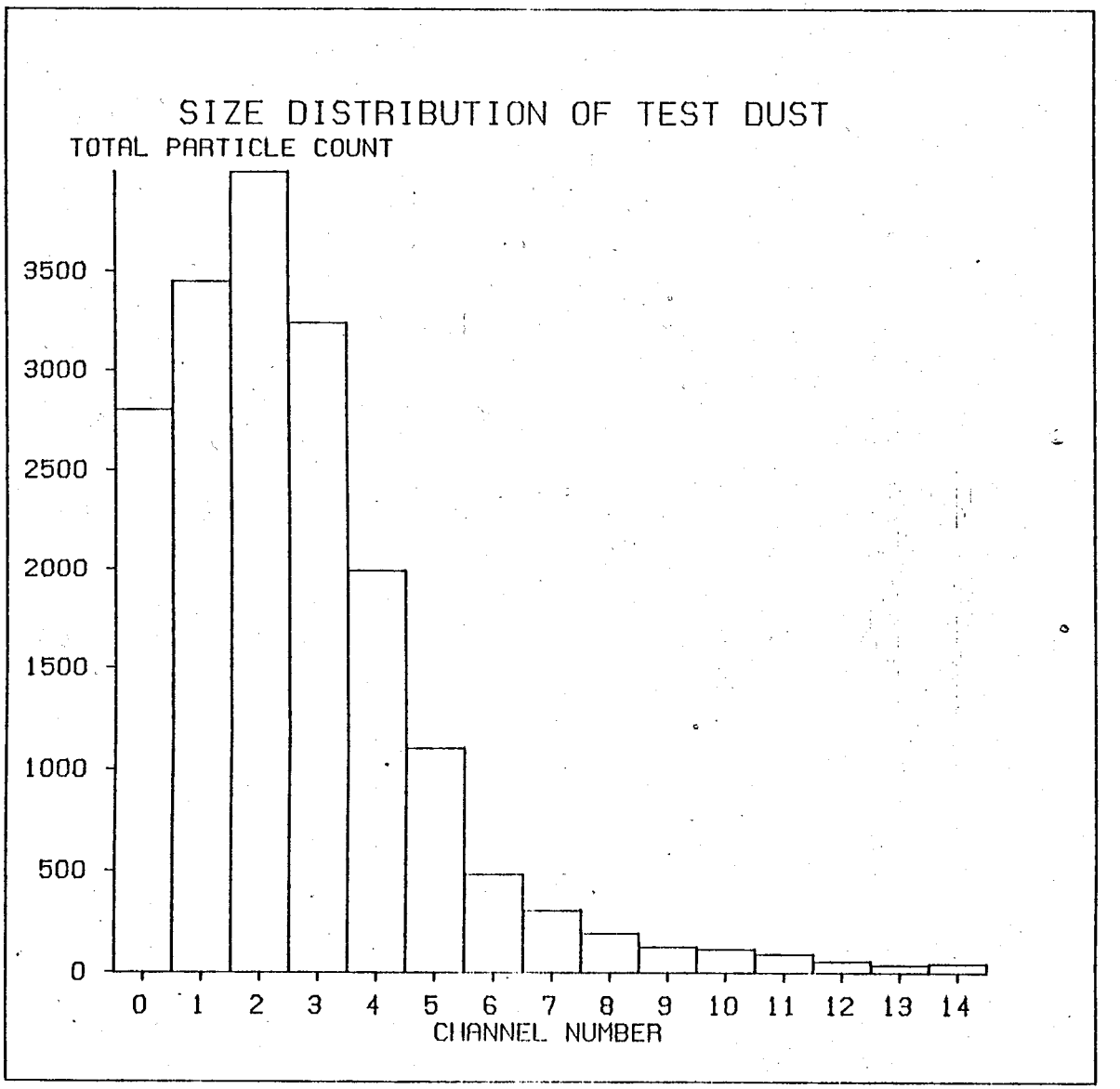
SIZE DISTRIBUTION OF TEST DUST
TOTAL PARTICLE COUNT
3500
3000
2500
2000
1500
1000
500
0
0 1 2 3 4 5 6 7 8 9 10 11 12 13 14
CHANNEL NUMBER

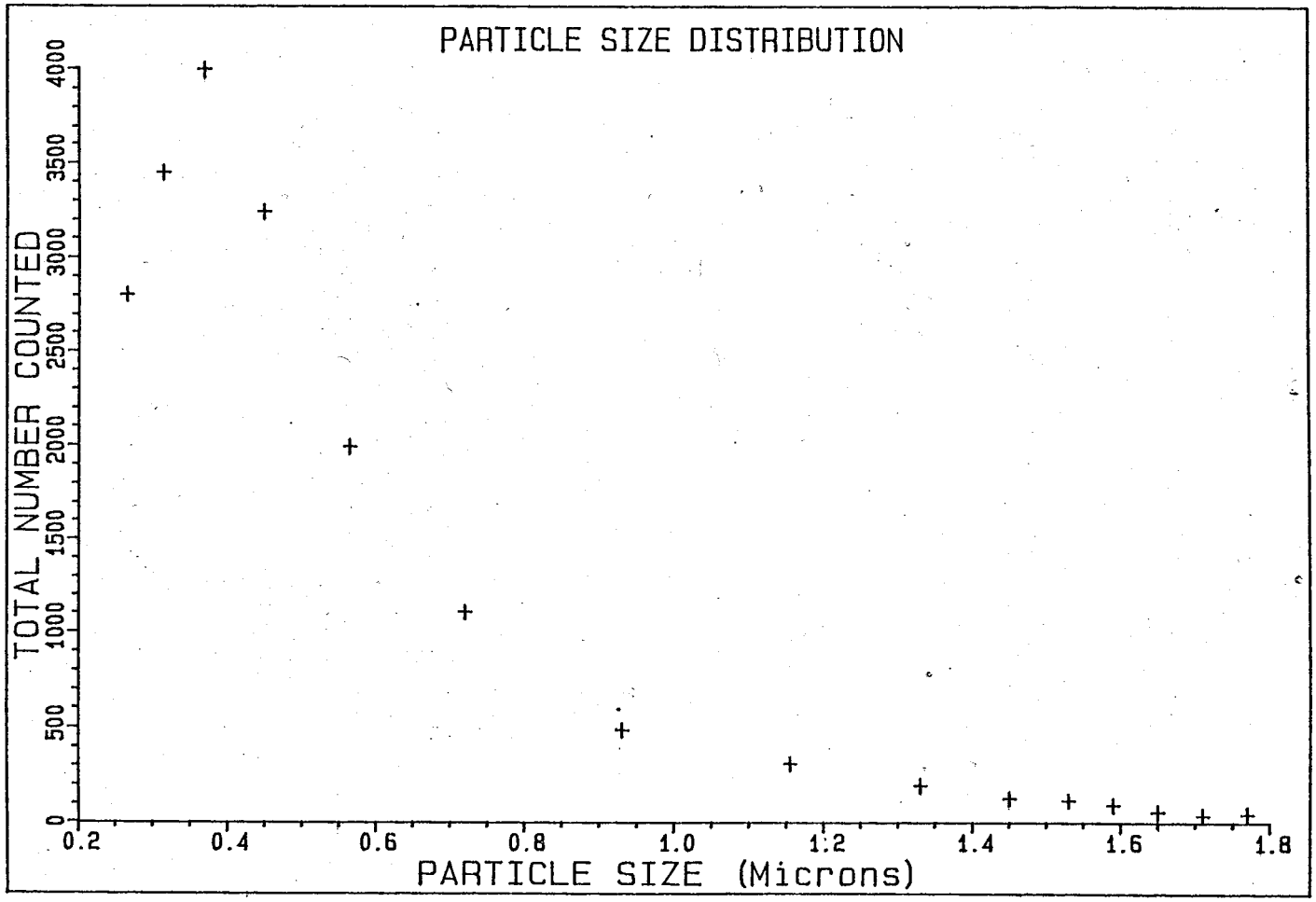
PARTICLE SIZE DISTRIBUTION
TOTAL NUMBER COUNTED
0
500
1000
1500
2000
2500
3000
3500
4000
0.2
0.4
0.6
0.8
1.0
1.2
1.4
1.6
1.8
PARTICLE SIZE (Microns)

REFERENCES

1 Dorman R G, Dust control and air cleaning, p. 551, International series of monographs in heating, ventilation and refrigeration, vol 9, Pergamon press, 1974.

2 ACID RAIN, A review of the phenomena in the EEC and Europe, Environmental resources Ltd., Published by Grahan and Trotman for the Commission of the European Communities, 1983).

3 Derwent R, The occurrence and significance of air pollution by photochemically produced ozone in the British Isles, 1982-1985, Warren Spring Laboratory, Report LR227, 1976.

4 Davies C N, Dust is dangerous, Faber and Faber, London, 1954.

5 Ashby E and Anderson M, The politics of clean air, Monographs on Science and Technology, and Society, Clarendon Press Oxford p. 104-105, 1981.

6 Stern A C, Air Pollution, Volumes 1 and 2, Academic Press, New York, 1962.

7 User guide to fire and explosion hazards in the drying of particulate materials; Institute of chemical engineers, 1977.

8 Dust explosion in factories; Booklet number 22, Health and safety executive, Her Majesty's stationary office, 1970.

9 Explosion venting, code 68, National Fire Protection, USA, 1978.

10 Douglas W C, Particulate contamination and microelectronics manufacture: An introduction; IBM Thomas J Watson Centre, York Town Heigths, NY 10598. Aerosol Science Technology, The Journal of the American association for aerosol research. Vol. 5, Number 3, 1986.

11 Microbial aspect of Pollution, p. 71-89, edited by Syke and Skinner, Academic Press, London, 1971.

12 Stenhouse J I T, High inertia fibrous filtration-option conditions, Filtration and Separation, 15(2), pp. 128-134, 1978.

13 Industrial Pollution Control Handbook, (Pollution control in the phamaceutical industry, p. 17-1 to 17-34), edited by Herbert F L, 1971.

14 Wells R M, Magnetic Filtration in Magnetic Systems, Filtration and Separation, 1977.

15 Filtration principles and practices part 1, Chemical processing and Engineering, Vol. 10, edited by Clyde Orr, Marcel Dekker Inc., NewYork and Basel.

16 Wallis B A, Mineral Processing Technology, (An introduction to the practical aspects of ore treatment and mineral recovery, SI/Metric Units), 3rd Edition,Pergamon Press, 1985.

17 Oberteuffer J A, High Gradien Magnetic Separation: Basic principles, Devices and Applications, Industrial application of magnetic separation, Proc. of an Int. Con. at Franklin Pierce College, Ringe, New Hampshire, July 30-August 4, 1978.

18 Oathley C, Electric and Magnetic Fields (An Introduction), p.12, Cambridge University press, Cambridge, 1976.

19 Oberteuffer J A and Arvidson Bo R, General design features of industrial HGM filters and separators, IEEE Proceedings, Rindge, New Hampshire, 1978.

20 ASHRAE Handbook, (1981 Fundermentals), Section 2.

21 User guide to dust and fume control, 2nd Edition, Institute of Chemical Engineers.

22 Batel W, Dust extraction technology, p. 59, 1976.

23 Gooding C H and Sigmon T W, Particulate emission control by HGMS, Magnetic Separation Conference, New Hampshire, 1978.

24 Kihlstedt P G and Skold B, Concentration of magnetic ores with dry magnetic separators of the Mortsell-Sala type , 5th International Minerals Processing Conference, Institute of Mineral and Metallurgy, London, pp. 69, 1963.

25 Taggart A F, Elements of ore dressing, pp. 44, John Wiley and Sons Inc., New York, p.13-26, 1909.

26 Yarar B and Kitchener J A, Selective flocculation of minerals, Inst. Min. and Met. Trans. ,1971.

27 Stone W T D, Determination of the basic characteristics of a multi-pole collecting surface for strongly magnetic particles of small dimension, 7th Inter. Mineral Processing Congress, Prague, pp. 69, 1970.

28 Taggart A F, Handbook of mineral dressing, John Wiley and Sons, New York, p. 13-23, 1945.

29 Here is a Totally New Method of Sewage Treatment, House and Home, McGraw-Hill, Inc., 1972.

30 Latour de C, Magnetic separation in water pollution control, IEEE Tran. Magnetics, vol. Mag-9, Sept. 1973.

31 Stone W J D, Wet magnetic separator for feebly magnetic minerals 2, 5th Inter. Minerals Precessing Congress Proc. Instit. of Mineral and Metallurgy London, p. 733, 1963.

32 Jones G H, The separation of strongly magnetic particles particularly those of small dimensions, 7th Inter. Minerals Processing Congress, Proc. p. 405, 1964.

33 Minnick L J, The application of the Roto-Flux magnetic separator to pulverized coal fly ash, Am. Soc. Mech. Eng., p. no. 61-WA-313, 1961.

34 Melville D, Red blood cells in HGMS, IEEE Proceedings, Rindge, New Hampshire, 1978.

35 Davies C N, Air Filtration, Academic Press, New York, 1973.

36 Lee K W and Liu B Y, Theoretical study of aerosol filtration by fibrous filters, Aerosol Sci. Technology, 1:147-161, 1982.

37 Boucher R F and Lua A C, Pressure losses in Random wire matrices at intermediate Reynolds Number, J. Aerosol Sci., Vol. 15, No. 5, pp 625-636, 1984.

38 Application of HGMS to fine particle control, Industrial Env. Prot. Lab., Office of research and Development, U S Env. Prot. Agency, North Carolina, 227, 1977.

39 Stenhouse J I and Freshwater D C, Particle adhesion in fibrous filters, Trans. Instn. Chem. Engrs, Vol. 54, 1976.

40 Devies C N and Peetz C V, Proc. R. Soc., p 234-269, 1956.

41 Application of HGMS to fine particle control, Environmental Protection Technology Series. EPA-600/2-77-230, 1977.

42 Ranz W E and Wong J B, Impaction of dust and smoke particles on surface and body collectors, Industrial and Engineering Chemistry, Vol 44, number 6, pp 1371-1381, June 1952.

43 Birss R R, Gerber R, Parker M R, Theory and design of axially ordered filters for high intensity magnetic separation, IEEE Trans. on Magnetics, Vol. MAG-12, No. 6, 1976.

44 Friedlander F J, Takayasu M, Retting J B and Kentzer C P, Studies of single wire parallel stream type of HGMF, IEEE Trans. on Magnetics, Mag-14, No 5, 1978.

45 Svarovsky L, Solid-Gas separation (Handbook of powder technology), Edited by J C Williams and T Allen,

Elsevier, volume 3.

46 Elliot M N and Horsley D C, Gas cleaning in the nuclear fuel industry, Filtration and Separation, 15(1), pp. 27-31, 1978.

47 Krupp H, Particle adhesion, Theory and Experiments, Advances Colloidal Interface Science, Vol. 1, pp 111-139, 1967.

48 Loffler F, (a) Study of adhesion forces between solid particles and fiber surfaces; (b) Adhesion of dust particles to fiber and particle surfaces, Staub Rein Luft, 26, (7), 274-280, 1966, Staut_Reinh. Luft, 28, (11), 456-462, 1968.

49 Kottler W, Krupp H and Rabenhorst H; Adhesion of electrically charged particles, 2 angew Physik 24, 4, 219-223, 1968.

50 Svarovsky L, Solid-Gas Separation, Handbook of Powder Technology, p. 92, Vol. 3, Elsevier Sci. Pub. Com., 1981.

51 Zebel G , Deposition of aerosol flowing past a cylindrical fiber in a uniform electric field, Journal of colloidal science, Vol. 20, pp 522-54, 1965.

52 Bean C P, Theory of magnetic filtration, Bulletin of American Physics Soc., vol 16, pp 350, 1971

53 Oberteuffer J A, High gradient magnetic separation, IEE Trans. Magn., vol. MAG-9, pp 303-306, 1973.

54 Watson J H P, Magnetic filtration, Journal of applied Physics, vol 44, pp 4209-4213, 1973.

55 Lawson W F, The dynamics of paramagnetic particles near a magnetic wire M S Thesis, West Virginia University, Morgantown, WV ,1976

56 Lawson W F, Simons W H, and Treat R P, The dynamics of a praticle attracted by a magnetized wire, Journal of applied Physics, vol 48, No. 8, 1977.

57 Jackson J D, Classical Electrodynamics, 2nd Edition, pp. 198, New York, 1941.

58 Underwood R L, Calculation of incompressible flow past a circular cylinder at moderate Reynolda number, Journal of Fluid Mechanics, vol. 37, pp 95, 1969.

59 Corcoran W H, Opfel J B, and Saga B H, Momentum Transfer in Fluids, Academic Press Inc., New York, 1956.

60 Thom A, The flow past circular cylinders at low speeds, Proc. R. Soc. A., vol 141, pp. 657, 1933.

61 Okeke O O, Ph.D progress report, Dept. of Mechanical Engineering, University of Sheffield, (Unpublished), 1985.

62 Cumming D L, Himmelblau D, Oberteuffer J, Capture of small paramagnetic particles by magnetic forces from low speed fluid flows, pp. 569, ChE Journal, vol 22, no. 3, 1976.

63 Zimmel Y, Effects of concentration and characteristic distribution of electromagnetic separation of polydisperse mixtures, IEEE Trans. on Mags., Vol. 20, No. 4, 1984.

64 Carnahan B, Luther H A, and Wikes J D, Applied numerical methods, John Wiley and sons Inc., New York, 1969.

65 Kunii D and Levenspiel, Fluidization Engineering, Robert E Krieger Pub., p 73 and 76, (1977).

66 British Standard 893, Methods for the measurement of the concentration of particulate material in ducts carrying gases, 1978, (Confirmed 1986).

67 Noss P, Measurement methods and instruments for determining the dust contents of gas streams, Brennstoff-Warme-Kraft, 4, 227/233, 1952.

68 Dennis R , Samples W R, Anderson D M and Silverman L, Isokinetic Sampling Probe, Ind. Eng. Chem., 42, 294/302, 1957.

69 Davies C N, Sampling of Aerosols. Entry of particles into sampling tubes and heads, Steib-Reinhalt, Luft, 28, (6), 219/225, 1968.

70 Ruping G, Significance of Dust stream measurement by Isokinetic sampling probes, Staub-Reinhalt, Luft, 28, (4), 137/144, 1978

71 Walter E, Problems of sampling probes and partial stream sampling for dust content determination in gas streams, Staub, (53), 880/898, 1957.

72 Vitols V, Theoretical limits of errors due to anisokinetic sampling of particulate matter. J Air pollution Control Association, 16, (2), 79/84 1966.

73 Boucher R F and Lua A C, HGMF of gasous flows, International Symposium, Electrical and Magnetic Separation and Filtration Technology, Antwerp, 1984.

74 Wakeman R J, and Holdich R G, Theoretical and experimental modelling of solid and liquid pressure in batch sedimentation, World Filtration Cong. 3, Upland press, Croydon, England, 1,346, 1982.

75 Boucher R F and Markland E, Fundamentals of Fluidics, 1971.

76 Benedict R P, Fundamentals of pipe flow, A Wiley Inter Science Publication, p 376, 1981.

77 Boucher R F and Tippett J P, An investigation into the advantages of fluidics in fluid processing, part 2, An inventry of power fluidics, FFA TN 1982-25.

78 Comparin R A, On the limitation and special effects in fluidic jet amplifiers, ASME symp., Fluidic Jet Control Devices, 1962.

79 Stenning A and Ozgu M R, Transient switching of monostable fluid amplifiers, paper X6, 6th Cranfield Fluidics Conference, 1972.

LIST OF PUBLICATIONS

Publications arising from this investigation yet:

1. R F Boucher and O O Okeke, High Gradient Magnetic Filtration (HGMF) of paramagnetic dust using randomly packed cylindrical fibres, Filtech Conference, Utrecht, Holland, 23-25 Sept., 1987.

2. R F Boucher and O O Okeke, Choice of Woven Wire as a High Gradient Filtration (HGMF) Medium for paramagnetic dust. (To be published in the Journal of Aerosol Science Technology).